

Enabling RF Technology for Ultrahigh Field MRI:
Development and Application of
Self-Grounded Bow-Tie Dipole Antenna

vorgelegt von
Dipl.-Ing., B. Sc.
Thomas Wilhelm Eigentler
ORCID: 0000-0001-8252-450X

an der Fakultät V – Verkehrs- und Maschinensysteme
der Technischen Universität Berlin
zur Erlangung des akademischen Grades

Doktor der Ingenieurwissenschaften
- Dr.-Ing. -

genehmigte Dissertation

Promotionsausschuss:

Vorsitzender: Prof. Dr. rer. nat. Tobias Schäffter

Gutachter: Prof. Dr.-Ing. Marc Kraft

Gutachter: Prof. Dr. rer. nat. Thoralf Niendorf

Tag der wissenschaftlichen Aussprache: 09. März 2022

Berlin 2022

Zusammenfassung

Die Magnetresonanztomographie (MRI) ist ein wichtiges bildgebendes Diagnoseverfahren mit der Anwendung in vielen medizinischen Disziplinen. Die Forschung zu ultrahohen Magnetfeldern (UHF, $B_0 \geq 7.0$ T) im humanen Bereich wird durch technische und wissenschaftliche Errungenschaften getrieben und basiert auf einer höheren Sensitivität, einem verbesserten Signal-Rausch-Verhältnisses (SNR) sowie eine Veränderung der gewebspezifischen MR Eigenschaften. Die höhere Feldstärke resultiert auch in einer erhöhten Radiofrequenz (RF) für die MRI Signalübertragung (= Larmorfrequenz, $f \approx 298$ MHz bei $B_0 = 7.0$ T). Die Wellenlänge des RF Signals im Gewebe ist dabei bezogen zur Zielanatomie (e.g. Schädel, Oberkörper und Abdomen) verkürzt was zu konstruktiven und destruktiven Interferenzen des elektromagnetischen Feldes (EMF) führt. Diese Interferenzen ergeben ein heterogenes RF Transmissionsfeld (B_1^+) mit Abschattungen, massiven Signalabfällen oder Signalausfällen welche die Vorteile der UHF-MRI durch eine beeinträchtigte Bildqualität schmälert.

Die UHF Herz MR (CMR) profitiert von einem SNR-Gewinn sowie von veränderten gewebspezifischen MR Eigenschaften bei höheren Feldstärken. Jedoch wird die B_1^+ Verteilung, neben der gegebenen RF wellenlängenabhängigen Heterogenität, durch dielektrische Gradienten im Bereich des Thorax zusätzlich beeinträchtigt. Die anwendungsbezogene Forschung und Entwicklung auf dem Gebiet der UHF-CMR konzentriert sich auf die Verbesserung der Quantifizierung der Herzkammernmorphologie, des myokardialen T_1 - und T_2^* -Mappings, der Fett-Wasser-Bildgebung und der Gefäßbildung inklusive der Flussbildung (4D-Flow). Die Weiterentwicklung dieser Methoden streben eine breite klinische Anwendung an und profitieren von einer homogenen B_1^+ Verteilung im Herzen und in der Gefäßstruktur. Das primäre Ziel der der Forschung und Entwicklung von RF Antennenarraytechnologie ist eine Optimierung der B_1^+ Verteilung. Das sekundäre Ziel ist die Verbesserung der Effizienz durch die Verringerung der spezifischen Absorptionsrate (SAR) mittels einer elektrischen Feldoptimierung. Die Kontrolle des elektrischen Feldes kann aber auch über die konventionelle MR Bildgebung hinaus genutzt werden und ermöglicht konzeptionell eine lokalisierte und gezielte RF induzierte thermische Intervention. Die Kombination von MRI und thermischen Interventionen in einem integrierten Thermal MR System ermöglicht die Anpassung und Verbesserung der lokalen Intervention durch eine Supervision der Behandlung mittels MR-Thermometrie. Das Thermal MR System stellt damit eine technologische Plattform dar, welche eine umfassende Untersuchung der Auswirkungen der Temperatur auf molekulare, biochemische und physiologische Prozesse erlaubt. Letztlich kann die Plattform Erkenntnisse darüber liefern, wie die Temperatur für Diagnosen und Therapien in vivo genutzt werden kann.

Die Kontrolle der EMF Verteilung durch ein RF Antennen Array ist abhängig von den Abstrahlungseigenschaften der einzelnen Antennenelemente. Elektrische Dipole stellen durch eine linear polarisierte Stromverteilung und eine Abstrahlungsrichtung orthogonal zur Antenne eine vielversprechende Option dar. Allerdings ist die Kanalzahl und damit der Freiheitsgrad für die EMF Optimierung bei bisher vorgestellten Antennenkonzepten durch die Größe und die Kopplung zwischen den Elementen begrenzt. Der erste Abschnitt dieser Arbeit befasst sich mit dem Entwurf, der Implementierung und der Validierung einer Self-Grounded Bow-Tie (SGBT) Antenne in Kombination mit einem dielektrisch gefüllten Gehäuse. Eine schmalbandige Antennenvariante wird in einer 32-Kanal Sende-/Empfangs-Array Konfiguration für UHF-CMR bei 7,0 T vorgestellt. Der zweite Abschnitt befasst sich mit der Entwicklung eines modifizierten breitbandigen SGBT-Konzepts für das Thermal MR System. Diese Antennenvariante erhöht die Freiheitsgrade für die Optimierung der elektrischen Feldverteilung um die Interventionsfrequenz und erlaubt eine Verbesserung der lokalen Erwärmung (Größe, Homogenität und Spezifität). Im dritten Abschnitt dieser Arbeit wird die Implementierung und Validierung eines Signalgenerators in Verbindung mit der im zweiten Abschnitt vorgestellten Breitbandantennenvariante vorgestellt. Der Signalgenerator erzeugt ein Interventionssignal mit der zeitabhängigen Anpassung von Amplitude, Phase und Frequenz für jeden Kanal. Die Entwicklungen und Erkenntnisse dieser Arbeit bieten einen konzeptionellen Rahmen für eine Vielzahl von realen Anwendungen, welche von der konventionellen MRI bis zu einem integrierten interventionellen Thermal MR System reichen.

Abstract

Magnetic resonance imaging (MRI) is an important diagnostic imaging modality free of ionizing radiation. Sensitivity gain, signal-to-noise ratio (SNR) considerations, and changes in the tissue dependent MRI properties. Together with technical and scientific developments further research into increasing the magnetic field strength is justified, culminating in human applications at ultrahigh magnetic field (UHF, $B_0 \geq 7.0$ T) MRI. Elevating the field strength results in an increased radiofrequency (RF) for signal transmission and reception in MRI (= Larmor frequency, $f \approx 298$ MHz at $B_0 = 7.0$ T). The wavelength of this RF signal becomes sufficiently short when passing through tissue relative to the size of the target anatomy of the brain, upper torso, or abdomen. This phenomenon leads to constructive and deconstructive interference of the electromagnetic field (EMF) distribution, which results in a high susceptibility for non-uniformities in the magnetic RF transmission field (B_1^+). This detrimental excitation field distribution can cause shading, massive signal drop-off or even signal voids, and potentially offset the benefits of UHF-MRI due to compromised image quality.

UHF cardiovascular MR (CMR) benefits from SNR gains and changes in the tissue dependent MRI properties, but the B_1^+ distribution – in addition to the wavelength dependent non-uniformities – is further compromised by a dielectrically heterogeneous tissue environment. Research on UHF-CMR focuses on the improvement of the cardiac chamber morphology quantification, myocardial T_1 - and T_2^* -mapping, fat-water imaging, and vascular imaging (4D-flow). These applications benefit from a homogenous B_1^+ within the heart and the vascular structure. Several published reports on the development of RF antenna array technology tailored for UHF-CMR address this challenge with ideas and achievements to enable broad clinical UHF-CMR applications in the future. The primary objective of advancing this RF technology is to achieve a uniform B_1^+ distribution in the heart and the vascular structure with optimizing the magnetic field pattern. The second objective is the improvement of the RF antenna's efficiency with the reduction of the specific absorption rate (SAR), which is achieved by an optimization of the electric field pattern. The control of the electric field is furthermore conceptually appealing beyond conventional MR imaging modalities and useful for localized and targeted RF induced thermal intervention. Combining MRI with a thermal intervention modality in an integrated Thermal MR system permits direct supervision of the treatment via MR-thermometry, as well as adapting and improving the focal point quality of the RF power deposition. The Thermal MR system is a platform for comprehensive investigation of the effects of temperature on molecular, biochemical, and physiological processes, ultimately yielding insights into temperature utilization for diagnosis and therapy in vivo.

EMF control of an RF antenna array depends on the radiation pattern of the antenna elements. Electrical dipoles are promising for UHF-MRI due to a linear polarized current pattern and an energy deposition perpendicular to the antenna. However, the channel count and therefore the degree of freedom for EMF shaping of previously reported antenna concepts is limited by the geometric extent and the coupling between the elements. The first section of this work addresses the design, implementation, and validation of a novel small-sized Self-Grounded Bow-Tie (SGBT) antenna, in combination with a dielectrically filled housing. The narrowband SGBT antenna variant is used in a 32-channel transmit/receive array configuration for UHF-CMR at 7.0 T. The second section focuses on the development of a modified broadband SGBT concept for the Thermal MR system. The broadband antenna increases the degree of freedom with an adaptation of the intervention frequency to improve the focal point quality (size, homogeneity, and specificity). The third section presents the implementation and validation of a signal generator in conjunction with the broadband SGBT variant introduced in section two. The device allows the generation of the intervention signal with a time dependent, channel-wise adaptation of amplitude, phase, and frequency. The work of this thesis offers a technical and conceptual framework for an increased degree of freedom for EMF shaping for a multitude of applications ranging from UHF-MRI to interventional MRI.

Table of Contents

Table of Figures.....	ix
Table of Tables.....	x
Abbreviations.....	xi
1 Introduction.....	1
1.1 Rationale.....	1
1.2 Magnetic Resonance Imaging.....	4
1.3 Cardiovascular Magnetic Resonance Imaging at Ultrahigh Field ($B_0 = 7.0$ T).....	7
1.4 Thermal Magnetic Resonance (Thermal MR).....	9
1.5 Development of Radiofrequency Field Technology in an Ultrahigh Field MRI Environment.....	11
1.5.1 Radiofrequency Technology Design Objectives for Ultrahigh Field MRI.....	11
1.5.2 Radiofrequency Technology Design Objectives for Thermal MR.....	12
1.5.3 Radiative Elements.....	13
1.5.4 Signal Generation for Thermal MR.....	15
1.6 Validation Processes.....	16
1.6.1 Radiofrequency Antenna Characteristics Assessment.....	16
1.6.2 Signal Generation Characteristics Assessment for Thermal MR.....	17
1.6.3 Transmission Field Mapping.....	17
1.6.4 Parallel Imaging.....	18
1.6.5 MR-thermometry.....	19
2 Published Manuscripts.....	21

2.1	32-Channel Self-Grounded Bow-Tie Transceiver Array for Cardiac MR at 7.0 Tesla	21
2.2	Wideband Self-Grounded Bow-Tie Antenna for Thermal MR.....	40
2.3	Design, Implementation, Evaluation and Application of a 32-Channel Radio Frequency Signal Generator for Thermal Magnetic Resonance Based Anti-Cancer Treatment	55
3	Discussion	79
3.1	Self-Grounded Bow-Tie Antenna	79
3.2	Narrowband Antenna Application for Cardiovascular MRI.....	83
3.3	Broadband Antenna Application for Thermal MR	87
3.4	RF Signal Chain Systems Design for Thermal MR	90
4	Conclusions and Outlook	93
	References	96
	List of Author’s Publications	107
	Acknowledgements	111

Table of Figures

Figure 1: Self-Grounded Bow-Tie antenna building block in (a) a narrowband antenna variant and (b) a broadband antenna variant.	4
Figure 2: Definition of the net magnetization (M) and the contribution of the M_{xy} and M_z . The flip angle is a function of the energy of the external B_1 field. Figure adapted from key publication. ¹⁶	5
Figure 3: Block diagram of the envisioned Thermal MR setup. The work in this thesis describes in detail the 32-channel signal generator in the thermal intervention signal chain and the SGBT antenna as an element of the SGBT applicator.	10
Figure 4: Synopsis of radiation pattern of dipole antennas with the 3D far-field function and a 2D far-field function at the xy -plane. The antennas are (a) the narrowband Self-Grounded Bow-Tie antenna, (b) the broadband Self-Grounded Bow-Tie antenna, (c) the Bow-Tie antenna, (d) the fractionated dipole, and (e) a 500 mm dipole antenna.	80
Figure 5: B_1^+ field distribution of the introduced narrowband Self-Grounded Bow-Tie antenna building block (a) with and (b) without hydrogel pad. The E-field distribution of the antenna system (c) with (d) without hydrogel pad. The antennas were tuned and matched to 297.2 MHz in this visualization. ..	82
Figure 6: Electric surface current distribution on (a) the broadband Self-Grounded Bow-Tie antenna and (b) the narrowband Self-Grounded Bow-Tie antenna immersed in water as dielectric. The broadband antenna variant uses a low-loss, low-permittivity material to spread the current distribution and increase the broadband behaviour of the antenna. The presented antennas were tuned and matched to 297.2 MHz for a better comparison.	88
Figure 7: First Thermal MR applicator prototype based on the introduced wideband Self-Grounded Bow-Tie building block design. The prototype includes 20-channels in a circular, two-row arrangement for head applications for example.	95

Table of Tables

Table 1: Synopsis of statistics on the parallel imaging performance up to $R = 4$ for the 32-channel Self-Grounded Bow-Tie⁵², 32-channel loop antenna⁹², 8-channel Fractionated dipole combined with 16-channel loop antenna⁸⁸, and 16-channel Bow-Tie⁸⁷. Except for the 8-channel Fractionated dipole combined with 16-channel loop antenna which uses SENSE, GRAPPA is used. 32-channel loop antenna and 16-channel Bow-Tie one subject is investigated therefore the statistic is presented as mean value. 86

Abbreviations

^{19}F	...	Fluorine
^1H	...	Hydrogen
2D	...	two dimensional
3D	...	three dimensional
ACS	...	autocalibration signals
AFI	...	actual flip angle imaging
ASL	...	arterial spin labelling
B_0	...	static magnetic field
B_1	...	time varying magnetic flux density
B_1^+	...	magnetic transmission field
B_1^-	...	magnetic reception field
BMI	...	body-mass-index
BOLD	...	blood oxygenation level dependent
CMR	...	cardiovascular magnetic resonance
COV	...	coefficient of variation
CT	...	computer tomography
CTX	...	combined transmit
D_2O	...	deuterium oxide
DREAM	...	dubbed dual refocusing echo acquisition method
EF	...	extreme field
E-field	...	electric field
EM	...	electromagnetic
EMF	...	electromagnetic field
FRM	...	finite element method
FIT	...	finite integration technique
FLASH	...	fast low-angle shot
FOV	...	field of view
g-factor	...	geometry factor in parallel imaging
GPS	...	global positioning system
GRAPPA	...	generalized autocalibrating partial parallel acquisition
GRE	...	gradient echo

IEC	...	International Electrotechnical Commission
\vec{J}	...	angular momentum vector
l_a	...	self-grounded bow-tie antenna length
LLS	...	linear least squares
\vec{M}	...	net magnetization vector
\vec{M}_{xy}	...	xy component of the net magnetization vector
\vec{M}_z	...	z component of the net magnetization vector
MLS	...	magnitude least squares
MRI	...	magnetic resonance imaging
NMR	...	nuclear magnetic resonance
NVA	...	network vector analyser
OECD	...	Organisation for Economic Co-operation and Development
PFCE	...	perfluoro-15-crown-5-ether
PLL	...	phase-locked loop
PRFS	...	proton resonance frequency shift
PTX	...	parallel transmit
R	...	reduction factor in parallel imaging
RF	...	radiofrequency
ROI	...	region of interest
S-matrix	...	scattering matrix
SAR	...	specific absorption rate
SAR _{10g}	...	specific absorption rate average over 10 g tissue / material
SENSE	...	sensitivity encoding
SGBT	...	self-grounded bow-tie
SI	...	signal intensity
SI _α	...	signal intensity ration for actual flip angle imaging
SMASH	...	simultaneous acquisition of spatial harmonics
SNR	...	signal to noise ratio
SWI	...	susceptibility weighted imaging
T	...	Tesla
T ₁	...	longitudinal relaxation time

T_2	...	transverse relaxation time
T_2^*	...	effective transverse relaxation time
$\tan(\delta)$...	dielectric loss tangent
TE	...	echo time
Thermal MR	...	thermal magnetic resonance
TR	...	relaxation time
TR_α	...	relaxation time ratio for actual flip angle imaging
TV	...	target volume
TX	...	transmit
UHF	...	ultrahigh field
UISNR	...	ultimate intrinsic signal to noise ratio
V_{actual}	...	actual voltage for actual flip angle imaging
\vec{V}_{exc}	...	excitation vector of a radiofrequency array
$V_{\text{reference}}$...	reference voltage for actual flip angle imaging
VGA	...	variable gain amplifier
VOPs	...	virtual observation pointy
w_a	...	self-grounded bow-tie antenna width
Z	...	impedance
α	...	self-grounded bow-tie antenna aperture angle
α_{actual}	...	actual flip angle
α_s	...	proportionality constant for proton resonance frequency shift
α_{nominal}	...	nominal flip angle for actual flip angle imaging
$\alpha_{\text{reference}}$...	reference flip angle for actual flip angle imaging
χ	...	magnetic susceptibility
ϵ_r	...	relative permittivity
γ	...	gyromagnetic ratio
μ_r	...	relative permeability
$\vec{\mu}$...	magnetic moment
ω_0	...	larmor frequency
ω_{local}	...	local resonance frequency shift due to nuclei shielding effect
Φ_{target}	...	target function for shim optimization

Φ_{SAR}	...	maximum specific absorption rate for shim optimization
φ_{ref}	...	reference image for magnetic resonance thermometry
φ_t	...	image at timepoint t for magnetic resonance thermometry
ρ	...	density
σ	...	conductivity
σ_s	...	screening variable for proton resonance frequency shift
τ	...	pulse duration
ϑ_s	...	nuclei screening constant for proton resonance frequency shift

1 Introduction

Non-invasive imaging technologies are key to early diagnosis and an effective treatment of pathological conditions in the clinical routine of various medical disciplines. Magnetic resonance imaging (MRI) enables the visualization of the body's inner structures without the use of ionising radiation used in x-ray and computer tomography (CT). It offers an excellent soft tissue contrast at a high penetration depth as well as high spatial and temporal resolution. Such benefits drive the demand for MRI systems as well as MRI diagnostic scans. The registered MRI units per 1.000.000 inhabitants within countries of the Organisation for Economic Co-operation and Development (OECD) range between 0.45 (Israel, 2018) and 22.64 (Germany, 2017).¹ The mean installation rate of MRI devices per year among the registered OECD countries in the 10-year timeframe from 2008-2018 was 10%.¹ In the countries of the European Union a mean of 12% per year was observed, with a maximum increase of 33% per year for Lithuania.¹ Recognizing the advantages of MRI, the number of exams per 1.000 inhabitants within the OECD range between 2.2 (Netherlands, 2018) and 124.6 (Germany, 2017).² While MRI technology is widely applied, developments and scientific findings continue to add relevant diagnostic value. The work of this thesis demonstrates the development of radiofrequency (RF) hardware for cardiovascular diagnostics as well as thermal intervention within an MRI system.

1.1 Rationale

MRI scanners can be classified by their static magnetic field strength (B_0) in Tesla (T). Continuous improvements in engineering facilitates an increased B_0 , enabling an elevated signal-to-noise ratio (SNR).³⁻¹⁰ In clinical routine magnetic field strengths of $B_0 \leq 3$ T are widely used. For scientific purposes as well as in specialized clinical applications, ultrahigh field (UHF, $B_0 \geq 7.0$ T) are in use and under investigation. The gain in SNR can be translated into enhanced spatial and temporal resolution.¹¹⁻¹⁵

The B_0 increase furthermore results in an elevation of the specific precession frequency (Larmor frequency) of MR nuclei. The Larmor frequency scales linearly with B_0 (≈ 42.58 MHz/T) resulting in approximately 298 MHz for 7.0 T for hydrogen (^1H) MRI, the most commonly used nuclei in clinical applications.¹⁶ The wavelength at this frequency of 1 m in free space is reduced to 12-13 cm when propagating through human tissue with a specific dielectric constant (ϵ_r).¹¹⁻¹⁵ This physical

phenomenon may result in constructive and deconstructive interference of the electromagnetic field (EMF) distribution, and hence in a non-homogeneous magnetic transmission field (B_1^+). This may lead to an unwanted signal intensity (SI) variation and in the worst case to signal voids.^{13,14,17} An important measure is the wavelength to field of view (FOV) size ratio. In regions of the body where this ratio is below 1.0, B_1 field non-uniformities dominate. Torso imaging, and in particular MRI of the upper thorax and cardiovascular MRI (CMR), is one of the most challenging endeavours at ≥ 7.0 T. Electromagnetically, the challenge of the short wavelength is exacerbated by the dielectric heterogeneous tissue environment. Furthermore, movement of the heart and the lung requires a fast imaging modality and prospective/retrospective gating for the image acquisition.¹⁴ The increase in SNR at UHF is beneficial to improve image quality, reduce examination time, and enhance or establish contrast mechanisms, with the ultimate goal to map and assess cardiac physiology and pathology.^{11,12,14,15,18,19} For example, the SNR increase can be used to obtain a 12-fold improvement in spatial resolution versus standardized clinical CMR protocols for cardiac chamber morphology quantification.²⁰ This allows improved visualization of fine anatomic structures like the valvar system. UHF fat-water CMR at high resolution with increased chemical shift between fat and water allows explorations into intramyocardial, epicardial, and pericardial fat.^{11,14,21,22} A further application demonstrating enhanced SNR at UHF is the improvement of time-resolved velocity (vascular) imaging using 4D flow sensitized techniques. Applying 4D flow at UHF-MRI holds the promise for improving the study of dynamic effects like flow patterns and wall shear stress assessment in disease.²³⁻²⁵ Prolongation in the longitudinal relaxation time (T_1) at UHF-MRI enables sufficient blood-myocardium contrast for gradient-echo imaging and supports improvements of quantitative CMR.^{14,19,26,27} For quantitative CMR T_1 and effective transverse relaxation time (T_2^*) mapping methods hold the promise to detect diseased tissue (e.g. myocardial infarction or vascular stenosis).²⁷⁻³¹ The increased SNR and the difference of the relaxation times compared to lower field strengths is key to identify novel findings and conclusions from UHF-CMR, but are tied to a homogeneous B_1^+ field distribution in the experiments. The homogenization of B_1^+ is objective to an optimized phase of the signals in an RF antenna array.^{14,15,32} Further degree of freedom is facilitated with controlling the phase and amplitude simultaneously for each independent RF channel.^{13-15,19,32}

In addition to the objective to homogenize the B_1^+ field by adapting the magnetic field in a given region of interest (ROI), exercising control of the electric field (E-field) distribution is feasible. The E-field distribution within tissue results in a global and local increase of the specific absorption rate (SAR) averaged over 10 g of tissue (= SAR_{10g}). In MRI, this represents a limiting factor in the maximum energy available for an investigation. But an intentional SAR increase in a target volume (TV) results in a localized and targeted temperature rise, which is conceptually appealing in the treatment

of pathologies or the investigation of the temperature response of in vivo tissue.^{33–38} Similar to the formation of a locally homogenized B_1^+ distribution, a homogenized temperature rise in the TV is bound to a shaping approach enabling a constructive E-field interference. In the process, healthy tissue should be spared and temperature should be increased to 42–45°C in TV only.³⁹ This concept has more limitations compared to the B_1^+ field shaping and requires a high degree of freedom, where adjustment of the phase and amplitude of the single channels in an RF array is a minimum requirement.^{37,38} Additional improvement of the focal point quality is achieved with allowing an adaptation of the frequency of the intervention RF signal.^{40–42} To allow a further increase of freedom a time-multiplexed beamforming⁴³, a mixed frequency approach⁴⁴, a time- and frequency-multiplexed approach⁴⁵ can be used to improve the focal point quality.^{46,47} Combining the thermal intervention with the versatile contrast mechanisms of MRI in an integrated Thermal MR setup is an attractive concept, as temperature rise can be measured non-invasively through MR-thermometry. This allows the implementation of a control loop concept in a thermal intervention thereby increasing safety.^{48–51} There is an unmet scientific and medical need for Thermal MR with a single RF applicator that allows imaging at ≥ 7.0 T and RF heating with the freedom of adjusting amplitude, phase, and frequency for each channel in the RF applicator. This approach requires a wideband antenna RF array combined with a highly accurate signal generation for the thermal intervention.

The work of this thesis demonstrates an integrated line of advancing RF technology for UHF-MRI. The first section of this work presents the design, implementation, and validation of a Self-Grounded Bow-Tie (SGBT) building block for UHF-CMR (Figure 1a).⁵² The signature characteristic of this antenna type is its strong main lobe directivity at a small size. To reduce the overall antenna size further, a dielectrically filled housing is used to shorten the effective RF wavelength.^{53–56} The second section focuses on the development of a modified broadband SGBT concept as key element of a fully integrated thermal intervention within an 7.0 T MRI (Figure 1b).⁵⁴ The broadband antenna characteristic allows high degree of freedom to improve the interventional focal point quality. The third section presents the implementation and validation of a signal generator in conjunction with the broadband antenna variant introduced in section two.⁵⁷ The device enables a high flexibility in the Thermal MR setup by generating the intervention signals with respect to phase, amplitude, and frequency for each channel of the RF antenna array individually. The findings and drawn conclusions are adaptable and expandable to other UHF-MRI and thermal intervention applications and offers a framework for a high degree of freedom EMF control.

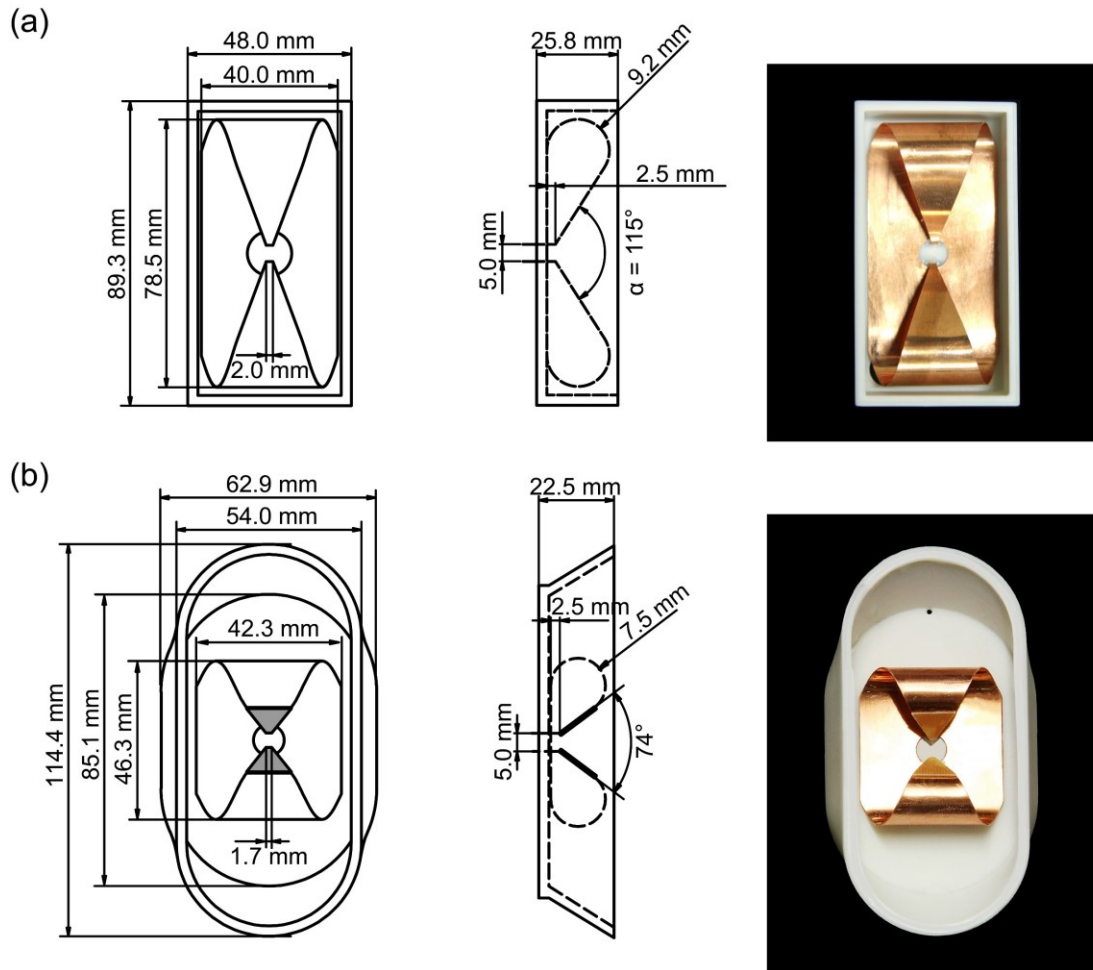


Figure 1: Self-Grounded Bow-Tie antenna building block in (a) a narrowband antenna variant and (b) a broadband antenna variant.

1.2 Magnetic Resonance Imaging

MRI is a key element in the clinical routine for diagnosis of pathologies and treatment planning as well as monitoring. Compared to x-ray and CT it offers excellent soft tissue contrast. Furthermore, MRI offers a high penetration depth as well as good spatial and temporal resolution without ionizing radiation. The versatility of MRI provides a wide variety of opportunities for innovations and applications for the clinical routine as well as basic scientific research.

MRI is based on the nuclear magnetic resonance (NMR) effect, which describes the absorption and emission of RF energy in material and tissue within a static magnetic field.^{58,59} ^1H , which is most widely used in MRI applications, has the quantum mechanical properties required for NMR.

Other nuclei exhibit properties for NMR as well (e.g., ^{14}N , ^{19}F , ^{23}Na). A detailed explanation of the quantum mechanical processes necessary for a nuclei to exhibit NMR is beyond the scope of this thesis, and is further elaborated in key publications on this topic.¹⁶ A simplified perspective represents a spin as a circulating current resulting in a magnetic moment defined by

$$\vec{\mu} = \gamma \vec{J} \tag{1}$$

with the gyromagnetic ratio γ and the angular momentum vector \vec{J} . The presence of an angular momentum allows the nucleus to be aligned with B_0 and to be used for MRI. The B_0 alignment follows the Zeeman effect and can either be parallel (low energy) or anti-parallel (high energy). The absorption or emission of energy results in a transition of the spins between the energy states, whereby the magnetic field B_1 has a specific precession, the Larmor frequency. The Larmor precession follows

$$\omega_0 = \gamma B_0 \tag{2}$$

and with the nuclei-specific gyromagnetic ratio scales linearly with B_0 . To summarize further effects in the MRI acquisition, the net magnetization vector (\vec{M}) is introduced. \vec{M} can be interpreted as a magnetic vector, which is the sum of all spins in a defined volume of material or tissue. In the equilibrium state \vec{M} is parallel to the B_0 field (z-axis, Figure 2).

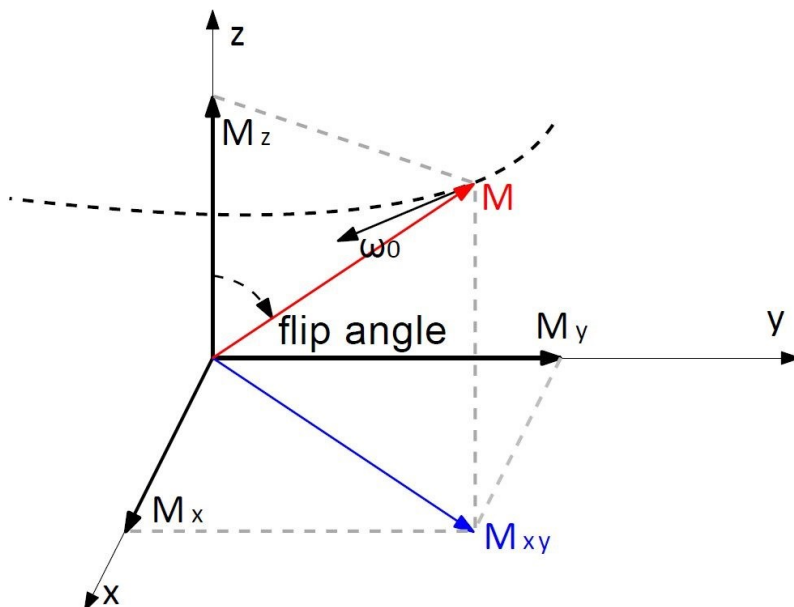


Figure 2: Definition of the net magnetization (\vec{M}) and the contribution of the \vec{M}_{xy} and \vec{M}_z . The flip angle is a function of the energy of the external B_1 field. Figure adapted from key publication.¹⁶

Increasing the energy through transmission of B_1 to the system results in tipping \vec{M} out of the equilibrium state into precession at Larmor frequency. \vec{M} can be split into \vec{M}_z and \vec{M}_{xy} , with the latter rotating around the z-axis on the xy-plane, where the amplitude ratio is dependent on the energy used in the transmission (Figure 2). With no external B_1 field present, \vec{M}_{xy} will reduce with \vec{M}_z increasing until the equilibrium state is reached, whereby this process emits a magnetic radiofrequency field at Larmor frequency again. Besides the B_0 a RF transmission and receiving component is necessary to transmit a B_1^+ and receive a B_1^- field from the material or tissue. As B_1^+ is defined as the right circularly (counter-clockwise) polarized component, B_1^- is defined as the left (clockwise) circularly polarized component of B_1 .^{60,61} This relationship can be illustrated with the “handedness” of the transmit (from the transmitter to the material/tissue) and receive (from the material/tissue to the receiver) direction, where the field must be opposite rotating in order to agree with the direction of the nucleus precession.^{60,61} Nuclei are dependent on their local environment and therefore their magnetic environment. Hence, chemical components can be differentiated and tissue contrast can be observed in clinical applications. This is the key aspect of NMR and MRI to allow an intrinsic tissue contrast due to different relaxation times for a nucleus.

Besides the necessary magnetic field for NMR, Maxwell’s equations describe that an electric field is present simultaneously. This electric field and material or tissue conductivity results in RF energy absorption and hence, in an increased temperature. An arbitrary measure to assess this RF energy deposition is defined as SAR.⁶² SAR in [W/kg] is given at the location \vec{r} by

$$SAR = \int \frac{\sigma(\vec{r}, \vec{f}) |\mathbf{E}\text{-field}(\vec{r})|^2}{\rho(\vec{r})} d\vec{r} \quad (3)$$

where $\sigma(\vec{r}, \vec{f})$ is the conductivity, $|\mathbf{E}\text{-field}(\vec{r})|$ is the magnitude of the electric field, and $\rho(\vec{r})$ is the tissue density. The SAR metric is used in numerical simulations to assess the safety of RF related absorption in order to limit the temperature rise in the whole body as well as in local regions. SAR, is not equivalent to the actual temperature rise, but is used as a method to address RF safety considerations. MRI limits for the SAR_{10g} are summarized by the International Electrotechnical Commission (IEC) in the guideline 60601-2-33.⁶² Following this guideline, the whole body SAR for body transmit systems is limited to 2 W/kg for the normal mode and 4 W/kg for the first level mode averaged over the total patient mass. The SAR_{10g} for local (partial) areas is 10 W/kg for the normal mode and 20 W/kg for the first level scanner mode.⁶² The limits are given for any 6 minute period of the scan session.⁶²

MRI can be interpreted as a spatial determination of the NMR effect; whereby locally varying magnetic fields (magnetic field gradients) are used for a spatial encoding of a received signal. In the most general application, this information is based on the local field dependent Larmor frequency and phase offsets of receiving signals. Further information on the gradient system including its physical and mathematical implications are beyond the scope of this work and are further elaborated in key publications on this topic.¹⁶

1.3 Cardiovascular Magnetic Resonance Imaging at Ultrahigh Field ($B_0 = 7.0$ T)

UHF-MRI will be referred to in this work as MRI at a static magnetic field strength $B_0 = 7.0$ T. The main motivation for increasing the static magnetic field strength is to increase the SNR, because the number of spins available for NMR following the previously introduced Zeeman effect (Section 1.2) is increased.¹⁶ Theoretically achievable SNR values at various field strengths are defined as ultimate intrinsic SNR (UISNR), where – based on electromagnetic considerations – an upper bound of a certain FOV is calculated.^{6–9,11} Already at an early stage of MRI research, it was shown that the NMR signal scales proportional to B_0^2 .³ Taking noise considerations into account, UISNR scales with $B_0^{1.5}$, which is in good agreement with studies on SNR growth rates ($B_0^{1.65}$ for 3.0 T, 7.0 T and 9.4 T)¹⁰ and SNR growth factors (1.4 to 2.0 for field strength improvement from 4.0 T to 7.0 T)⁵. Studies reveal that an UISNR gain is feasible with increasing the magnetic field strengths, but this gain is not homogeneously distributed in the FOV, resulting in an elevated gain in regions close to the RF antenna area and a lower gain for deep lying voxels.¹¹

For UHF-CMR a 2.1 fold increase compared to an equivalent application at 1.5 T was found.⁶³ The increase in SNR at UHF is beneficial to improve image quality, reduce examination time, and enhance or establish contrast mechanisms, with the ultimate goal to map and assess cardiac physiology and pathology.^{11,12,14,15,18,19} The SNR increase relative to 1.5 T can be used to obtain a 12-fold improvement in spatial resolution versus standardized clinical CMR protocols for cardiac chamber morphology quantification.²⁰ This allows improved visualization of fine anatomic structures like the valvar system. UHF fat-water CMR at high resolution with increased chemical shift between fat and water allows explorations into intramyocardial, epicardial, and pericardial fat.^{11,14,21,22} A further application demonstrating enhanced SNR at UHF is the improvement of time-resolved velocity (vascular) imaging using 4D flow sensitized techniques. Applying 4D flow at UHF-MRI holds the promise for improving the study of dynamic effects like flow patterns and the assessment of the wall shear stress in disease.^{23–25} The imaging of even smaller structures like coronary arteries was found to be

improved, but still remains challenging.⁶⁴ Prolongation in the longitudinal relaxation time (T_1) at UHF-MRI (myocardium $T_1 = 1925$ ms at 7.0 T²⁷ vs 950 ms at 1.5 T⁶⁵) enables sufficient blood-myocardium contrast for gradient-echo imaging and supports improvements of quantitative CMR.^{14,19,26,27} For quantitative CMR T_1 and effective transverse relaxation time (T_2^*) mapping methods hold the promise to detect diseased tissue (e.g. myocardial infarction or vascular stenosis).²⁷⁻³¹

The increased SNR and the difference of the relaxation times compared to lower field strengths is key to obtaining novel findings and conclusions from UHF-CMR. Nevertheless, pioneering early clinical applications of 7.0 T MRI are predominately used for head and extremity examinations, because of an unfortunate RF wavelength to FOV size ratio. At 7.0 T (approximately 298 MHz), the wavelength in tissue is shortened from approximately 1 m in free space to only $12-13$ cm, according to the electromagnetic (EM) wave shortening factor defined by $\sqrt{\epsilon_r \mu_r}$ (with $\mu_r = 1$ in biological tissue).¹¹⁻¹⁶ Based on this short EM wavelength in tissue, the wavelength to FOV size ratio for the human thorax is below 1.0 , resulting in non-uniformities of the EMF distribution.⁶⁶ This non-uniformities effect is further exacerbated due to the dielectrically highly heterogeneous tissue environment. These two obstacles for UHF-CMR are the main reason that no volume resonator body coil (birdcage coil) is used. These volume resonator coils are widely spread for MRI ≤ 3.0 T in clinical applications and for smaller target regions at UHF-MRI such as head and extremities, where the wavelength to FOV ratio is close to 1.0 .¹⁷ Promising is the use of local surface RF elements with multiple RF feeding channels for B_1^+ transmission.^{13,15} The so-called RF antenna arrays are able to increase the degree of freedom for B_1^+ shaping. Detailed introduction into the design process of such RF elements can be found in Section 1.5.

The wavelength and tissue environment responsible for non-uniformities of the B_1^+ field provokes deconstructive and constructive interferences of the E-field, where the constructive forms locally elevated SAR following Equation (3). Based on the short wavelength at UHF-MRI, the local SAR_{10g} is commonly the restricting factor following the IEC guideline 60601-2-33 for the limitation of the total power available for RF pulse (Section 1.2).⁶² This knowledge results in further design considerations for local transmit elements in Section 1.5.

1.4 Thermal Magnetic Resonance (Thermal MR)

Biological processes are highly sensitive to temperature changes, making the aberrant temperature distribution in tissue a critical attribute for life.⁶⁷⁻⁶⁹ The thermal consequences of pathological processes have led to a strong interest in temperature as a clinical parameter, but its' investigation has been widely hindered by the lack of a non-invasive method to manipulate and characterize temperature.^{34,70,71} The Thermal MR setup combines a thermal intervention with an UHF-MRI system and is therefore conceptionally appealing, because the versatile MRI contrast mechanisms including MR-thermometry can be used for non-invasive assessment of the temperature distribution in vivo. In addition, the Thermal MR system allows ¹⁹F MRI enabling research in the directions of therapeutics tracking as well as their accumulation assessment.⁷²⁻⁷⁵ The combination of a localized thermal intervention and ¹⁹F MRI suggests furthermore investigations on the controlled release of therapeutics from a thermosensitive nanocarrier with the goal to boost treatment and reduce side-effects.⁷⁶⁻⁷⁸

Non-invasive thermal intervention within an MRI system can be realized based on two physical modalities: the focusing of ultrasound or EM waves. MR guided ultrasound facilitates a high energy deposition in a small target size. This permits thermo-ablation as well as mild thermal interventions (mild hyperthermia) that does not initially destroy cells thermally. Nevertheless, focused ultrasound is limited to a small TV and requires focal point steering procedure to cover a clinically relevant TV.^{79,80} Thermal intervention based of RF power deposition of constructive interfering EM waves on the other hand allows a homogeneous coverage of a clinically relevant, larger TV. Therefore, EM based thermal interventions are promising with regard to mild thermal interventions.⁸¹⁻⁸³ Studies and simulations of targeted RF interventions have shown that an UHF-MR instrument can be adapted to generate focused energy deposition by the use of RF antenna arrays.^{40,56,84}

In contrast to conventional MRI application, as introduced in Section 1.2 and Section 1.3, Thermal MR makes additional use of the E-field distribution, which is commonly the limiting factor in MRI. Similar to the shaping of a constructive interference of B_1^+ at UHF-CMR (Section 1.3) the fundamental idea of Thermal MR is to achieve a constructive E-field interference. Following Equation (3) a high E-field itself implies elevated SAR, resulting in a temperature increase. The target area might be a function of subject variability, and is dependent on the application and the goal of the thermal intervention. The adaptability of the focus point to the specific need can be summarized with the term focal point quality, which describes the focal point size, homogeneity, and location of the energy

1.4 Thermal Magnetic Resonance (Thermal MR)

distribution in the target. Besides the radiation pattern of the single antenna elements and the channel count, which are discussed in Section 1.5, the intervention frequency has a significant impact on the focal point quality.^{40–42} Studies on the ultimate intrinsic SAR (UISAR) revealed that depending on the localization and target size, a frequency optimized RF induced thermal intervention is achieved.⁴¹ A time-multiplexed beamforming⁴³ or a mixed frequency approach⁴⁴ are conceptionally appealing for online focal point quality improvement.^{46,47} Furthermore, it was reported that a time- and frequency-multiplexed approach for a thermal intervention procedure with a range of frequencies applied sequentially is beneficial to improve the focal point quality.⁴⁵ It is suggested to apply a limited number of intervention vectors sequentially (intervention matrix), as a function of amplitude, phase, and frequency, for a limited time duration.⁴⁵ To realize this promising multiplexed approach within an MRI environment an RF antenna system as well as a high-fidelity signal generation system are required to allow on-the-fly adaptation of the thermal intervention vector in a multiplexed approach. The MR-thermometry-based control loop concept allows for an interleaved measurement within the thermal intervention (Figure 3). The envisioned integrated Thermal MR system consists of a second control loop, which utilizes a stable intervention RF signal (Figure 3). To further address these objectives, antenna design and signal generator concepts are described in Section 1.5.

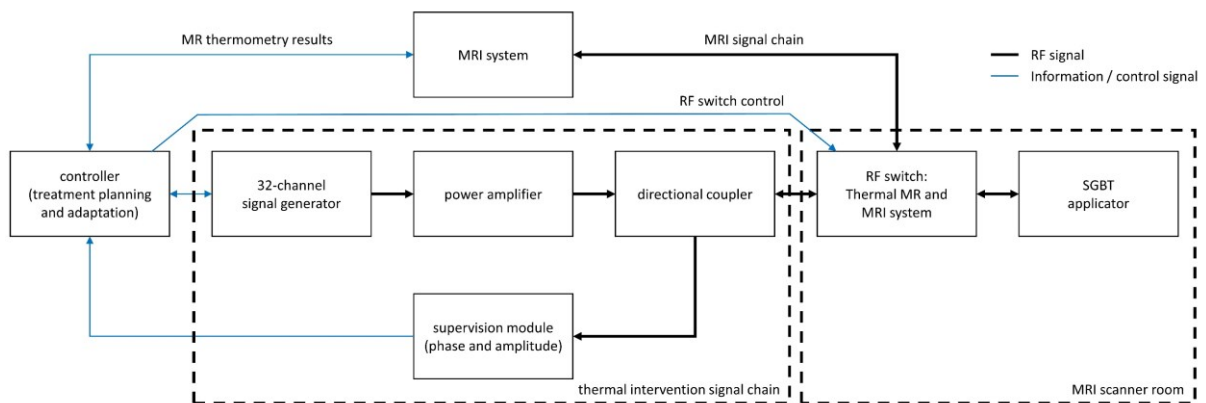


Figure 3: Block diagram of the envisioned Thermal MR setup. The work in this thesis describes in detail the 32-channel signal generator in the thermal intervention signal chain and the SGBT antenna as an element of the SGBT applicator.

1.5 Development of Radiofrequency Field Technology in an Ultrahigh Field MRI Environment

UHF-CMR applications (Section 1.3) as well as the broadband thermal interventions (Section 1.4) require a radiative element; an antenna to transmit an EM wave at a defined frequency or at a defined frequency range. Dipole antenna configurations have gained increased attention for UHF-CMR and RF induced thermal interventions. Electric dipoles have the trait of a linearly polarized current pattern, where RF energy is directed perpendicular to the dipole along the Poynting vector to the object under investigation.^{14,85–90} This results in a symmetrical, rather uniform EMF distribution with increased penetration depth.^{14,85–90} Pioneering RF antenna array developments include stripline-elements¹⁹, stripline waveguide like elements⁹¹, loop elements^{22,30,92–94}, dipoles^{95,96}, slot-antennas⁹⁷, loop-dipoles^{88,98}, and dipole building block elements^{86,87} to be used in studies. Both UHF-CMR and thermal intervention benefit from a high channel count to enhance the degree of freedom for EMF shaping. The goal for the imaging regime is to achieve a homogeneous B_1^+ distribution whereas the goal for the thermal intervention regime is an improved focal point quality. The geometrical decoupling of reported dipole and loop-dipole configurations limits the number of transmit (TX) elements placed on the human body, thus restricting the degree of freedom for EMF shaping.^{88,95,98} Reports on high permittivity dielectric and low loss materials for EM wavelength shortening, referred to as building block designs, allow high-density RF antenna arrays with providing sufficient decoupling.^{54,56} This will allow a high channel count in multiple rows for a rather small ROI (e.g. the human heart).^{54,56,86} The adapted SGBT building block constitutes a proven candidate to be used in the UHF-CMR regime, as well as in the broadband thermal intervention regime. It's strong main lobe enhances the EMF directivity at a low coupling between next neighbour elements and provides the basis for a high density RF antenna array.^{55,99} In contrast to commercially available MRI hardware, the generation of RF signal for thermal intervention requires a comparably long duration and an increased channel count. The multi-channel (32-channel) signal generator forms a key element in the infrastructure to operate the broadband SGBT antenna in thermal interventions.

1.5.1 Radiofrequency Technology Design Objectives for Ultrahigh Field MRI

UHF-CMR based on ^1H requires transmission and reception of signal at the defined Larmor frequency for 7.0 T. In the design study, a whole-body MR scanner (MAGNETOM, Siemens Healthineers, Erlangen, Germany) was used at a Larmor frequency of 297.2 MHz. Based on the short EM wavelength in tissue and the heterogeneous tissue environment, UHF-CMR is particularly

susceptible to non-uniformities in the B_1^+ distribution. Research proposes several directions for B_1^+ non-uniformity compensation include RF pulse design as well as localized multi-channel RF antenna array technology. From a RF design perspective, an increased channel count results in increased degree of freedom for B_1^+ shaping (Section 1.3) within the ROI (e.g. the human heart). Furthermore, an increased channel count can be used for an enhanced distribution of superficial SAR and allow an improved SAR management. The SGBT building block tailored to a narrowband application is conceptually appealing, because of its small geometry and good EM field penetration depth. The narrowband SGBT antenna integrates the tuning and matching network as well as the common mode suppression network (cable-trap) on the individual antenna building block, making the antenna array a highly modular system. The signal generation for MRI is performed with an 8 kW RF power amplifier (RFPA, Stolberg HF-Technik AG, Stolberg-Vicht, Germany) integrated in the MRI System. The design, optimization, implementation, and validation of the antenna is provided in Section 2.1 and in the publication “32-Channel Self-Grounded Bow-Tie Transceiver Array for Cardiac MR at 7.0 Tesla” by Eigentler TW. et al.⁵²

1.5.2 Radiofrequency Technology Design Objectives for Thermal MR

The objective of the envisioned Thermal MR setup is to combine a thermal intervention with an imaging antenna array within an MRI environment to allow ^1H and ^{19}F imaging, MR-thermometry, and RF power deposition in a TV (Section 1.4). The focal point quality for the thermal intervention is governed by the radiation pattern of the single RF transmit element, the channel count, and the thermal intervention frequency of the applicator.⁴⁰⁻⁴² A time-multiplexed beamforming, a mixed frequency, or a time- and frequency-multiplexed approach are conceptually appealing for online focal point quality improvement.^{43,45-47} The mixed frequency and the time- and frequency-multiplexed intervention⁴⁵ requires a broadband antenna system as well as a multi-channel signal generation (Section 1.4). The antenna system – similar to the antenna design objective in Section 1.5.1 – needs to be small in order to increase the channel count and the degree of freedom for EMF shaping. MRI at 7.0 T requires an antenna capable to transmit and receive EM signal at approximately 298 MHz (see Section 1.4), whereas the mixed frequency and the time- and frequency-multiplexed intervention needs an EMF transmission at a broad frequency range. The SGBT building block tailored to fulfil these requirements was adapted with a low-loss low-permittivity material at the tip area to increase the broadband impedance match of the antenna to a 50 Ω transmission line. Furthermore, the building block itself was geometrically optimized to increase the broadband antenna performance. A detailed explanation can be found in Section 2.2 and in the publication “Wideband Self-Grounded Bow-Tie Antenna for Thermal MR” by Eigentler TW. et al.⁵⁴

The RF signal required for the thermal intervention can be subdivided into two systems: the 8 kW RF signal generation integrated in the MRI system for imaging and the multi-channel RF signal generator for the thermal intervention. The first is used for the image acquisition and MR-thermometry, whereas the second provides the thermal intervention vector or matrix (phase, amplitude, frequency for a certain time duration) at the required fidelity. The 32-channel signal generator is based on a phase-locked-loop (PLL) approach which – based on MR-thermometry measurements and power loss measurements – allows the adaptation and correction of the focal point quality. The signal generator is scalable with respect to the channel count and is presented in Section 2.3 and in the publication “*Design, Implementation, Evaluation and Application of a 32-Channel Radio Frequency Signal Generator for Thermal Magnetic Resonance Based Anti-Cancer Treatment*” by Han H. et al.⁵⁷

1.5.3 Radiative Elements

Numerical simulations are a key tool for modern developments and optimization processes of products (e.g. RF technology). The numerical simulation-based design process can be subdivided into (i) the EMF simulation, (ii) the post-processing and co-simulation, and (iii) EMF shaping.

Electromagnetic Field Simulations

EMF simulations were performed using the finite integration technique (FIT) and the finite difference time domain (FDTD) solver of CST Microwave Studio (CST Studio Suite 2020, Dassault Systèmes, Vélizy-Villacoublay Cedex, France). The simulations were performed for tissue-mimicking phantom setups, and for the human voxel models Ella and Duke from the virtual population.¹⁰⁰ The dielectric material specification of the phantoms were measured with an open-end coaxial probe.¹⁰¹ Tissue properties were defined at 297.2 MHz according to the tissue database of the IT'IS Foundation.¹⁰²

Post Processing and Co-Simulation

Based on the EMF simulation results, the tuning and matching circuit elements, B_1^+ and SAR_{10g} distributions, as well as temperature distributions were derived. B_1^+ efficiency was calculated by dividing the magnetic transmit RF field by the root mean square of the input power in kW.

The co-simulation for the narrowband SGBT for UHF-CMR was performed in Matlab 2019b (Mathworks, Natick, MA) for channel-wise tuning and matching ($f = 297.2$ MHz).¹⁰³ EMF simulation results were scaled accordingly, and with the material matrices used to calculate the B_1^+ fields and

SAR_{10g} distributions. For further optimization processes, virtual observation points (VOPs) were used to compress the SAR_{10g} matrices and reduce computational effort.^{104,105} Supplementary co-simulation calculations include the RF power loss calculation, the intrinsic transmit and SNR as optimum superposition of B₁.^{103,106} Details on the co-simulation and post-processing are in the Methods of the publication “32-Channel Self-Grounded Bow-Tie Transceiver Array for Cardiac MR at 7.0 Tesla” by Eigentler TW. et al.⁵²

Temperature simulations were performed using a uni-directional, thermal transient solver of CST Microwave Studio’s post-processing routine. The boundary condition was open with an initial material and ambient temperature of 20°C. Details on the temperature simulations are in the Methods of the publications “Wideband Self-Grounded Bow-Tie Antenna for Thermal MR” by Eigentler TW. et al and “Design, Implementation, Evaluation and Application of a 32-Channel Radio Frequency Signal Generator for Thermal Magnetic Resonance Based Anti-Cancer Treatment” by Han H. et al.^{54,57}

Electromagnetic Field Shaping

The EMF shaping in an MRI context describes a manipulation of phase and amplitude of the signal of each channel to achieve a constructive interference of B₁⁺ within the ROI. In the context of a thermal intervention, EMF shaping has the objective to achieve a constructive E-field interference and hence a temperature rise in the target at a defined focal point quality. This thesis will focus on the constructive interference calculation for B₁⁺ for MRI; the improvement of the focal point quality is further elaborated in key publications in the field of thermal intervention and hyperthermia.^{37,38,45}

From a hardware perspective, surface RF transmit elements for B₁⁺ shimming can either be driven in a static/dynamic shim in parallel transmit (PTX) or a static shim setup in a combined transmit (CTX) mode.^{13–15,19,32} At UHF-CMR and other imaging disciplines at ≥7.0 T, an improved homogeneous B₁⁺ distribution without signal voids can only be achieved in a spatially limited volume or slice, which is defined as the ROI. Whereas PTX (dynamic or static) allows a subject-specific calculation of the excitation vector for the imaging, a wide implementation within clinical routine is still hindered by the additional workload (e.g. in vivo B₁⁺ mapping) required to calculate the excitation vector without exceeding local and global SAR constraints.³² The approach presented in “32-Channel Self-Grounded Bow-Tie Transceiver Array for Cardiac MR at 7.0 Tesla” by Eigentler TW. et al. uses a CTX shimming where the phase information is implemented in the hardware of the signal chain of the RF antenna array.⁵² To acknowledge the inter-subject variability, two voxel models (Ella and Duke) were convoluted into one dataset for the phase optimization. The B₁⁺ target function (Φ_{target}) is defined to maximize the min(B₁⁺) (MaxMin), minimize the coefficient of variation (COV), minimize the linear least

square (LLS), or minimize the magnitude least squares (MLS) within the ROI.³² To calculate a B_1^+ to SAR efficient excitation vector, a combined optimization can be used following

$$\Phi_{tot} = \Phi_{target} + \lambda \Phi_{SAR} \quad (4)$$

$$\Phi_{SAR} = \max \left(\overrightarrow{V}_{exc}^T \mathbf{Q} \overrightarrow{V}_{exc} \right) \quad (5)$$

with \mathbf{Q} being the full SAR matrix or the VOPs to reduce computational effort and \overrightarrow{V}_{exc} the excitation vector for imaging.³² The variable λ allows for scaling between the maximum SAR and the B_1^+ results within the ROI. Alternatively, a multi-objective optimization can be used, where objective 1 is the B_1^+ target function and objective 2 is the maximum SAR. The shimming process is a global optimization process of Φ_{tot} performed by a genetic or a multi-objective algorithm implemented in the global optimization toolbox (Mathworks, Natick, MA) in Matlab 2019b.

1.5.4 Signal Generation for Thermal MR

The signal generation for a thermal intervention is, in contrast to the pulse generation for MRI, designed for a continuous RF signal. The signal is generated in two 16-channel RF synthesizer modules, with modulation of the single channels in (i) phase, (ii) frequency, and (iii) amplitude. The control of (i) and (ii) is accomplished with a PLL chip ADF4356 (Analog Devices, Norwood, MA, USA) for each channel. The PLL is based on a continuous phase correction with a high resolution ($360^\circ/2^{24}$) and an adaptable frequency range of 54 MHz to 6800 MHz. For (iii), a variable gain amplifier (VGA) chip ADL5330 (Analog Devices, Norwood, MA, USA) controls the amplitude of the individual channels. The individual components are managed centrally and controlled via a field-programmable gate array chip ZU3EG (Xilinx, San Jose, CA, USA). Further system classifications are described in Section 2.3 and the publication “*Design, Implementation, Evaluation and Application of a 32-Channel Radio Frequency Signal Generator for Thermal Magnetic Resonance Based Anti-Cancer Treatment*” by Han H. et al.⁵⁷

1.6 Validation Processes

The assessment of the developments described above in terms of their expected RF characteristics were assessed through a validation process. The validation process is a crucial step in the RF technology development process, in order to assure the compliance of safety measures before moving to in vivo studies and interventions. Based on the RF characteristic assessment, phantom experiments were conducted to prove the safety aspects. Subsequently, an in vivo imaging study was conducted to prove the usability.

1.6.1 Radiofrequency Antenna Characteristics Assessment

Bench measurements to assess the antennas RF characteristics were performed on a network vector analyser (NVA) to measure the impedance (Z) and scattering (S) matrix of an antenna or the whole RF antenna array. Over a defined frequency range, the Z-matrix and the S-matrix describe the RF characteristics of a system. Both matrices contain reciprocal information; the first contains the complex input and coupling impedance and the second contains the input reflection and coupling of the RF wave with respect to the RF antenna array.

A perfectly tuned and matched (50Ω) system shows for the main diagonal a $Z_{ii} = 50 + j0 \Omega$, which converts to a minimum reflection of S_{ij} . The coupling of a system is represented by the off-diagonal elements in the Z- and S-matrix, whereas for the Z-matrix, real and imaginary parts can be interpreted as electric and magnetic coupling. A perfectly decoupled system has $Z_{ij} = 0 + j0 \Omega$ for the off-diagonal. Through certain measures (e.g. decoupling capacitor, impedance transformation), the magnetic coupling (imaginary) can be compensated. The resistive coupling (real) is based on currents induced in the subject, and can only be minimized through a re-design of the RF antenna array design.¹⁰⁷ For the S-Matrix, a perfectly decoupled system is found when S_{ij} is minimized. The features above are true for transceiver arrays and receive-only arrays. Receive-only arrays enable further decoupling measures (e.g. preamplifier decoupling); however, this is not in the focus of this work and will not be discussed further.

1.6.2 Signal Generation Characteristics Assessment for Thermal MR

Bench measurements to assess the performance of the signal generator were performed using an oscilloscope to measure the switching times. For this test, the switching of amplitude, phase, and frequency was conducted with a reference signal provided by an oscillator output of the global positioning system (GPS). The switching times were assessed using an external trigger pulse and measuring the time delays between the pulse and the RF signal output modification. Phase differences of the RF output signal was evaluated using the oscilloscope.

1.6.3 Transmission Field Mapping

The B_1^+ field pattern is a crucial information for RF antenna and RF antenna array developments at UHF-MRI. It is used to allow an array performance test in a realistic environment and to assess the safety aspects of the antenna by benchmarking the results against simulations. Together with the previously introduced B_1^+ field non-uniformities at UHF-MRI, this has triggered increased interest in techniques for mapping. The most prominent techniques are the actual flip angle imaging (AFI)^{108,109}, phase imaging^{110,111}, dubbed dual refocusing echo acquisition mode (DREAM)¹¹², double angle method¹¹³, saturated turbo fast low-angle shot (FLASH)¹¹⁴, and Block-Siegert shift imaging^{115,116} approaches.^{117–119} These and other techniques use two acquired images, where the magnitude or phase information are combined by either subtraction or division, to generate a third image which is in turn used to calculate the flip angle distribution.¹¹⁷ The comparison of the presented techniques in 2-dimensional (2D) and 3-dimensional (3D) acquisitions reveal that flip angle-dependent uncertainties exists, and that the relative SAR varies across the B_1^+ mapping techniques.¹¹⁷ While SAR is relevant in an in vivo setup, this constraint is not limiting in phantom experiments.

In this thesis, the B_1^+ mapping is based on AFI for phantom experiments as well as on an AFI variant¹²⁰ for in vivo studies. The AFI method is a 3D imaging approach, exhibiting a SAR efficient modality compared to other 3D methods.¹¹⁷ It is based on two gradient echo (GRE) magnitude images (SI_1 and SI_2) acquired at two different repetition times (TR_1 and TR_2). The flip angle, which is called actual flip angle (α_{actual}) in this thesis, is defined by

$$\alpha_{\text{actual}} \approx \arccos \frac{TR_{\alpha} SI_{\alpha} - 1}{TR_{\alpha} - SI_{\alpha}} \quad (6)$$

with $TR_\alpha = TR_1/TR_2$ and $SI_\alpha = SI_1/SI_2$.¹⁰⁸ In comparison, the DREAM exhibits a lower SAR, but is sensitive to flow induced artifacts and has a limited dynamic flip angle range, which makes this approach impractical to use in UHF-CMR.^{112,121}

The B_1^+ field map is based on the previous acquired α_{actual} and the nuclei specific γ following

$$B_1^+ = \frac{\alpha_{\text{actual}}}{\gamma \tau} \quad (7)$$

with τ being the pulse duration time of a rectangular pulse.¹²² B_1^+ efficiency is calculated by scaling Equation (7) by the input power. The power in turn is defined by the actual voltage (V_{actual}) used in the system and the RF wave impedance $Z_0 = 50 \Omega$. V_{actual} is scaled by the ratio of the nominal flip angle of the sequence (α_{nominal}) and the reference flip angle of the system ($\alpha_{\text{reference}}$) following

$$V_{\text{actual}} = \frac{\alpha_{\text{nominal}}}{\alpha_{\text{reference}}} V_{\text{reference}} \quad (8)$$

Throughout this thesis, we used the Siemens whole-body MRI system's $V_{\text{reference}}$, calibrated with $\alpha_{\text{reference}} = \pi$. The B_1^+ efficiency with the scaling to the power of the excitation pulse in \sqrt{W} is defined according to Equation (7) and Equation (8) by

$$B_1^+ = \frac{\alpha_{\text{actual}}}{\gamma \tau} \frac{\alpha_{\text{reference}}}{\alpha_{\text{nominal}}} \frac{\sqrt{Z_0}}{V_{\text{reference}}} \quad (9)$$

1.6.4 Parallel Imaging

Parallel imaging is an essential method in MRI to reduce examination time, which can in turn be invested in higher spatial and temporal resolution, and in an increased volume coverage.¹²³ The conceptual idea behind the method is a form of undersampling of the acquired data in the frequency domain (k-space).¹²⁴ To reconstruct the missing data, information on the coil sensitivity needs to be acquired in a patient-specific manner, during or prior to the undersampled scan.¹²⁴ In addition to the well-established methods of simultaneous acquisition of spatial harmonics (SMASH)¹²⁵, sensitivity encoding (SENSE)¹²⁶, and generalized autocalibrating partial parallel acquisition (GRAPPA)¹²⁷ other methods have been introduced and combined with novel reconstruction methods.^{123,124}

In this thesis parallel imaging is based on a cartesian GRAPPA¹²⁷, a method whereby missing data resulting from undersampling is reconstructed in the k-space. Based on the reduction factor (R) lines in the phase encoding direction are not acquired. The antenna array sensitivity profile is estimated from additional, so called autocalibration signal (ACS) lines recorded in the center of the k-space.¹²⁷ The acquired data of multiple lines of all receivers are used to fit to the ACS lines of a single antenna. With this fit information the missing data of the single antenna is calculated in the k-space.¹²⁷ This method is repeated for all channels of the receiver array and allow a channel-wise image reconstruction. The reconstructed images of the single channels can be combined to a whole image, e.g. with a sum of squares reconstruction.¹²⁷ Further information on the GRAPPA parallel imaging method is elaborated in key publications on this topic.¹²⁷

Within this thesis, an offline image reconstruction of GRAPPA accelerated images was used in Matlab 2019b.¹²⁸ This method allows the calculation of SNR-scaled images and generates geometry factor (g-factor) maps. Based on the SNR information the calculation of contrast-to-noise ratio (CNR) is feasible. For CNR, the SNR of the myocardium is subtracted from the SNR of the ventricular blood pool.¹²⁹

1.6.5 MR-thermometry

Localized temperature rise based on a non-invasive thermal intervention (Section 1.4) encourages the supervision of the thermal focal point quality through MR-thermometry. Methods for MR-thermometry are commonly based on temperature-dependent MR parameters such as the proton density, the T_1 and T_2 relaxation times, the diffusion coefficient, the magnetization transfer, spectroscopy, and the proton resonance frequency shift (PRFS).^{48,50,51} Additionally, temperature-sensitive contrast agents are a possibility, to acquire temperature distribution non-invasively.^{48,50,51} Dependend on the used method, an absolute (e.g. spectroscopic) or a relative (e.g. PRFS) temperature distribution can be measured.^{48,49,51} The relative measurement requires the acquisition of a baseline/reference image before the intervention.^{48,49,51} For in vivo situations, the downside of many methods are summarized with the acquisition time needed (T_1 thermometry, spectroscopy), the non-linear relationship to temperature rise (T_2 thermometry), and other mixed effects (e.g. proton density thermometry with short TR impairs T_1 effects).⁴⁸ This work focuses on the MR-thermometry gold standard: the PRFS.⁵⁰ A detailed description of this and various other methods used for MR-thermometry can be found in key publications.⁴⁸⁻⁵¹

The linearity, temperature sensitivity, and near independence of tissue types (with the exception of fatty tissue) make the PRFS method appealing to be used for MR-thermometry.^{48–51} PRFS is based on the temperature-dependent variation of the local magnetic field, which is formulated by

$$B_{\text{local}} = (1 - \vartheta_s) B_0 \quad (10)$$

with the screening constant ϑ_s defined through $\vartheta_s = \left(\frac{2\chi}{3} + \sigma_s \right)$, where χ is the magnetic susceptibility and σ is the screening variable.^{16,48} As a consequence, the local resonance frequency following Equation (2) becomes

$$\omega_{\text{local}} = \gamma (1 - \vartheta_s) B_0. \quad (11)$$

The screening effect of the ^1H nuclei in a molecular structure like H_2O is reduced based on the temperature dependent EM bond in the molecule.¹³⁰ The higher the temperature, the higher the screening effect within the molecule, and hence a lower local B_0 with the consequence of a decreased ω_{local} .⁴⁸ The average screening constant ϑ_s of H_2O scales approximately linearly ($-1.03 \pm 0.02 \cdot 10^{-8}$ per $^\circ\text{C}$) with temperatures of -15°C to 100°C .^{48,50,130} This effect can be used to detect phase differences between the reference/baseline image acquired before the thermal intervention (φ_{ref}) and the image acquired during or after the thermal intervention (φ_t).^{50,131} For in vivo tissue and with neglecting the temperature dependent magnetic susceptibility a voxel-wise calculation of the temperature rise follows

$$\Delta T = \frac{\varphi_t - \varphi_{\text{ref}}}{\gamma \alpha_s \text{TE} B_0}. \quad (12)$$

with the proportional constant α_s being in the reported range of $0.9\text{--}1.0 \cdot 10^{-8}$ per $^\circ\text{C}$ for tissue (except fatty tissue) and TE being the echo time of the image acquisition.^{49,132,133} Due to a time delay between φ_{ref} and φ_t (e.g. magnet drift and motion), temperature-dependent effects (e.g. magnetic susceptibility), and other effects like for example perfusion may be misinterpreted in a temperature change. The correction and reduction of these effects is critical for PRFS based thermometry, and is in detail elaborated in key publications on this topic.⁴⁹

2 Published Manuscripts

2.1 32-Channel Self-Grounded Bow-Tie Transceiver Array for Cardiac MR at 7.0 Tesla

The potential benefits of UHF-CMR and its implementation into the clinic are limited by multiple physics-related phenomena which result in non-uniform B_1^+ distributions. Several publications discuss enabling RF antenna technology for UHF-CMR (Section 1.5) to overcome these shortcomings. Dipole antenna configurations have gained increased attention for UHF body MRI applications, because of their linear polarized current pattern with a perpendicular directed RF energy deposition. This results in a symmetrical excitation field with increase in penetration depth.^{85–88} Compared to the Thermal MR (Section 1.4 and 1.5.2), UHF-CMR RF hardware operates at 297.2 MHz on a narrowband frequency range (Section 1.2). The narrowband SGBT building block employs a high channel density for dipole antennas used within an MRI environment. The high channel density allows a high channel count, enabling an increased degree of freedom for B_1^+ shaping and SAR_{10g} management for MRI applications. The reported antenna design process included an optimization process of the antenna itself and its EMF shaping approach to allow a constructive B_1^+ interference within the ROI while limiting the SAR_{10g} . The B_1^+ optimization approach used the human voxel models Ella and Duke in a single convoluted dataset, to achieve a more generalized shim for all subjects of the in vivo study. The imaging study showed the applicability of both the optimized antenna design and the optimized B_1^+ shim for UHF-CMR.

The narrowband SGBT building block employs a tuned and matched antenna system for UHF-CMR. The findings prove the concept of a massively miniaturized dipole antenna system, which allows for an increased channel count and hence greater degree of freedom for EMF shaping. In addition to shaping the B_1^+ field and the reducing the maximum SAR_{10g} , the high channel system can be used for E-field shaping, and to limit the superficial SAR_{10g} .

Publication

Eigentler TW, Kuehne A, Boehmert L, Dietrich S, Els A, Waiczies H, Niendorf T. 32-Channel Self-Grounded Bow-Tie Transceiver Array for Cardiac MR at 7.0 Tesla. *Magn Reson Med*. 2021; 86(5):2862-2879. doi: <https://doi.org/10.1002/mrm.28885>.

Received: 24 February 2021 | Revised: 20 April 2021 | Accepted: 18 May 2021

DOI: 10.1002/mrm.28885

FULL PAPER

Magnetic Resonance in Medicine

32-Channel self-grounded bow-tie transceiver array for cardiac MR at 7.0T

Thomas Wilhelm Eigentler^{1,2}  | Andre Kuehne³  | Laura Boehmert¹  |
 Sebastian Dietrich⁴  | Antje Els¹ | Helmar Waiczies³  | Thoralf Niendorf^{1,3,5} 

¹Berlin Ultrahigh Field Facility (B.U.F.F.), Max Delbrück Center for Molecular Medicine in the Helmholtz Association, Berlin, Germany

²Chair of Medical Engineering, Technische Universität Berlin, Berlin, Germany

³MRI.TOOLS GmbH, Berlin, Germany

⁴Physikalisch-Technische Bundesanstalt (PTB), Braunschweig and Berlin, Germany

⁵Experimental and Clinical Research Center (ECRC), a joint cooperation between the Charité Medical Faculty and the Max Delbrück Center for Molecular Medicine in the Helmholtz Association, Berlin, Germany

Correspondence

Thoralf Niendorf, Berlin Ultrahigh Field Facility (B.U.F.F.), Max Delbrück Center for Molecular Medicine in the Helmholtz Association, Robert-Roessle-Strasse 10, 13125 Berlin, Germany.
 Email: thoralf.niendorf@mdc-berlin.de

Funding information

H2020 European Research Council, Grant/Award Number: 743077; EURSTARS initiative of the European Union, Grant/Award Number: E! 12074; German Federal Ministry for Education and Research, Grant/Award Number: MENTORA_4_EU and FKZ 01QE1815

Purpose: Design, implementation, evaluation, and application of a 32-channel Self-Grounded Bow-Tie (SGBT) transceiver array for cardiac MR (CMR) at 7.0T.

Methods: The array consists of 32 compact SGBT building blocks. Transmission field (B_1^+) shimming and radiofrequency safety assessment were performed with numerical simulations and benchmarked against phantom experiments. In vivo B_1^+ efficiency mapping was conducted with actual flip angle imaging. The array's applicability for accelerated high spatial resolution 2D FLASH CINE imaging of the heart was examined in a volunteer study ($n = 7$).

Results: B_1^+ shimming provided a uniform field distribution suitable for female and male subjects. Phantom studies demonstrated an excellent agreement between simulated and measured B_1^+ efficiency maps (7% mean difference). The SGBT array afforded a spatial resolution of $(0.8 \times 0.8 \times 2.5) \text{ mm}^3$ for 2D CINE FLASH which is by a factor of 12 superior to standardized cardiovascular MR (CMR) protocols. The density of the SGBT array supports 1D acceleration of up to $R = 4$ (mean signal-to-noise ratio (whole heart) ≥ 16.7 , mean contrast-to-noise ratio ≥ 13.5) without impairing image quality significantly.

Conclusion: The compact SGBT building block facilitates a modular high-density array that supports accelerated and high spatial resolution CMR at 7.0T. The array provides a technological basis for future clinical assessment of parallel transmission techniques.

KEYWORDS

cardiovascular MRI, electrical dipole, parallel imaging, RF coil, transceiver array, ultrahigh field MRI

This is an open access article under the terms of the Creative Commons Attribution-NonCommercial License, which permits use, distribution and reproduction in any medium, provided the original work is properly cited and is not used for commercial purposes.

© 2021 The Authors. *Magnetic Resonance in Medicine* published by Wiley Periodicals LLC on behalf of International Society for Magnetic Resonance in Medicine

1 | INTRODUCTION

Advances in cardiovascular MR (CMR) at ultrahigh magnetic field strengths (UHF, $B_0 \geq 7.0T$) foreshadow some of the potential benefits to be expected as this technology moves to translational research and clinical science.^{1,2} Transferring UHF-CMR into the clinic remains a major challenge since the advantages are sometimes hampered by concomitant physics-related phenomena. UHF-CMR is particularly susceptible to non-uniformities in the radiofrequency (RF) transmission field (B_1^+). To address this obstruction several reports refer to the development of enabling technology tailored for UHF-CMR.³ Research directions for B_1^+ inhomogeneity compensation include RF pulse design and enabling multi-channel RF coil technology. Pioneering RF array developments for CMR at 7.0T include stripline-elements,⁴ stripline waveguide like elements,⁵ loop elements,⁶⁻¹⁰ dipoles^{11,12}, slot-antennas,¹³ loop-dipoles,^{14,15} and dipole building block elements.^{16,17}

Dipole antenna configurations have gained increased attention for UHF-CMR. Electric dipoles run the trait of a linearly polarized current pattern, where RF energy is directed perpendicular to the dipole along the Poynting vector to the object under investigation resulting in a symmetrical, rather uniform excitation field with increased penetration depth.^{14,16-18} At UHF-MRI linear (curl-free) current patterns provided by electric dipoles help to approach ultimate intrinsic signal-to-noise ratio (SNR).¹⁹ Current dipole and loop-dipole RF arrays rely on geometrical decoupling limiting the number of transmitting (TX) elements that can be placed per unit area.^{11,14,15} Yet, a high number of elements is favorable to increase the degrees of freedom and improve B_1^+ at a deep-seated cardiac region of interest (ROI).²⁰ For reception (RX) a high number of RF array elements afford parallel imaging with increased acceleration.²¹ High-permittivity and low-loss dielectric materials facilitate dipole antenna shortening and are promising to provide sufficient decoupling allowing high channel count RF arrays.^{16,22,23}

To summarize, RF arrays tailored for UHF-CMR should meet the requirements of patient safety, patient comfort, and ease of clinical use to harmonize the technical specifications with the clinical needs. This includes lightweight, flexibility, the capability to accommodate multiple body habitus and anatomical variants, a modular and multi-dimensional arrangement of RF building blocks together with a sensitive region large enough to cover the human heart.²⁴ Recent investigations demonstrated the feasibility of a Self-Grounded Bow-Tie (SGBT) building block at 7.0 T MRI.^{23,25} The hallmark of this antenna type is its strong main lobe directivity and small size, based on a dielectrically filled housing for effective wavelength shortening and antenna size reduction.^{23,26,27} Recognizing these opportunities it is conceptually appealing to pursue the development of an SGBT-based high-density TX/RX RF array tailored for UHF-CMR. To meet this goal this work reports on the design, implementation, evaluation,

and application of a modular, lightweight 32-channel SGBT TX/RX array for CMR at 7.0 T. For this purpose, the proposed RF array is examined in electromagnetic field (EMF) simulations and benchmarked against phantom experiments. The feasibility of the RF array is demonstrated for high spatial resolution 2D CINE imaging of the heart in healthy subjects as a mandatory precursor to broader patient studies.

2 | METHODS

2.1 | Ethics statement

For the in vivo feasibility study, subjects without any known history of cardiac disease were included after approval by the local ethical committee (registration number EA1/256/19, Ethikausschuss am Campus Charité – Mitte, Berlin, Germany). Informed written consent was obtained from each volunteer prior to the study.

2.2 | RF antenna building block design

The RF antenna building block consists of an SGBT antenna with a dielectric-filled housing (Figure 1).^{23,27} The SGBT dipole antenna has a strong main lobe directivity and limited back radiation due to the self-grounded backplane.²⁶ The antenna was manufactured with a 0.3 mm copper sheet, to ensure a mechanically robust setup. The additive manufactured housing is based on lithography (Form2, Formlabs, Somerville, MA, United States of America) and filled with deuterium oxide (D₂O, 99.9%, $\epsilon_r \approx 81$ at 297.2 MHz, Sigma Aldrich GmbH, Munich, Germany) as dielectric to shorten the effective RF wavelength and to reduce the overall antenna size. The building block surface facing the object under investigation consists of a 0.5 mm FR-4 sheet (Figure 1C). From the SGBT antenna tip, a parallel transmission line was connected to the tuning and matching network at the backside of the building block containing, a variable nonmagnetic ceramic capacitor (~1-23 pF, Voltronics Inc., Denville, NJ, United States of America) and a nonmagnetic air-core inductor (12.2 nH, Coilcraft Inc., Cary, IL, United States of America). The circuit network was covered with lithography-based manufactured housing for the individual element (Figure 1C,D).

2.3 | Cardiac array assembly

To constitute the high-density TX/RX cardiac array sixteen SGBT building blocks were combined to form the anterior section. Sixteen SGBT building blocks were integrated into the posterior section (Figure 2). For this purpose, the SGBT building blocks were placed next to each other as close as

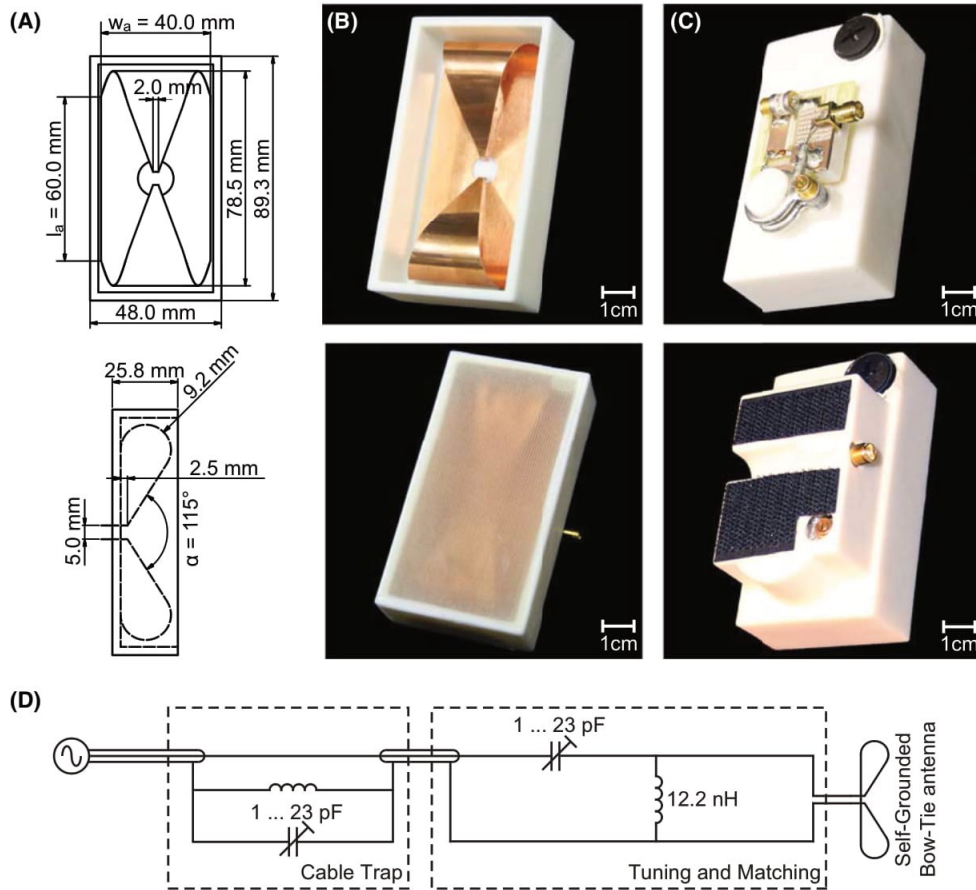


FIGURE 1 A, Schematic bottom view (top) and side view (bottom) of the SGBT antenna building block including the dimensions. B, Manufactured SGBT antenna inside the open (top) and closed (bottom, 0.5 mm FR-4), additive manufactured housing. C, Backside of the building block showing the electrical circuit and the cover including the hook-and-loop fastener used to connect building blocks for the assembly of the 32 channel TX/RX array (bottom). D, Schematic visualization of the circuit including the tuning and matching and the solenoid cable trap with 1.5 windings.

possible with three rows of building blocks along the head-foot direction. A shift of the array to the left side of the subject was introduced to place the center of the antenna array above the heart (Figure 2A). The anterior RF building blocks were fixed by hook-and-loop fasteners allowing a flexible connection between the building blocks and a close-fitting to the upper torso, regardless of sex or body mass index (BMI). For the posterior section, a holder system was made from acrylonitrile butadiene styrene (ABS) material using a rapid prototyping system (BST 1200es, Dimension Inc., Eden Prairie, MN, USA). The holder system accommodated the SGBT building blocks and was integrated into the patient table cushions, hence no extra free magnet bore space is consumed. To reduce EMF reflections, a hydrogel pad was placed between the anterior and posterior sections of the RF array and the object under investigation (Figure 2C). The hydrogel ($\epsilon_r \approx 82$,

$\sigma \approx 0.17$ S/m) consists of xanthan (0.4% mass fraction, Roth AG, Arlesheim, Switzerland), locust bean gum (0.4% mass fraction, Merck KGaA, Darmstadt, Germany), and agarose (0.2% mass fraction, Roth AG, Arlesheim, Switzerland) filled in a vacuum-sealed bag.²⁸ For RF safety and to avoid excessive local specific absorption rate (SAR) in the vicinity of the conductors, the thickness (≥ 5 mm) of the hydrogel pad and the design of the building block casing assures a minimum distance between the RF array and the object.

2.4 | Hardware

MR experiments were conducted on a 7.0T whole-body MR scanner (MAGNETOM, Siemens Healthineers, Erlangen, Germany) equipped with an 8 kW RF power amplifier (RFPA,

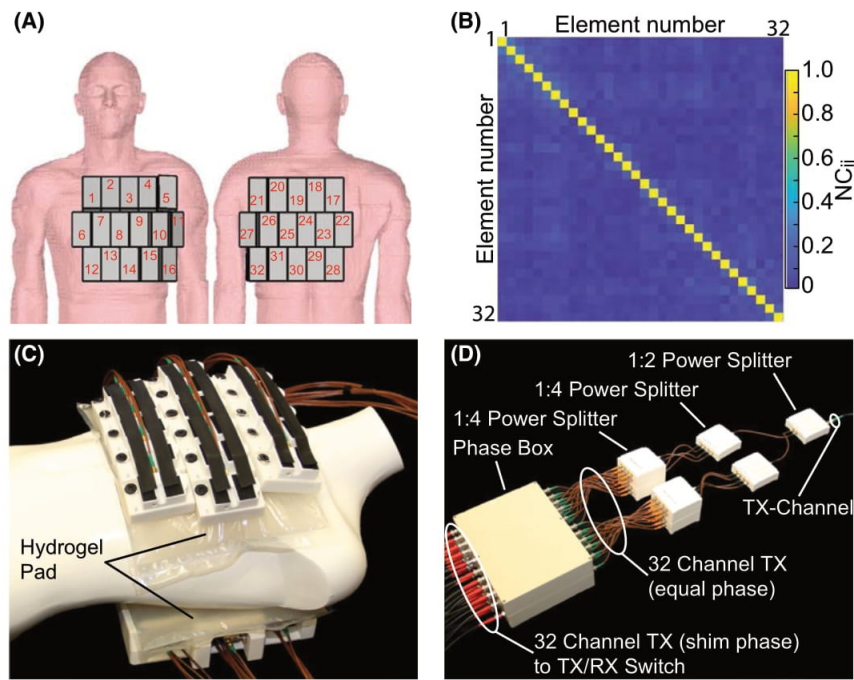


FIGURE 2 A, Schematic view of the antenna arrangement for the 32-channel cardiac array on the human voxel model Duke together with the channel nomenclature. B, Averaged, measured noise correlation (NC) matrix of the 32-channel SGBT building block array of all subjects involved in the CMR study. C, Implementation used in the feasibility study with the anterior section fixed by hook-and-loop fasteners. The posterior section was placed in an additive manufactured holder system and was integrated into the patient table's cushions. Hydrogel pads were used to improve an electromagnetic impedance match to reduce electromagnetic reflections between the building blocks and the object under investigation. D, Cascade of one 1:2, two 1:4, and eight 1:4 power splitters (Power Splitter 297.2 MHz, MRI.TOOLS GmbH, Berlin, Germany) resulting in a 32-channel equal phase transmit (TX) signal feeding the phase box, containing single-channel phase adjustments (α_{exc}) by using phase-shifting coaxial cables. The phase-shifted TX signal is connected to four multi-purpose interface boxes equipped with TX/RX switches and integrated low-noise preamplifiers (Stark Contrast, Erlangen, Germany)

Stolberg HF-Technik AG, Stolberg-Vicht, Germany) and a gradient system with a maximum slew rate of 170 mT/m/ms and gradient strength of 38 mT/m. To drive the RF array, the transmit signal was divided into 32 equal amplitude signals using a cascade of one 1:2, two 1:4, and eight 1:4 Wilkinson power splitters with lumped elements (Power Splitter 297.2 MHz, MRI.TOOLS GmbH, Berlin, Germany). The phase adjustments (α_{exc}) of the individual channels were incorporated by using phase-shifting coaxial cables (Figure 2D). The 32-channels of the proposed cardiac array were connected to the MR signal chain using four eight-channel multi-purpose interface boxes with transmit/receive switches and integrated low-noise preamplifiers (Stark Contrast, Erlangen, Germany).

2.5 | EMF simulations

EMF simulations were performed using the finite integration technique (FIT) solver of CST Microwave Studio (CST Studio Suite 2020, Dassault Systèmes, Vélizy-Villacoublay Cedex,

France) with a broadband excitation at 297.2 ± 50.0 MHz. The simulations were performed for a rectangular phantom setup ($156 \times 374 \times 318$ mm³, $\epsilon_r = 48$, $\sigma = 0.47$) and for the human voxel models Ella and Duke from the virtual population.²⁹ The voxel models were used from the upper neck to the navel at a resolution of $1.0 \times 1.0 \times 1.0$ mm³. The dielectric material specification of the phantom was measured with an open-end coaxial probe.³⁰ Tissue properties were defined at 297.2 MHz according to the tissue database of the IT'IS Foundation.³¹ All simulations were performed within a model of the MRI bores' RF shield. The simulation resolution was kept below $4.0 \times 4.0 \times 4.0$ mm³ for all configurations. B_1^+ efficiency was calculated by dividing the magnetic transmit RF field by the root mean square of the input power in kW.

2.6 | Evaluation and optimization of SGBT

The antenna dimensions width (w_a), length (l_a), and dihedral angle (α) were investigated using CST Microwave Studio

to achieve the highest possible B_1^+ efficiency divided by the building blocks' footprint (B_1^+ efficiency to footprint ratio). For this purpose, the SGBT building block and the hydrogel pad were placed centrally above the heart of the human voxel models (Ella and Duke) and the lateral wall of the heart was used as ROI as indicated in Figure 3A.

2.7 | Co-simulation, transmission field shaping, and SAR calculation

A co-simulation was performed in MATLAB 2019b (MathWorks, Natick, MA) for channel-wise tuning and matching ($f = 297.2$ MHz) with a lossy capacitance (equivalent series resistance = 0.2Ω , equivalent series inductance = 1 nH) and a lossy inductance ($Q = 45$).³² EMF simulation results were scaled accordingly and together with the material matrices used to calculate B_1^+ fields and SAR distributions averaged over 10g tissue or material (SAR_{10g}). To reduce the computational effort for the B_1^+ shimming approach the channel-wise transmission field was regridded to an isotropic resolution of $4.0 \times 4.0 \times 4.0$ mm³ and SAR_{10g} was compressed using virtual observation points (VOPs) at an overestimation factor of 0.01.^{33,34} RF power loss calculation was performed using a quadratic-form-based framework for loss analysis in multichannel arrays.³⁵ All results referring to the power absorption were calculated without losses in the signal chain, ie, the reference plane was at the input of the balun on the SGBT antenna. The intrinsic transmit efficiency and the intrinsic SNR distributions were calculated as an optimum superposition of B_1^+ and B_1^- with respect to the power absorbed by the voxel model. Assuming complete dominance of sample noise, this yields a theoretical upper bound for the B_1^+ shimming performance and is proportional to image SNR.³² The intrinsic measures were contrasted with the realistic transmit efficiency and the realistic SNR with considering all coil losses. The performance ratio (%) of the RF array reveals the ratio of the intrinsic and the realistic B_1^+ and B_1^- superpositions. The values derived in this way can be used to quantitatively compare expected SNR and transmit efficiency of different arrays and to assess theoretical electromagnetic upper bounds.^{36,37}

EMF shaping was performed using a combined approach for Ella and Duke, where the minimum B_1^+ in the ROI is maximized by using the target function

$$f(exc) = \min(B_{1Ella}^+(exc)) + \delta \cdot \min(B_{1Duke}^+(exc)) - \lambda \cdot \max(VOP_{Ella}(exc) + VOP_{Duke}(exc))$$

with the B_1^+ scaling factor ($\delta = 1 \dots 4$) and VOPs scaling factor ($\lambda = 0.001 \dots 5$). The phase optimization was performed with a generic algorithm implemented in the global optimization toolbox of MATLAB 2019b.

2.8 | Phantom experiments for EMF simulations validation

To examine the RF characteristics of the cardiac array and of the signal chain, bench measurements were performed using a four-channel vector network analyzer (ZNB 4, Rohde & Schwarz, Memmingen, Germany) in conjunction with a switching matrix (ZN-Z84, Rohde & Schwarz, Memmingen, Germany).

A custom-made rectangular phantom ($156 \times 374 \times 318$ mm³) consisting of deionized water, sucrose (1425.7 g/L), NaCl (58.7 g/L), agarose (25 g/L), and CuSO₄ (0.75 g/L) was used to validate the EMF simulations obtained for the 32-channel SGBT antenna building block array. Simulated B_1^+ efficiency distributions were benchmarked against measured B_1^+ efficiency maps for transversal slices through each of the three SGBT antenna building block rows. For this evaluation, two-phase setting modes were used: (1) the equal phase excitation ($\alpha_1 \dots \alpha_{32} = 0^\circ$) and (2) the phase shim excitation (α_{exc}) obtained with the proposed optimization algorithm.

B_1^+ efficiency field measurements were conducted with a non-slice-selective actual flip angle imaging (AFI) method (spatial resolution = $1.0 \times 1.0 \times 2.5$ mm³, rectangular pulse PD = 1 ms TE = 2.19 ms, TR₁ = 42 ms, TR₂ = 122 ms, BW = 500 Hz/Px, nominal FA = 50°, V_{ref} = 520 V, 64 slices) and calculated offline in MATLAB 2019b.³⁸ Measured losses in the signal chain of the MRI system were considered in the simulation results. Pixel-by-pixel difference maps were calculated using a in plane resolution of 1.0×1.0 mm² where the B_1^+ mask ($B_1^+ \geq 4 \mu T/\sqrt{kW}$ in simulation without losses) was used for cropping low signal areas. An ROI was defined in the phantom to evaluate the simulation and measurement results.

2.9 | Volunteer studies

The in vivo study was performed in seven healthy subjects (three females, four males; age = 29-59; average BMI = 23.8 ± 2.1 kg/m²; minimum BMI = 20.2 kg/m²; maximum BMI = 27.2 kg/m²). The study design contained B_1^+ efficiency mapping (two subjects), 2D CINE FLASH imaging (seven subjects), assessment of spatial resolution enhancement (four subjects), and parallel imaging (four subjects). For retrospective cardiac gating and prospective cardiac triggering electrocardiogram (ECG) electrodes and an MR stethoscope (EasyACT, MRI.TOOLS GmbH, Berlin, Germany) were placed between the hydrogel pad and the anterior chest wall.

To facilitate 3D flip angle measurement, a radial phase encoding (RPE) gradient-echo acquisition scheme was modified to acquire two interleaved TRs, which enables the computation of absolute B_1^+ efficiency maps according to the AFI approach (RPE-AFI).³⁸ RPE-AFI was obtained with: spatial resolution = $5.0 \times 5.0 \times 5.0$ mm³, rectangular pulse PD = 0.5 ms, TE = 2.04 ms, TR₁ = 10 ms, TR₂ = 50 ms, nominal

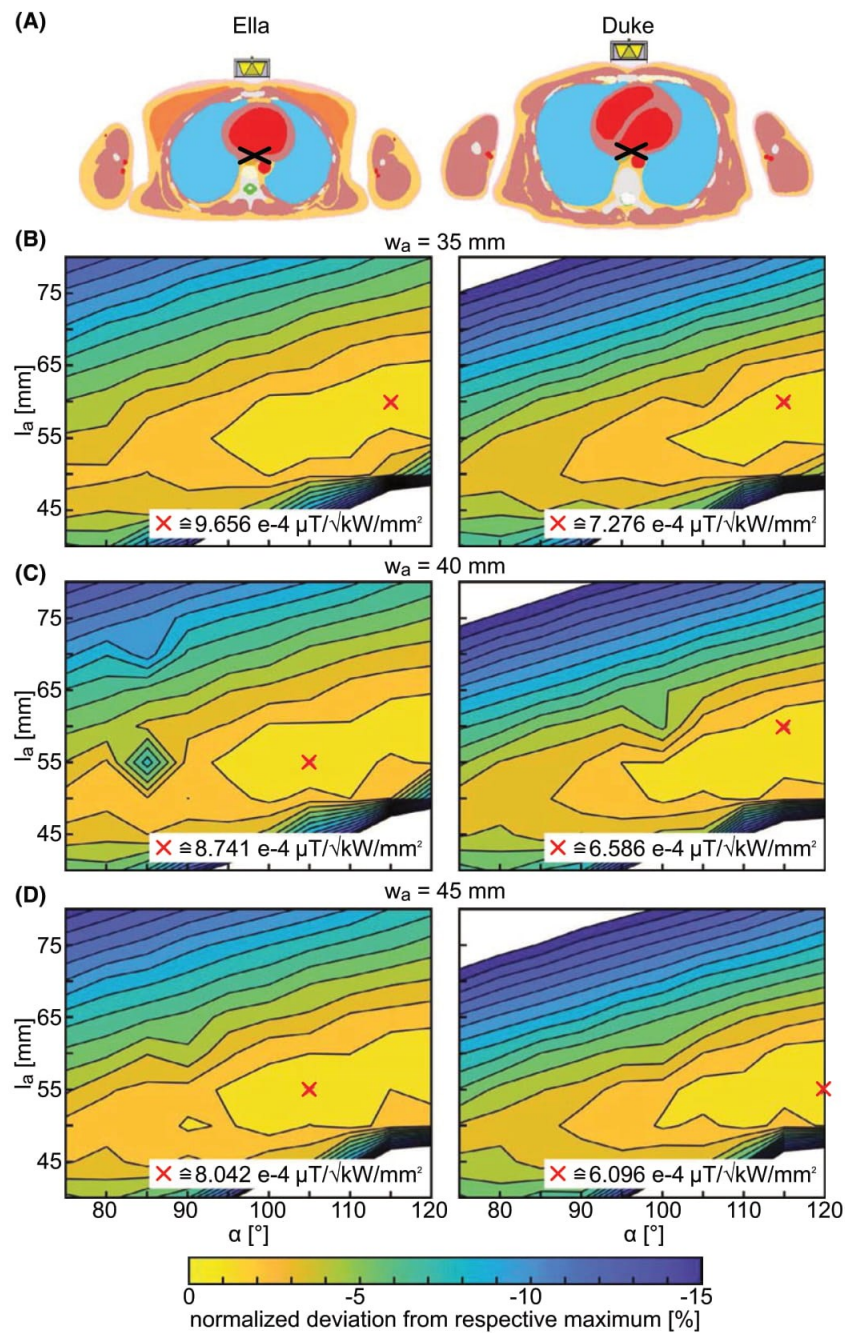


FIGURE 3 Summary of the results obtained for the optimization of the SGBT antenna geometry using the human voxel model Ella and Duke. A, The ROI used for the B_1^+ efficiency calculation within the optimization is marked by the black cross. The normalized deviation [%] from the respective maximum of the ratio between the B_1^+ efficiency and the footprint of the building block is shown for a parametric sweep ($\alpha = 75^\circ \dots 120^\circ$ and $I_a = 40$ mm \dots 80 mm) and an antenna width of $w_a = 35$ mm (B), $w_a = 40$ mm (C), and $w_a = 45$ mm (D). The maximum B_1^+ efficiency to building block footprint ratio is highlighted by a red cross for each parameter sweep

FA = 66°, $V_{\text{ref}} = 520$ V, and 12 readouts per radial line following Dietrich S. et al.³⁹

2D CINE FLASH imaging of the heart was performed to obtain short axis (SAX), two-chamber (2CV), three-chamber (3CV), and four chamber (4CV) views of the human heart (spatial resolution = $1.1 \times 1.1 \times 2.5$ mm³, TE = 2.09 ms, TR = 4.55 ms, GRAPPA R = 2, views per segment = 10, cardiac phases = 30, BW = 446 Hz/Px, nominal FA = 22°, $V_{\text{ref}} = 520$ V). Imaging parameters were slightly adjusted for subject 1, subject 3, and subject 7 (TE = 2.14-2.17 ms, TR = 4.72-5.58 ms). The noise correlation matrix was derived from averaging noise pre-scans obtained for each subject without RF excitation.⁴⁰

2D CINE FLASH imaging targeting the 4CV and the SAX were performed for spatial resolutions: (1) $1.8 \times 1.8 \times 6.0$ mm³ according to standardized protocols used in CMR practice⁴¹ (TE = 1.75 ms, TR = 3.96 ms, views per segment = 10, cardiac phases = 30), (2) $1.4 \times 1.4 \times 4.0$ mm³ (TE = 1.84 ms, TR = 4.14 ms, views per segment = 10, cardiac phases = 30), (3) $1.1 \times 1.1 \times 2.5$ mm³ (see above), and (4) $0.8 \times 0.8 \times 2.5$ mm³ (TE = 2.11 ms, TR = 4.75 ms, GRAPPA R = 2, views per segment = 10, cardiac phases = 30). The normalized signal intensity profile along a circumferential trajectory inside the myocardium was plotted for a mid-ventricular SAX at end-diastole for four subjects. The results were labeled using the common segmentation of the myocardium.⁴²

The antenna arrays' parallel imaging performance was evaluated using acceleration factors of up to R = 6 and GRAPPA reconstruction.⁴³ Prospective imaging of the 4CV and SAX was used at a resolution of $1.1 \times 1.1 \times 2.5$ mm³ (TE = 2.5 ms, TR = 4.55 ms, views per segment = 10, BW = 446 Hz/Px, and a nominal FA = 22° at $V_{\text{ref}} = 520$ V). The phase encoding direction was kept the same for all reduction factors within a subject (4CV-AP: subject 2 and 5; 4CV-RL: subject 4 and 6; SAX-AP: subject 2 and 4; SAX-HF: subject 5 and 6). Offline image reconstruction was performed in MATLAB 2019b.⁴⁴ Pseudo replicas (500) were used to calculate the SNR scaled images and geometry factor (g-factor) maps. Contrast-to-noise ratio (CNR) was calculated by subtracting the SNR values of the myocardium from the SNR values of the ventricular blood pool in the 4CV and SAX.⁴⁵ The acquired data was assessed for each individual subject ($\text{SNR}_{\text{whole-heart,mean}} \cdot \text{SNR}_{\text{myocardium,mean}} \cdot \text{g-factor}_{\text{whole-heart,mean}} \cdot \text{g-factor}_{\text{whole-heart,max}}$, and CNR) and statistically analyzed for all subjects enrolled in the parallel imaging study.

3 | RESULTS

3.1 | RF antenna building block design and characteristics

The results of the EMF simulations are summarized in Figure 3, suggesting a small antenna width for an

enhanced B_1^+ efficiency to footprint ratio. Coupling between the elements, on the other hand, favors an increased antenna width, resulting in a lower coupling between SGBT building blocks in an RF array. The final antenna design ($w_a = 40.0$ mm, $l_a = 69.0$ mm, $\alpha = 115.0^\circ$) was defined as a trade-off between the B_1^+ efficiency to footprint ratio and the decoupling behavior. The result was deduced from the EMF simulations with the human voxel model Duke, because of the reduced B_1^+ efficiency compared to Ella (Figure 3). Following the implementation, the SGBT building block exhibits a weight of 156 g and a size of $89.3 \times 48.0 \times 25.8$ mm³. This SGBT building block configuration allows a nearest-neighbor coupling of $S_{ij} \leq -11.2$ dB at 0° relative angle and 0 mm distance between the SGBT building blocks when placed on the thorax of the human voxel models Duke ($S_{ij} = -12.7$ dB) and Ella ($S_{ij} = -11.2$ dB). The decoupling performance relies on geometrical decoupling and allows the use in an RF array without additional decoupling measures (eg, impedance transformation network and preamplifier decoupling). In comparison, EMF simulations with $w_a = 35$ mm and $w_a = 45$ mm revealed a coupling of $S_{ij} \leq -10.6$ dB and $S_{ij} \leq -12.3$ dB. The power absorption analysis of a single channel revealed that on average 61% and 71% of the input is absorbed in the body of Ella and Duke for the 32-channel array. The other losses are comprised of a material including the hydrogel pad (20-26%), coupling (8-11%), and lumped element losses (~1%).

3.2 | Cardiac array assembly

The anterior and posterior sections consist of sixteen SGBT building blocks each, covering a surface area of about 686 cm², respectively (Figure 2A). The total weight of the anterior section is approximately 2.5 kg. In the experimental setup the reflection and the coupling coefficient were found to be $S_{ii} < -10.2$ dB and $S_{ij} < -14.1$ dB. Figure 2B shows the noise correlation matrix which revealed a value of -0.258 or below within the array for all subjects.

3.3 | Hardware

The power splitters introduced losses of -0.27 dB for the 1:2 and -0.49 dB for the 1:4 with a maximum phase error of 1° each. The phase cables were encapsulated in a box and manufactured with less than 2.2° phase deviation. Including all other parts of the system (cables between the described elements, the antenna cables, the TX/RX switch boxes, and the phase cables) the losses were found to be -5.15 dB at a cumulative worst-case phase error of 9.9°.

3.4 | Co-simulation, transmission field shaping, and SAR calculation

Numerical simulations of the 32-channel RF array revealed a reflection of $S_{ii} < -27$ dB and coupling of $S_{ij} < -12$ dB. The factor δ of the proposed mixed B_1^+ shimming within

the heart of Ella and Duke allowed a B_1^+ efficiency gain for Duke at the expense of Ella. Dependent on the B_1^+ scaling factor δ and the VOPs scaling factor λ an optimum phase set was calculated maximizing the minimum B_1^+ of both voxel models. The optimized phase set ($\alpha_{exc} = -[0; 275; 241; 191; 135; 48; 0; 241; 204; 164; 128; 310; 273; 239; 169; 108; 0;$

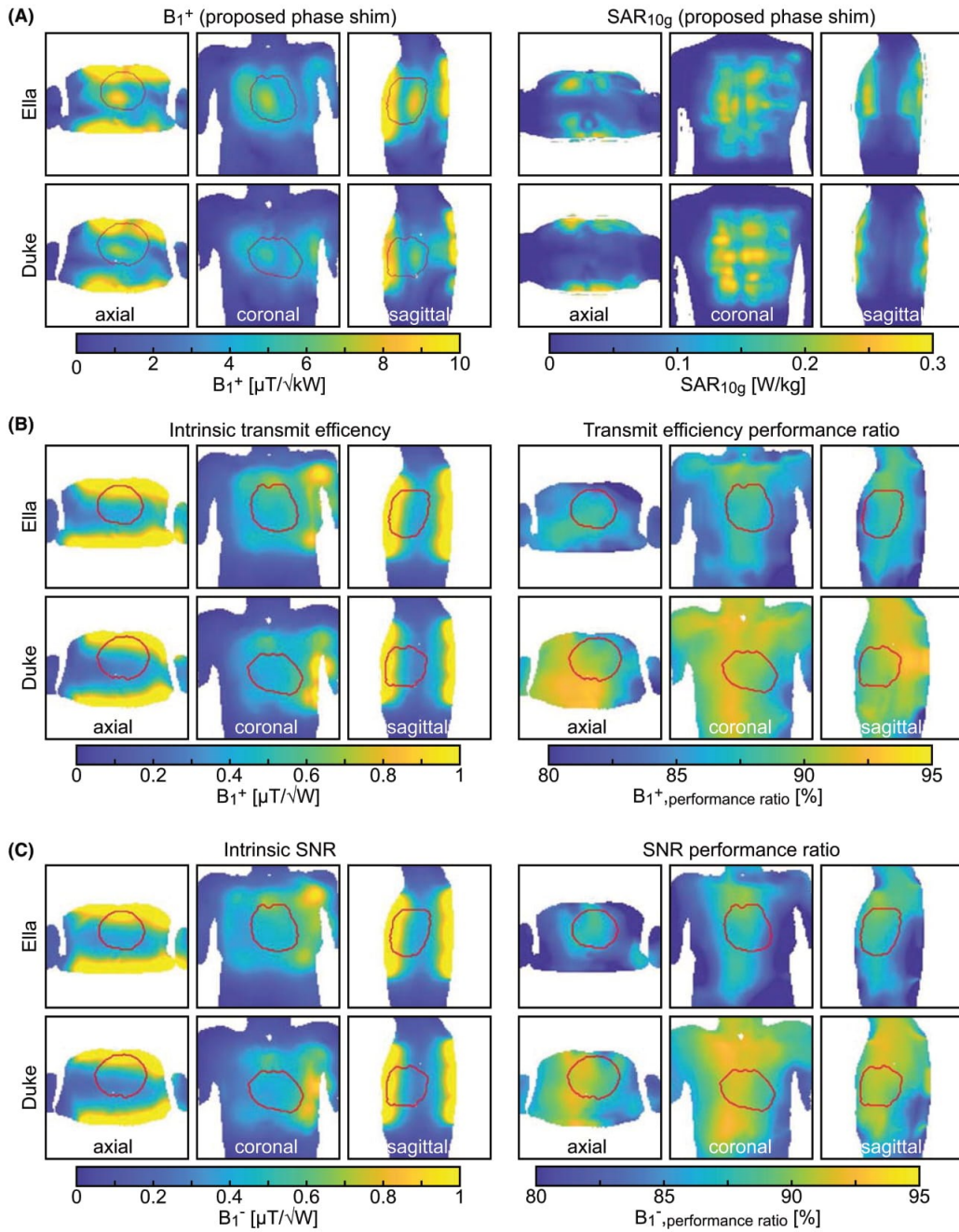


FIGURE 4 Summary of results obtained from the proposed optimized phase shim excitation ($\alpha_{\text{exc}} = [-0; 275; 241; 191; 135; 48; 0; 241; 204; 164; 128; 310; 273; 239; 169; 108; 0; 34; 33; 24; 9; 97; 126; 135; 115; 61; 38; 95; 82; 32; 311; 0]^\circ$) using the human voxel models Ella and Duke. A, B_1^+ efficiency is visualized for three orthogonal slices through the center of the cardiac ROI (highlighted in red). SAR_{10g} is visualized as a maximum projection for three orthogonal views. For Ella, the simulations revealed (mean \pm SD [min]) $B_1^+ = (6.2 \pm 1.8 [3.4]) \mu\text{T}/\sqrt{\text{kW}}$ and $\text{SAR}_{10g,\text{max}} = 0.25 \text{ W/kg}$. Duke showed $B_1^+ = (5.6 \pm 1.9 [2.8]) \mu\text{T}/\sqrt{\text{kW}}$ and $\text{SAR}_{10g,\text{max}} = 0.30 \text{ W/kg}$. B, Intrinsic transmit efficiency and transmit efficiency performance ratio for the three orthogonal slices through the center of the cardiac ROI for Ella and Duke. For Ella, the intrinsic transmit efficiency revealed (mean \pm SD [min]) $B_1^+ = (0.68 \pm 0.27 [0.36]) \mu\text{T}/\sqrt{\text{W}}$ and $B_{1,\text{performance ratio}}^+ = (87.4 \pm 1.2 [82.7])\%$. For Duke, $B_1^+ = (0.61 \pm 0.31 [0.24]) \mu\text{T}/\sqrt{\text{W}}$ and $B_{1,\text{performance ratio}}^+ = (89.9 \pm 1.4 [83.2])\%$ was obtained. C, The intrinsic SNR and SNR performance ratio for three orthogonal slices through the cardiac ROI of Ella and Duke. For Ella, an intrinsic SNR (mean \pm SD [min]) of $B_1^- = (0.66 \pm 0.25 [0.36]) \mu\text{T}/\sqrt{\text{W}}$ and $B_{1,\text{performance ratio}}^- = (87.2 \pm 1.5 [82.0])\%$ was observed. For Duke, $B_1^- = (0.60 \pm 0.30 [0.26]) \mu\text{T}/\sqrt{\text{W}}$ and $B_{1,\text{performance ratio}}^- = (90.1 \pm 1.4 [85.3])\%$ was estimated

34; 33; 24; 9; 97; 126; 135; 115; 61; 38; 95; 82; 32; 311; 0]°) corresponding to $\delta = 2.0$ and $\lambda = 0.025$ showed both, a fair balance of the B_1^+ efficiency results of Ella and Duke with considerable low SAR_{10g} .

Figure 4A shows the B_1^+ efficiency distribution within the heart of the human voxel models for the proposed optimized phase shim excitation. A B_1^+ efficiency distribution of (mean \pm SD [min]) $(6.2 \pm 1.8 [3.4]) \mu\text{T}/\sqrt{\text{kW}}$ for Ella and $(5.6 \pm 1.9 [2.8]) \mu\text{T}/\sqrt{\text{kW}}$ for Duke was obtained. The SAR_{10g} distributions (Figure 4A) were normalized to an average total power of 1.0 W and demonstrate a maximum of 0.30 W/kg for both voxel models (0.25 W/kg for Ella and 0.30 W/kg for Duke). Considering the described hardware losses in the RF chain and a maximum allowed SAR_{10g} of 20 W/kg in the first level controlled mode, the input power was limited to 8.1 W per channel including a safety factor of 1.7.⁴⁶ The intrinsic transmit efficiency revealed (mean) 0.68 $\mu\text{T}/\sqrt{\text{W}}$ for Ella and 0.61 $\mu\text{T}/\sqrt{\text{W}}$ for Duke, while the realistic transmit efficiency was 0.59 $\mu\text{T}/\sqrt{\text{W}}$ for Ella and 0.55 $\mu\text{T}/\sqrt{\text{W}}$ for Duke, corresponding to a transmit efficiency performance ratio of 87.4% for Ella and 89.9% for Duke. The intrinsic SNR revealed 0.66 $\mu\text{T}/\sqrt{\text{W}}$ for Ella and 0.60 $\mu\text{T}/\sqrt{\text{W}}$ for Duke, while the realistic SNR was 0.58 $\mu\text{T}/\sqrt{\text{W}}$ for Ella and 0.54 $\mu\text{T}/\sqrt{\text{W}}$ for Duke. The SNR performance ratio was found to be 87.2% for Ella and 90.1% for Duke. The power absorption analysis of α_{exc} demonstrated that 65% and 74% of the input power is absorbed in the body of Ella and Duke. The other losses are comprised of 13-16% material including the hydrogel pad, 10-16% coupling, and 1% lumped element losses.

3.5 | Phantom experiments for EMF simulations validation

The simulated and measured B_1^+ efficiency maps showed a good quantitative agreement with the signal chain losses and the patient table cable losses of -6.37 dB (an additional -1.22 dB on top of the -5.15 dB losses) being included. Figure 5 shows the data for three slices through the phantom. The absolute (simulation – measurement) voxel difference obtained for all three slices was found to be (mean \pm SD)

$(-0.26 \pm 0.45) \mu\text{T}/\sqrt{\text{kW}}$ for an equal phase excitation and $(-0.01 \pm 0.50) \mu\text{T}/\sqrt{\text{kW}}$ for the proposed optimized phase excitation. The difference relative to the simulation results is $(-6.1 \pm 12.3)\%$ and $(-2.2 \pm 14.5)\%$ for the equal and the proposed phase excitation (α_{exc}). The B_1^+ efficiency distribution within the ROI in Figure 5C shows (mean \pm SD [min]) $(4.30 \pm 0.34 [3.34]) \mu\text{T}/\sqrt{\text{kW}}$ for the simulation and $(3.90 \pm 0.44 [2.43]) \mu\text{T}/\sqrt{\text{kW}}$ for the measurement.

3.6 | Volunteer study

Figure 6 shows in vivo flip angle maps and the corresponding thresholded B_1^+ efficiency distributions ($\text{FA} \leq 15^\circ$) for sagittal, coronal, and transversal views through the heart. In vivo B_1^+ efficiency (mean \pm SD) within the cardiac ROI was $2.8 \pm 0.9 \mu\text{T}/\sqrt{\text{kW}}$ for the female (subject 4) and $2.3 \pm 0.7 \mu\text{T}/\sqrt{\text{kW}}$ for the male (subject 5). For comparison with the simulation results (Ella: $6.2 \pm 1.8 \mu\text{T}/\sqrt{\text{kW}}$; Duke: $5.6 \pm 1.9 \mu\text{T}/\sqrt{\text{kW}}$), the in vivo data are scaled by the measured losses (-6.37 dB) and correspond to $5.8 \mu\text{T}/\sqrt{\text{kW}}$ for the female subject and $4.8 \mu\text{T}/\sqrt{\text{kW}}$ for the male subject as a mean value for the cardiac ROI.

Figure 7 shows the 4CV, 3CV, 2CV, and SAX views of the heart obtained from 2D CINE FLASH using the optimized phase setting (α_{exc}). For the acquisition, an in-plane spatial resolution of $1.1 \times 1.1 \text{ mm}^2$ and a slice thickness of 2.5 mm were used. The image quality over all subjects included in our feasibility study was consistent without major signal voids due to destructive interferences.

4CV and SAX views of the heart at increasing spatial resolutions are shown in Figure 8. The overall image quality and enhancements in the spatial resolution enabled the visualization of fine subtle anatomic structures including the compact layer of the right ventricular free wall and the remaining trabecular layer. Pericardium, mitral, and tricuspid valves and their associated papillary muscles, and trabeculae are identifiable. The high spatial resolution protocol ($0.8 \times 0.8 \times 2.5 \text{ mm}^3$) presents a 12-fold improvement in the spatial resolution versus a standardized clinical CMR protocol.⁴¹ A normalized signal intensity distribution obtained for the left ventricular myocardium

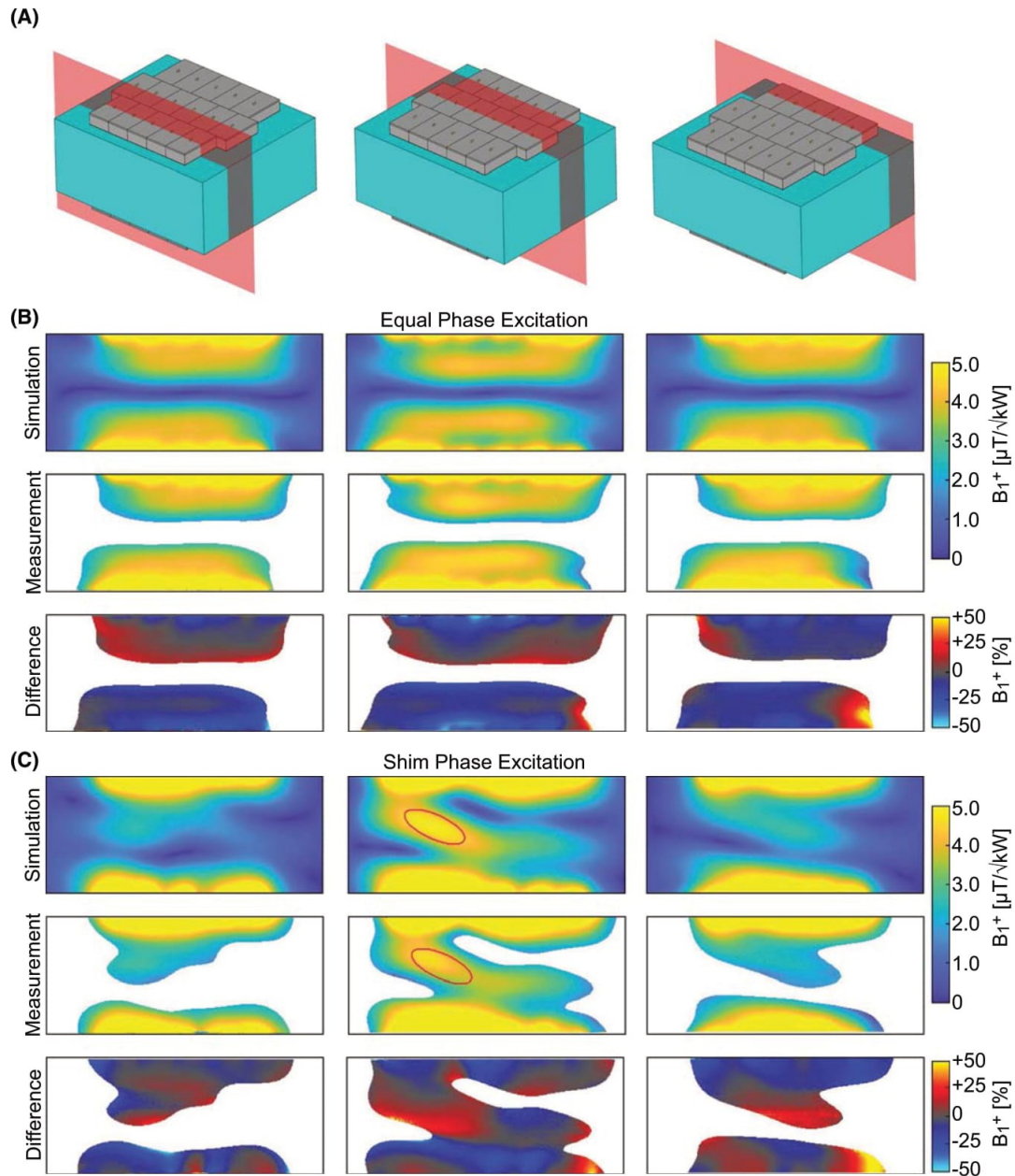


FIGURE 5 A) Illustration of the setup and slice positioning (slice 1-3) used for B_1^+ efficiency simulations and measurements. B_1^+ distribution obtained for equal phase excitation ($\alpha_1 \dots \alpha_{32} = 0^\circ$) (B) and proposed optimized phase shim excitation (α_{exc}) (C), including B_1^+ efficiency simulation results, B_1^+ efficiency mapping, and relative difference map in percent. For the measurement, a 3D AFI (spatial resolution = $1.0 \times 1.0 \times 5.0 \text{ mm}^3$, TE = 1.94 ms, TR₁ = 29 ms, TR₂ = 109 ms, nominal FA = 50°, V_{ref} = 520 V, 64 slices) was used. For the ROI marked in red, the optimized phase shim excitation (α_{exc}) shows (mean ± SD [min]) $B_1^+ = (4.30 \pm 0.34 [3.34]) \mu\text{T}/\sqrt{\text{kW}}$ for the simulation and $B_1^+ = (3.90 \pm 0.44 [2.43]) \mu\text{T}/\sqrt{\text{kW}}$ for the measurement

is shown in Figure 8C for each spatial resolution. The results show no major signal voids for the SAX and a signal intensity variation of approximately $\pm 50\%$ with the lowest signal being found in the lateral wall of the left ventricle.

Figure 9 shows a dataset including SNR maps and g-factor maps for R = 2 to R = 6. The spatial resolution ($1.1 \times 1.1 \times 2.5 \text{ mm}^3$) presents a 6-fold improvement in the spatial resolution versus a standardized clinical CMR protocol.⁴¹ For

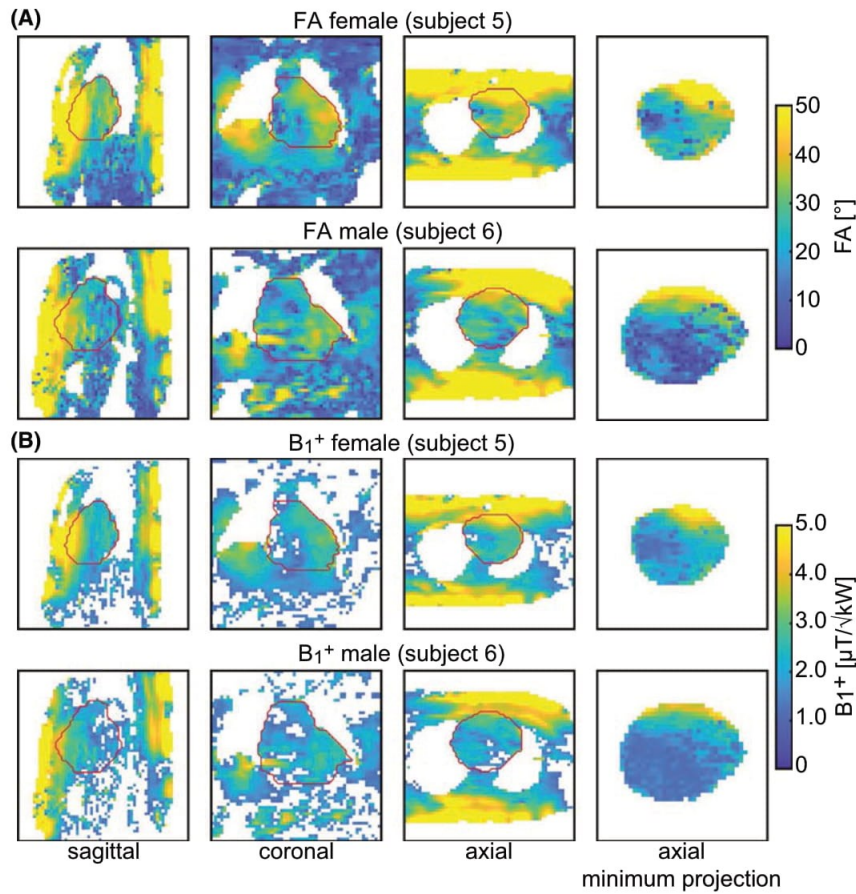


FIGURE 6 A, In vivo flip angle (FA) maps acquired with a 3D radial sampled free-breathing AFI (spatial resolution = $5.0 \times 5.0 \times 5.0$ mm³, rectangular pulse PD = 0.5 ms TE = 2.04 ms, TR₁ = 10 ms, TR₂ = 50 ms, nominal FA = 66°, V_{ref} = 520 V, and 12 readouts per radial line) in a female and male human subject. B, B₁⁺ efficiency maps calculated based on FA results with FA ≤ 15° rejected. FA and B₁⁺ are shown for a sagittal (first column), coronal (second column), and axial slice (third column) through the heart (cardiac ROI highlighted in red) as well as a minimum projection in the axial direction (4th column). For the female subject, the in vivo measurements revealed (mean ± SD) FA = (35.7 ± 11.7)° and B₁⁺ = (2.8 ± 0.9) μT/√kW. For the male subject, FA = (28.2 ± 10.1)° and B₁⁺ = (2.3 ± 0.7) μT/√kW were observed

all acceleration factors used for the acquisition of 4CV and SAX views, the CNR mean and standard deviation, as well as the SNR_{whole-heart,mean} and the SNR_{myocardium,mean} mean, minimum, and maximum are summarized in Table 1 for all subjects. The mean g-factor_{whole-heart,mean} of all subjects was ranging between 1.1 (R = 2) and 2.4 (R = 6) for the 4CV and between 1.1 (R = 2) and 2.5 (R = 6) for the SAX. In analogy the analysis of the g-factor_{whole-heart,max} allows the assessment of the worst-case noise amplification. For R = 4 it was found to be (mean [max]) 2.2 [2.7] for the 4CV and 2.0 [2.4] for the SAX. This performance affords the acquisition of up to 4 slices per breath-hold with clinically acceptable image quality. Noise amplification associated with 1D parallel imaging increased severely with R = 6 as demonstrated in Figure 9.

4 | DISCUSSION

This work reports on the design, implementation, evaluation, and application of a modular 32-channel SGBT TX/RX array tailored for CMR at 7.0 T. The compact SGBT antenna building blocks support a flexible and reconfigurable arrangement of a high-density array that conveniently conforms to an average upper torso. The in vivo CMR feasibility study revealed good image quality, anatomic coverage, B₁⁺ penetration depth, blood myocardium contrast (ie, CNR), and SNR. The overall image quality and the high spatial resolution help to reduce partial volume effects. These improvements may be particularly useful for visualizing small rapidly moving structures like valve cusps, assessing subtle anatomical features such as

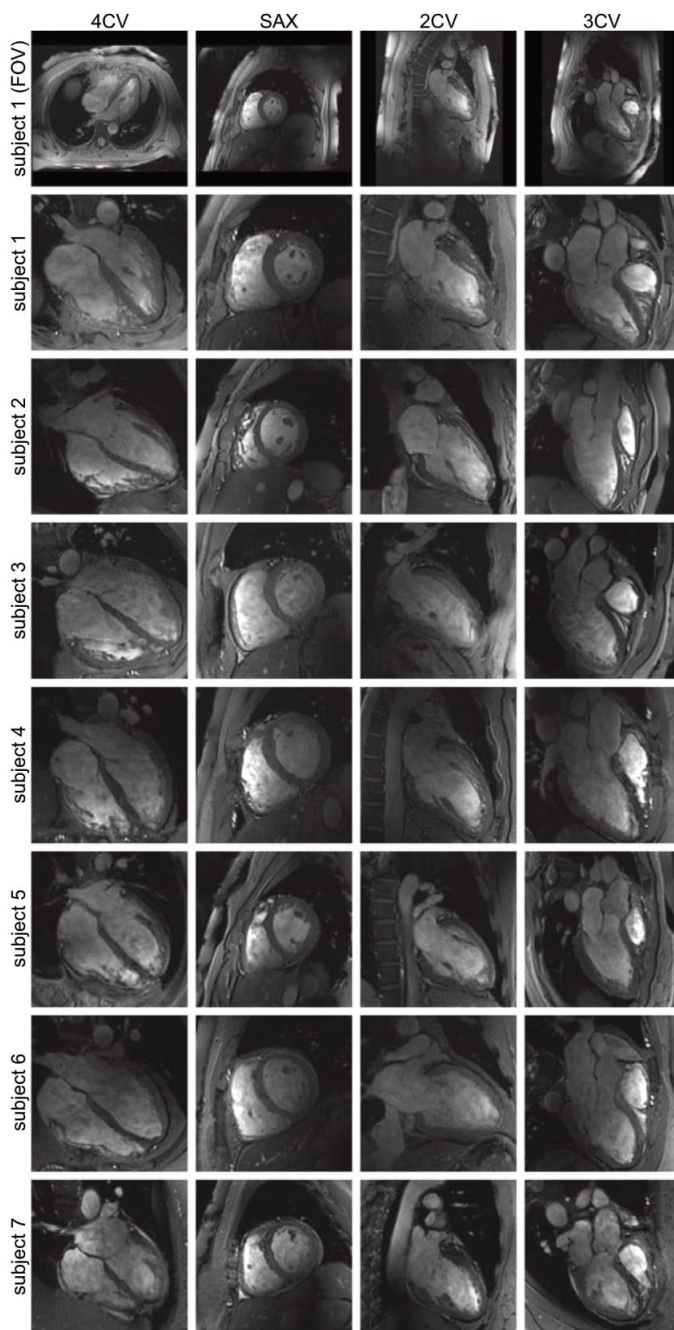


FIGURE 7 End-diastolic 4CV, SAX, 2CV, and 3CV derived from 2D CINE FLASH imaging (spatial resolution = $1.1 \times 1.1 \times 2.5 \text{ mm}^3$, TE = 2.09 ms, TR = 4.55 ms, GRAPPA R = 2; views per segment = 10, cardiac phases = 30, BW = 446 Hz/Px, nominal FA = 22° , $V_{\text{ref}} = 520 \text{ V}$). Subject 1 is shown as a whole field of view (FOV) and as ROI magnified view. All seven subjects (three female, four male; age: 29-59; BMI: $23.8 \pm 2.1 \text{ kg/m}^2$) were examined without subject-specific adjustment of the SGBT antenna array geometry or the phase set

trabeculae, or extending morphologic assessment to the right ventricle including patients with congenital heart disease.^{47,48}

The footprint of the SGBT building block ($89.3 \times 48.0 \times 25.8 \text{ mm}^3$) is reduced by 64% versus a very well established fractionated dipole ($300 \times 40 \times 20 \text{ mm}^3$),¹¹ 59% versus

a bow-tie building block ($150 \times 70 \times 40 \text{ mm}^3$),¹⁷ 43% versus a single-side adapted dipole ($143 \times 70 \times 42 \text{ mm}^3$),¹⁶ and 87% versus a self-matched leaky-wave antenna ($384 \times 85 \times 18 \text{ mm}^3$).⁵ The weight of the proposed building block is 156 g which is 56 g heavier compared to a 32-channel cardiac loop

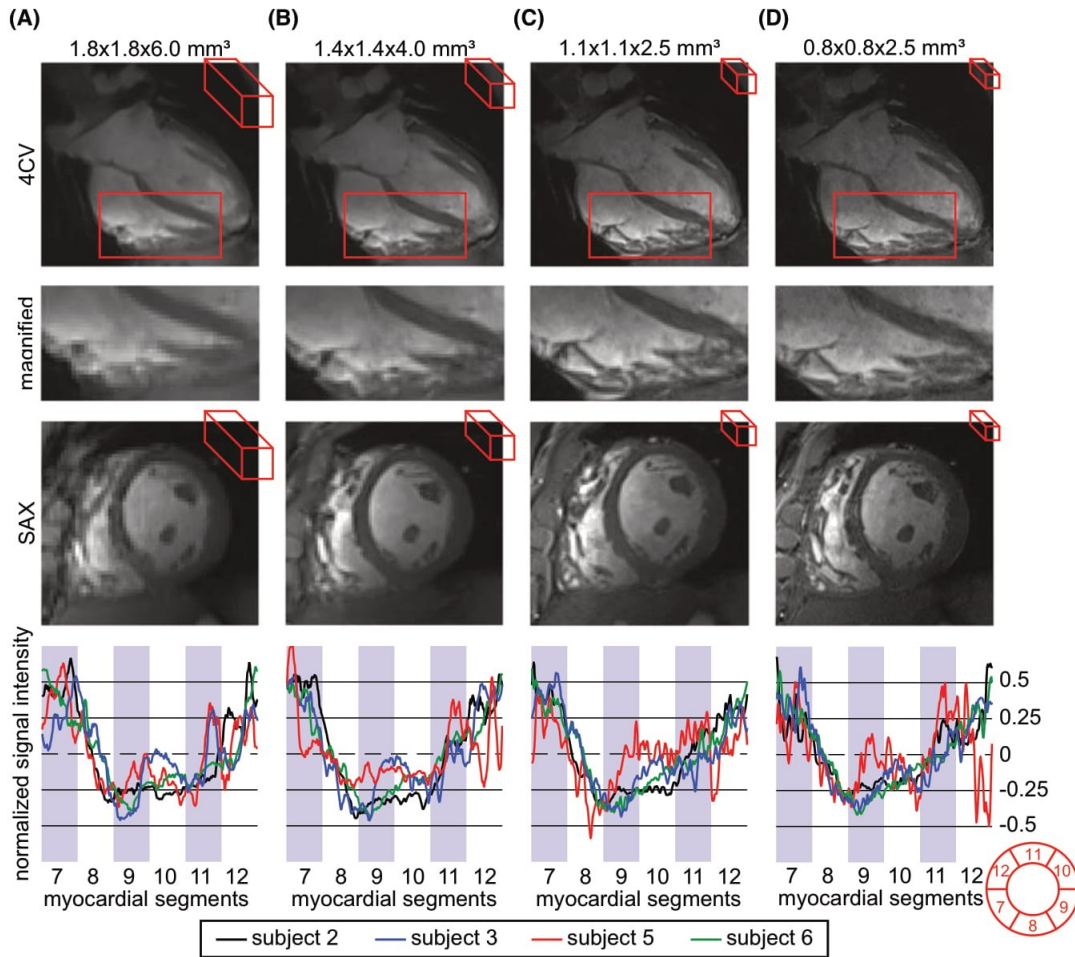


FIGURE 8 The 4CV (first row), magnified view of a section of the right ventricle (second row), and SAX view (third row) of the heart using different in-plane resolutions and slice thicknesses ranging from standard clinical protocols $1.8 \times 1.8 \times 6.0 \text{ mm}^3$ (A) and $1.4 \times 1.4 \times 4.0 \text{ mm}^3$ (B) to enhanced spatial resolutions $1.1 \times 1.1 \times 2.5 \text{ mm}^3$ (C) and $0.8 \times 0.8 \times 2.5 \text{ mm}^3$ (D). Normalized signal intensity plot (fourth row) along a circular trajectory through the myocardium of the mid-ventricular SAX views at end-diastole. For this purpose, standard segmentation of the myocardium was used⁴²

element configuration with approximately 100 g (per channel), but 264 g lighter compared to a 16-channel cardiac bow-tie building block configuration exhibiting a weight of 420 g per building block (size $40 \times 150 \times 70 \text{ mm}^3$ filled with D_2O).^{6,17} As the hydrogel pad is an integral part of the SGBT antenna array, the weight of the pad adds 1.3 kg, which results in additional 81 g per channel for the anterior part of the antenna array.

The combined (Ella and Duke) B_1^+ shim procedure aimed to balance B_1^+ for both models and to provide a more generalized phase shim (α_{exC}) that supports a broader spectrum of cardiac anatomy. Individual B_1^+ optimization revealed a B_1^+ efficiency (mean \pm SD [min]) of $(6.2 \pm 1.4 [4.0]) \mu\text{T}/\sqrt{\text{kW}}$

for Ella and $(5.8 \pm 2.0 [3.0]) \mu\text{T}/\sqrt{\text{kW}}$ for Duke. Previous reports on transmission field shaping of loop antenna configurations tailored for CMR at 7.0 T documented a B_1^+ efficiency of $7.4 \pm 3.6 \mu\text{T}/\sqrt{\text{kW}}$ (4 channel array), $5.4 \pm 3.1 \mu\text{T}/\sqrt{\text{kW}}$ (8 channel array), and $6.5 \pm 3.1 \mu\text{T}/\sqrt{\text{kW}}$ (16-channel array).⁷ This translates into an at least 55% higher standard deviation and 38% higher coefficient of variation (ratio of standard deviation to mean), resulting in a reduced B_1^+ homogeneity. The maximum $\text{SAR}_{10\text{g}}$ obtained for both human voxel models does not exceed 0.3 W/kg per Watt of input power using the proposed optimized phase set. This outcome is improved or similar to previously reported RF array configurations tailored for CMRI at 7.0 T.^{6,8-10,14,15,17,49} Simulation results

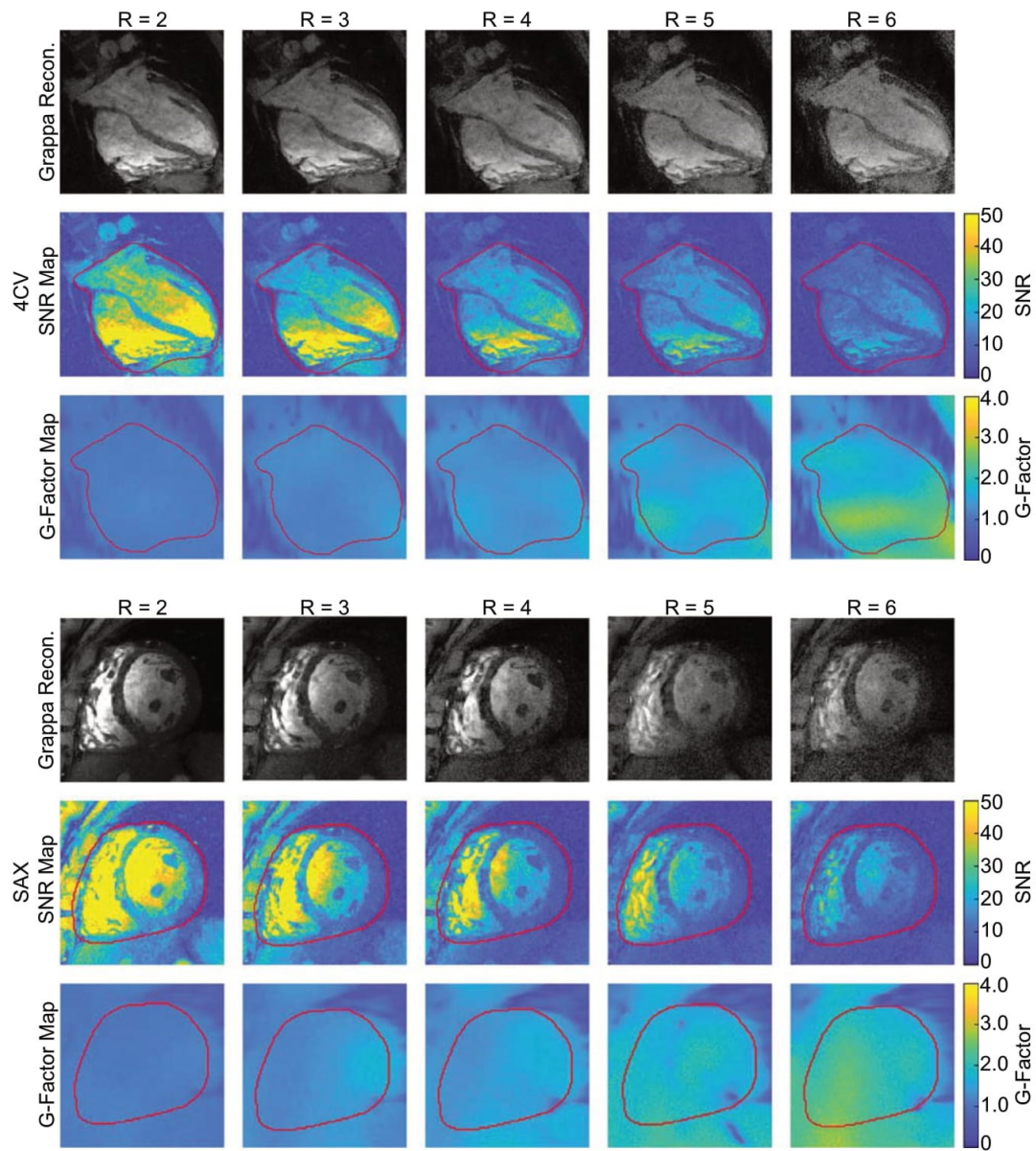


FIGURE 9 Results (female, subject 2) derived from 1D parallel imaging using acceleration factors ranging from R = 2 to R = 6. GRAPPA accelerated 2D CINE FLASH (spatial resolution = $1.1 \times 1.1 \times 2.5 \text{ mm}^3$, TE = 2.5 ms, TR = 4.55 ms, views per segment = 10, BW = 446 Hz/Px, nominal FA = 22° , $V_{\text{ref}} = 520\text{V}$) images (first and 4th row), SNR scaled maps (second and fifth row), and g-factor map (third and sixth row) for 4CV (A) and SAX view (B); both with phase encoding direction A-P

derived for a 32-channel loop array configuration tailored for CMR at 7.0 T revealed a realistic transmit efficiency of (mean) $0.47 \mu\text{T}/\sqrt{\text{W}}$ for Ella and of $0.44 \mu\text{T}/\sqrt{\text{W}}$ for Duke and a transmit efficiency performance ratio of 73.5% for Ella and 74.9% for Duke.⁶ This suggests an at least 25% improved realistic transmit efficiency at an elevated performance ratio

for the SGBT antenna array ($0.59 \mu\text{T}/\sqrt{\text{W}}$ and 87.4% for Ella, $0.55 \mu\text{T}/\sqrt{\text{W}}$, and 89.9% for Duke). The simulated B_1 superpositions for the SGBT antenna array revealed that the efficiency reduction due to intrinsic coil losses is relatively constant throughout the ROI. This presents an advantage over loop arrays, where peripheral SNR experiences a stronger

TABLE 1 4CV and SAX view analysis of GRAPPA accelerated image acquisition at increasing reduction factors (R) of four subjects (two female / two male)^a

View	Analysis	R = 2	R = 3	R = 4	R = 5	R = 6
4CV	CNR: Mean \pm Std	27.0 \pm 1.9	19.5 \pm 2.1	13.5 \pm 1.9	9.9 \pm 1.7	6.3 \pm 1.7
	SNR _{whole-heart,mean} : Mean [Min Max]	31.6 [29.6 34.2]	22.9 [20.6 24.7]	16.7 [15.5 18.8]	12.2 [10.6 14.9]	8.6 [7.5 11.0]
	SNR _{myocardium,mean} : Mean [Min Max]	18.4 [16.0 20.7]	13.6 [10.9 16.1]	10.1 [8.3 12.6]	7.0 [5.6 9.7]	5.2 [4.3 7.2]
	g-factor _{whole-heart,mean} : Mean [Max]	1.1 [1.1]	1.3 [1.4]	1.5 [1.6]	1.9 [2.1]	2.4 [2.7]
	g-factor _{whole-heart,max} : Mean [Max]	1.3 [1.4]	1.8 [2.1]	2.2 [2.7]	3.3 [4.4]	4.3 [5.2]
SAX	CNR: Mean \pm Std	41.0 \pm 5.5	26.9 \pm 3.0	19.9 \pm 2.9	12.5 \pm 1.9	8.4 \pm 2.3
	SNR _{whole-heart,mean} : Mean [Min Max]	38.2 [32.7 42.4]	26.7 [24.0 30.4]	19.5 [16.6 21.8]	14.0 [11.8 16.9]	9.5 [8.0 11.7]
	SNR _{myocardium,mean} : Mean [Min Max]	18.4 [16.6 19.6]	13.3 [11.2 16.9]	9.7 [8.6 10.9]	7.5 [6.3 8.5]	5.5 [4.6 6.1]
	g-factor _{whole-heart,mean} : Mean [Max]	1.1 [1.1]	1.3 [1.4]	1.5 [1.6]	1.9 [2.2]	2.5 [3.0]
	g-factor _{whole-heart,max} : Mean [Max]	1.3 [1.3]	1.7 [1.9]	2.0 [2.4]	2.8 [3.1]	4.0 [4.6]

^aThe data contain the contrast-to-noise ratio (CNR, mean and SD), the SNR for the whole heart and the myocardium (mean, minimum, and maximum), and the geometry factor (g-factor, mean, and max).

degradation due to coil losses compared to more central locations.⁵⁰

The hydrogel pad promotes the performance by enhancing EMF coupling to the subject. Without the hydrogel pad and an optimized phase set, the mean B_1^+ efficiency in the heart is reduced by 45% for Ella and 39% for Duke in the same simulation setup, co-simulation, and B_1^+ shimming approach. The calculation of the optimal B_1 superposition for simulations without the hydrogel pad revealed a lower performance ratio for B_1^+ (Ella: 52%, Duke: 60%) and B_1^- (Ella: 49%, Duke: 57%).

The phantom study revealed a good agreement between simulations and measurements which is documented by a difference of 7% of the mean B_1^+ efficiency values within the defined ROI. The in vivo mean B_1^+ efficiency (female: $B_1^+ = 2.8 \mu\text{T}/\sqrt{\text{kW}}$, male: $B_1^+ = 2.3 \mu\text{T}/\sqrt{\text{kW}}$) showed a deviation of 6% and 14% versus the simulations (Ella: $B_1^+ = 2.9 \mu\text{T}/\sqrt{\text{kW}}$; Duke: $B_1^+ = 2.7 \mu\text{T}/\sqrt{\text{kW}}$) including the losses in the RF signal chain of -6.37 dB.

The small antenna building block size combined with the excellent decoupling behavior enables the setup of high-density arrays, where the building blocks can be arranged close to each other without additional decoupling measures. The compactness of the RF array benefits parallel imaging performance, where electrodynamics dictates a rapid SNR degeneration at high 1D accelerations. In recognition of the benefits of the SGBT antenna, the high-density RF array might be translated into a reduction of noise amplification in parallel imaging with the goal to preserve SNR by using 2D acceleration versus 1D acceleration.⁵¹⁻⁵³ 2D parallel imaging of the heart is only practical in the slice direction if compact RF elements such as the SGBT are used as RF arrays. The mean whole heart SNR values and CNRs of the proposed SGBT

antenna array outperform the SNR and CNR reported for a 32-channel loop array configuration with the exception of the SAX view at $R = 6$.⁶ For the 4CV and the SAX view at $R = 4$ the mean SNR_{whole-heart,mean} was 17 and 20 for the SGBT design versus 11 and 17 for the 32-channel loop array.⁶ The mean CNR for 4CV and SAX at $R = 4$ were found to be 14 and 20 for the SGBT antenna array which compares to 3 and 10 for the loop array configuration.⁶ The benchmarking of the mean g-factor_{whole-heart,mean} revealed lower values for $R \leq 3$, whereas increased reduction factors ($R > 3$) showed superior performance of the loop array compared to the SGBT array.⁶ Due to differences in the acquisition and the image reconstruction, the results of this comparison need to be interpreted with caution and are subject to variations in the GRAPPA reconstruction.

The SGBT building block was matched and tuned to a resonance frequency of 297.2 MHz in this work. It can be conveniently adapted to a wideband configuration supporting resonance frequencies of up to 600 MHz which would facilitate CMR at magnetic field strengths of up to 14.0 T.^{23,27} A high-density TX/RX array accommodating wideband SGBTs would afford $^1\text{H}/^{19}\text{F}$ CMR which would promote translational research by benefitting explorations into molecular CMR including assessment of cardiac inflammation.^{54,55}

Recognizing the opportunities of adding a thermal intervention dimension to an MRI device for studying the role of temperature in biological systems and disease our high-density RF array opens a trajectory to an integrated, multi-purpose RF applicator. This applicator accommodates RF-induced heating, in vivo temperature mapping using MR thermometry, anatomic and functional MRI, and the option for x-nuclei MRI (Thermal MR).⁵⁶⁻⁶¹ Potential clinical applications extend beyond diagnostic cardiac imaging and can

serve as a platform to treat cardiovascular diseases, where localized RF intervention might be used, eg, terminate defective electrical pathways. Studies will reveal whether UHF-MR guided targeted RF heating for focal RF ablation can be used to terminate defective electrical pathways in the heart, and offer an alternative approach to current invasive intracardiac catheterization for the treatment of tachycardia.

5 | CONCLUSIONS

To conclude, the presented high-density transceiver array supports CMR at 7.0 T using a single feeding RF power amplifier mode without the need for subject-specific shimming or coil adjustments for the considered BMI range. The proposed cardiac TX/RX array is compatible with a multiple feeding RF power amplifier mode and contributes to the technological basis for the future clinical assessment of parallel transmit techniques designed for cardiac MR at ultrahigh magnetic fields. This work demonstrated the feasibility of the proposed modular TX/RX array for cardiac MR but the range of applications can be extended to renal imaging, abdominal imaging, pelvic imaging, thorax, and lumbar spine imaging, as well as other large-volume imaging MR applications by reconfiguring the SGBT building block-based array. With appropriate multi-transmit systems that offer more than today's state-of-the-art 8 or 16 TX channels, one might envisage the implementation of cardiac coil arrays with 32 and more TX/RX elements with the ultimate goal to break ground for many elements upper torso or body RF coil array.

ACKNOWLEDGMENTS

This project has received funding in part (TWE, TN) from the European Research Council (ERC) under the European Union's Horizon 2020 research and innovation program under grant agreement No 743077 (ThermalMR). AK, HW, and TN were supported by a grant from the EURSTARS initiative of the European Union (E! 12074) and from the Federal Ministry for Education and Research (MENTORA_4_EU, FKZ.01QE1815).

The authors wish to thank Sebastian Schmitter (Physikalisch-Technische Bundesanstalt (PTB), Braunschweig and Berlin, Germany) for technical support on B_1^+ efficiency mapping and Christoph Aigner (Physikalisch-Technische Bundesanstalt (PTB), Braunschweig and Berlin, Germany) for fruitful discussions on image reconstruction and post-processing. Open access funding enabled and organized by Projekt DEAL.

DATA AVAILABILITY STATEMENT

The antenna model with the manufacturing tool models, the transmission field shaping approach, and parts of the image reconstruction and post-processing of this study are openly available at <https://doi.org/10.17605/OSF.IO/NGHFS>.

ORCID

Thomas Wilhelm Eigentler  <https://orcid.org/0000-0001-8252-450X>

Andre Kuehne  <https://orcid.org/0000-0002-4133-5056>

Laura Boehmert  <https://orcid.org/0000-0002-8703-3133>

Sebastian Dietrich  <https://orcid.org/0000-0002-1610-909X>

Helmar Waiczies  <https://orcid.org/0000-0001-6651-4790>

Thoralf Niendorf  <https://orcid.org/0000-0001-7584-6527>

REFERENCES

- Niendorf T, Schulz-Menger J, Paul K, Huelnhagen T, Ferrari VA, Hodge R. High field cardiac magnetic resonance imaging: a case for ultrahigh field cardiac magnetic resonance. *Circ Cardiovasc Imaging*. 2017;10:1-13.
- Niendorf T, Paul K, Oezerdem C, et al. W(h)ither human cardiac and body magnetic resonance at ultrahigh fields? Technical advances, practical considerations, applications, and clinical opportunities. *NMR Biomed*. 2016;29:1173-1197.
- Padormo F, Beqiri A, Hajnal JV, Malik SJ. Parallel transmission for ultrahigh-field imaging. *NMR Biomed*. 2016;29:1145-1161.
- Snyder CJ, DelaBarre L, Metzger GJ, et al. Initial results of cardiac imaging at 7 Tesla. *Magn Reson Med*. 2009;61:517-524.
- Solomakha G, Svejda JT, van Leeuwen C, et al. A self-matched leaky-wave antenna for ultrahigh-field magnetic resonance imaging with low specific absorption rate. *Nat Commun*. 2021;12:1-11.
- Graessl A, Renz W, Hezel F, et al. Modular 32-channel transceiver coil array for cardiac MRI at 7.0T. *Magn Reson Med*. 2014;72:276-290.
- Winter L, Kellman P, Renz W, et al. Comparison of three multichannel transmit/receive radiofrequency coil configurations for anatomic and functional cardiac MRI at 7.0T: implications for clinical imaging. *Eur Radiol*. 2012;22:2211-2220.
- Thalhammer C, Renz W, Winter L, et al. Two-dimensional sixteen channel transmit/receive coil array for cardiac MRI at 7.0 T: design, evaluation, and application. *J Magn Reson Imaging*. 2012;36:847-857.
- Dieringer MA, Renz W, Lindel T, et al. Design and application of a four-channel transmit/receive surface coil for functional cardiac imaging at 7T. *J Magn Reson Imaging*. 2011;33:736-741.
- Gräßl A, Winter L, Thalhammer C, et al. Design, evaluation and application of an eight channel transmit/receive coil array for cardiac MRI at 7.0T. *Eur J Radiol*. 2013;82:752-759.
- Raaijmakers AJE, Italiaander M, Voogt IJ, et al. The fractionated dipole antenna: a new antenna for body imaging at 7 Tesla. *Magn Reson Med*. 2016;75:1366-1374.
- Steenma B, Moortele P-F, Ertürk A, et al. Introduction of the snake antenna array: geometry optimization of a sinusoidal dipole antenna for 10.5T body imaging with lower peak SAR. *Magn Reson Med*. 2020;84:2885-2896.
- Alon L, Lattanzi R, Lakshmanan K, et al. Transverse slot antennas for high field MRI. *Magn Reson Med*. 2018;80:1233-1242.
- Steenma BR, Voogt IJ, Leiner T, et al. An 8-channel Tx/Rx dipole array combined with 16 Rx loops for high-resolution functional cardiac imaging at 7 T. *Magn Reson Mater Physics, Biol Med*. 2018;31:7-18.
- Ertürk MA, Raaijmakers AJE, Adriany G, Uğurbil K, Metzger GJ. A 16-channel combined loop-dipole transceiver array for 7 Tesla body MRI. *Magn Reson Med*. 2017;77:884-894.

16. Raaijmakers AJE, Ipek O, Klomp DWJ, et al. Design of a radiative surface coil array element at 7 T: the single-side adapted dipole antenna. *Magn Reson Med.* 2011;66:1488-1497.
17. Oezerdem C, Winter L, Graessl A, et al. 16-channel bow tie antenna transceiver array for cardiac MR at 7.0 Tesla. *Magn Reson Med.* 2016;75:2553-2565.
18. Raaijmakers AJE, Luijten PR, van den Berg CAT. Dipole antennas for ultrahigh-field body imaging: a comparison with loop coils. *NMR Biomed.* 2016;29:1122-1130.
19. Lattanzi R, Sodickson DK. Ideal current patterns yielding optimal signal-to-noise ratio and specific absorption rate in magnetic resonance imaging: computational methods and physical insights. *Magn Reson Med.* 2012;68:286-304.
20. Lattanzi R, Sodickson DK, Grant AK, Zhu Y. Electrodynamic constraints on homogeneity and radiofrequency power deposition in multiple coil excitations. *Magn Reson Med.* 2009;61:315-334.
21. De Zwart JA, Ledden PJ, Kellman P, Van Gelderen P, Duyn JH. Design of a SENSE-optimized high-sensitivity MRI receive coil for brain imaging. *Magn Reson Med.* 2002;47:1218-1227.
22. Winter L, Özerdem C, Hoffmann W, et al. Design and evaluation of a hybrid radiofrequency applicator for magnetic resonance imaging and RF induced hyperthermia: electromagnetic field simulations up to 14.0 Tesla and proof-of-concept at 7.0 Tesla. Yacoub E, ed. *PLoS One.* 2013;8:e61661.
23. Eigentler TW, Winter L, Han H, et al. Wideband self-grounded bow-tie antenna for thermal MR. *NMR Biomed.* 2020;33:e4274.
24. Niendorf T, Graessl A, Thalhammer C, et al. Progress and promises of human cardiac magnetic resonance at ultrahigh fields: a physics perspective. *J Magn Reson.* 2013;229:208-222.
25. Eigentler TW, Boehmert L, Kuehne A, Wenz D, Oberacker E, Han H. Compact self grounded bow tie antenna resonator for cardiac MRI at 7.0 Tesla. In Proceedings of the 27th Annual Meeting of ISMRM, Montreal, CA, 2019. p. 0436.
26. Yang J, Kishk A. A novel low-profile compact directional ultra-wideband antenna: the self-grounded bow-tie antenna. *IEEE Trans Antennas Propag.* 2012;60:1214-1220.
27. Takook P, Persson M, Gellermann J, Trefná HD. Compact self-grounded Bow-Tie antenna design for an UWB phased-array hyperthermia applicator. *Int J Hyperth.* 2017;33:387-400.
28. Trefná HD, Ström A. Hydrogels as a water bolus during hyperthermia treatment. *Phys Med Biol.* 2019;64:115025.
29. Christ A, Kainz W, Hahn EG, et al. The Virtual Family—development of surface-based anatomical models of two adults and two children for dosimetric simulations. *Phys Med Biol.* 2010;55:N23-N38.
30. Athey TW, Stuchly MA, Stuchly SS. Measurement of radio frequency permittivity of biological tissues with an open-ended coaxial line: part I. *IEEE Trans Microw Theory Tech.* 1982;30:82-86.
31. IT'IS Foundation. *Tissue Properties Database V4.0.* Zürich: IT'IS Foundation. <https://itis.swiss/virtual-population/tissue-properties/overview/>.
32. Lemdiasov RA, Obi AA, Ludwig R. A numerical postprocessing procedure for analyzing radio frequency MRI coils. *Concepts Magn Reson Part A.* 2011;38A:133-147.
33. Kuehne A, Waiczies H, Niendorf T. Massively accelerated VOP compression for population-scale RF safety models. In Proceedings of the 25th Annual Meeting of ISMRM, Honolulu, HI, 2017. p. 0478.
34. Eichfelder G, Gebhardt M. Local specific absorption rate control for parallel transmission by virtual observation points. *Magn Reson Med.* 2011;66:1468-1476.
35. Kuehne A, Goluch S, Waxmann P, et al. Power balance and loss mechanism analysis in RF transmit coil arrays. *Magn Reson Med.* 2015;74:1165-1176.
36. Lakshmanan K, Cloos M, Brown R, Lattanzi R, Sodickson DK, Wiggins GC. The "loopole" antenna: a hybrid coil combining loop and electric dipole properties for ultra-high-field MRI. *Concepts Magn Reson Part B, Magn Reson Eng.* 2020;2020:1-9.
37. Georgakis IP, Polimeridis AG, Lattanzi R. A formalism to investigate the optimal transmit efficiency in radiofrequency shimming. *NMR Biomed.* 2020;33:1-18.
38. Yarnykh VL. Actual flip-angle imaging in the pulsed steady state: a method for rapid three-dimensional mapping of the transmitted radiofrequency field. *Magn Reson Med.* 2007;57:192-200.
39. Dietrich S, Aigner CS, Kolbitsch C, et al. 3D Free-breathing multichannel absolute mapping in the human body at 7T. *Magn Reson Med.* 2021;85:2552-2567.
40. Kellman P, McVeigh ER. Image reconstruction in SNR units: a general method for SNR measurement. *Magn Reson Med.* 2005;54:1439-1447.
41. Kramer CM, Barkhausen J, Bucciarelli-Ducci C, Flamm SD, Kim RJ, Nagel E. Standardized cardiovascular magnetic resonance imaging (CMR) protocols: 2020 update. *J Cardiovasc Magn Reson.* 2020;22:17.
42. Cerqueira MD, Weissman NJ, Dilsizian V, et al. Standardized myocardial segmentation and nomenclature for tomographic imaging of the heart. *J Cardiovasc Magn Reson.* 2002;4:203-210.
43. Griswold MA, Jakob PM, Heidemann RM, et al. Generalized auto-calibrating partially parallel acquisitions (GRAPPA). *Magn Reson Med.* 2002;47:1202-1210.
44. Hansen MS, Beatty P. ISMRM 2014 Sunrise Course on Parallel Imaging. ISMRM 22. Annual Meeting. https://github.com/hansenms/ismrm_sunrise_matlab. Published 2014.
45. Robson PM, Grant AK, Madhuranthakam AJ, Lattanzi R, Sodickson DK, McKenzie CA. Comprehensive quantification of signal-to-noise ratio and g-factor for image-based and k-space-based parallel imaging reconstructions. *Magn Reson Med.* 2008;60:895-907.
46. Meliadó EF, van den Berg CAT, Luijten PR, Raaijmakers AJE. Intersubject specific absorption rate variability analysis through construction of 23 realistic body models for prostate imaging at 7T. *Magn Reson Med.* 2019;81:2106-2119.
47. von Knobelsdorff-Brenkenhoff F, Tkachenko V, Winter L, et al. Assessment of the right ventricle with cardiovascular magnetic resonance at 7 Tesla. *J Cardiovasc Magn Reson.* 2013;15:1-9.
48. Al-Wakeel-Marquard N, Ferreira da Silva T, Jeuthe S, et al. Measuring myocardial extracellular volume of the right ventricle in patients with congenital heart disease. *Sci Rep.* 2021;11:1-9.
49. Boehmert L, Kuehne A, Waiczies H, et al. Cardiorenal sodium MRI at 7.0 Tesla using a 4/4 channel 1 H/ 23 Na radiofrequency antenna array. *Magn Reson Med.* 2019;82:2343-2356.
50. King SB, Varosi SM, Duensing GR. Eigenmode analysis for understanding phased array coils and their limits. *Concepts Magn Reson Part B Magn Reson Eng.* 2006;29B:42-49.
51. Ohliger MA, Grant AK, Sodickson DK. Ultimate intrinsic signal-to-noise ratio for parallel MRI: electromagnetic field considerations. *Magn Reson Med.* 2003;50:1018-1030.
52. Wiesinger F, Boesiger P, Pruessmann KP. Electrodynamics and ultimate SNR in parallel MR imaging. *Magn Reson Med.* 2004;52:376-390.
53. Niendorf T, Hardy CJ, Giaquinto RO, et al. Toward single breath-hold whole-heart coverage coronary MRA using highly accelerated

- parallel imaging with a 32-channel MR system. *Magn Reson Med*. 2006;56:167-176.
54. Ramos IT, Henningsson M, Nezafat M, et al. Simultaneous assessment of cardiac inflammation and extracellular matrix remodeling after myocardial infarction. *Circ Cardiovasc Imaging*. 2018;11:1-13.
55. Rothe M, Jahn A, Weiss K, et al. In vivo 19 F MR inflammation imaging after myocardial infarction in a large animal model at 3 T. *Magn Reson Mater Physics, Biol Med*. 2019;32:5-13.
56. Oberacker E, Kuehne A, Oezerdem C, et al. Radiofrequency applicator concepts for thermal magnetic resonance of brain tumors at 297 MHz (7.0 Tesla). *Int J Hyperth*. 2020;37:549-563.
57. Ji Y, Winter L, Navarro L, et al. Controlled release of therapeutics from thermoresponsive nanogels: a thermal magnetic resonance feasibility study. *Cancers*. 2020;12:1380.
58. Han H, Eigentler TW, Wang S, et al. Design, implementation, evaluation and application of a 32-channel radio frequency signal generator for thermal magnetic resonance based anti-cancer treatment. *Cancers (Basel)*. 2020;12:1720.
59. Winter L, Oezerdem C, Hoffmann W, et al. Thermal magnetic resonance: physics considerations and electromagnetic field simulations up to 23.5 Tesla (1GHz). *Radiat Oncol*. 2015;10:201.
60. Han H, Oberacker E, Kuehne A, et al. Multi-channel RF supervision module for thermal magnetic resonance based cancer therapy. *Cancers (Basel)*. 2021;13:1001.
61. Oberacker E, Diesch C, Nadobny J, et al. Patient-specific planning for thermal magnetic resonance of glioblastoma multiforme. *Cancers (Basel)*. 2021;13:1867.

How to cite this article: Eigentler TW, Kuehne A, Boehmert L, et al. 32-Channel self-grounded bow-tie transceiver array for cardiac MR at 7.0T. *Magn Reson Med*. 2021;00:1–18. <https://doi.org/10.1002/mrm.28885>

2.2 Wideband Self-Grounded Bow-Tie Antenna for Thermal MR

Targeted thermal intervention within an MRI system offers the opportunity to employ an antenna system that combines anatomical (^1H) as well as therapeutic (^{19}F) imaging, thermal intervention, and MR-thermometry in a single device. The focal point quality for the RF power deposition in the thermal intervention is governed by the radiation pattern of the single RF transmit elements, the channel count, and the thermal intervention frequency of the applicator.^{40–42} The RF applicator represents the last element in the signal chain for the Thermal MR setup (Figure 3). The wideband SGBT building block employs an antenna system with allowing an adjustment of the amplitude, phase, and frequency of the intervention signal (Section 1.5.2). Its small footprint and low coupling enable a high channel density which increases the degree of freedom for EMF shaping. The broadband ability supports time-multiplexed beamforming⁴³, a mixed frequency approach⁴⁴, and a time- and frequency-multiplexed⁴⁵ signal transmission to the subject. The usability of the single wideband SGBT antenna is shown in a phantom imaging study and thermal intervention experiments at 300 MHz, 400 MHz, and 500 MHz, as well as for in vivo imaging experiments. For the MRI study a whole-body 7.0 T was used, but the broadband characteristics of the introduced antenna supports field strengths beyond this as well. Due to the broadband antenna concept, it is independent to variations loading conditions, and facilitate ^{19}F MRI without additional tuning. ^{19}F MRI is of high interest for therapeutic localization and tracking. Furthermore the RF induced thermal intervention in combination with ^{19}F MRI can be used to supervise the release of fluorinated therapeutics from thermosensitive nanocarriers.⁷⁶

The wideband SGBT building block is a multipurpose antenna element allowing ^1H and ^{19}F MRI (approximately 7.0 T to 14.0 T), RF induced broadband thermal intervention, and MR-thermometry. With the free adjustment of the frequency of intervention signal it offers an extension of the features provided by the narrowband SGBT antenna system (Section 1.4).

Publication

Eigentler TW, Winter L, Han H, Oberacker E, Kuehne A, Waiczies H, Schmitter S, Boehmert L, Prinz C, Trefna H, Niendorf T. Wideband Self-Grounded Bow-Tie Antenna for Thermal MR at 7.0 Tesla. *NMR Biomed.* 2020; 33(5):e4274. doi: <https://doi.org/10.1002/nbm.4274>.

Received: 22 July 2019 | Revised: 7 January 2020 | Accepted: 27 January 2020

DOI: 10.1002/nbm.4274



RESEARCH ARTICLE

NMR
IN BIOMEDICINE WILEY

Wideband Self-Grounded Bow-Tie Antenna for Thermal MR

Thomas Wilhelm Eigentler^{1,2} | Lukas Winter^{1,3} | Haopeng Han^{1,4} |
 Eva Oberacker¹ | Andre Kuehne⁵ | Helmar Waiczies⁵ | Sebastian Schmitter³ |
 Laura Boehmert^{1,6} | Christian Prinz^{1,6} | Hana Dobsicek Trefna⁷ |
 Thoralf Niendorf^{1,5,8}

¹Berlin Ultrahigh Field Facility (B.U.F.F.), Max-Delbrück-Center for Molecular Medicine in the Helmholtz Association, Berlin, Germany

²Technische Universität Berlin, Chair of Medical Engineering, Berlin, Germany

³Physikalisch-Technische Bundesanstalt (PTB), Braunschweig und Berlin, Berlin, Germany

⁴Institute of Computer Science, Humboldt-Universität zu Berlin, Berlin, Germany

⁵MRI.TOOLS GmbH, Berlin, Germany

⁶Charité - Universitätsmedizin Berlin, corporate member of Freie Universität Berlin, Humboldt-Universität zu Berlin, and Berlin Institute of Health (BIH), Berlin, Germany

⁷Department of Electrical Engineering, Chalmers University of Technology, Gothenburg, Sweden

⁸Experimental and Clinical Research Center (ECRC), a joint cooperation between the Charité Medical Faculty and the Max-Delbrück-Center for Molecular Medicine in the Helmholtz Association, Berlin, Germany

Correspondence

Thoralf Niendorf, PhD, Max Delbrück Center for Molecular Medicine in the Helmholtz Association, Robert Roessle Strasse 10, 13125 Berlin, Germany.
 Email: thoralf.niendorf@mdc-berlin.de

Funding information

Bundesministerium für Bildung und Forschung, Grant/Award Number: FKZ 13GW0102A, FKZ 13GW0102B; H2020 European Research Council, Grant/Award Number: 743077

Abstract

The objective of this study was the design, implementation, evaluation and application of a compact wideband self-grounded bow-tie (SGBT) radiofrequency (RF) antenna building block that supports anatomical proton (¹H) MRI, fluorine (¹⁹F) MRI, MR thermometry and broadband thermal intervention integrated in a whole-body 7.0 T system.

Design considerations and optimizations were conducted with numerical electromagnetic field (EMF) simulations to facilitate a broadband thermal intervention frequency of the RF antenna building block. RF transmission (B_1^+) field efficiency and specific absorption rate (SAR) were obtained in a phantom, and the thigh of human voxel models (Ella, Duke) for ¹H and ¹⁹F MRI at 7.0 T. B_1^+ efficiency simulations were validated with actual flip-angle imaging measurements. The feasibility of thermal intervention was examined by temperature simulations ($f = 300, 400$ and 500 MHz) in a phantom. The RF heating intervention ($P_{in} = 100$ W, $t = 120$ seconds) was validated experimentally using the proton resonance shift method and fiberoptic probes for temperature monitoring. The applicability of the SGBT RF antenna building block for in vivo ¹H and ¹⁹F MRI was demonstrated for the thigh and forearm of a healthy volunteer.

The SGBT RF antenna building block facilitated ¹⁹F and ¹H MRI at 7.0 T as well as broadband thermal intervention (234–561 MHz). For the thigh of the human voxel models, a B_1^+ efficiency $\geq 11.8 \mu\text{T}/\sqrt{\text{kW}}$ was achieved at a depth of 50 mm. Temperature simulations and heating experiments in a phantom demonstrated a temperature increase $\Delta T > 7$ K at a depth of 10 mm.

The compact SGBT antenna building block provides technology for the design of integrated high-density RF applicators and for the study of the role of temperature in

Abbreviations used: ¹H, proton; ¹⁹F, fluorine; AFI, actual flip-angle imaging; B_1^+ , transmit radio frequency field; EM, electromagnetic; EMF, electromagnetic field; ϵ_r , relative dielectric constant; FR4, flame-retardant substrate (class 4); MR thermometry, magnetic resonance thermometry; PFCE, perfluoro-15-crown-ether; PRFS, proton resonance frequency shift; PTFE, polytetrafluoroethylene; RF, radiofrequency; RFPA, radiofrequency power amplifier; SAR, specific absorption rate; SAR_{10g} , specific absorption rate averaged over 10 g material or tissue; S_{ij} , scattering matrix entry ij ; SGBT, self-grounded bow-tie; Thermal MR, thermal magnetic resonance; UHF-MR, ultrahigh field magnetic resonance.

This is an open access article under the terms of the Creative Commons Attribution-NonCommercial License, which permits use, distribution and reproduction in any medium, provided the original work is properly cited and is not used for commercial purposes.

© 2020 The Authors. NMR in Biomedicine published by John Wiley & Sons Ltd

NMR in Biomedicine. 2020:e4274.
<https://doi.org/10.1002/nbm.4274>

wileyonlinelibrary.com/journal/nbm | 1 of 14

(patho-) physiological processes by adding a thermal intervention dimension to an MRI device (Thermal MR).

KEYWORDS

broadband antenna, magnetic resonance, radiofrequency antenna, self-grounded bow-tie, thermal intervention, thermal magnetic resonance, ultrahigh field MR

1 | INTRODUCTION

Temperature is a critical attribute of life, since biological processes are highly sensitive to temperature changes. The aberrant thermal properties of pathological tissues have led to a strong interest in temperature as a clinical parameter, but this interest has been hampered by the lack of non-invasive methods to measure and manipulate temperature.¹⁻⁵ Vigorous efforts in fundamental research and (bio)engineering of electromagnetic (EM)-induced heating has resulted in an enormous body of literature, paving the way for further technical developments.⁶⁻⁸

Targeted radiofrequency (RF)-induced thermal intervention based on constructive interference of EM waves transmitted within an MRI system is conceptually appealing for pursuing image-guided mild hyperthermia and other thermal interventions including controlled release of therapeutics from nanocarriers that bestow environmental responsiveness to physiologically relevant changes in temperature.^{6,9} The efficacy and release profiles of MR-sensitive fluorine payloads from thermos-responsive nanocarriers can be monitored and quantified with ¹⁹F MRI, which could provide an ideal means to monitor the release kinetics and bioavailability of an MR visible cargo in vivo, which would be a major leap forward to temperature-induced drug delivery in vivo.¹⁰ In vivo thermometry and thermal dose management are essential for temperature-triggered interventions or drug delivery, and are at the forefront of the awareness and attention of the corresponding research communities. Similar to proton, the fluorine resonance frequency is also affected by temperature and can be exploited for temperature monitoring of fluorinated probes.¹¹

Ensuring a patient- and problem-oriented adaptation of the size, uniformity and location of the RF energy deposition in the target region is highly relevant for the thermal intervention, with the focal point quality being governed by the radiation pattern of the single RF transmit element, the RF channel count and the thermal intervention radiofrequency of the RF applicator.¹²⁻¹⁵ Reports on the radiation pattern of resonant structures underline the benefits of dipole antenna arrays for enhancing the focal point quality in thermal interventions.¹⁶ These pioneering developments include dipole configurations with a reduced size, using high-permittivity dielectric and low-loss materials for antenna shortening en route to high-density arrays.^{17,18} The thermal intervention frequency is a significant parameter that impacts the focal point quality. While long RF wavelengths in tissue at 64 MHz (1.5 T) are not suitable to focus EM energy within small targeted areas, the shortened wavelength in tissue at ≥ 297 MHz (7.0 T) enables stronger focusing of RF fields, thanks to more localized interference patterns.^{14,18} Theoretical research and numerical simulations of targeted RF heating have shown how an ultrahigh field MR (UHF-MR) instrument can be adapted to generate highly focused heat in regions of tissue by the use of RF antenna arrays.¹⁸ Studies on ultimate intrinsic specific absorption rate (SAR) and RF applicator concepts suggested high frequencies of up to 1 GHz for a highly focused EM energy deposition.^{12,13} Antenna count and positioning also influence the focal point quality.¹³ Increasing the number of antennas enables a lower surface RF energy deposition, while the focal point quality can be improved by longitudinal steering using multiple rings of antenna along the z-dimension.^{13,19} A variable frequency increases the degrees of freedom (amplitude, phase and frequency) to modulate the focal point quality.^{13,19,20} Reports on this subject suggest an ideal intervention frequency or a mix of intervention frequencies for a particular target and target location.¹⁹⁻²³ A compact wideband antenna setup based on a self-grounded bow-tie (SGBT) antenna is a potential answer to the need for multiple rings and a high channel count setup to enable broadband thermal intervention.^{19,22-24} While several previous reports on RF antenna systems have addressed these multiple issues individually,^{8,15,18-20,25} our objective with this new design was to achieve a comprehensive solution.

Recognizing the opportunities of adding a thermal intervention dimension to an MRI device (Thermal MR) for studying the role of temperature in biological systems and disease, this work reports on the design process, implementation, evaluation and application of a compact wideband SGBT building block. We demonstrate the suitability of this design for thermal intervention, proton (¹H) MRI, ¹H MR temperature mapping and fluorine (¹⁹F) MRI in a single device, integrated in a whole-body 7.0 T MRI system.

2 | METHODS

2.1 | RF antenna building block design considerations

The RF antenna building block consists of an SGBT antenna with a dielectric material filled housing (Figure 1A). The SGBT antenna is based on a design with a strong main lobe directivity and limited back radiation due to the self-grounded backplane.²⁴ This feature makes it an ideal

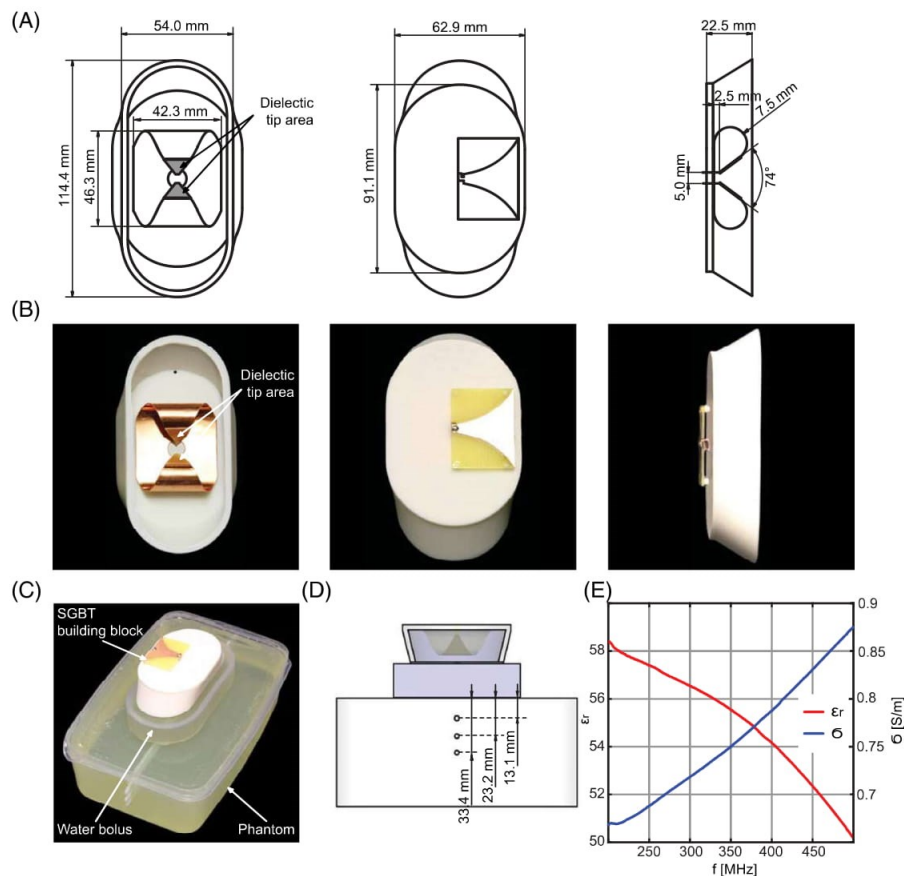


FIGURE 1 (A) Basic scheme of the SGBT building block, balun and SGBT antenna design. (B) Additively manufactured building block with the SGBT antenna placed inside the housing and with the balun positioned on top of the building block. (C) Experimental setup with SGBT building block, water bolus and phantom used for magnetic transmission field assessment and thermometry measurements. (D) Basic scheme of the setup including the positioning of small tubes within the phantom (length = 210 mm; width = 140 mm; depth = 64 mm) for accommodating fiberoptic probes for temperature measurements or a fluorinated compound for fluorine MRI. (E) Measured broadband material characteristics of the used phantom for a frequency ranging from 200 to 500 MHz

candidate for a highly efficient thermal intervention antenna with the ability of MR imaging at 7.0 T.^{22,23} A deuterium oxide (D_2O , 99.9%, $\epsilon_r \approx 81$ at 297.2 MHz, Sigma Aldrich GmbH, Munich, Germany) filled housing was used to shorten the effective transmit RF wavelength to reduce the overall antenna size.¹⁷⁻¹⁹

The SGBT antenna was manufactured with 0.3 mm copper, to guarantee a mechanically robust antenna system. A low-permittivity dielectric material was used to improve the broadband characteristics by spreading the electric field in the tip area of the antenna.¹⁹ The dielectric material thickness was found to have a minor influence on the broadband characteristics, so that 0.5 mm FR4 was used to limit the degrees of freedom for the antenna optimization. Additive manufacturing based on lithography (Form2, Formlabs, Somerville, MA) was used to model the housing of the building block (Figure 1B). A balanced to unbalanced (balun) transformer, manufactured of copper-coated FR4 composite, was employed to match a 50 Ω coaxial device (coaxial cable) to the antenna port and vice versa.²⁶ A microstrip exponential taper was used to combine the balun with impedance matching.^{20,24} To enhance the efficiency and directivity of a dipole antenna for targeted heating, a water bolus between the radiating element (here, the SGBT building block) and the subject or phantom was used.^{8,27} The water bolus was filled with deionized water (H_2O) to minimize costs; it was separated from the D_2O -filled building block with a 0.5 mm FR4 layer. The water bolus (with the dimensions 59.0 x 119.4 x 20 mm³) was manufactured from a waterproof latex cover stabilized by a plastic ring (thickness = 5 mm).

2.2 | RF antenna building block optimization approach

The software package CST Microwave Studio 2018 (Computer Simulation Technology GmbH, Darmstadt, Germany) was used for numerical electromagnetic field (EMF) simulations and optimization. Interactions between the components of the RF antenna building block were evaluated step-by-step: (i) submerging the antenna in distilled water, (ii) placing the antenna within the building block housing with the water bolus installed, and (iii) combining the SGBT building block with the exponential stripline balun. The complex interaction of the components of the antenna design required evaluation and optimization of the geometry of the combined setup, whereas the optimization parameter space is multidimensional and listed in Table 1, including upper and lower limits as well as the optimization result. A genetic optimization algorithm implemented in CST was applied for the multidimensional optimization.²⁸ The population of the algorithm was set to 4 × 8 at a mutation rate of 60% with a maximum number of iterations of 60. The cost function used a reflection coefficient $S_{11} \leq -13$ dB for 260 to 600 MHz and $S_{11} \leq -10$ dB for 600 to 700 MHz with the objective to enable fluorine imaging ($f_{19F} = 279.6$ MHz), proton imaging ($f_{1H} = 297.2$ MHz) and MR thermometry at 7.0 T, as well as supporting a broadband frequency regime for thermal interventions. For the optimization process, a rectangular box (length = 240 mm, width = 240 mm, height = 150 mm) filled with muscle tissue mimicking material was used. For this purpose the dispersive material specifications were provided by the IT'IS Foundation (Zurich, Switzerland) for a broad frequency range.²⁹ This setup was used instead of an upper thigh of the virtual population to limit the computational effort.³⁰ The basic feasibility of a high-density array of SGBT antenna building blocks was evaluated and confirmed in EMF simulations and measurements of the nearest neighbor coupling. To cover all possible arrangements in an array configuration, the coupling (S_{21}) of the reference antenna (Ref) to the antennas A, B, and C was exemplarily investigated.

2.3 | EMF, SAR and temperature simulations

Evaluation simulations of dielectric losses, transmit RF B_1^+ field, SAR distribution and temperature were performed with the time domain solver of CST Microwave Studio 2018. Dielectric losses were analyzed for the individual components (balun, antenna, building block and water bolus) of the proposed SGBT building block. The B_1^+ efficiency was calculated by dividing the transmit RF field by the square root of the input power. Simulations were performed for a phantom validation setup (length = 210 mm, width = 140 mm, depth = 64 mm, shown in Figure 1) and for the human voxel models Ella and Duke from the virtual population using a voxel resolution of $1.0 \times 1.0 \times 1.0$ mm³.³⁰ For the simulations, the SGBT building block and the water bolus were positioned (i) in the center of the phantom surface (Figure 1D) and (ii) at the surface above the center region of the left thigh of the human voxel models. The boundary region distance between the SGBT building block filling and the water bolus was considered as 0.5 mm FR4; the water bolus latex cover was found to be ≥ 0.02 mm and was neglected in the simulations. The measured dielectric parameters of the phantom (based on an open-end coaxial probe setup)³¹ and the tissue specifications²⁹ for the human voxel models were defined as dispersive to support the broadband intervention (Figure 1E). The mesh resolution was kept at $\leq 4.0 \times 4.0 \times 4.0$ mm³ for both phantom and voxel model studies. The evaluation differentiates between two modes: (i) the imaging mode at $f_{19F} = 279.6$ MHz and $f_{1H} = 297.2$ MHz, and (ii) the thermal intervention mode at $f_1 = 300$ MHz, $f_2 = 400$ MHz and $f_3 = 500$ MHz. For the imaging mode, both B_1^+ efficiency distribution and SAR distribution according to IEC 62704-1 standards were examined.³² SAR was normalized to 1 W input power and averaged over 10 g of tissue (SAR_{10g}). Evaluation of the B_1^+ efficiency and SAR_{10g} distribution were assessed for a

TABLE 1 Metrics, including boundaries used and results obtained for the genetic optimization of the SGBT building block and the exponential stripline balun. The building block dimensions were considered without the housing (3 mm thickness manufactured, 0.5 mm FR4 substrate). The overall antenna length ($l_{total} = 46.3$ mm) is defined with the radius of the antenna bending radius ($r = 7.5$ mm). The building block length top ($l_{building\ block} = 85.1$ mm) is defined with the building block scaling factor and the building block width top

Description	Lower limit	Upper limit	Optimization result
Antenna aperture angle, [°]	65	100	74
Antenna length backplane [mm]	25.0	35.0	31.3
Antenna width backplane [mm]	27.0	45.0	42.3
Antenna pin width [mm]	1.5	3.0	1.7
Balun antenna connector [mm]	1.5	6.0	4.5
Balun width [mm]	30.0	55.0	39.3
Building block width top [mm]	40.0	60.0	56.9
Building block length bottom [mm]	70.0	110.0	108.4
Building block height [mm]	12.0	30.0	18.9
Building block scale factor	1.01	1.60	1.49

central transversal slice through the left thigh of Ella and Duke. Temperature simulations were performed with a uni-directional, thermal transient solver in CST Microwave Studio's postprocessing routine. For this purpose, material parameter estimations used for the thermal intervention were derived from the literature, including phantom density (1230.89 g/l), heat capacity (2.9635 J/g/K) and thermal conductivity (0.4355 W/m/K).^{33,34}

2.4 | Hardware

Bench measurements of the reflection coefficient were performed using an eight-channel vector network analyzer (VT 8, Rohde & Schwarz, Memmingen, Germany) and analyzed in MATLAB (MathWorks, Natick, MA). ¹H MRI, ¹⁹F MRI and MR thermometry were conducted using a 7.0 T whole-body MRI system (MAGNETOM, Siemens Healthineers, Erlangen, Germany) equipped with an 8 x 1 kW RF amplifier (Stolberg HF-Technik AG, Stolberg-Vicht, Germany) and a gradient system with a maximum slew rate of 170 mT/m/ms and gradient strength of 38 mT/m (Siemens Healthineers). The heating regime setup consisted of an external signal generator (SMGL, Rohde & Schwarz) and a custom-made power amplifier supporting continuous 100 W forward power at the desired frequencies of $f_1 = 300$ MHz, $f_2 = 400$ MHz and $f_3 = 500$ MHz.

2.5 | Validation of EMF and temperature simulations

EMF and temperature simulations were validated using a custom-made phantom (Figure 1C-E) filled with deionized water, sucrose (994.0 g/l), NaCl (38.8 g/l), agarose (20.0 g/l) and CuSO₄ (0.75 g/l). Three vertically aligned polytetrafluorethylene (PTFE) plastic tubes (inner diameter = 2 mm) were placed at increasing depths in the center of the phantom to accommodate fiberoptic probes (Omniflex, Neoptix, Québec, Canada) for temperature measurements.

The performance of the developed RF antenna building block and its reflection coefficient was validated for the phantom and a healthy male human subject (aged 29 years). For transmit RF field validation, B_1^+ mapping was conducted in the phantom using 3D actual flip angle-imaging (AFI) (spatial resolution = $1.0 \times 1.0 \times 5.0$ mm³, TE = 2.07 ms, TR₁ = 35 ms, TR₂ = 115 ms, nominal FA = 30°, scan time = 2.25 minutes per slice, 96 slices).³⁵ The deviation of the measured B_1^+ field from the loss-corrected simulated B_1^+ efficiency field was calculated for the central transversal slice through the phantom. A comparison with the simulations of the B_1^+ efficiency field along three vertical lines in the transversal slice was conducted for the central, 10 mm left and 10 mm right lines. Temperature simulations were validated in a phantom study by performing heating experiments at frequencies f_1 , f_2 and f_3 in conjunction with MR thermometry at 7.0 T. The antenna was connected to an external RF power amplifier (RFPA) for the heating experiments and manually reconnected to the MRI signal chain for thermometry. RF heating was performed in the iso-center of the MRI bore at room temperature (~297 K) for 120 seconds continuously applying $P_{in} = 100$ W at the antenna building block. Cable losses of <-1.9 dB were compensated for by adjusting the output amplitude of the RF power amplifier at all examined frequencies. 2D MR thermometry was conducted using the proton resonance frequency shift (PRFS) method by applying a dual gradient-echo method (spatial resolution = $1.5 \times 1.5 \times 4.0$ mm³, TE₁ = 2.26 ms, TE₂ = 6.34 ms, TR = 102 ms, scan time = 0.44 minutes) before and after the RF heating period.³⁶⁻³⁹ The relative temperature mapping of PRFS after the heating process was compared with fiberoptic probe measurements.

2.6 | Ethics statement

For the in vivo feasibility study, a subject without any known history of disease was included after approval by the local ethical committee (registration number DE/CA73/5550/09, Landesamt für Arbeitsschutz, Gesundheitsschutz und technische Sicherheit, Berlin, Germany). Informed written consent was obtained from the volunteer prior to the study.

2.7 | ¹H and ¹⁹F MR imaging

Phantom and in vivo studies were performed to demonstrate the ¹⁹F and ¹H imaging characteristics of the SGBT building block. The tubes within the phantom, previously used for temperature measurements, were filled with high fluorine content nanoparticles prepared according to the literature.⁴⁰ ¹⁹F-rich nanoparticles were prepared by emulsifying perfluoro-15-crown-5-ether (1200 mmol/L) (PFCE; Fluorochem, Hadfield, UK) with Pluronic F-68 (Sigma-Aldrich).⁴⁰ For the in vivo study, 15 g of flufenamic acid (101 mmol/L), a nonsteroidal antiinflammatory drug containing ¹⁹F (Mobilat, Stada, Bad Vilbel, Germany) was sealed in a latex bag and placed on the forearm or the upper thigh of a healthy male volunteer.¹⁰ The imaging protocol (one sagittal and three transversal slices) included:

- Phantom ^1H : FLASH, spatial resolution = $0.5 \times 0.5 \times 2.5 \text{ mm}^3$, TR = 50 ms, TE = 2.86 ms, nominal FA = 40° , receiver bandwidth = 260 Hz/Px, scan time = 1.18 minutes;
- Phantom ^{19}F : RARE, spatial resolution = $0.5 \times 0.5 \times 5.0 \text{ mm}^3$, TR = 1000 ms, TE = 5.20 ms, nominal FA = 180° , echo train length = 4, averages = 8, receiver bandwidth = 592 Hz/Px, scan time = 12.51 minutes;
- Forearm ^1H : FLASH, spatial resolution = $0.5 \times 0.5 \times 2.5 \text{ mm}^3$, TR = 90 ms, TE = 3.86 ms, nominal FA = 30° , receiver bandwidth = 260 Hz/Px, scan time = 1.18 minutes;
- Forearm ^{19}F : RARE, spatial resolution = $1.5 \times 1.5 \times 5.0 \text{ mm}^3$, TR = 2360 ms, TE = 5.60 ms, nominal FA = 180° , echo train length = 16, averages = 8, receiver bandwidth = 337 Hz/Px, scan time = 2.27 minutes;
- Thigh ^1H : FLASH, spatial resolution = $0.5 \times 0.5 \times 2.5 \text{ mm}^3$, TR = 90 ms, TE = 3.86 ms, nominal FA = 30° , receiver bandwidth = 260 Hz/Px, scan time = 2.20 minutes;
- Thigh ^{19}F : RARE, spatial resolution = $1.5 \times 1.5 \times 5.0 \text{ mm}^3$, TR = 2000 ms, TE = 5.60 ms, nominal FA = 180° , echo train length = 16, averages = 8, receiver bandwidth = 337 Hz/Px, scan time = 2.12 minutes.

3 | RESULTS

3.1 | Characterization of the RF antenna building block

Figure 1 shows the building block with an SGBT antenna and a stripline balun after the optimization process. The weight of the filled building block was $m = 150 \text{ g}$, with dimensions of $114.4 \times 54.0 \times 22.5 \text{ mm}^3$.

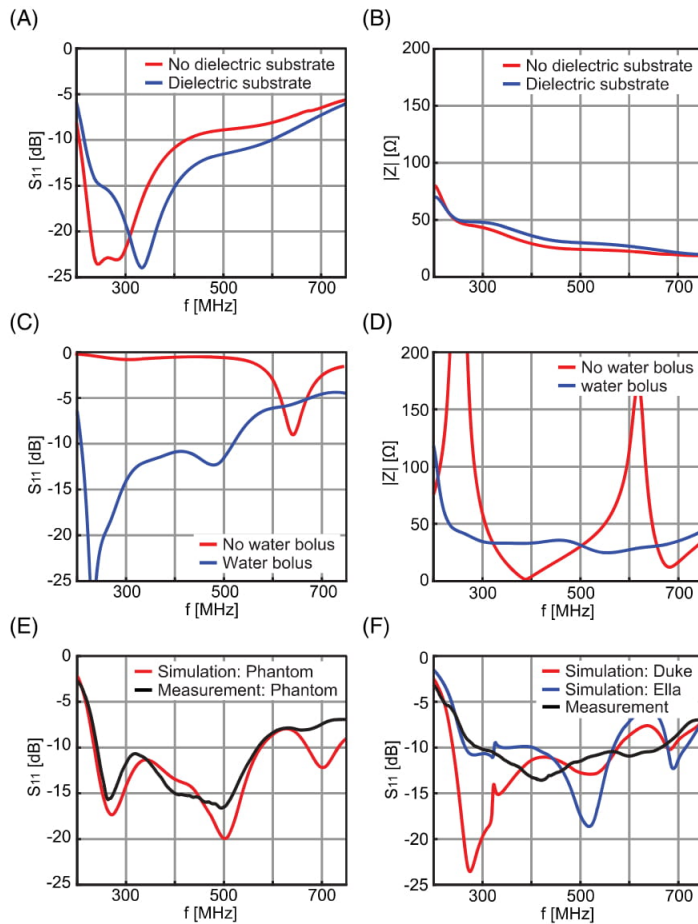


FIGURE 2 (A) Reflection coefficient (S_{11}) and (B) input impedance (Z_{11}) simulation results for the optimized antenna design immersed in distilled water with and without the dielectric layer at the tip area of the antenna. (C) S_{11} and (D) Z_{11} simulation results for the antenna within the optimized building block with and without the water bolus. (E) S_{11} simulation and measurement results of the building block antenna with balun design for the experimental setup. (F) S_{11} simulation results of the thigh of the human voxel model Duke and Ella, and experimental measurement of a healthy volunteer

EMF simulations of the individual components revealed the contributions of the RF antenna, building block, water bolus and balun to the broadband characteristics of the proposed RF antenna building block. The reflection coefficient of the antenna immersed in water showed broadband behavior with a resonance at 335 MHz. The bandwidth was increased using a low dielectric material at the tip area (Figure 2A).¹⁹ With the dielectric material, the antenna impedance decreased from $50.6 \Omega - j 19.3 \Omega$ at 234 MHz to $28.5 \Omega + j 0.8 \Omega$ at 560 MHz (Figure 2B). The water bolus between the subject and the RF antenna building block ensured EMF propagation at a broadband frequency range (Figure 2C,D). The bolus resulted in more wideband behavior of the reflection coefficient, and a more constant impedance ($49.8 \Omega - j 3.9 \Omega$ at 234 MHz to $21.4 \Omega + j 14.5 \Omega$ at 560 MHz) at the antenna feed for the SGBT building block (Figure 2C,D). Introducing the balun allowed matching of a 50Ω coaxial cable to the 43.5Ω differential antenna port (stripline width = 4.5 mm). The combination of the RF antenna building block with the balun resulted in an overall bandwidth of 340 MHz (for $S_{11} < -10\text{dB}$, $f = 235$ to 575 MHz).

The simulated S_{11} parameters in the phantom were in good agreement with the measured values from 250 to 650 MHz (Figure 2E). The measured cut-off frequency was increased by 6 MHz compared with the simulation, with an overall linear difference between simulation and measurement of $3.3\% \pm 1.9\%$ (mean \pm SD). The reflection coefficient obtained from simulations with the RF antenna building block placed on the left thigh of the human voxel model Duke and Ella exhibited a bandwidth of $\Delta f = 337$ MHz for Duke and $\Delta f = 303$ MHz with an increased minimum of $S_{11} < -9.4$ dB for Ella (Figure 2F). The measurement of the healthy subject provided a broadband response with an enhanced overall bandwidth ranging from 292 to 664 MHz for $S_{11} < -10$ dB.

Simulation and measurement of the nearest neighbor coupling between individual SGBT building blocks revealed exemplary $S_{ij} < -17$ dB for possible antenna arrangements in an array configuration (Figure 3).

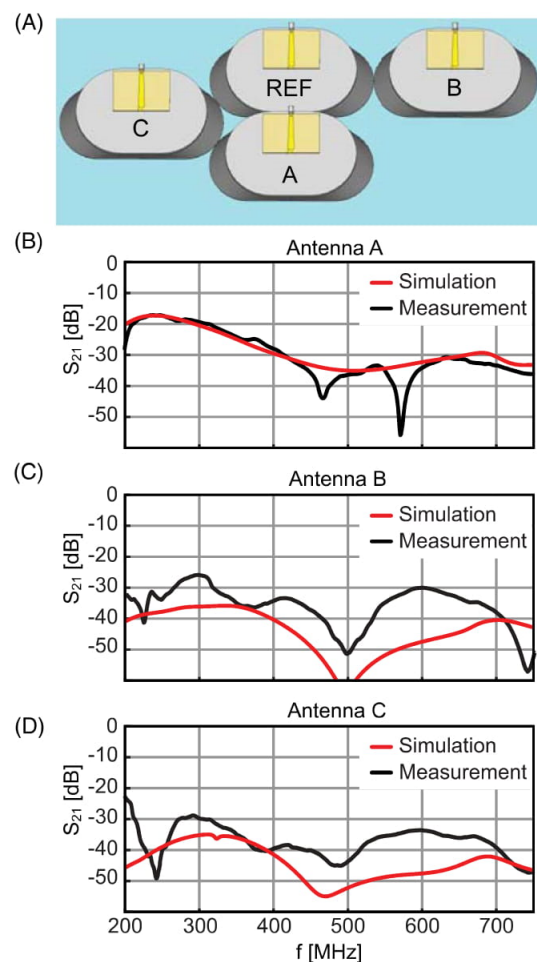


FIGURE 3 (A) Experimental setup used for the exemplary assessment of nearest-neighbor coupling of the SGBT building block. Simulated and measured coupling parameter (S_{21}) of the reference antenna (REF) to (B) antenna A, (C) antenna B and (D) antenna C

3.2 | EMF, SAR and temperature simulations

The dielectric power losses of the RF antenna building block and the water bolus ranged from 8.8% at 300 MHz to 15.6% at 500 MHz for the accepted RF power at the coaxial cable connector. The major part of the losses was due to the filled building block (5.2% at 300 MHz to 8.4% at 500 MHz) and the water bolus (2.5% at 300 MHz to 5.3% at 500 MHz). Losses for the SGBT antenna were $\leq 0.5\%$, whereas the balun showed losses of $\leq 1.4\%$ for ≤ 500 MHz. B_1^+ efficiency maps and SAR distributions for ^{19}F and ^1H obtained for the human voxel models are illustrated in Figure 4. Ella showed a minor decrease in the transmission field efficiency compared with Duke. For Duke and Ella, a B_1^+ efficiency $\geq 11.8 \mu\text{T}/\sqrt{\text{kW}}$ was achieved at a depth of 50 mm (Figure 4A,B). The 1 W-normalized $\text{SAR}_{10\text{g}}$ distribution at $f_{19\text{F}} = 279.6$ MHz and $f_{1\text{H}} = 297.2$ MHz showed a maximum $\text{SAR}_{10\text{g}} = 1.8$ W/kg for Ella and $\text{SAR}_{10\text{g}} = 3.0$ W/kg for Duke (Figure 4C,D). Considering the measured hardware losses of -3.2 dB for the RF imaging signal chain, the input power was limited to 7.0 W, to stay within the 10 W/kg for $\text{SAR}_{10\text{g}}$ limits of the IEC guidelines for the normal operating mode.⁴¹ The simulations on the phantom revealed a B_1^+ efficiency of $\geq 11.1 \mu\text{T}/\sqrt{\text{kW}}$ at a depth of 50 mm (Figure 5).

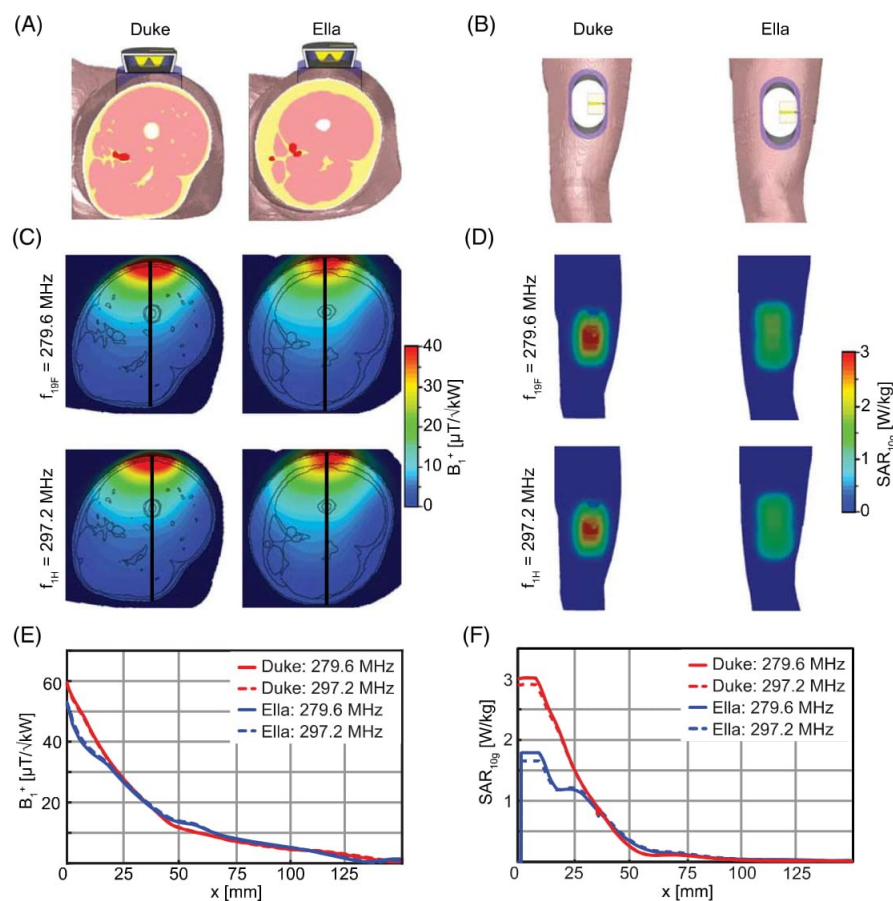


FIGURE 4 Experimental arrangement of the building block and the water bolus placed on the left thigh of the human voxel model Duke and Ella: (A) cut plane in z-direction and (B) top view. (C) Radiofrequency transmission (B_1^+) field simulation maps of the left thigh of the human voxel models for fluorine (^{19}F) and proton (^1H). (D) Specific absorption rate (SAR) averaged over 10 g tissue ($\text{SAR}_{10\text{g}}$) at $f_{19\text{F}} = 279.6$ MHz and $f_{1\text{H}} = 297.2$ MHz of the left thigh of the human voxel models. (E) Comparison of the B_1^+ field along the center line (marked in (C)) derived from the EMF simulations of the thigh of Duke and Ella. (F) Comparison of the $\text{SAR}_{10\text{g}}$ distribution along the indicated center line (marked in (C)) of the thigh of Duke and Ella

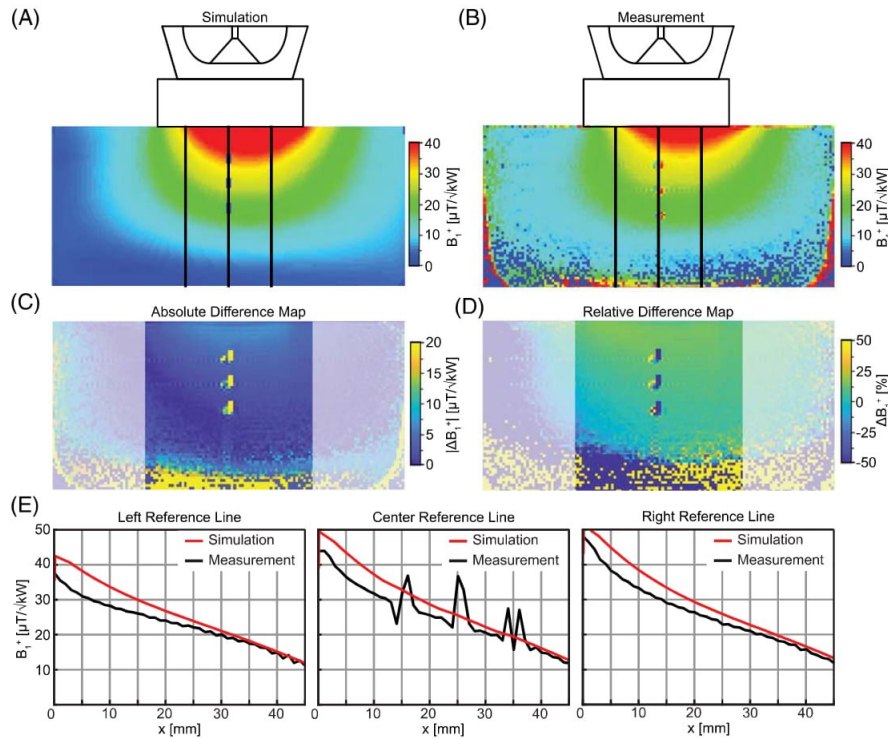


FIGURE 5 Radiofrequency transmission (B_1^+) efficiency map obtained from (A) numerical simulations and (B) experiments based on the actual flip angle imaging technique (AFI) of the indicated SGBT building block with the water bolus on the phantom. (C) Absolute and (D) relative difference maps of the simulation and the measurement of the phantom setup. (E) B_1^+ field values obtained from simulations and measurements along the lines (marked in (A) and (B)) in the phantom

Temperature simulations demonstrated the wideband thermal intervention feasibility providing a comparable heating pattern in the phantom at $f_1 = 300$ MHz, $f_2 = 400$ MHz and $f_3 = 500$ MHz (Figure 6).

3.3 | Validation of EMF and temperature simulations

The simulated B_1^+ efficiency maps showed qualitative and quantitative agreement with the results derived from experimental B_1^+ mapping. The difference map revealed a deviation of less than $6.7 \mu\text{T}/\sqrt{\text{kW}}$ (or 17%) for the central area underneath the RF antenna building block by considering the measured -3.2 dB losses in the RF signal chain. The B_1^+ profiles along the lines indicated in Figure 5A,B demonstrate both the quantitative and qualitative agreement between the simulation and the measurement.

Connecting the SGBT building block to the MRI RF signal chain employed for imaging experiments and MR thermometry took $t_{\text{maximum}} = 1.15$ minutes. A relative difference map between simulation and MR thermometry temperature distribution and a profile along the central axis underneath the antenna, including the fiberoptic probes, is shown in Figure 6C,D. The difference between the temperature simulations and MR thermometry along the indicated vertical lines of Figure 6A,B is 0.79 ± 0.36 K for f_1 , 0.82 ± 0.36 K for f_2 and 1.19 ± 0.38 K for f_3 (mean \pm SD). An overall difference between simulation and measurement of 0.94 ± 0.40 K (mean \pm SD) for all profiles in the performed thermal interventions was calculated. The mean difference between the fiberoptic probe measurements and MR thermometry was 0.66 K for all probe locations (Figure 6D). Probe position 1 showed a higher relative deviation (>15.4%) compared with the other measurement points (<9.3%) for all intervention frequencies (Figure 6D).

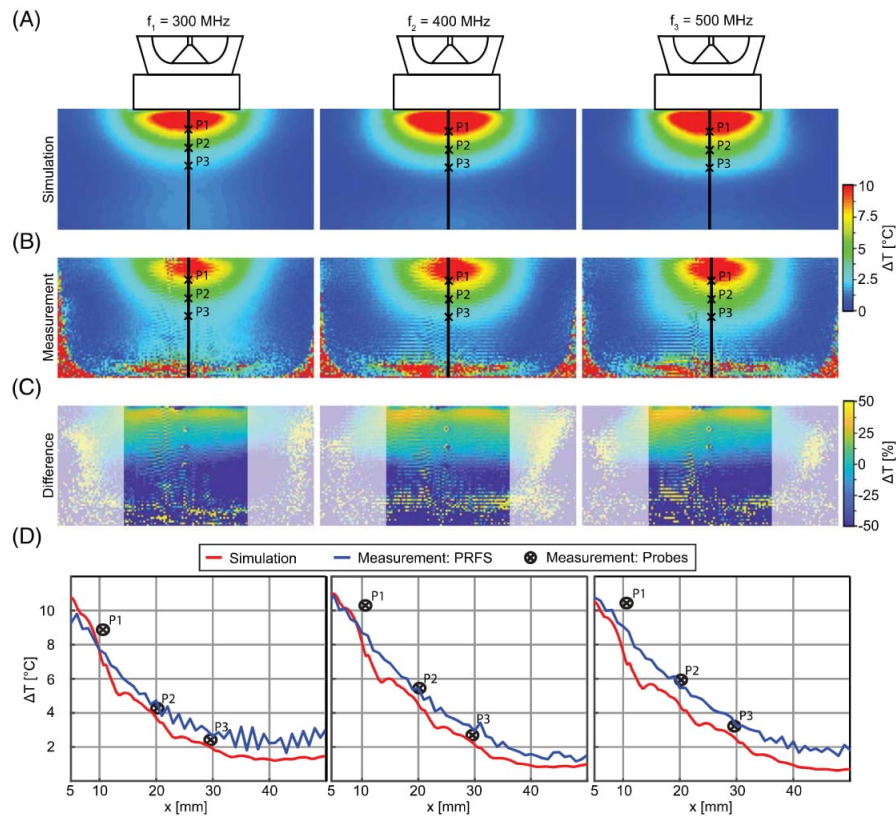


FIGURE 6 (A) Temperature simulations in the phantom after 120 seconds of thermal intervention at continuous $P_{in} = 100$ W at the antenna port for $f_1 = 300$ MHz, $f_2 = 400$ MHz and $f_3 = 500$ MHz. Highlighted are the reference line and three fiberoptic probe positions (P1-P3) used for one-dimensional plots. (B) Temperature measurements were obtained with MR thermometry based on proton resonance frequency shift (PRFS). The reference line and three fiberoptic probe positions (P1-P3) used for one-dimensional plots are highlighted. (C) Difference maps obtained from the numerical simulations and measurements of the phantom setup. (D) Comparison of the RF heating-induced temperature changes obtained from temperature simulations and experimental measurements

3.4 | ^1H and ^{19}F MR imaging

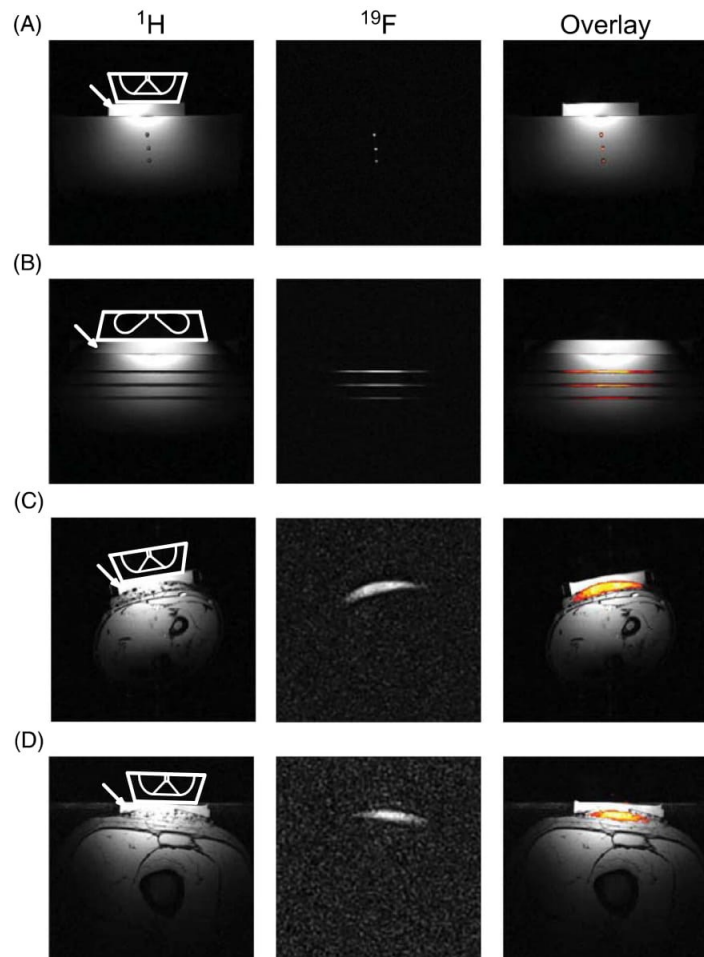
Imaging PFCE in the phantom study, as well as the fluorinated topical drug in the in vivo studies, showed sufficient signal to locate the compounds in the proton reference images. This demonstrates the feasibility of ^{19}F and ^1H imaging with the proposed broadband SGBT antenna building block without additional tuning and matching circuits (Figure 7).

4 | DISCUSSION

This work demonstrates the design and optimization of a novel wideband SGBT building block to support thermal intervention, ^1H MRI, ^1H MR temperature mapping and ^{19}F MRI integrated in a whole-body 7.0 T MRI system.

The water bolus has a significant role in the overall SGBT building block behavior; it ensures proper coupling between the building block and the object under investigation, allowing impedance matching, and forming a short waveguide-like element. This promotes the performance by (i) affording a compact size of the antenna building block, (ii) enhancing EMF coupling to the subject, and (iii) enabling broadband characteristics of the antenna. Additionally, flowing water within the bolus could be used to allow for superficial cooling during thermal interventions.^{8,19,27,42} Without proper impedance matching by the water bolus, the reflection coefficient showed a single self-resonance at ~ 645 MHz. With the water bolus installed, the SGBT antenna design and the building block optimization yielded a nearly constant impedance and low-reflection coefficient for a wide bandwidth. Adapting the exponential stripline balun to the impedance at the feeding pins of the antenna allows a connection to a 50 Ω

FIGURE 7 Proton image (^1H), fluorine image (^{19}F) and $^{19}\text{F}/^1\text{H}$ overlay. The position of the RF building block is outlined in white; the water bolus is indicated by an arrow in the ^1H images. Illustrated are (A) phantom axial slice, (B) phantom sagittal slice, (C) forearm axial slice and (D) thigh axial slice



coaxial cable. This low-loss stripline balun is advantageous for high-peak and average-power applications such as MR imaging and thermal interventions.

The proposed compact SGBT building block affords a size reduction of 55% and 72% compared with previously reported SGBT ($107 \times 78 \times 31 \text{ mm}^3$) and bow-tie ($150 \times 70 \times 40 \text{ mm}^3$) RF antenna building block configurations, respectively.^{18,22} A previous implementation of a single-side adapted dipole antenna that used high dielectric material to shorten the wavelength had a volume of $143 \times 70 \times 42 \text{ mm}^3$; our proposed design is 72% smaller in volume than this.¹⁷ The size reduction is even more pronounced when benchmarking the proposed SGBT building block against pioneering dipole designs without a dielectric cavity, such as fractionated dipole ($l = 300 \text{ mm}$),⁴³ snake dipole⁴⁴ or meander dipole ($l = 320 \text{ mm}$) designs.⁴⁵ For example, a well-established implementation of the fractionated dipole uses a housing with a size of $\sim 300 \times 40 \times 20 \text{ mm}^3$; our compact SGBT configuration results in a volume reduction of 52% compared with this, and a reduction in the antenna length of nearly a factor of three.⁴³ The compact size of the RF antenna building block and its low nearest neighbor coupling is suitable for high-density and many-element RF array configurations, which is crucial for improving the focal point quality of thermal interventions and for approaching the ultimate SAR amplification factors predicted by numerical simulations.¹²⁻¹⁴

The proposed antenna design shows an efficiency of 91.2% at 300 MHz and 84.4% at 500 MHz, with the dielectric losses being mainly attributed to the filled building block and the water bolus. The efficiency of the proposed building block could be increased using dedicated low-loss, high-permittivity dielectrics (eg, ceramics) close to the copper part of the SGBT antenna. The compact SGBT building block supports imaging at 7.0 T with a B_1^+ efficiency of $\geq 11.8 \mu\text{T}/\sqrt{\text{kW}}$ at a depth of 50 mm for ^1H and ^{19}F MRI. Although the coupling of the electric field from the building block to the subject increases due to the water bolus, the superficial SAR is still comparable with other array antenna designs by scaling the results to 1 W input power per channel.^{17,43} Incorporating ^{19}F MRI adds additional value to the thermal intervention by providing the

capacity for detection and quantification of fluorinated compounds, allowing research and implementation on fluorinated, thermally activated drugs (eg, release of fluorinated compounds from thermosensitive carriers).^{10,46,47} Further to ¹⁹F and ¹H imaging, the SGBT antenna building block supports RF-induced heating for a broad frequency range. Arranged in an RF array, this feature facilitates the adjustment of the thermal intervention frequency, providing an extra degree of freedom to the thermal intervention.^{12,14,19} The proton-based MR thermometry has the potential to acquire three-dimensional temperature maps, enabling a feedback loop to control RF power deposition during a thermal intervention.⁴⁸ Our temperature simulations, MR thermometry and temperature measurements showed good agreement with a temperature rise of $\Delta T > 7$ K at a depth of 10 mm. It is a recognized limitation of our proof-of-principle study that manual switching was used to change between the RFPAs used for thermal intervention and for MRI. Due to a time delay between RF heating and MR thermometry, an underestimation of the monitored temperature could occur. For clinical implementation with multiple antennas, a controllable switch is beneficial to avoid time delays and connection errors for sequential RF heating and MR thermometry.

Phantom and in vivo imaging experiments demonstrated the feasibility of a broadband RF antenna concept for ¹H and ¹⁹F imaging without tuning and matching based on discrete inductive and capacitive elements. For ¹⁹F in vivo imaging, the 15 g of topical ointment used in the proof-of-principle study showed sufficient SNR to visualize and register the ¹⁹F image with the ¹H image. Analytically, this mass of the substance has $\sim 2.9 \times 10^{21}$ fluorine atoms. This correlates to a bolus of the antitumor drug 5-fluorouracil administered intravenously (3.3×10^{21} fluorine atoms), which afterward distributes via the blood circulation.⁴⁹ In the serum, 5-fluorouracil is present at a concentration of 1.1 and 5.9 $\mu\text{g/mL}$ in the center of a tumor.⁵⁰ In the tumor, this results in a local level of 2.7×10^{19} fluorine atoms/L, which is four orders of magnitude below the administered bolus concentration. Such differences in the total numbers of fluorine atoms can be addressed by increased averaging, using reduced matrix size, lower SNR thresholds and optimized scan parameters.

The broadband characteristics of the RF antenna building block are well suited for thermal interventions, since the presented RF antenna building block is less sensitive to loading conditions based on (i) a temperature increase and impedance change of the dielectric building block due to losses during the high (average) power transmission, (ii) a temperature-dependent impedance change of the water bolus or target tissue, (iii) patient movement, and (iv) intersubject variability. The balun design shows a weak suppression of common mode on the cable, which could lead to artifacts in the acquired images or crosstalk in an array configuration. A narrowband cable-trap or bazooka balun can be used to minimize the common-mode effects for MRI, where the broadband behavior is not affected. Arranging the stripline balun and the cable connector orthogonal to the electric field allowed minimization of the common-mode effects for the supported frequency bandwidth without using a blocking circuit. Whereas no signal was observed for the SGBT building block (filled with D₂O), deuterium oxide can be used to avoid the proton signal of the water bolus (filled with H₂O).

5 | CONCLUSION

The electric and magnetic characteristics of the SGBT building block support ¹H and ¹⁹F (MRI), broadband thermal intervention (RF hyperthermia) and therapy control (MR thermometry) in an integrated device. The compact design can be exploited for the design of high-density RF applicators, offering an increased degree of freedom based on high channel count, phase and amplitude manipulation, as well as adjustable intervention frequency for each channel.

ACKNOWLEDGEMENTS

The authors wish to thank A.J.E. Raaijmakers (Utrecht Medical Center, Utrecht, the Netherlands) for fruitful discussions and for providing the dimensions of his dipole antenna systems.

This project has received funding in part from the European Research Council (ERC) under the European Union's Horizon 2020 research and innovation program under grant agreement No 743077 (ThermalMR). H.W. and E.O. were supported by a grant from the Federal Ministry for Education and Research (KMU innovativ Medizintechnik, 3-in-1 THERAHEAT, FKZ 13GW0102A, B).

FUNDING INFORMATION

This project has received funding in part from the European Research Council (ERC) under the European Union's Horizon 2020 research and innovation program under grant agreement No 743077 (ThermalMR). H.W. and E.O. were supported by a grant from the Federal Ministry for Education and Research (KMU innovativ Medizintechnik, 3-in-1 THERAHEAT, FKZ 13GW0102A, B).

ORCID

Thomas Wilhelm Eigentler  <https://orcid.org/0000-0001-8252-450X>

Haopeng Han  <https://orcid.org/0000-0003-1205-2900>

Andre Kuehne  <https://orcid.org/0000-0002-4133-5056>

Helmar Waiczies  <https://orcid.org/0000-0001-6651-4790>

Laura Boehmert  <https://orcid.org/0000-0002-8703-3133>

Christian Prinz  <https://orcid.org/0000-0003-3330-031X>

Hana Dobsicek Trefna  <https://orcid.org/0000-0001-6025-0819>

Thoralf Niendorf  <https://orcid.org/0000-0001-7584-6527>

REFERENCES

- Datta NR, Ordóñez SG, Gaipi US, et al. Local hyperthermia combined with radiotherapy and/or chemotherapy: Recent advances and promises for the future. *Cancer Treat Rev*. 2015;41:742-753.
- Hooper VD. Accuracy of noninvasive core temperature measurement in acutely ill adults: the state of the science. *Biol Res Nurs*. 2006;8:24-34.
- van Rhooen GC, Wust P. Introduction: Non-invasive thermometry for thermotherapy. *Int J Hyperth*. 2005;21:489-495.
- Titsworth WL, Murad GJA, Hoh BL, Rahman M. Fighting fire with fire: The revival of thermotherapy for gliomas. *Anticancer Res*. 2014;34:565-574.
- Dewhirst MW, Lee C-T, Ashcraft KA. The future of biology in driving the field of hyperthermia. *Int J Hyperth*. 2016;32:4-13.
- Lo YT, Lee SW. *Antenna Handbook: Theory, Applications, and Design*. Springer Science & Business Media; 2013. <http://link.springer.com/10.1007/978-1-4615-6459-1>
- Brace C. Thermal tumor ablation in clinical use. *IEEE Pulse*. 2011;2:28-38.
- Togni P, Rijnen Z, Numan WCM, et al. Electromagnetic redesign of the HYPERcollar applicator: toward improved deep local head-and-neck hyperthermia. *Phys Med Biol*. 2013;58:5997-6009.
- Issels RD, Lindner LH, Verweij J, et al. Neo-adjuvant chemotherapy alone or with regional hyperthermia for localised high-risk soft-tissue sarcoma: a randomised phase 3 multicentre study. *Lancet Oncol*. 2010;11:561-570.
- Ji Y, Waiczies H, Winter L, et al. Eight-channel transceiver RF coil array tailored for 1H/19F MR of the human knee and fluorinated drugs at 7.0 T. *NMR Biomed*. 2015;28:726-737.
- Prinz C, Delgado PR, Eigentler TW, Starke L, Niendorf T, Waiczies S. Toward 19F magnetic resonance thermometry: spin-lattice and spin-spin-relaxation times and temperature dependence of fluorinated drugs at 9.4 T. *Magn Reson Mater Phys Biol Med*. 2019;32:51-61.
- Guérin B, Villena JF, Polimeridis AG, et al. Computation of ultimate SAR amplification factors for radiofrequency hyperthermia in non-uniform body models: impact of frequency and tumour location. *Int J Hyperth*. 2018;34:87-100.
- Winter L, Niendorf T. Electrodynamics and radiofrequency antenna concepts for human magnetic resonance at 23.5 T (1 GHz) and beyond. *Magn Reson Mater Phys Biol Med*. 2016;29:641-656.
- Winter L, Oezerdem C, Hoffmann W, et al. Thermal magnetic resonance: physics considerations and electromagnetic field simulations up to 23.5 Tesla (1GHz). *Radiat Oncol*. 2015;10:201.
- Oberacker E, Kuehne A, Nadobny J, et al. Radiofrequency applicator concepts for simultaneous MR imaging and hyperthermia treatment of glioblastoma multiforme. *Curr Dir Biomed Eng*. 2017;3:473-477.
- Raaijmakers AJE, Luijten PR, van den Berg CAT. Dipole antennas for ultrahigh-field body imaging: a comparison with loop coils. *NMR Biomed*. 2016; 29:1122-1130.
- Raaijmakers AJE, Ipek O, Klomp DWJ, et al. Design of a radiative surface coil array element at 7 T: The single-side adapted dipole antenna. *Magn Reson Med*. 2011;66:1488-1497.
- Paulides MM, Bakker JF, Zwamborn APM, van Rhooen GC. A head and neck hyperthermia applicator: Theoretical antenna array design. *Int J Hyperth*. 2007; 23(1):59-67.
- Takook P, Persson M, Gellermann J, Trefna HD. Compact self-grounded Bow-Tie antenna design for an UWB phased-array hyperthermia applicator. *Int J Hyperth*. 2017;33:387-400.
- Takook P, Trefna HD, Zeng X, Fhager A, Persson M. A computational study using time reversal focusing for hyperthermia treatment planning. *Prog Electromagn Res B*. 2017;73:117-130.
- Kok HP, Van Stam G, Bel A, Crezee J. A mixed frequency approach to optimize locoregional RF hyperthermia. 2015 European Microwave Conference (EuMC) "Freedom Through Microwaves". *EuMC*. 2015:773-776.
- Winter L, Trefna HD, Ji Y, Huelnhagen T, Niendorf T. Ultrahighfield, One for all: Ultra-wideband (279-500MHz) self-grounded bow-tie antenna for MR, and thermal. In: *ISMRM-ESMRMB 26. Joint Annual Meeting 2018*:#4281.
- Eigentler TW, Winter L, Han H, et al. Ultra-Wideband Self-Grounded Bow-Tie Antenna Building Block for Thermal Intervention, Diagnostic MRI and MR Thermometry at 7.0 Tesla. In: *ISMRM 27. Annual Meeting 2019*:#3827.
- Yang J, Kishk A. A novel low-profile compact directional ultra-wideband antenna: the self-grounded bow-tie antenna. *IEEE Trans Antennas Propag*. 2012;60:1214-1220.
- Paulides MM, Mestrom RMC, Salim G, et al. A printed Yagi-Uda antenna for application in magnetic resonance thermometry guided microwave hyperthermia applicators. *Phys Med Biol*. 2017;62:1831-1847.
- Kazempour A, Begaud X. Calculable dipole antenna for EMC measurements with low-loss wide-band balun from 30 MHz to 2 GHz. *Electromagnetics*. 2005;25:187-202.
- Rijnen Z, Togni P, Roskam R, Van De Geer SG, Goossens RHM, Paulides MM. Quality and comfort in head and neck hyperthermia: A redesign according to clinical experience and simulation studies. *Int J Hyperth*. 2015;31:823-830.
- Jones EA, Joines WT. Design of Yagi-Uda antennas using genetic algorithms. *IEEE Trans Antennas Propag*. 1997;45:1386-1392.
- IT'IS Foundation. Tissue Properties Database V4.0. IT'IS Foundation.
- Christ A, Kainz W, Hahn EG, et al. The virtual family - development of surface-based anatomical models of two adults and two children for dosimetric simulations. *Phys Med Biol*. 2010;55:N23-N38.
- Athey TW, Stuchly MA, Stuchly SS. Measurement of Radio Frequency Permittivity of Biological Tissues with an Open-Ended Coaxial Line: Part I. *IEEE Trans Microw Theory Tech*. 1982;30:82-86.
- IEC Committee. IEEE 62704-1-2017 - IEC/IEEE International Standard for Determining the Peak Spatial Average Specific Absorption Rate (SAR) in the Human Body from Wireless Communications Devices, 30 MHz - 6 GHz. Part 1: General Requirements for using the Finite Difference. 2017.

33. Asadi M. *Beet-Sugar Handbook*. John Wiley & Sons. Wiley-Interscience; 2007. <https://www.wiley.com/en-us/Beet+Sugar+Handbook-p-9780471763475>.
34. Buchanan EJ. Economic design and operation of process heat exchange equipment. *Proc S Afr Sug Technol Ass*. 1966;44:89-101.
35. Yarnykh VL. Actual flip-angle imaging in the pulsed steady state: A method for rapid three-dimensional mapping of the transmitted radiofrequency field. *Magn Reson Med*. 2007;57:192-200.
36. Depoorter J, Dewagter C, Dedeene Y, Thomsen C, Stahlberg F, Achten E. The proton-resonance-frequency-shift method compared with molecular diffusion for quantitative measurement of two-dimensional time-dependent temperature distribution in a phantom. *J Magn Reson Ser B*. 1994;103: 234-241.
37. Bing C, Staruch RM, Tillander M, et al. Drift correction for accurate PRF-shift MR thermometry during mild hyperthermia treatments with MR-HIFU. *Int J Hyperth*. 2016;32:673-687.
38. Rieke V, Butts PK. MR thermometry. *J Magn Reson Imaging*. 2008;27:376-390.
39. Winter L, Oberacker E, Paul K, et al. Magnetic resonance thermometry: Methodology, pitfalls and practical solutions. *Int J Hyperth*. 2016;32:63-75.
40. Waiczies S, Lepore S, Sydow K, et al. Anchoring dipalmitoyl phosphoethanolamine to nanoparticles boosts cellular uptake and fluorine-19 magnetic resonance signal. *Sci Rep*. 2015;5:8427.
41. International Electrotechnical Commission. IEC 60601-2-33 Medical electrical equipment - Part 2-33: Particular requirements for the basic safety and essential performance of magnetic resonance equipment for medical diagnosis. *Int Electrotech Comm*. 2015;1-121.
42. Drizdal T, Paulides MM, van Holthe N, van Rhooen GC. Hyperthermia treatment planning guided applicator selection for sub-superficial head and neck tumors heating. *Int J Hyperth*. 2018; 34(6):704-713.
43. Raaijmakers AJE, Italiaander M, Voogt IJ, et al. The fractionated dipole antenna: A new antenna for body imaging at 7 Tesla. *Magn Reson Med*. 2016; 75:1366-1374.
44. Steensma B, Viviana A, Andrade O, Klomp D, Luijten P, Raaijmakers A. Body imaging at 7 Tesla with much lower SAR levels: an introduction of the Snake Antenna array. *Proc Intl Soc Mag Reson Med*. 2016;24:0395.
45. Chen G, Cloos M, Sodickson DK, Wiggins G. A 7T 8 channel transmit-receive dipole array for head imaging: dipole element and coil evaluation. *Proc Intl Soc Mag Reson Med*. 2014;22(22):4572.
46. Langereis S, Keupp J, van Velthoven JL, et al. A temperature-sensitive liposomal 1 H CEST and 19 F contrast agent for MR image-guided drug delivery. *J Am Chem Soc*. 2009;131:1380-1381.
47. de Smet M, Langereis S, van den Bosch S, Gröll H. Temperature-sensitive liposomes for doxorubicin delivery under MRI guidance. *J Control Release*. 2010;143:120-127.
48. Ranneberg M, Weiser M, Weihrauch M, Budach V, Gellermann J, Wust P. Regularized antenna profile adaptation in online hyperthermia treatment. *Med Phys*. 2010;37:5382-5394.
49. Bécouarn YH, Brunet RC, Rouhier MLP, et al. High dose folinic acid and 5-fluorouracil bolus and continuous infusion for patients with advanced colorectal cancer. *Cancer*. 1995;76:1126-1131.
50. Zheng J-F, Wang H-D. 5-Fluorouracil concentration in blood, liver and tumor tissues and apoptosis of tumor cells after preoperative oral 5'-deoxy-5-fluorouridine in patients with hepatocellular carcinoma. *World J Gastroenterol*. 2005;11:3944-3947.

How to cite this article: Eigentler TW, Winter L, Han H, et al. Wideband Self-Grounded Bow-Tie Antenna for Thermal MR. *NMR in Biomedicine*. 2020;e4274. <https://doi.org/10.1002/nbm.4274>

2.3 Design, Implementation, Evaluation and Application of a 32-Channel Radio Frequency Signal Generator for Thermal Magnetic Resonance Based Anti-Cancer Treatment

With the RF applicator representing the last element in the signal chain of the Thermal MR setup, the 32-channel RF signal generator employs the signal source for a broadband thermal intervention. It supports the broadband antenna system and allows a time-multiplexed⁴³, mixed frequency⁴⁴, and time- and frequency-multiplexed⁴⁵ signal generation.^{46,47} The signal generator is a key element of the thermal intervention platform and drives the amplitude, phase and frequency setting for the thermal intervention. The high degree of freedom for E-field shaping can improve the focal point quality for various objectives of a thermal intervention. Furthermore, a feedback loop supervising the stability of the signals improves the safety and for example temperature drifts can be corrected on-the-fly. The feasibility and applicability of the signal generator was shown in phantom MR-thermometry as well as phantom E-field mapping experiments. The signal generator is based on a PLL system and offers a low-cost alternative to commercially available systems. Compared to commercial systems, the design provides a large number of channels, which is scalable, if more channels are needed. The reported device offers different communication and control interfaces to simplify the integration into the envisioned Thermal MR setup.

The 32-Channel RF signal generator allows to drive the previously introduced wideband SGBT building block for a thermal intervention. It is therefore a critical element in the envisioned integrated thermal intervention setup (Section 1.4).

Publication

Han H, Eigentler TW, Wang S, Kretov E, Winter L, Hoffmann W, Grass E, Niendorf T. Design, Implementation, Evaluation and Application of a 32-Channel Radio Frequency Signal Generator for Thermal Magnetic Resonance Based Anti-Cancer Treatment. *Cancers*. 2020; 12(7):1720. doi: <https://doi.org/10.3390/cancers12071720>.



Article

Design, Implementation, Evaluation and Application of a 32-Channel Radio Frequency Signal Generator for Thermal Magnetic Resonance Based Anti-Cancer Treatment

Haopeng Han ^{1,2}, Thomas Wilhelm Eigentler ^{1,3}, Shuailin Wang ⁴, Egor Kretov ¹, Lukas Winter ⁵, Werner Hoffmann ⁵, Eckhard Grass ^{2,6} and Thoralf Niendorf ^{1,7,8,*}

¹ Berlin Ultrahigh Field Facility (B.U.F.F.), Max Delbrück Center for Molecular Medicine in the Helmholtz Association (MDC), 13125 Berlin, Germany; haopeng.han@mdc-berlin.de (H.H.); thomas.eigentler@mdc-berlin.de (T.W.E.); egor.kretov@mdc-berlin.de (E.K.)

² Humboldt-Universität zu Berlin, Institute of Computer Science, 10099 Berlin, Germany; grass@informatik.hu-berlin.de

³ Technische Universität Berlin, Chair of Medical Engineering, 10623 Berlin, Germany

⁴ Beijing Deepvision Technology Co., Ltd., Beijing 100085, China; wangshuailin@deepvision-tech.com

⁵ Physikalisch-Technische Bundesanstalt (PTB), 10587 Berlin, Germany; lukas.winter@ptb.de (L.W.); werner.hoffmann@ptb.de (W.H.)

⁶ IHP—Leibniz-Institut für innovative Mikroelektronik, 15236 Frankfurt (Oder), Germany

⁷ Experimental and Clinical Research Center (ECRC), a joint cooperation between the Charité Medical Faculty and the Max Delbrück Center for Molecular Medicine, 13125 Berlin, Germany

⁸ MRI.TOOLS GmbH, 13125 Berlin, Germany

* Correspondence: thoralf.niendorf@mdc-berlin.de; Tel.: +49-30-9406-4505

Received: 18 May 2020; Accepted: 22 June 2020; Published: 28 June 2020



Abstract: Thermal Magnetic Resonance (ThermalMR) leverages radio frequency (RF)-induced heating to examine the role of temperature in biological systems and disease. To advance RF heating with multi-channel RF antenna arrays and overcome the shortcomings of current RF signal sources, this work reports on a 32-channel modular signal generator (SG_{PLL}). The SG_{PLL} was designed around phase-locked loop (PLL) chips and a field-programmable gate array chip. To examine the system properties, switching/settling times, accuracy of RF power level and phase shifting were characterized. Electric field manipulation was successfully demonstrated in deionized water. RF heating was conducted in a phantom setup using self-grounded bow-tie RF antennae driven by the SG_{PLL}. Commercial signal generators limited to a lower number of RF channels were used for comparison. RF heating was evaluated with numerical temperature simulations and experimentally validated with MR thermometry. Numerical temperature simulations and heating experiments controlled by the SG_{PLL} revealed the same RF interference patterns. Upon RF heating similar temperature changes across the phantom were observed for the SG_{PLL} and for the commercial devices. To conclude, this work presents the first 32-channel modular signal source for RF heating. The large number of coherent RF channels, wide frequency range and accurate phase shift provided by the SG_{PLL} form a technological basis for ThermalMR controlled hyperthermia anti-cancer treatment.

Keywords: thermal magnetic resonance; radio frequency heating; radio frequency signal generator; radio frequency antenna; hyperthermia

1. Introduction

Temperature is a critical parameter of life with diverse biological implications and intense clinical interest. The aberrant thermal properties of pathological tissue have led to a strong interest in temperature as a clinical parameter. Mild regional hyperthermia (HT, $T = 40\text{--}44\text{ }^{\circ}\text{C}$) is a potent sensitizer for chemotherapy (CH) and radiotherapy (RT), and a clinically proven adjuvant anti-cancer treatment in conjunction with RT and/or CH that significantly improves survival [1–7]. The clinical efficacy of hyperthermia has been demonstrated in randomized studies for specific tumor indications including RT+HT for recurrent breast cancer [8]. Vigorous fundamental and (bio)engineering research into electromagnetic radiation has resulted in a large body of literature documenting technical advances in HT devices [9]. HT devices are increasingly capable of the personalized radio frequency (RF)-induced heating of target tissue volumes guided by sophisticated treatment planning procedures and thermal dose control [10–17]. Thermal Magnetic Resonance (ThermalMR) is an HT variant that accommodates RF-induced heating [17–26], temperature mapping using MR thermometry (MRT) [26–29], anatomic and functional imaging and the option for x-nuclei MR imaging (MRI) in a single, multi-purpose RF applicator.

Targeted RF-induced heating is based on constructive and destructive interferences of electromagnetic (EM) waves transmitted with a multi-channel RF applicator. To achieve precise formation of the energy focal point, accurate thermal dose control and safety management, the transmitted RF signals' frequency, amplitude and phase need to be regulated in real-time. Thus, the RF signal source is the key component for facilitating appropriate frequency, amplitude and phase settings of the RF signals. The radiation pattern of the single RF transmit element, the RF channel count and the RF frequency of the RF applicator are of high relevance for ensuring a patient and problem-oriented adaptation of the size, uniformity and location of the RF energy deposition in the target region [19,21,22,24,30]. The (re)design of multi-channel RF applicator configurations showed more than twofold enhancement of the RF power focusing capability by increasing the number of RF antennae from 12 to 20 [31,32]. Increasing the number of RF antennae resulted in higher RF power absorption and enhanced tumor coverage ratios in deep-seated brain tumors in children [33]. The optimal operating RF frequency depends on the RF applicator characteristics and the target tissue parameters [34]. Lower RF frequencies focus EM energy to larger regions and have lower energy losses inside and outside tissue. Higher RF frequencies facilitate focusing EM energy onto small targets. Numerical simulations and evaluation studies investigated the optimal RF frequency [24]. For regional hyperthermia improvement of the RF power absorption in the target region versus regions outside the target was demonstrated when increasing the RF frequency from 100 MHz to 150 MHz and 200 MHz [35,36]. The optimal heating frequency was examined for seven tumor locations using RF frequencies ranging from 400–900 MHz [37]. For superficial tumors, the highest average specific absorption ratio (aSAR) was obtained with higher frequencies where aSAR was improved with increasing the number of RF antennae. For deep-seated tumors, the highest aSAR was reported for lower frequencies. Studies on ultimate SAR amplification factors and RF applicator concepts suggested the use of high frequencies up to 1 GHz for a highly focused EM energy deposition [21,30]. Time-multiplexed beamforming, a mixed frequency approach and multi-frequency SAR focusing provide other directions into optimization of RF heating performance [38–40]. Recently, an iterative multiplexed vector field shaping (MVFS) approach was introduced to solve the time- and frequency multiplexed problem of constrained RF-induced hyperthermia [24]. This work underlined the need of wideband signal generators by demonstrating the contribution of distinct frequencies to the RF heating and by showing that these frequencies and contributions depend on the target geometry.

To summarize, advancing high-fidelity RF hyperthermia requires pioneering strategies that exploit a wider range of RF frequencies and high-density RF antenna arrays with miniaturized RF building blocks that permit independent frequency, amplitude and phase control for each channel. Hardware implementations for RF heating typically operate at a fixed frequency and have a limited number of RF channels [10,32,41–47]. Recognizing these opportunities and challenges, this work reports on the design, implementation, evaluation, validation and application of a 32-channel modular signal generator (SG_{PLL}) that uses phase-locked loop (PLL) circuit blocks and permits high amplitude,

phase and frequency tuning resolution. This setup is designed to operate between 0.06–3.0 GHz and can be used as the signal source for ThermalMR. To our knowledge, this is the first PLL based multi-channel modular signal source for RF heating with frequency, phase and amplitude adjustment functions integrated.

2. Results

2.1. System Characterization

Implementation of the designed 32-channel RF signal generator was successfully performed with the two 16-channel frequency synthesizer modules integrated in the AXIe (Advanced Telecommunications Computing Architecture (ATCA) Extensions for Instrumentation and Test [48]) chassis as illustrated in Figure 1. The hardware module has a size of $(284 \times 322 \times 29)$ mm³ and a weight of 2.58 kg including the front panel and the protection covers. The red intelligent platform management controller (IPMC) mezzanine card [49] was included to comply with the AXIe-1 specification [48]. It communicates with the AXIe system module in the chassis for tasks such as power management, temperature monitoring, backplane pin assignment, etc. A set of fans is integrated in the chassis to dissipate heat generated by the modules. The power consumption of one module was measured to be 7.32 W with a CPU usage of 100% and the RF section switched off. Typical power consumption was 50.42 W when all the 16 RF channels were outputting 0 dBm signals. When the power levels of all the 16 RF channels were set to -4 dBm, the total power consumption started to exceed 50 W which is the maximum allowed power consumption for one unmanaged AXIe module [48]. Peripheral circuits working with the IPMC card were implemented for temperature probing of the module and for adjustment of the chassis (fan speed, etc.) accordingly in case the power consumption for one module exceeds 50 W.

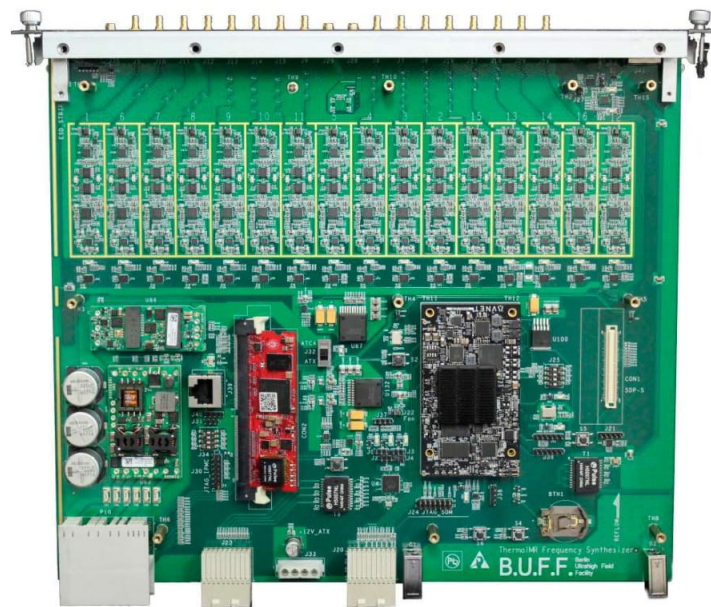


Figure 1. Cont.



Figure 1. Sixteen-channel frequency synthesizer module (top): The black module is a system-on-module unit AES-ZU3EG-1-SOM-I-G (Avnet, Phoenix, AZ, USA); the red module is an open source intelligent platform management controller card. Electromagnetic interference shielding covering the 16 RF channels was not installed for acquisition of the photo. The top cover of this module was also removed for better presentation. Two 16-channel frequency synthesizer modules installed in the AXIe chassis are shown at the bottom.

Videos S1–S3 demonstrate live adjustments of the signal frequency, amplitude and phase. Videos S4–S6 show the switching/settling time measurements of frequency, amplitude and phase with the results detailed in Table 1. Amplitude calibrations were conducted for channel one and channel two for three frequencies: 300 MHz, 600 MHz and 900 MHz. Figure 2 shows the relationship between the digital to analog converter (DAC) control words and the signal amplitudes. Good linearity was achieved for power levels between -25 dBm to 10 dBm. It requires a larger control word to output the same power level for a higher frequency. This complies with the characteristics of the voltage controlled variable gain amplifier (VGA) chip ADL5330 [50]. Table 2 lists the test results of the phase shift experiments. An average absolute phase shift error of 0.06° with a maximum phase shift error of 0.16° was measured for all tested cases. The phase shift error showed no dependency on the phase shift value. Test results at 900 MHz showed slightly higher phase errors versus phase errors obtained at lower frequencies.

Table 1. Test results of the switching/settling times for frequency, amplitude and phase.

	Mean	Minimum	Maximum	Standard Deviation
Frequency switching time (ms)	2.208	1.872	2.582	0.219
Amplitude settling time (μ s)	617	320	810	143
Phase settling time (μ s)	196	140	290	40

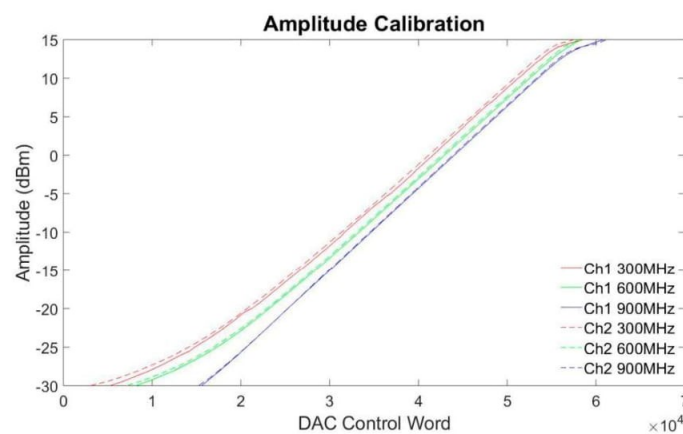


Figure 2. Amplitude calibrations for two channels at three frequencies: 300 MHz, 600 MHz and 900 MHz.

2.3 Design, Implementation, Evaluation and Application of a 32-Channel Radio Frequency Signal Generator for Thermal Magnetic Resonance Based Anti-Cancer Treatment

Table 2. Test results of the phase shift experiments.

Phase Shift c (°)	Phase Reading a (°) before Shift	Phase Reading b (°) after Shift	Measured Shift b–a (°)	Phase Shift Error (c–(b–a)) mod 360 (°)
300 MHz				
0.5	0.5588	1.0553	0.4965	0.0035
1	0.9936	1.9973	1.0037	–0.0037
5	0.4629	5.459	4.9961	0.0039
10	1.0537	11.0544	10.0007	–0.0007
15	0.6694	15.7225	15.0531	–0.0531
45	0.6919	45.75	45.0581	–0.0581
90	0.2352	90.2764	90.0412	–0.0412
100	0.4318	100.4639	100.0321	–0.0321
180	0.4238	179.5796	180.0034	–0.0034
200	0.4315	–159.5768	–160.0083	0.0083
270	0.6984	–89.2514	–89.9498	–0.0502
300	0.4575	–59.5542	–60.0117	0.0117
600 MHz				
0.5	1.0714	1.5928	0.5214	–0.0214
1	1.0517	2.1267	1.075	–0.075
5	1.1045	6.1592	5.0547	–0.0547
10	1.0741	11.2004	10.1263	–0.1263
15	1.1124	16.1507	15.0383	–0.0383
45	1.19	46.254	45.064	–0.064
90	1.1915	91.185	89.9935	0.0065
100	1.1294	101.1894	100.06	–0.06
180	1.1242	–178.8824	–180.0066	0.0066
200	0.9942	–158.9036	–159.8978	–0.1022
270	1.082	–88.783	–89.865	–0.135
300	–1.8299	–61.7925	–59.9626	–0.0374
900 MHz				
0.5	–18.8026	–18.1841	0.6185	–0.1185
1	–18.8053	–17.6564	1.1489	–0.1489
5	–18.8533	–13.7494	5.1039	–0.1039
10	–18.9628	–8.8075	10.1553	–0.1553
15	–18.8442	–3.8403	15.0039	–0.0039
45	–19.2507	25.888	45.1387	–0.1387
90	–19.246	70.7953	90.0413	–0.0413
100	–19.2349	80.806	100.0409	–0.0409
180	–19.2853	160.8254	180.1107	–0.1107
200	–19.2892	–179.1758	–159.8866	–0.1134
270	–19.3033	–109.251	–89.9477	–0.0523
300	–17.7194	–77.6205	–59.9011	–0.0989

2.2. E-Field Manipulation and Mapping

Electric field (E-field) simulations and measurements ($f = 400$ MHz) are shown in Figure 3 for two E-field focusing point settings. For this purpose, the E-field maps obtained from simulations and measurements were normalized. For all eight RF channels using the same RF phase and amplitude setting, the E-field focusing point is located at the center of the transversal plane through the middle of the antenna array (Figure 3A–E). Figure 3F–J show the results obtained for positioning the E-field focus in an arbitrary (off-center) location. The measured E-field distribution patterns agree with the E-field maps derived from the electromagnetic field (EMF) simulations. The same E-field distribution was observed in all four experiments, each using a different set of eight out of 32 RF channels.

2.3 Design, Implementation, Evaluation and Application of a 32-Channel Radio Frequency Signal Generator for Thermal Magnetic Resonance Based Anti-Cancer Treatment

Cancers 2020, 12, 1720

6 of 23

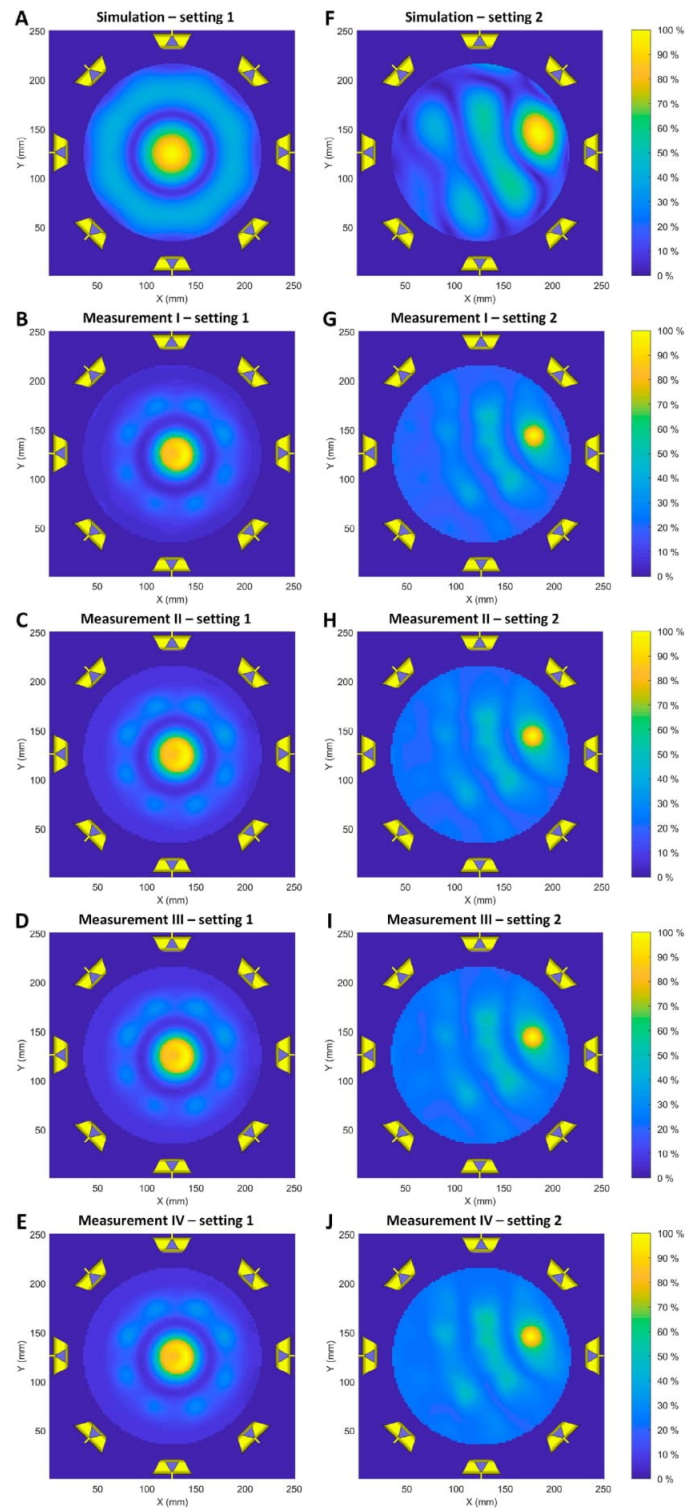


Figure 3. E-field simulations and measurements ($f = 400$ MHz) obtained for the central plane of the self-grounded bow-tie (SGBT) antennae array. (A–E) Normalized E-field maps with the E-field focus being placed in the center of the transversal plane through the middle of the SGBT antenna array. (F–J) Normalized E-field maps with the E-field focus being positioned off-center in the same transversal plane used for the center position. Two phase and amplitude settings were tested in the simulations and measurements. All eight RF channels were set to the same phase (0°) and amplitude (10 dBm) in setting 1. In setting 2, the phases of the eight RF channels were set to $[6.04^\circ, -154.96^\circ, 25.86^\circ, -32.9^\circ, -178.5^\circ, -7.46^\circ, -3^\circ, -155.89^\circ]$ and the amplitudes were set to $[-1.15$ dBm, -14.11 dBm, -13.01 dBm, -3.72 dBm, 2.22 dBm, 10 dBm, 9.2 dBm, 3.32 dBm]. A different set of eight out of 32 RF channels was used for measurement I–IV.

2.3. Single Channel RF Heating

The results deduced from single channel RF heating in numerical temperature simulations and experiments are detailed in Figure 4 for $f_1 = 300$ MHz, $f_2 = 400$ MHz and $f_3 = 500$ MHz. RF at higher frequencies induced higher temperature changes (ΔT) in the phantom. Figure 4M–O depict ΔT profiles obtained for a center line placed across the transversal slice at the middle of the phantom for temperature simulations (Figure 4A–C), experimental RF heating using the commercial SMGL (R&S, Munich, Germany) signal generator (Figure 4D–F) and experimental RF heating employing the RF signal generator developed in this work (Figure 4G–I). Figure 4J–L show the differences in RF-induced temperature changes obtained from MRT for the developed signal generator (Figure 4G–I) and the commercial SMGL signal generator (Figure 4D–F). Almost identical temperature changes across the phantom were observed. The maximum temperature increase derived from MRT was $\Delta T = 5.3$ °C, 7.8 °C and 10.6 °C for heating at 300 MHz, 400 MHz and 500 MHz. These temperature changes are 1.7 °C, 1.7 °C and 2.5 °C lower than the corresponding maximum temperature increases yielded by the numerical temperature simulations. Fiber optic temperature measurements confirmed the MRT results.

2.4. Dual Channel RF Heating

Figure 5 summarizes the results derived from numerical simulations and experiments using the two-channel RF heating setup at 400 MHz. Figure 5J–L depict the difference in the temperature changes obtained with MRT for RF heating using proposed signal generator (Figure 5G–I) and the commercial M8190A (Keysight, Santa Rosa, CA, USA) arbitrary waveform generator (Figure 5D–F). Similar to the single channel experiments, almost identical temperature changes across the phantom were observed. Temperature profiles obtained from center lines across the phantom (Figure 5M–O) demonstrated the same interference patterns created in the experiments compared with the simulations. For phase setting $\phi = 0^\circ$, the induced temperature increase due to constructive interference was $\Delta T_{\max} = 2.6$ °C in the middle of the phantom (Figure 5A,D,G). This interference pattern was moved around 18 mm to the left towards channel two when a 90° phase shift was applied to channel one on the right (Figure 5B,E,H). A destructive interference was created in the middle of the phantom when the phase difference was set to 180° between the two channels. For this phase mode two constructive interferences around 64 mm apart from each other were generated symmetrically in the phantom (Figure 5C,F,I). Readings from the fiber optic temperature sensor accord with the MRT results.

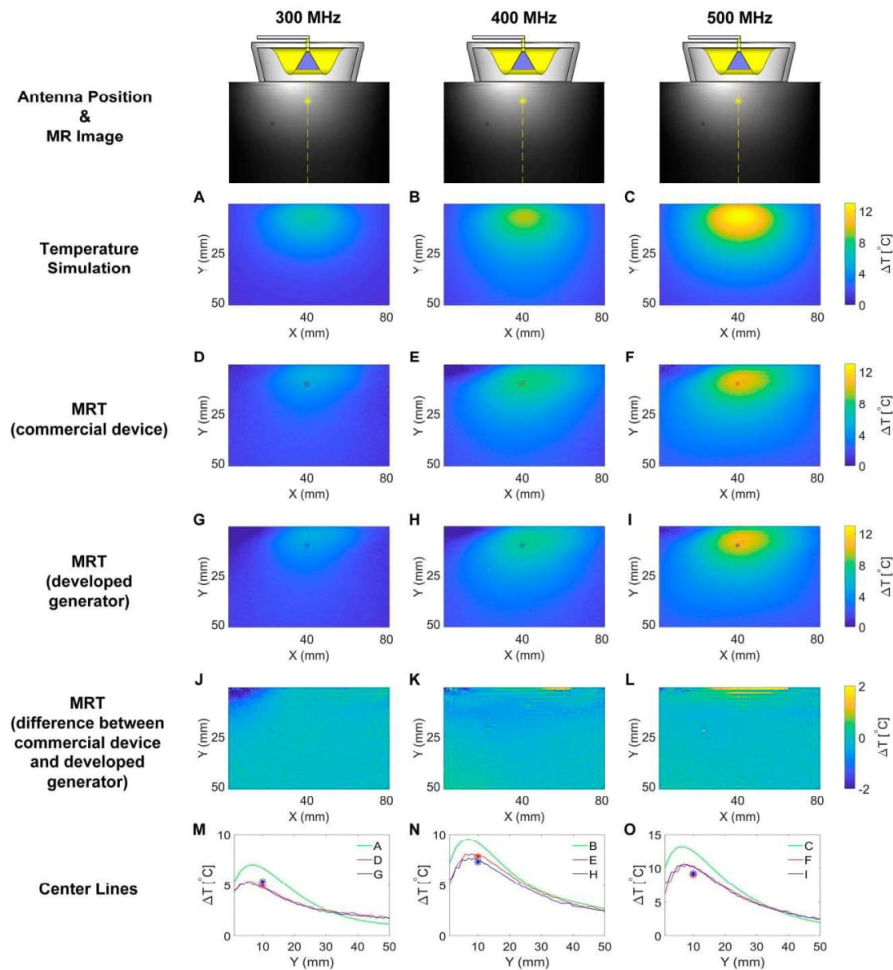


Figure 4. Maps of temperature changes (ΔT) obtained from the numerical simulations and experiments using a single channel connected to an SGBT antenna for RF heating ($t = 10$ min, P_{in} at port = 17.78 W). Each column shows results for one frequency: 300 MHz, 400 MHz and 500 MHz. A transversal slice in the middle of the phantom aligned with the center of the SGBT antenna was selected for the temperature simulations and for MR thermometry (MRT). The first row demonstrates the position of the antenna and the MR image of the phantom. The yellow lines indicate the center lines and the yellow stars indicate the position of the fiber optic temperature sensor. Figure (A–C) illustrate temperature changes obtained from temperature simulations. Figure (D–F) show maps of temperature changes derived from MRT for RF heating using the commercial signal generator (SMGL, R&S, Munich, Germany). The red stars in these figures indicate the position of the fiber optic temperature sensor. Figure (G–I) depict maps of temperature changes deduced from MRT of RF heating using the signal generator developed in this work. The blue stars in these figures represent the position of the fiber optic temperature sensor. Figure (J–L) outline ΔT difference maps benchmarking the temperature changes obtained for RF heating using the proposed signal generator against those observed for the commercial SMGL signal generator. The bottom row (Figure (M–O)) show ΔT profiles for a center line obtained for the center slice of the phantom for temperature simulations (A–C), experimental RF heating using the commercial SMGL signal generator (D–F) and experimental RF heating employing the RF signal generator setup developed in this work (G–I). The blue stars and red stars indicate readings from the temperature sensor for heating with our signal generator and with SMGL, respectively.

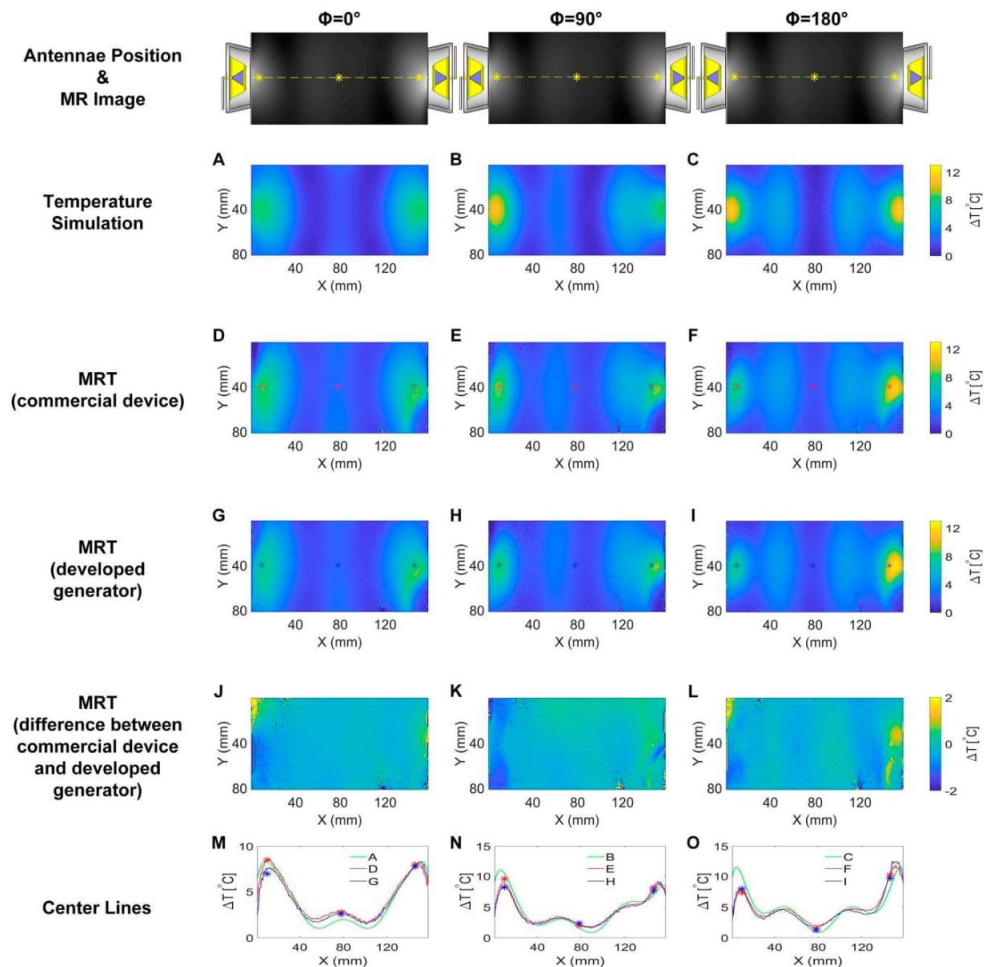


Figure 5. Maps of temperature changes (ΔT) obtained from the numerical simulations and experiments using two channels ($f = 400$ MHz) for RF heating ($t = 10$ min, P_{in} at port = 17.78 W) with each channel being connected to an SGBT antenna. The first row demonstrates the position of the antennae and the MR image of the phantom. The yellow lines indicate the center lines and the yellow stars indicate the position of the fiber optic temperature sensor. Each column shows results obtained for one phase setting: $\phi = 0^\circ$, $\phi = 90^\circ$ and $\phi = 180^\circ$. The phases were set to the right channel while the left channel was fixed to $\phi = 0^\circ$. A transversal slice in the middle of the phantom aligned with the center of the RF applicator was selected for MR thermometry. Figure (A–C) illustrate temperature changes obtained from temperature simulations. Figure (D–F) show maps of temperature changes derived from MRT for RF heating using the commercial signal generator (M8190A, Keysight). The red stars in these figures indicate the position of the fiber optic temperature sensor. Figure (G–I) depict maps of temperature changes deduced from MRT of RF heating using the signal generator developed in this work. The blue stars in these figures represent the position of the fiber optic temperature sensor. Figure (J–L) outline ΔT difference maps benchmarking the temperature changes obtained for RF heating using the proposed signal generator against those observed for the commercial M8190A signal generator. The bottom row (Figure (M–O)) show ΔT profiles obtained for a center line placed across the center slice of the phantom for temperature simulations (A–C), experimental RF heating using the commercial M8190A signal generator (D–F) and experimental RF heating employing the RF signal generator setup developed in

this work (G–I). The blue stars and red stars indicate readings from the temperature sensor for heating with our signal generator and with M8190A, respectively. Constructive interference patterns were observed in the middle of the phantom for phase setting $\phi = 0^\circ$. This pattern was shifted ~18 mm to the left for phase setting $\phi = 90^\circ$. For phase setting $\phi = 180^\circ$, two symmetrical constructive interference patterns ~64 mm apart from each other and a destructive interference pattern in the middle of the phantom were observed.

3. Discussion

3.1. System Characterization

The 32-channel signal generator consists of two PLL-based modular frequency synthesizers. This modularity and the working principle of PLLs support convenient implementation of $n > 32$ number of RF channels. In a ThermalMR setting, the RF signal could potentially come from the MR scanner; however, the current maximum number of independent transmission RF channels in a state-of-the-art MR scanner is constrained to a single TX channel for the combined mode transmission regime and eight or sixteen for the parallel transmission mode with RF signals being constrained to a small transmitter bandwidth covering a fixed center frequency (Larmor frequency). It is fair to anticipate that the number of transmitter RF channels will increase to meet the needs of ThermalMR which would be in favor of small size antenna building blocks at higher frequencies, which afford high density RF applicator configurations. Previous experimental works mostly operated at one of the ISM (Industrial, Scientific and Medical) frequencies (e.g., 434 MHz, 915 MHz and 2.4 GHz) and typically a single channel commercial signal source in conjunction with an RF power splitter and RF phase shifters architecture was adopted [43,47]. ThermalMR exploits a wider frequency range with the proposed signal generator which covers a wide frequency range from 60 MHz to 3 GHz. The compact modular PLL based design implemented in this study provides a theoretically unlimited number of coherent, independent RF channels and a wide frequency range, thus facilitating future ThermalMR developments.

Live adjustments of the RF signal were demonstrated in Videos S1–S3. The high-performance field-programmable gate array (FPGA) chip makes it possible to carry out adjustments through executing Python scripts on its ARM processor. Unstable signals were observed in Videos S4–S6 during transitions. These unstable transitions can be bypassed by setting the RF switch chips included in the signal path. No significant delay is added by this approach since the switching time of the RF switch chips is typically as low as 150 ns [51]. The switching/settling times are sufficient for ThermalMR applications. Especially, the fast and stable signal switching/settling implemented here is necessary for ThermalMR applications where real-time signal adjustments are needed, e.g., in online interference pattern control [52,53], in time-multiplexed beamforming [38], or in a mixed frequency approach [39]. Fast switching is also desirable during system initialization where recursive adjustments could be involved. However, generating excitation RF pulses suitable for MRI typically requires an amplitude settling time of less than 0.1 μ s, which is a recognized limitation of the developed 32-channel RF signal generator.

In Figure 2, a slight difference between channels on the control words for generating the same signals was observed. This difference was produced by the variations of the components on the RF signal path. A larger control word is required to output the same power level for a higher frequency. The dependency of the control words on system parameters such as frequency and RF channel can be eliminated by applying a power meter and a feedback control algorithm. A home-built multi-channel power and phase meter was developed to implement more precise control over the output signal amplitude.

In the phase shift experiments, test results (Table 2) at 900 MHz showed slightly higher phase errors versus phase errors obtained at lower frequencies. This is due to the higher phase jitter of the PLL's output at higher frequencies. The starting phases after synchronization before phase shifting were different for the tested frequencies. It was mainly caused by the difference in the signal path

lengths between the two channels. This phase mismatch can be synchronized/compensated by applying the phase meter and a synchronization algorithm. The high accuracy of the phase shifting function of the signal generator is essential for ThermalMR applications since the desired focal point formation highly depends on precise phase arrangement of transmitted RF signals. This PLL-based phase shifting approach showed substantial improvement in flexibility, resolution, feasibility and accuracy over other approaches such as standalone phase shifter based and modulation-based phase shifting. For example, an 8-bit digital phase shifter (DST-10-480/1S, Pulsar Microwave, Clifton, NJ, USA) was used in an experimental setup [44]. It can only generate 256 phases and covers a limited frequency range. For this approach, the maximum insertion loss is as high as 6 dB and the phase uncertainty is $\pm 3\%$ at center frequency [54]. For modulation-based phase shifting [55], the resolution and the accuracy of the phase shift are usually confined by the number of points in the modulation constellation diagram and the accuracy of the DACs. DDS based signal generator could provide accurate phase shift with fine resolution. However, the maximum output frequency of a DDS is limited to about 1/3 the sampling clock frequency [56]. If higher frequencies are needed, harmonics in higher Nyquist zones need to be filtered out with band-pass filters. It is difficult to cover a wide frequency range with a DDS system. Here, we addressed these constraints by employing the PLL based signal synthesizing approach which provides a wide frequency range (0.06–3 GHz) and fine phase adjustment resolution ($360^\circ/2^{24}$).

3.2. E-Field Manipulation and Mapping

The controlled deposition of electromagnetic energy in the target is essential to RF-induced hyperthermia. The results obtained from the E-field manipulation experiments demonstrate the signal generator's capability of controlling the RF signals to generate desired E-field patterns based on constructive and destructive interferences of electromagnetic waves. Our approach demonstrated that all 32 RF channels were functioning correctly in synthesizing the desired E-field patterns. The E-field amplitudes derived from the measurements are inferior to the E-field simulations. This difference is caused by the nonlinear sensitivity of our home-built E-field probe.

3.3. Single Channel RF Heating

Maps of temperature changes (ΔT) obtained from the numerical simulations and experiments using a single channel connected to a self-grounded bow-tie (SGBT) antenna for RF heating showed that RF at higher frequencies induced higher ΔT in the phantom. This is caused by the higher loss of the RF signal in the phantom at higher frequencies. The MRT results revealed ΔT profiles which are in accordance with the simulation results. The maximum temperature increases derived from MRT were lower than the corresponding maximum temperature increases yielded by the numerical simulations. This difference is caused by the changeover time ($\Delta t = 50$ s) needed to switch the cable connection from the home-built RF power amplifier (RFPA) to the MR scanner right after the heating process. The temperature in the phantom drops due to heat dissipation during this change over time.

3.4. Dual Channel RF Heating

A second channel was added to the single channel RF heating experiments to examine interference patterns created by phase shifts. Similar to the single channel experiments, almost identical temperature changes across the phantom between the designed signal generator and the high-end commercial one were observed. Temperature profiles obtained from center lines across the phantom underline the equivalence in RF heating performance of the proposed signal generator and the M8190A. The interference patterns created by RF heating are in accordance with numerical temperature simulations. The differences between MRT and temperature simulation have a slightly different pattern compared with corresponding differences obtained for the single channel heating experiments. This was caused by the imperfection of the RFPAs whose outputs were impacted by the crosstalk (which depends on the phase settings) between the two SGBT antennae.

To summarize, the experimental results demonstrated the suitability of the designed signal generator for ThermalMR. Compared with commercial signal generators, this design provides large number of channels and various communication interfaces implemented here make it very convenient to be integrated into a more complex system, e.g., an MR scanner. The high-performance processor adopted in the design provides ample processing power for applications that need real-time signal adjustments and flexible configurations. The PLL circuit implemented in this design occupies little printed circuit board (PCB) area and permits a compact modular design. The adoption of PLL is also cost-effective compared to other architectures of comparable performance. Although the maximum frequency tested here was 1.2 GHz, the signal generator supports higher frequencies up to 3 GHz. This wide frequency range extends its usage from RF-induced mild hyperthermia to microwave ablation [57].

4. Materials and Methods

4.1. Hardware Design

The 32-channel RF signal generator hardware consists of two 16-channel RF synthesizer modules. Figure 6 shows its block diagram. The 16-channel RF synthesizer module is an AXIe compliant modular design. The 16 RF channels are identical in circuit design with the output impedance matched to 50 Ohm. Each channel is equipped with an independent low-dropout power regulator that powers the noise sensitive components in the channel. The RF signal generation was designed around the phase-locked loop chip ADF4356 (Analog Devices, Norwood, MA, USA). This PLL chip could generate a frequency range of 54 MHz to 6800 MHz. A very fine frequency resolution with practically no residual frequency error is afforded by the PLL's 52-bit modulus. The synthesized signal's phase can be adjusted with a theoretical resolution of $360^\circ/2^{24}$. Two low-pass filters with a bandwidth of 400 MHz and 1.2 GHz were added to filter out the harmonics of the RF signals. RF switch chips HMC245A (0 to 3.5 GHz, Analog Devices) were used to select among different filter paths. The signal amplitude can be manipulated by a voltage controlled variable gain amplifier (VGA) chip ADL5330 (10 MHz to 3 GHz, Analog Devices) which provides a wide gain control range. The gain of the VGA is adjustable linearly in decibel and was controlled by the voltage output of a 16-bit digital to analog converter (DAC) AD5683 (Analog Devices). The 16 PLL chips on the module were locked to the same reference signal. A low jitter 2-input selectable 1:16 clock buffer CDCLVP1216 (Texas Instruments, Dallas, TX, USA) was used to fan out the reference signal to 16 PLL chips. The reference signal can be selected either from the output of an on board programmable low jitter crystal oscillator Si549 (Silicon Labs, Austin, TX, USA) or from the external reference signal input. The routings of the LVPECL (low-voltage positive emitter-coupled logic) reference signals for the PLLs as well as the routings of the signals from the output of the VGA to the SMB (subminiature version B) connectors at the board edge were length matched with minimum variations among the 16 channels.

The whole system was managed by a quad-core ARM Cortex-A53 processor which resides in a field-programmable gate array chip ZU3EG (Xilinx, San Jose, CA, USA). The FPGA seats at the core of a system-on-module unit AES-ZU3EG-1-SOM-I-G (Avnet, Phoenix, AZ, USA). Various interfaces were implemented with the FPGA: a Gbit Ethernet port, a serial port, an SD (secure digital) card interface, GPIO (general purpose input/output) connections, three status LED (light-emitting diode) indicators, trigger input/output and a reset input were connected to the front panel; a Gbit Ethernet port, a 4-lane PCIe (peripheral component interconnect express) port and 4-lane LVDS (low-voltage differential signaling) signals were connected to the backplane per the requirements of the AXIe specification [48]. The Ethernet interface to the front panel, the PCIe port, the SD card interface and the serial port were implemented with the hard-core peripherals within the processor system whereas the rest of the interfaces were realized using the programmable logic resources in the FPGA. AXI (Advanced Extensible Interface) bus-based IP (intellectual property) cores were developed utilizing the FPGA logic to configure the PLL chips, RF switches, DAC chips and the clock buffer.

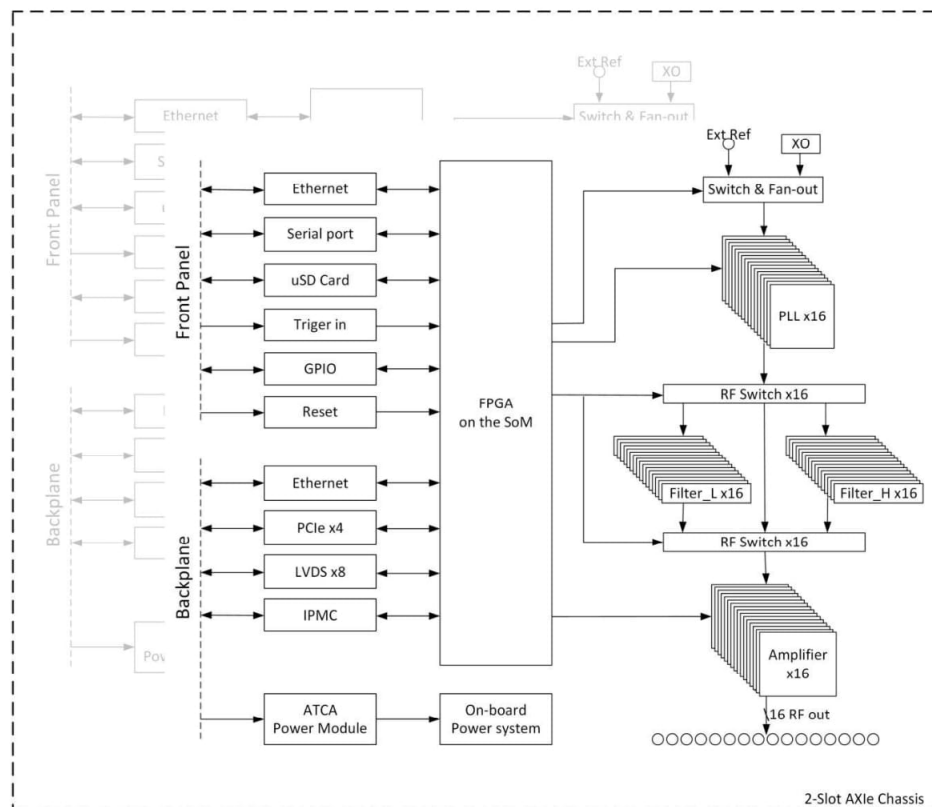


Figure 6. System block diagram of the 32-channel RF signal generator. Two 16-channel AXIe RF signal synthesizer modules were installed into a 2-slot AXIe chassis to form a 32-channel RF signal generator. The modules communicate with each other through the backplane LVDS connections. The chassis provides power to the modules through its backplane.

This 16-channel RF synthesizer module works with any AXIe compatible chassis. Commercial-off-the-shelf chassis were used to save the effort of designing the data exchange mechanism, communication interfaces, power supply and cooling system. Two modules were installed into a 2-slot AXIe chassis M9502A (Keysight, Santa Rosa, CA, USA) to form a 32-channel RF signal generator. The modules communicate with each other through the backplane LVDS connections. The module in the lower slot is a master module and controls the other one. An open source intelligent platform management controller (IPMC) mezzanine card [49] can be installed into the mini dual in-line memory module (DIMM) socket on the AXIe module. The chassis provides power to the modules through its backplane. An ATCA power input module PIM400KZ (ABB, Zurich, Switzerland) was used to interface the -48 V DC (direct current) power supply from the backplane. A DC-DC converter ESTW010A0B (ABB) converts the -48 V DC to 12 V DC which then served as the main power supply of the module. A 12 V DC power input socket was also implemented on the module to enable standalone operation.

4.2. Software Design

The module is running openSUSE LEAP 15.1 Linux operating system [58]. Python scripts were programmed to interact with the IP cores which control the RF components on the board. The programs manipulate the IP cores through memory mapped register reading and writing. A web based graphical user interface was developed to provide a more user-friendly interface to configure the system as

demonstrated in Figure 7. All the 32 RF channels can be set to the same configuration specified by the user in the initialization function block. System-wide options, e.g., reference clock selection and filter path selection were also implemented in this block. Parameters can be loaded from/saved to configuration files so that the configuration process is less tedious and errors from manual input can be avoided. Each channel can be configured individually in the following blocks. Signal properties such as frequency, phase and amplitude are set according to the parameters specified in the input text boxes.

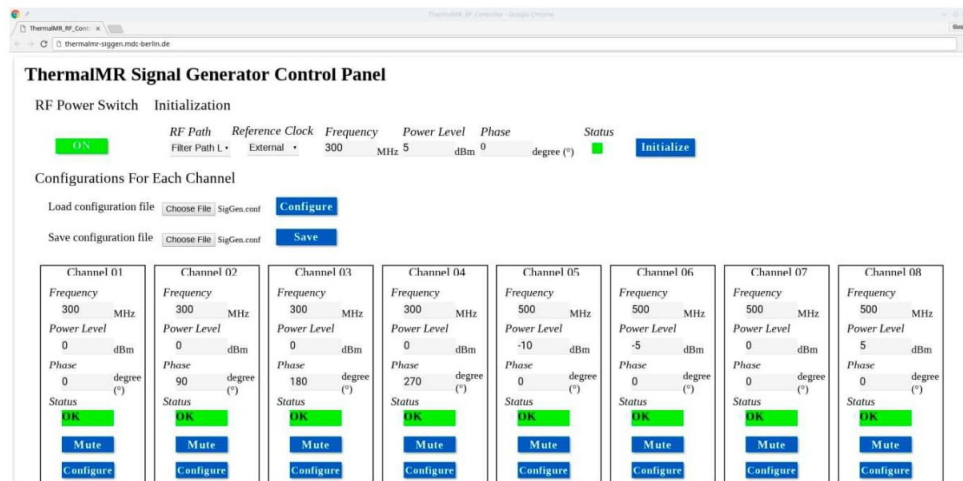


Figure 7. The web-based graphic user interface used for controlling the 32-channel signal generator. For simplicity only eight out of 32 channels are shown. The RF Power Switch controls the power supply to the analog circuits in the signal generator. The status indicator shows green when the corresponding channel runs normally. If errors happen, the indicator turns into red. Each channel can be muted independently by pressing the Mute button.

4.3. System Characterization

For system evaluation, the reference clock for the PLLs was provided by a GPS (global positioning system) disciplined oscillator's output distributed by an 8-channel clock distributor CDA-2990 (National Instruments, Austin, TX, USA). The power level of the PLL output was set to 5 dBm. All tests were conducted at room temperature (22 °C) with the signal generator warmed up for 30 min.

The power consumption of the module was measured in standalone operation mode with all the RF components being powered on and off. FPGA logics and Python scripts were implemented to test the module's ability of manipulating the frequency, amplitude and phase of the RF signals. Maximum switching/settling times for changes in these properties were examined. A single pulse generated by a universal pulse generator (UPG100, ELV, Leer, Germany) was used to trigger the change. The trigger signal (via a T-connector) and the RF output from the module were connected to an oscilloscope (DPO7254, Tektronix, Beaverton, OR, USA) to measure the switching/settling times. In total, 50 measurements with 10 frequency points ranging from 100 MHz to 1000 MHz in increments of 100 MHz were conducted for testing the PLL frequency lock time. Amplitude changes ($n = 18$ measurements) were assessed for a range of -30 dBm to 15 dBm with a step size of 5 dBm for testing the amplitude switching/settling time. Various phase changes were also carried out for testing the phase switching time.

The signal amplitude of each channel is controlled by the combination of a DAC and a VGA. Amplitude calibration was conducted to map 16-bit DAC control words to specific signal power levels. Signals at three frequencies (300 MHz, 600 MHz and 900 MHz) were calibrated. The RF power level was monitored with a spectrum analyzer (ZVL, R&S, Munich, Germany). A Python script was developed to change the 16-bit control word of the DAC. The control words were recorded for 91 power levels spread over -30 dBm to 15 dBm with a step size of 0.5 dBm.

The accuracy of the phase shifting of the PLLs was tested employing the phase measurement function of an oscilloscope (MSOS054A, Keysight). The RF signal generated from channel one of the module was used as a reference signal. Various phase shift settings were applied to channel two. The phase relationships between the two channels were recorded before and after the phase shifting. Signals at three frequencies (300 MHz, 600 MHz and 900 MHz) were tested.

4.4. E-Field Manipulation and Mapping

E-field manipulation and E-field mapping were conducted in EMF simulations and in experiments to demonstrate the signal generator's performance for E-field focusing. For this purpose, eight arbitrary RF channels (four from each module of the signal generator) were used to generate 400 MHz RF signals using tailored amplitude and phase settings. The RF signals were connected to eight wideband self-grounded bow-tie (SGBT) antennae [23] immersed in deionized water. The SGBT antennae were arranged in a circular array. An open source 3D multipurpose measurement system (COSI Measure) [59] and a home-built E-field probe were used to map the E-field distribution. Figure 8 illustrates the experimental setup. Two E-field patterns: (a) the E-field focusing point was placed in the center of the transversal plane through the middle of the SGBT antenna array; (b) the E-field focusing point was set to an arbitrary point in the transversal plane through the middle of the SGBT antenna array. The amplitude and phase settings for each E-field pattern were obtained from an alternating projections-based EM field optimizer [60]. The amplitude and phase settings were fed to the signal generator for E-field mapping and to CST Microwave Studio 2018 (Computer Simulation Technology GmbH, Darmstadt, Germany) for E-field numerical simulation. For the simulation, the CST frequency domain solver was adopted with a tetrahedral mesh type. The maximum mesh size was set to $4.0 \times 4.0 \times 4.0$ mm³ including an adaptive mesh refinement to improve the mesh quality. The mesh size is sufficient for the problem since further reduction (10%) of the maximum mesh size did not yield substantial changes (<0.3%) in the simulation results. We used open boundary condition which is implemented as a perfectly matched layer (PML) with additional 3 m (4 wavelengths at 400 MHz) distance added between the model and the PML. The experiment was repeated four times. For each run, a different set of eight RF channels was used, so that all 32 RF channels were tested.

4.5. Single Channel RF Heating

Single channel heating experiments with the signal generator were conducted at 300 MHz, 400 MHz and 500 MHz. The output RF signal from channel one was fed to a home-built RF power amplifier (RFPA). The amplified signal was connected to an SGBT antenna through a directional coupler (BDC0810-50/1500, BONN Elektronik, Holzkirchen, Germany) and the feed through penetration panel of the MR scanner room. By adjusting the amplitude settings of channel one, a 42.5 dBm (17.78 W) signal was generated at the feeding port of the SGBT antenna. The power level was monitored by checking the forward coupled signal output of the directional coupler with a home-built power and phase meter. Figure 9 demonstrates the experimental setup. The antenna was applied to a muscle-mimicking agarose phantom (Figure 10, length = 160 mm, width = 116 mm, height = 178 mm, density = 1231.77 g/L, heat capacity = 3.00 (J/g)/K, thermal conductivity = 0.43 W/(m*K), NaCl: 5.48 g, Sugar: 2601 g, Agar: 52 g, Deionized H₂O: 2600 g, CuSO₄: 1.95 g [61]) placed in the isocenter of a 7.0 T human MR scanner (Magnetom, Siemens Healthineers, Erlangen, Germany). Table 3 summarizes the dielectric properties of this phantom, which were derived from the S-matrix measurement data using a vector network analyzer (ZVT 8, R&S, Munich, Germany). For benchmarking experimental data

2.3 Design, Implementation, Evaluation and Application of a 32-Channel Radio Frequency Signal Generator for Thermal Magnetic Resonance Based Anti-Cancer Treatment

with numerical simulations, temperature simulations were performed in CST Microwave Studio 2018. For this purpose, the phantom configuration used in the heating experiments was incorporated into the numerical simulations. The CST thermal transient solver was adopted with a hexahedral mesh type. The maximum mesh size was set to $2.0 \times 2.0 \times 2.0 \text{ mm}^3$, which is sufficient for the problem that decreasing the maximum mesh size by 10% does not yield substantial changes ($<0.01\%$) in the simulation results. We used open boundary condition with the ambient temperature $20 \text{ }^\circ\text{C}$ set at the boundary as constant temperature. The simulation started with an initial temperature of $20 \text{ }^\circ\text{C}$. RF heating with $P_{\text{in}} = 17.78 \text{ W}$ at the feeding port of the SGBT antenna and a duration of 10 minutes was applied for 300 MHz, 400 MHz and 500 MHz. MR thermometry using the PRFS approach [29,62,63] ($TR = 99 \text{ ms}$, $TE1 = 2.73 \text{ ms}$, $TE2 = 6.71 \text{ ms}$, voxel size = $1 \times 1 \times 5 \text{ mm}^3$) at 297.2 MHz was conducted before and after the RF heating for each frequency. Vegetable oil was used as a reference to correct the magnetic field drifts [64]. Fiber optic temperature sensors (Neoptix, Quebec, QC, Canada) were used to validate the MRT results. The heating experiments were repeated with the signal generator replaced by a commercial one (SMGL, R&S) to compare the results.

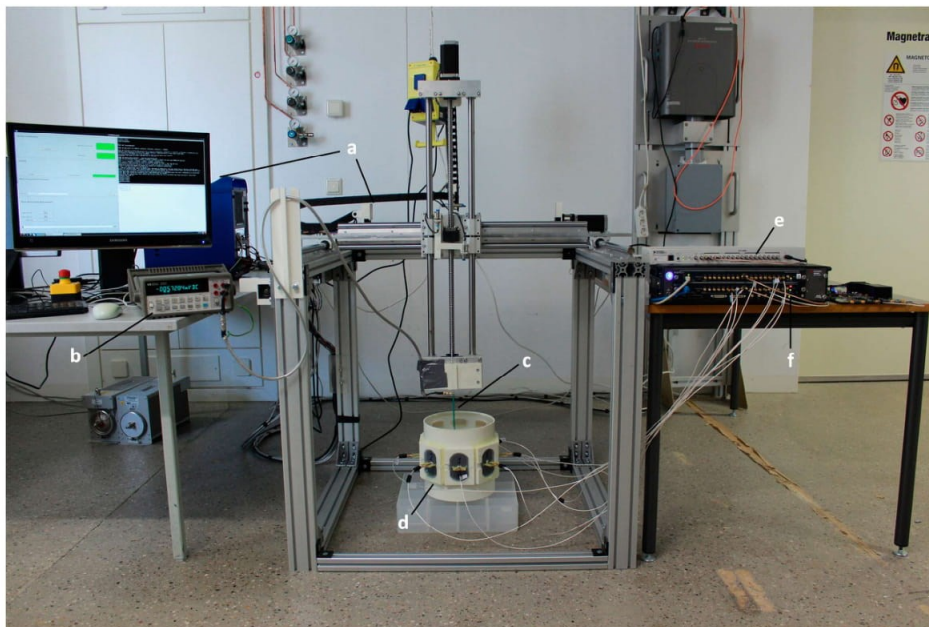


Figure 8. Experimental setup used for E-field mapping. (a) the COSI Measure setup, (b) digital multimeter (34401A, Keysight) connected to (c) the home-built E-field probe, (d) 8 SGBT antennae arranged in a circular array (diameter = 22 cm) immersed in deionized water, (e) clock distributor, (f) RF signal generator. COSI Measure moves the E-field probe with a step size of 2 mm in the central transversal plane of the antennae setup resulting in 6430 measurement points.

2.3 Design, Implementation, Evaluation and Application of a 32-Channel Radio Frequency Signal Generator for Thermal Magnetic Resonance Based Anti-Cancer Treatment

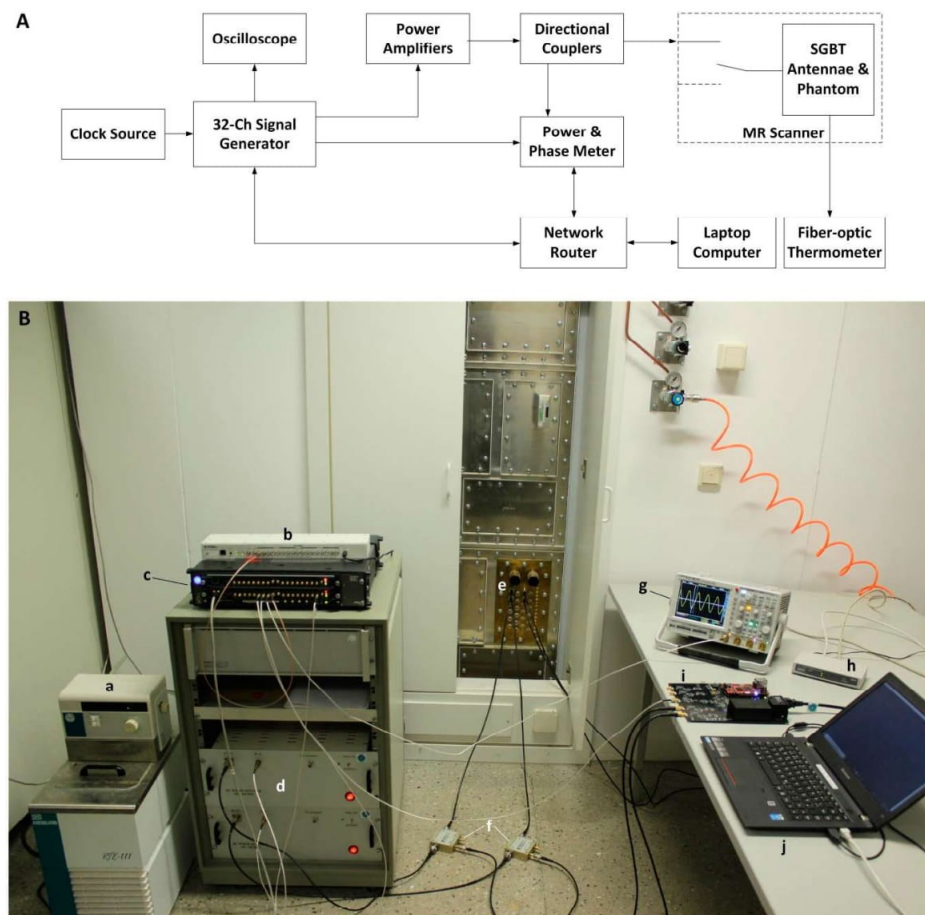


Figure 9. (A) Schematic of the experimental setup. Four RF signals were generated. One signal was connected to an oscilloscope for monitoring. Two signals were connected to RFPAs to drive the SGBT antennae and the last one was connected to the home-built power and phase meter as a reference signal. The forward coupled outputs of the directional couplers were fed to the power and phase meter. The signal generator, the power and phase meter and the laptop computer communicate with each other through network connections. (B) Setup used for the RF heating experiments comprising: (a) water cooling system, (b) clock distributor, (c) RF signal generator, (d) home-built RF power amplifiers, (e) penetration panel, (f) directional couplers, (g) oscilloscope, (h) network router, (i) home-built power and phase meter, (j) laptop for interacting with the equipment. The MR scanner and the fiber optic thermometer are not shown in the photo.

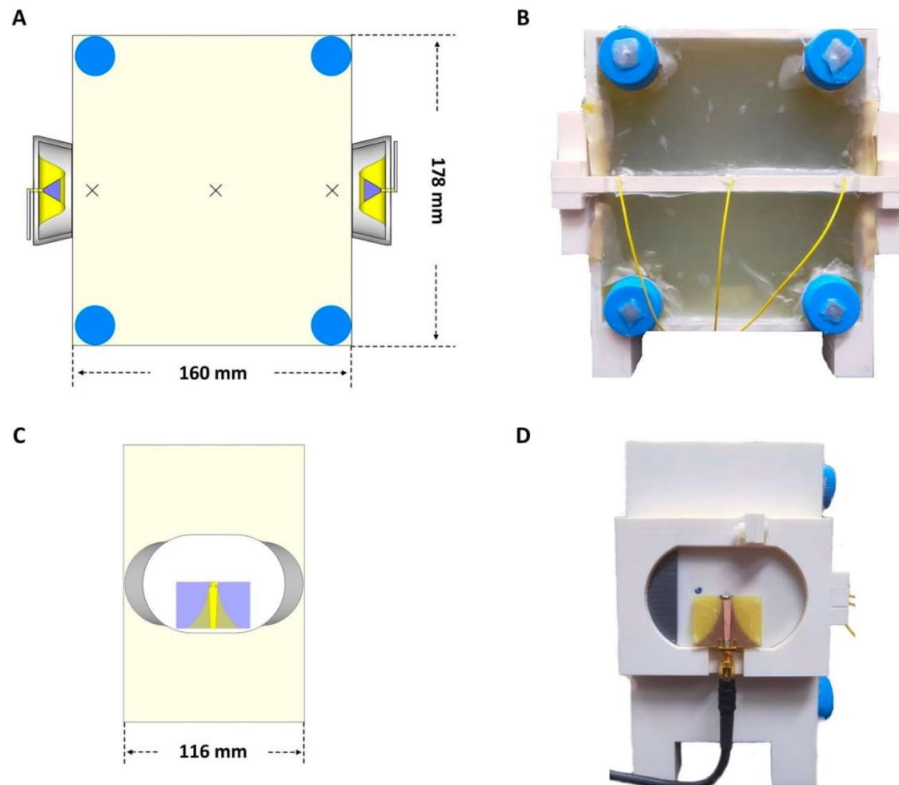


Figure 10. (A) The schematic of the front view (a transversal slice in the middle of the phantom) of the rectangular agarose phantom. The cross marks indicate the positions of fiber optic temperature sensors. (B) Front view of the rectangular agarose phantom: the yellow wires are fiber optic temperature sensors which were placed into the center of the phantom; the four blue tubes were filled with vegetable oil used as references for MR thermometry; the two antennae were installed opposing each other at two sides of the phantom. (C) The schematic of the lateral view of the phantom. (D) Lateral view of the phantom that shows one of the SGBT antennae. The printed circuit board on the antenna block is a balanced to unbalanced (balun) transformer for matching a 50 Ohm coaxial cable to the antenna port and vice-versa. A microstrip exponential taper was used to combine the balun with impedance matching.

Table 3. Dielectric properties of the phantom at frequencies of 300 MHz, 400 MHz and 500 MHz.

	300 MHz	400 MHz	500 MHz
Relative permittivity, ϵ_r	56.2091	54.3220	49.4599
Conductivity, σ (S/m)	0.1834	0.2535	0.3651

4.6. Dual Channel RF Heating

The RF heating experiment was extended to two channels to demonstrate the synthesizer's ability to accurately adjust the phase of the RF signals. Channel two was added to the setup of the single channel heating experiment. Both channels were set to generate 400 MHz RF signals. Each channel was connected to a home-built RF power amplifier. The outputs from the RFPAs were fed to two SGBT antennae through directional couplers and the feed through penetration panel. By adjusting the amplitude settings of the synthesizer, the RF power level at the feeding ports of the SGBT antennae was set to 42.5 dBm (17.78 W) for each channel. The antennae were positioned opposite to each other

and applied to the same phantom used for the single channel experiments (Figure 10). The phantom was placed in the isocenter of the 7.0 T MR scanner. The experimental setup is illustrated in Figure 9. The two forward coupled outputs from the directional couplers were connected to a home-built power and phase meter to monitor the power level and phase relationship of the two channels. Three heating experiments were conducted using three phase shifts ($\phi = 0^\circ$, $\phi = 90^\circ$ and $\phi = 180^\circ$) added to channel one. RF heating ($P_{in} = 17.78$ W at the feeding port of the SGBT antenna, $t = 10$ min) was applied for each phase setting. For benchmarking experimental data with numerical simulations, temperature simulations with the same frequency, power and phase settings were performed in CST Microwave Studio 2018. The CST thermal transient solver was adopted with a hexahedral mesh type. The maximum mesh size was set to $2.0 \times 2.0 \times 2.0$ mm³, which is sufficient for the problem that decreasing the maximum mesh size by 10% does not yield substantial changes (<0.01%) in the simulation results. We used open boundary condition with the ambient temperature 20 °C set at the boundary as constant temperature. The simulation started with an initial temperature of 20 °C. MRT using the PRFS approach (TR = 99 ms, TE1 = 2.73 ms, TE2 = 6.71 ms, voxel size = $1 \times 1 \times 5$ mm³) at 297.2 MHz was conducted before and after the RF heating. Vegetable oil was used as a reference to correct the magnetic field drift. Fiber optic temperature sensors were used to validate the MRT results. The RF heating experiments were repeated with the signal generator replaced by a commercial high-end 4-channel arbitrary waveform generator (M8190A, Keysight) for comparison.

5. Conclusions

This work demonstrates the development, implementation, evaluation, validation and application of a 32-channel RF signal generator system tailored for RF-induced heating. The RF heating experiments demonstrated the efficacy of the RF signal generator, which is competitive with high-end commercial signal generators equipped with a lower number of RF channels. The large number of coherent RF channels, wide frequency range, accurate phase shift, and highly flexible configurations provided by the signal generator form a technological basis for future hyperthermia applications driven by ThermalMR.

Supplementary Materials: The following are available online at <http://www.mdpi.com/2072-6694/12/7/1720/s1>, Video S1: Live adjustments of the frequency of the RF signals. Video S2: The continuous adjustments of the signal's amplitude. Video S3: Live adjustments of the phase of the RF signals. Video S4: Frequency switching time measurements. Video S5: Amplitude settling time measurements. Video S6: Phase settling time measurements.

Author Contributions: Conceptualization, H.H., L.W. and T.N.; methodology, H.H.; hardware, H.H.; software, H.H.; validation, H.H., T.W.E., E.K.; investigation, H.H.; resources, S.W., W.H., E.G. and T.N.; writing—original draft preparation, H.H.; writing—review and editing, H.H., T.W.E., S.W., E.K., L.W., W.H., E.G. and T.N.; visualization, H.H., T.W.E., E.K. and T.N.; supervision, T.N.; project administration, H.H., T.N.; funding acquisition, T.N. All authors have read and agreed to the published version of the manuscript.

Funding: This project has received funding from the European Research Council (ERC) under the European Union's Horizon 2020 research and innovation programme under grant agreement No. 743077 (ThermalMR).

Acknowledgments: We wish to acknowledge Jens Lehmann (IHP—Leibniz-Institut für innovative Mikroelektronik, Frankfurt (Oder), Germany) and Reiner Seemann (Physikalische Technische Bundesanstalt, Berlin, Germany) for technical and other assistance. We further wish to acknowledge Marcelo Vicente (Stanford University, CA, USA) for support on the IPMC card. This project has received funding from the European Research Council (ERC) under the European Union's Horizon 2020 research and innovation programme under grant agreement No. 743077 (ThermalMR).

Conflicts of Interest: Thoralf Niendorf is founder and CEO of MRI.TOOLS GmbH. Shuailin Wang is an employee of Beijing Deepvision Technology Co., Ltd.

References

1. Overgaard, J.; Bentzen, S.M.; Gonzalez Gonzalez, D.; Hulshof, M.C.C.M.; Arcangeli, G.; Dahl, O.; Mella, O. Randomised trial of hyperthermia as adjuvant to radiotherapy for recurrent or metastatic malignant melanoma. *Lancet* **1995**, *345*, 540–543. [[CrossRef](#)]
2. Horsman, M.R.; Overgaard, J. Hyperthermia: A potent enhancer of radiotherapy. *Clin. Oncol. (R Coll. Radiol.)* **2007**, *19*, 418–426. [[CrossRef](#)] [[PubMed](#)]

3. Lee Titsworth, W.; Murad, G.J.A.; Hoh, B.L.; Rahman, M. Fighting fire with fire: The revival of thermotherapy for gliomas. *Anticancer Res.* **2014**, *34*, 565–574.
4. Leopold, K.A.; Dewhirst, M.; Samulski, T.; Harrelson, J.; Tucker, J.A.; George, S.L.; Dodge, R.K.; Grant, W.; Clegg, S.; Prosnitz, L.R.; et al. Relationships among tumor temperature, treatment time, and histopathological outcome using preoperative hyperthermia with radiation in soft tissue sarcomas. *Int. J. Radiat. Oncol. Biol. Phys.* **1992**, *22*, 989–998. [[CrossRef](#)]
5. Kapp, D.S. Efficacy of adjuvant hyperthermia in the treatment of superficial recurrent breast cancer: Confirmation and future directions. *Int. J. Radiat. Oncol. Biol. Phys.* **1996**, *35*, 1117–1121. [[CrossRef](#)]
6. Vernon, C.C.; Hand, J.W.; Field, S.B.; Machin, D.; Whaley, J.B.; van der Zee, J.; van Putten, W.L.; van Rhoon, G.C.; van Dijk, J.D.; González González, D.; et al. Radiotherapy with or without hyperthermia in the treatment of superficial localized breast cancer: Results from five randomized controlled trials. International Collaborative Hyperthermia Group. *Int. J. Radiat. Oncol. Biol. Phys.* **1996**, *35*, 731–744. [[CrossRef](#)]
7. Hildebrandt, B. The cellular and molecular basis of hyperthermia. *Crit. Rev. Oncol./Hematol.* **2002**, *43*, 33–56. [[CrossRef](#)]
8. Oldenborg, S.; van Os, R.; Oei, B.; Poortmans, P. Impact of Technique and Schedule of Reirradiation Plus Hyperthermia on Outcome after Surgery for Patients with Recurrent Breast Cancer. *Cancers* **2019**, *11*. [[CrossRef](#)]
9. Adibzadeh, F.; Sumser, K.; Curto, S.; Yeo, D.T.B.; Shishegar, A.A.; Paulides, M.M. Systematic review of pre-clinical and clinical devices for magnetic resonance-guided radiofrequency hyperthermia. *Int. J. Hyperther.* **2020**, *37*, 15–27. [[CrossRef](#)]
10. Stauffer, P.R. Evolving technology for thermal therapy of cancer. *Int. J. Hyperther.* **2005**, *21*, 731–744. [[CrossRef](#)]
11. Trefná, H.D.; Crezee, H.; Schmidt, M.; Marder, D.; Lamprecht, U.; Ehmann, M.; Hartmann, J.; Nadobny, J.; Gellermann, J.; van Holthe, N.; et al. Quality assurance guidelines for superficial hyperthermia clinical trials: I. Clinical requirements. *Int. J. Hyperther.* **2017**, *33*, 471–482. [[CrossRef](#)] [[PubMed](#)]
12. Paulides, M.M.; Stauffer, P.R.; Neufeld, E.; Maccarini, P.F.; Kyriakou, A.; Canters, R.A.M.; Diederich, C.J.; Bakker, J.F.; van Rhoon, G.C. Simulation techniques in hyperthermia treatment planning. *Int. J. Hyperther.* **2013**, *29*, 346–357. [[CrossRef](#)] [[PubMed](#)]
13. Kok, H.P.; Wust, P.; Stauffer, P.R.; Bardati, F.; van Rhoon, G.C.; Crezee, J. Current state of the art of regional hyperthermia treatment planning: A review. *Radiat. Oncol.* **2015**, *10*, 1–14. [[CrossRef](#)] [[PubMed](#)]
14. Curto, S.; Aklan, B.; Mulder, T.; Mils, O.; Schmidt, M.; Lamprecht, U.; Peller, M.; Wessalowski, R.; Lindner, L.H.; Fietkau, R.; et al. Quantitative, Multi-institutional Evaluation of MR Thermometry Accuracy for Deep-Pelvic MR-Hyperthermia Systems Operating in Multi-vendor MR-systems Using a New Anthropomorphic Phantom. *Cancers* **2019**, *11*. [[CrossRef](#)] [[PubMed](#)]
15. Schooneveldt, G.; Dobšiček Trefná, H.; Persson, M.; de Reijke, T.M.; Blomgren, K.; Kok, H.P.; Crezee, H. Hyperthermia Treatment Planning Including Convective Flow in Cerebrospinal Fluid for Brain Tumour Hyperthermia Treatment Using a Novel Dedicated Paediatric Brain Applicator. *Cancers* **2019**, *11*. [[CrossRef](#)]
16. Kok, H.P.; Groen, J.; Bakker, A.; Crezee, J. Modelling Curved Contact Flexible Microstrip Applicators for Patient-Specific Superficial Hyperthermia Treatment Planning. *Cancers* **2020**, *12*, 656. [[CrossRef](#)]
17. Oberacker, E.; Kuehne, A.; Oezerdem, C.; Nadobny, J.; Weihrauch, M.; Beck, M.; Zschaek, S.; Diesch, C.; Eigentler, T.W.; Waiczies, H.; et al. Radiofrequency applicator concepts for thermal magnetic resonance of brain tumors at 297 MHz (7.0 Tesla). *Int. J. Hyperther.* **2020**, *37*, 549–563. [[CrossRef](#)]
18. Niendorf, T.; Oezerdem, C.; Ji, Y.; Oberacker, E.; Kuehne, A.; Waiczies, H.; Winter, L. Radiative RF antenna arrays for cardiac, brain and thermal magnetic resonance at ultrahigh and extreme magnetic field strengths: Concepts, electromagnetic field simulations and applications. In Proceedings of the 2017 International Conference on Electromagnetics in Advanced Applications (ICEAA), Verona, Italy, 11–15 September 2017; pp. 1567–1570, ISBN 978-1-5090-4451-1.
19. Winter, L.; Oezerdem, C.; Hoffmann, W.; van de Lindt, T.; Periquito, J.; Ji, Y.; Ghadjar, P.; Budach, V.; Wust, P.; Niendorf, T. Thermal magnetic resonance: Physics considerations and electromagnetic field simulations up to 23.5 Tesla (1GHz). *Radiat. Oncol.* **2015**, *10*, 1–12. [[CrossRef](#)]
20. Winter, L.; Oezerdem, C.; Hoffmann, W.; Santoro, D.; Müller, A.; Waiczies, H.; Seemann, R.; Graessl, A.; Wust, P.; Niendorf, T. Design and evaluation of a hybrid radiofrequency applicator for magnetic resonance imaging and RF induced hyperthermia: Electromagnetic field simulations up to 14.0 Tesla and proof-of-concept at 7.0 Tesla. *PLoS ONE* **2013**, *8*, e61661. [[CrossRef](#)]

21. Winter, L.; Niendorf, T. Electrodynamics and radiofrequency antenna concepts for human magnetic resonance at 23.5 T (1 GHz) and beyond. *MAGMA* **2016**, *29*, 641–656. [[CrossRef](#)]
22. Oberacker, E.; Kuehne, A.; Nadobny, J.; Zschaek, S.; Weihrauch, M.; Waiczies, H.; Ghadjar, P.; Wust, P.; Niendorf, T.; Winter, L. Radiofrequency applicator concepts for simultaneous MR imaging and hyperthermia treatment of glioblastoma multiforme. *Curr. Directions Biomed. Eng.* **2017**, *3*. [[CrossRef](#)]
23. Eigentler, T.W.; Winter, L.; Han, H.; Oberacker, E.; Kuehne, A.; Waiczies, H.; Schmitter, S.; Boehmert, L.; Prinz, C.; Trefna, H.D.; et al. Wideband Self-Grounded Bow-Tie Antenna for Thermal MR. *NMR Biomed.* **2020**, *41*, e4274. [[CrossRef](#)] [[PubMed](#)]
24. Kuehne, A.; Oberacker, E.; Waiczies, H.; Niendorf, T. Solving the Time- and Frequency-Multiplexed Problem of Constrained Radiofrequency Induced Hyperthermia. *Cancers* **2020**, *12*. [[CrossRef](#)] [[PubMed](#)]
25. Ji, Y.; Hoffmann, W.; Pham, M.; Dunn, A.E.; Han, H.; Özerdem, C.; Waiczies, H.; Rohloff, M.; Endemann, B.; Boyer, C.; et al. High peak and high average radiofrequency power transmit/receive switch for thermal magnetic resonance. *Magn. Reson. Med.* **2018**, *80*, 2246–2255. [[CrossRef](#)]
26. Ji, Y.; Winter, L.; Navarro, L.; Ku, M.-C.; Periquito, J.S.; Pham, M.; Hoffmann, W.; Theune, L.E.; Calderón, M.; Niendorf, T. Controlled Release of Therapeutics from Thermo-responsive Nanogels: A Thermal Magnetic Resonance Feasibility Study. *Cancers* **2020**, *12*. [[CrossRef](#)]
27. Young, I.R.; Hand, J.W.; Oatridge, A.; Prior, M.V. Modeling and observation of temperature changes in vivo using MRI. *Magn. Reson. Med.* **1994**, *32*, 358–369. [[CrossRef](#)]
28. Gellermann, J.; Włodarczyk, W.; Feussner, A.; Föhling, H.; Nadobny, J.; Hildebrandt, B.; Felix, R.; Wust, P. Methods and potentials of magnetic resonance imaging for monitoring radiofrequency hyperthermia in a hybrid system. *Int. J. Hyperth.* **2005**, *21*, 497–513. [[CrossRef](#)]
29. Winter, L.; Oberacker, E.; Paul, K.; Ji, Y.; Oezerdem, C.; Ghadjar, P.; Thieme, A.; Budach, V.; Wust, P.; Niendorf, T. Magnetic resonance thermometry: Methodology, pitfalls and practical solutions. *Int. J. Hyperth.* **2016**, *32*, 63–75. [[CrossRef](#)]
30. Guérin, B.; Villena, J.F.; Polimeridis, A.G.; Adalsteinsson, E.; Daniel, L.; White, J.K.; Rosen, B.R.; Wald, L.L. Computation of ultimate SAR amplification factors for radiofrequency hyperthermia in non-uniform body models: Impact of frequency and tumour location. *Int. J. Hyperth.* **2018**, *34*, 87–100. [[CrossRef](#)]
31. Togni, P.; Rijnen, Z.; Numan, W.C.M.; Verhaart, R.F.; Bakker, J.F.; van Rhoon, G.C.; Paulides, M.M. Electromagnetic redesign of the HYPERcollar applicator: Toward improved deep local head-and-neck hyperthermia. *Phys. Med. Biol.* **2013**, *58*, 5997–6009. [[CrossRef](#)]
32. Paulides, M.M.; Bakker, J.F.; Neufeld, E.; van der Zee, J.; Jansen, P.P.; Levendag, P.C.; van Rhoon, G.C. The HYPERcollar: A novel applicator for hyperthermia in the head and neck. *Int. J. Hyperth.* **2007**, *23*, 567–576. [[CrossRef](#)] [[PubMed](#)]
33. Takook, P.; Persson, M.; Trefna, H.D. Performance Evaluation of Hyperthermia Applicators to Heat Deep-Seated Brain Tumors. *IEEE J. Electromagn. RF Microw. Med. Biol.* **2018**, *2*, 18–24. [[CrossRef](#)]
34. Paulides, M.M.; Vossen, S.H.J.A.; Zwamborn, A.P.M.; van Rhoon, G.C. Theoretical investigation into the feasibility to deposit RF energy centrally in the head-and-neck region. *Int. J. Radiat. Oncol. Biol. Phys.* **2005**, *63*, 634–642. [[CrossRef](#)] [[PubMed](#)]
35. Paulsen, K.D.; Geimer, S.; Tang, J.W.; Boyse, W.E. Optimization of pelvic heating rate distributions with electromagnetic phased arrays. *Int. J. Hyperth.* **1999**, *15*, 157–186.
36. Seebass, M.; Beck, R.; Gellermann, J.; Nadobny, J.; Wust, P. Electromagnetic phased arrays for regional hyperthermia: Optimal frequency and antenna arrangement. *Int. J. Hyperth.* **2001**, *17*, 321–336. [[CrossRef](#)]
37. Takook, P.; Dobsicek, Trefna, H.; Zeng, X.; Fhager, A.; Persson, M. A Computational Study Using Time Reversal Focusing for Hyperthermia Treatment Planning. *PIER B* **2017**, *73*, 117–130. [[CrossRef](#)]
38. Zastrow, E.; Hagness, S.C.; van Veen, B.D.; Medow, J.E. Time-multiplexed beamforming for noninvasive microwave hyperthermia treatment. *IEEE Trans. Biomed. Eng.* **2011**, *58*, 1574–1584. [[CrossRef](#)]
39. Kok, H.P.; van Stam, G.; Bel, A.; Crezee, J. A mixed frequency approach to optimize locoregional RF hyperthermia. In Proceedings of the 2015 European Microwave Conference (EuMC 2015), Paris, France, 7–10 September 2015; IEEE: Piscataway, NJ, USA; pp. 773–776, ISBN 978-2-8748-7039-2.
40. Bellizzi, G.G.; Crocco, L.; Battaglia, G.M.; Isernia, T. Multi-Frequency Constrained SAR Focusing for Patient Specific Hyperthermia Treatment. *IEEE J. Electromagn. RF Microw. Med. Biol.* **2017**, *1*, 74–80. [[CrossRef](#)]

41. Bakker, J.F.; Paulides, M.M.; Westra, A.H.; Schippers, H.; van Rhooon, G.C. Design and test of a 434 MHz multi-channel amplifier system for targeted hyperthermia applicators. *Int. J. Hyperth.* **2010**, *26*, 158–170. [CrossRef]
42. Wust, P.; Föhling, H.; Helzel, T.; Kniephoff, M.; Wlodarczyk, W.; Mönich, G.; Felix, R. Design and test of a new multi-amplifier system with phase and amplitude control. *Int. J. Hyperth.* **1998**, *14*, 459–477. [CrossRef]
43. Schneider, C.J.; Kuijter, J.P.; Colussi, L.C.; Schepp, C.J.; van Dijk, J.D. Performance evaluation of annular arrays in practice: The measurement of phase and amplitude patterns of radio-frequency deep body applicators. *Med. Phys.* **1995**, *22*, 755–765. [CrossRef] [PubMed]
44. Trefná, H.D.; Togni, P.; Shiee, R.; Vrba, J.; Persson, M. Design of a wideband multi-channel system for time reversal hyperthermia. *Int. J. Hyperth.* **2012**, *28*, 175–183. [CrossRef] [PubMed]
45. Turner, P.F.; Tumeh, A.; Schaefermeyer, T. BSD-2000 approach for deep local and regional hyperthermia: Physics and technology. *Strahlenther. Onkol.* **1989**, *165*, 738–741.
46. Wust, P.; Föhling, H.; Wlodarczyk, W.; Seebass, M.; Gellermann, J.; Deuflhard, P.; Nadobny, J. Antenna arrays in the SIGMA-eye applicator: Interactions and transforming networks. *Med. Phys.* **2001**, *28*, 1793–1805. [CrossRef]
47. Curto, S.; Garcia-Miquel, A.; Suh, M.; Vidal, N.; Lopez-Villegas, J.M.; Prakash, P. Design and characterisation of a phased antenna array for intact breast hyperthermia. *Int. J. Hyperth.* **2018**, *34*, 250–260. [CrossRef] [PubMed]
48. AXIe Consortium. AXIe Specifications. Available online: <http://axistandard.org/axiespecifications.html> (accessed on 7 January 2020).
49. Vicente, M.; Gorski, T.; Svetek, A.; Tikalsky, J.; Fobes, R.; Dasu, S.; Smith, W. Next generation ATCA control infrastructure for the CMS phase-2 upgrades. In Proceedings of the Topical Workshop on Electronics for Particle Physics—PoS(TWEPP-17), Santa Cruz, CA, USA, 11–14 September 2017; Veneziano, S., Farthouat, P., Hall, G., Kluge, A., Rivetti, A., Smith, W., Marchioro, A., Hahn, F., de La Taille, C., Christiansen, J., et al., Eds.; Sissa Medialab: Trieste, Italy, 2017; p. 102.
50. Analog Devices Inc. ADL5330: Data Sheet. Available online: <https://www.analog.com/media/en/technical-documentation/data-sheets/ADL5330.pdf> (accessed on 7 January 2020).
51. Analog Devices Inc. HMC245A: GaAs MMIC SP3T Non-REFLECTIVE SWITCH, DC—3.5 GHz. Available online: <https://www.analog.com/media/en/technical-documentation/data-sheets/hmc245a.pdf> (accessed on 7 January 2020).
52. Stakhursky, V.L.; Arabe, O.; Cheng, K.-S.; Macfall, J.; Maccarini, P.; Craciunescu, O.; Dewhurst, M.; Stauffer, P.; Das, S.K. Real-time MRI-guided hyperthermia treatment using a fast adaptive algorithm. *Phys. Med. Biol.* **2009**, *54*, 2131–2145. [CrossRef]
53. Wust, P.; Weihrauch, M. Hyperthermia classic commentary: ‘Simulation studies promote technological development of radiofrequency phased array hyperthermia’ by Peter Wust et al., *International Journal of Hyperthermia* 1996; *12*: 477–494. *Int. J. Hyperth.* **2009**, *25*, 529–532. [CrossRef]
54. Pulsar Microwave Corporation. Digital Controlled Phase Shifter: Model: DST-10-480/1S. Available online: https://www.pulsarmicrowave.com/product/digital_phase_shifter/DST-10-480-1S (accessed on 7 January 2020).
55. Orzada, S.; Solbach, K.; Gratz, M.; Brunheim, S.; Fiedler, T.M.; Johst, S.; Bitz, A.K.; Shooshtary, S.; Abuelhaija, A.; Voelker, M.N.; et al. A 32-channel parallel transmit system add-on for 7T MRI. *PLoS ONE* **2019**, *14*, e0222452. [CrossRef]
56. Analog Devices Inc. Fundamentals of Direct Digital Synthesis (DDS). Available online: <https://www.analog.com/media/en/training-seminars/tutorials/MT-085.pdf> (accessed on 7 January 2020).
57. Dooley, W.C.; Vargas, H.I.; Fenn, A.J.; Tomaselli, M.B.; Harness, J.K. Focused microwave thermotherapy for preoperative treatment of invasive breast cancer: A review of clinical studies. *Ann. Surg. Oncol.* **2010**, *17*, 1076–1093. [CrossRef]
58. OpenSUSE Contributors. openSUSE Leap: 15.1. Available online: https://software.opensuse.org/distribution/s/leap/15_1 (accessed on 7 January 2020).
59. Han, H.; Moritz, R.; Oberacker, E.; Waiczies, H.; Niendorf, T.; Winter, L. Open Source 3D Multipurpose Measurement System with Submillimetre Fidelity and First Application in Magnetic Resonance. *Sci. Rep.* **2017**, *7*, 1–12. [CrossRef]

60. Lontas, C.A. Alternating projections of auxiliary vector fields for electric field optimization in temperature-guided hyperthermia. In Proceedings of the 2019 13th European Conference on Antennas and Propagation (EuCAP), Krakow, Poland, 31 March–5 April 2019; pp. 1–5.
61. Duan, Q.; Duyn, J.H.; Gudino, N.; de Zwart, J.A.; van Gelderen, P.; Sodickson, D.K.; Brown, R. Characterization of a dielectric phantom for high-field magnetic resonance imaging applications. *Med. Phys.* **2014**, *41*, 102303. [[CrossRef](#)] [[PubMed](#)]
62. Depoorter, J.; Dewagter, C.; Dedeene, Y.; Thomsen, C.; Stahlberg, F.; Achten, E. The Proton-Resonance-Frequency-Shift Method Compared with Molecular Diffusion for Quantitative Measurement of Two-Dimensional Time-Dependent Temperature Distribution in a Phantom. *J. Magn. Reson. Ser. B* **1994**, *103*, 234–241. [[CrossRef](#)]
63. Rieke, V.; Butts Pauly, K. MR thermometry. *J. Magn. Reson. Imaging* **2008**, *27*, 376–390. [[CrossRef](#)]
64. Kuroda, K.; Oshio, K.; Chung, A.H.; Hynynen, K.; Jolesz, F.A. Temperature mapping using the water proton chemical shift: A chemical shift selective phase mapping method. *Magn. Reson. Med.* **1997**, *38*, 845–851. [[CrossRef](#)] [[PubMed](#)]



© 2020 by the authors. Licensee MDPI, Basel, Switzerland. This article is an open access article distributed under the terms and conditions of the Creative Commons Attribution (CC BY) license (<http://creativecommons.org/licenses/by/4.0/>).

3 Discussion

The work of this thesis demonstrates the feasibility of a high-density RF array based on dipole antennas for body MRI and Thermal MR. It provides the design, application, and validation of a narrowband as well as a broadband antenna concept based on the SGBT antenna building block. The optimized antenna designs have a small footprint and facilitate a low coupling between the channels. This allows a high channel count, which supports a high of freedom for (i) B_1^+ shaping, for (ii) SAR management, and for (iii) focal point quality improvement for thermal interventions, as well as (iv) for spreading the superficial SAR. The broadband SGBT antenna building block offers the unique opportunity to choose freely the intervention frequency for targeted heating. The 32-channel signal generator is a key element in the Thermal MR setup and provides the thermal intervention vector and matrix. Both, the broadband SGBT and the signal generator allows investigations into time-multiplexed beamforming⁴³, a mixed frequency⁴⁴, and a time- and frequency-multiplexed⁴⁵ signal transmission to the subject.

3.1 Self-Grounded Bow-Tie Antenna

The SGBT antenna type was first demonstrated in the field of telecommunications as an extension of the Bow-Tie dipole, operating at a frequency range of approximately 2-15 GHz.⁵³ The antenna design, seagull-over-sea configuration (tilted Bow-Tie dipole over ground), shows an improved main lobe directivity due to its backplane, lowering in our case the unwanted and unproductive RF antenna array radiation. To reduce the antenna size, the seagull-over-sea was adapted with a self-grounded backplane formed by the backwards bending of the Bow-Tie dipole outskirts.⁵³ Compared to other dipole antennas such as the lambda-half dipole or the fractionated dipole, the introduced SGBT antenna designs have lower back radiation (Figure 4).

3.1 Self-Grounded Bow-Tie Antenna

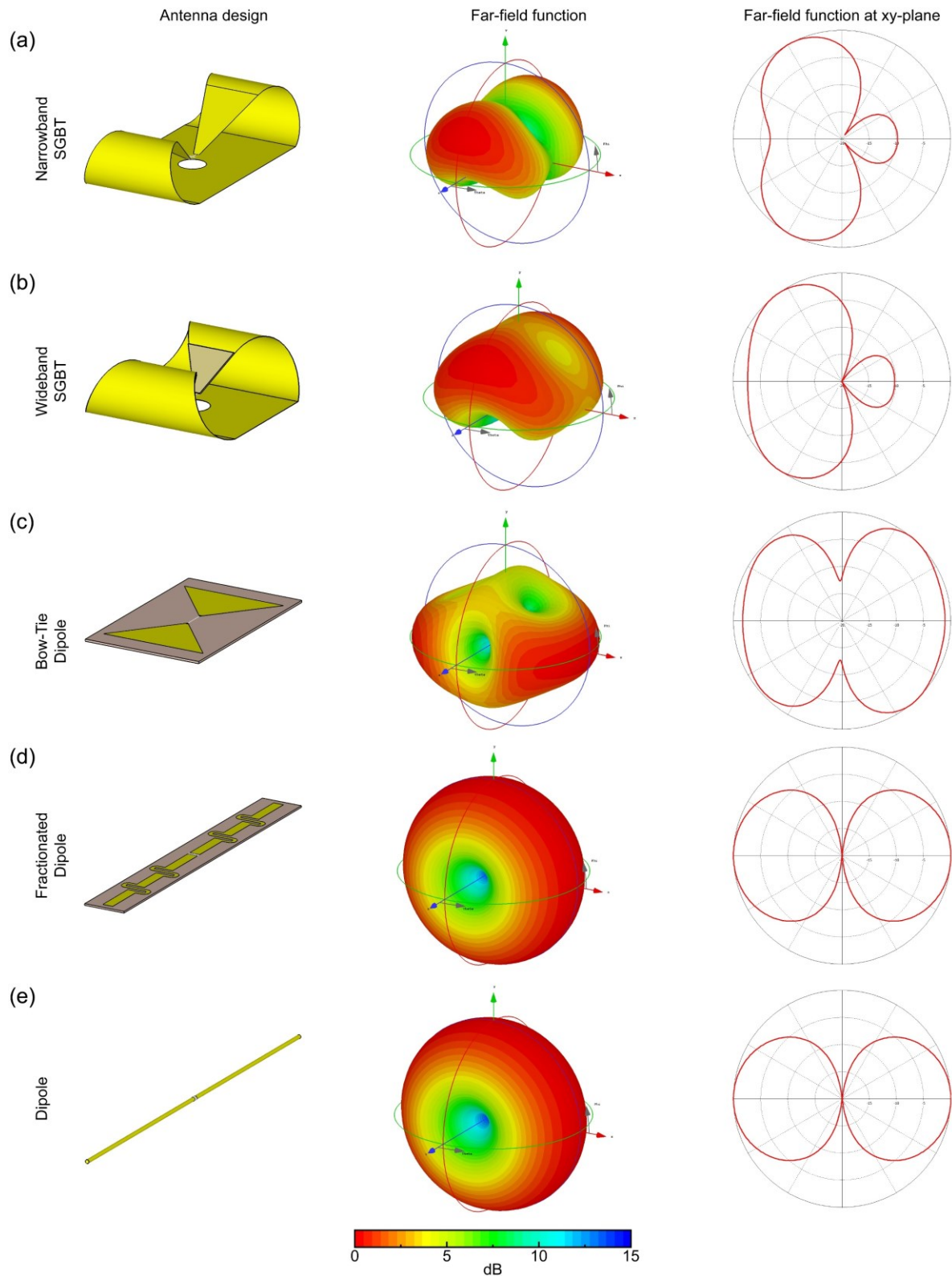


Figure 4: Synopsis of radiation pattern of dipole antennas with the 3D far-field function and a 2D far-field function at the xy-plane. The antennas are (a) the narrowband Self-Grounded Bow-Tie antenna, (b) the broadband Self-Grounded Bow-Tie antenna, (c) the Bow-Tie antenna, (d) the fractionated dipole, and (e) a 500 mm dipole antenna.

The applicability of this antenna type for MRI based applications requires a redesign and optimization of the antenna's geometry to lower frequencies (e.g. 297.2 MHz and approximately 280 MHz to 600 MHz). It was shown that a dielectrically filled housing further reduces the size of the antenna.^{52,54} Utilizing D₂O as dielectric with an $\epsilon_r \approx 80$ proves useful due to the lack of single proton nuclei in the molecule. Hence, no NMR signal is detectable in this compartment in an MRI acquisition.¹³⁴ Furthermore, D₂O is a low-loss material, limiting the material losses close to the conductive elements of the antenna system. Other low-loss materials are for example ceramics, which exhibit an increased ϵ_r . Prevailing practices establish the successful use of ceramic materials for EMF shaping through dielectric pads or within a Single-Side Adapted Dipole antenna configuration.^{86,135–137} However, the high density of ceramics increases the weight of the antenna system, thus incrementally increasing the pressure on the human body and therefore impairing a comfortable exam or intervention. Furthermore, a high ϵ_r for a reduced antenna size results in a mismatch in the dielectric constant of tissue at the observed frequencies. This mismatch results in increasing reflections of the EMF propagating between the subject and the antenna system.⁸⁶

Reducing the reflections of the propagating EMF between the antenna element and the phantom or subject is of high importance for the efficiency of the RF system. In the case of an antenna building block design, the reduction of the number of dielectric gaps – respectively dielectric material transitions – increases the efficiency. Introducing a dielectric pad between the antenna building blocks and the subject was shown to be feasible in an MRI environment. Comparing the numerical simulation results of the 32-channel narrowband SGBT array with dielectric pad to the same RF antenna array without a dielectric pad revealed, that the B_1^+ in the heart is reduced by 45% for Ella and 39% for Duke. This reduction is given for an optimized B_1^+ distribution for all models respectively; numerical limitations of the proposed global optimization process need to be considered in the comparison. Figure 5 shows the reduced transmission of the E-field and the reduced B_1^+ penetration depth for the tissue mimicking phantom experiment when no dielectric pad is installed. The material for the phantom in this study is equivalent to the phantom used in Section 2.1 ($\epsilon_r = 47.7$, $\sigma = 0,475$ S/m). The power loss calculation supports the efficiency reduction when no dielectric pad is used. With the array configuration and remaining material specifications constant, the absorbed power drops for Ella from 61% to 11% and for Duke from 71% to 15% with no dielectric pad used. The sum of the material and lumped element losses on the other hand increase from 27% to 73% for Ella and from 21% to 68% for Duke, whereas the losses for the lumped elements reveal a major increase of 34% for Ella and 32% for Duke. These results represent mean loss calculations for the whole antenna array, but with only one antenna powered simultaneously.

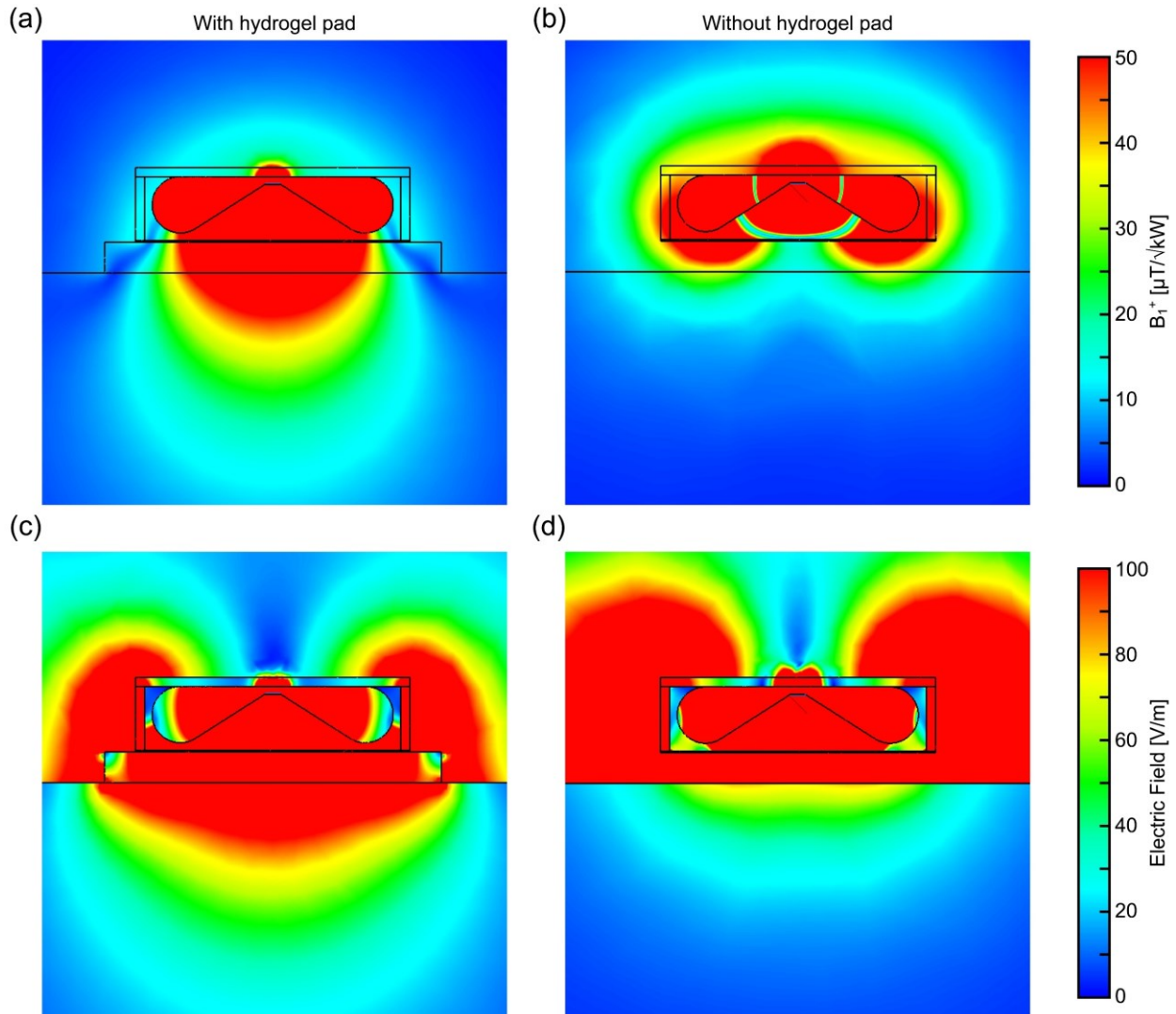


Figure 5: B_1^+ field distribution of the introduced narrowband Self-Grounded Bow-Tie antenna building block (a) with and (b) without hydrogel pad. The E-field distribution of the antenna system (c) with (d) without hydrogel pad. The antennas were tuned and matched to 297.2 MHz in this visualization.

Similar to the dielectric filled housing, the dielectric pad contains a low-loss material with a flexible design to adapt to the various shapes of the human body. The dielectric pad was manufactured using deionized H_2O ^{54,57} or hydrogel⁵² based on H_2O . The use of H_2O resulted in an MR signal from these compounds, but it did not impair the image quality. Nevertheless, signal of the dielectric pad can be avoided using D_2O . Dielectric pads are commonly used in thermal interventions and hyperthermia applications, but its application in an MRI environment is not widely spread.^{36,83,138} The reason for that might be the lack of need (e.g. lack of dipole antenna building blocks) and safety concerns based on potential leakage. To overcome the safety concerns, low-loss hydrogel pads offer a mechanically stable, but still flexible alternative.¹³⁹ The hydrogel is a dedicated low-loss material and

reported losses could be reproduced ($\tan(\delta) \approx 0.12$ at 300 MHz).⁵² Nevertheless, the losses of water ($\tan(\delta) \approx 0.015$ at 300 MHz) provided by the CST Microwave Studio 2020 database for the Debye water model are considerably lower. The effect of the elevated losses can be explored by the power loss calculation of the 32-channel SGBT array. In the case of the hydrogel placed between the antenna array and the subject, the material losses are 26% for Ella and 20% for Duke. In the case of a water pad, the measure was found to be reduced to 9% for Ella and 7% for Duke. This result emphasises the importance of correct loss estimations for EMF simulations. In this comparison, the antenna positions and all other material specifications of the 32-channel configuration was unchanged and the loss of all channels were averaged for a single channel excitation.

3.2 Narrowband Antenna Application for Cardiovascular MRI

The application of a narrowband antenna concept commonly requires some method of tuning and matching. Either the antenna design can be geometrically adapted to be tuned to the required frequency and matched to 50 Ω input impedance, or a tuning and matching circuit is required. This circuit design and the belonging elements (e.g., capacity, inductivity) are functions of the antennas' intrinsic complex impedance. In case of the introduced narrowband antenna design, a series capacitor and a parallel inductor was realized as circuit network. This network, like the antenna design itself, can be represented by an S-matrix, where the combination of the antenna S-matrix and the circuit S-matrix are optimized resulting in minimum reflection (Section 1.6.1).

The antenna optimization process was accomplished with the single antenna placed centrally above the heart of the human voxel models Ella and Duke. A parameter sweep was implemented with varying the antenna width (w_a), length (l_a), and the aperture angle (α) to increase the B_1^+ at the lateral wall of the voxel models. It was found that an increased l_a is beneficial for a high B_1^+ penetration depth. For a design decision the ratio of the B_1^+ to the footprint size was used in the numerical simulation study. The results on the introduced ratio suggested a small w_a as it scales linear with the antenna footprint, but the reduction of nearest neighbour coupling revealed a reciprocal approach. With the introduced antenna design (156 g at 89.3x48.0x25.8 mm³), a trade-off between the B_1^+ to footprint ratio and the decoupling performance was achieved. The antenna design optimum is based on a rather flat maximum (Figure 3, Section 2.1) where in the case of $w_a = 40$ mm a 1% reduction of the B_1^+ to footprint ratio is observed for a broad design parameter combination. This flat optimum underline that manufacturing inaccuracies are not impairing the antennas performance.

Based on the arrangement of the channels in an RF antenna array, a optimization is required to achieve a constructive interference of the B_1^+ field within the heart. This optimization is performed using a CTX shimming approach to avoid subject dependent adaptation and time-consuming preparation scans. The CTX approach allows a hardware implementation of the phase settings in the signal chain of the 7.0 T scanner. To cover a broad range of anatomies, the ROI was virtually enlarged beyond the actual myocardium. Furthermore, mixed shim approach was used, where the human voxel models Ella and Duke were combined in a single data set. The scaling of the B_1^+ results for Ella and Duke allowed to balance the RF antenna array performance for one subject against the other. This procedure reveals convincing results as no signal voids could be observed in the imaging study over a range of body-mass-indexes ($BMI = 23,8 \pm 2,1 \text{ kg/m}^2$).

Before performing an imaging study, the performance of the antenna system was benchmarked in phantom experiments against simulation results. A quantitative comparison relies on an exact measurement of the transmission losses of the system. These losses were measured from the patient-table connector to the single antennas, where the losses of the phase shifting cables are averaged because of their length and therefore loss variation. Considering all the losses in the signal chain, the AFI B_1^+ mapping revealed a mean difference of approximately 9% between the simulation and the measurement in the ROI of the depicted interference pattern in Figure 5 in Section 2.1. The use of a depicted ROI within this experiment is encouraging as imaging and manufacturing inaccuracies close to the vicinity of the antenna system might hide the overall simulation accuracy.

The phantom experiment results reveal a low discrepancy between simulation and measurement, suggesting an accurate numerical safety assessment based on SAR_{10g} . Furthermore an additional safety factor of 1.7 was included in the safety settings at the MRI system.¹⁴⁰ An in vivo study was performed including an AFI based B_1^+ mapping approach.¹²⁰ The B_1^+ maps for a female and a male subject respectively reveal a difference of 6% compared to Ella and 14% compared to Duke. The in vivo B_1^+ mapping suggests an overestimation due to the thresholded data (flip angle $\leq 15^\circ$). A quantitative and qualitative agreement between simulation and measurement was found, proving the previously conducted phantom experiments (Figure 6, Section 2.1). The imaging study revealed a stable inter-subject performance without visible signal voids for all views (Figure 7, Section 2.1).

SNR, CNR, and g-factor maps scale with increasing the GRAPPA reduction factor. Reported values of selected literature on UHF-CMR for a 32-channel loop antenna design, a 16-channel Bow-Tie antenna array, and a Fractionated loop-dipole antenna array configuration are summarized in Table 1 for clinically relevant reduction values $R = 2$ to $R = 4$.^{87,88,92} Comparing the proposed 32-channel SGBT array to the other dipole antenna configurations (16-channel Bow-Tie and Fractionated loop-dipole)

on the field of UHF-CMR, it was found that the reported CNR values could be outperformed. In contrary to the Fractionated loop-dipole antenna configuration, the SNR of the 16-channel Bow-Tie showed improved performance compared to the introduced antenna design. The mean g-factor values within the heart revealed lower values for the Fractionated dipole, hence a better performance compared to the SGBT array. In contrast, the g-factor values of the Bow-Tie antenna configuration only revealed lower values for $R = 4$ with respect to the introduced design. A loop antenna configuration at the same channel count as the SGBT array showed that the mean whole heart SNR values and CNRs improved with using the SGBT array. A similar tendency was observed for the mean g-factor values, where the introduced RF antenna array revealed lower values. It is important to notify, that a direct benchmarking of the parallel imaging performance on an experimental basis is only feasible when performing all measurements on the same MRI system, with the same under sampling method (e.g., SENSE or GRAPPA), the same sequence settings, and the same subject or phantom in the best case. Discrepancies impair a benchmarking and the provided comparisons need to be treated carefully. Furthermore, the mean g-factor value as a measure to compare the results is intrinsically misleading, as it reports on the average noise amplification due to under sampling. A more insightful measure is the maximum g-factor value within the ROI, as it represents the worst-case noise amplification.¹⁴¹

3.2 Narrowband Antenna Application for Cardiovascular MRI

Table 1: Synopsis of statistics on the parallel imaging performance up to R = 4 for the 32-channel Self-Grounded Bow-Tie⁵², 32-channel loop antenna⁹², 8-channel Fractionated dipole combined with 16-channel loop antenna⁸⁸, and 16-channel Bow-Tie⁸⁷. Except for the 8-channel Fractionated dipole combined with 16-channel loop antenna which uses SENSE, GRAPPA is used. 32-channel loop antenna and 16-channel Bow-Tie one subject is investigated therefore the statistic is presented as mean value.

Antenna System	View	Analyzis	R=2	R=3	R=4
32-Ch. Self-Grounded Bow-Tie ⁵²	4CV	CNR (Mean \pm Std)	27.0 \pm 1.9	19.5 \pm 2.1	13.5 \pm 1.9
		SNR _{whole-heart,mean} (Mean [Min])	31.6 [29.6]	22.9 [20.6]	16.7 [15.5]
		SNR _{myocardium,mean} (Mean [Min])	18.4 [16.0]	13.6 [10.9]	10.1 [8.3]
		g-factor _{whole-heart,mean} (Mean [Max])	1.1 [1.1]	1.3 [1.4]	1.5 [1.6]
	SAX	CNR (Mean \pm Std)	41.0 \pm 5.5	26.9 \pm 3.0	19.9 \pm 2.9
		SNR _{whole-heart,mean} (Mean [Min])	38.2 [32.7]	26.7 [24.0]	19.5 [16.6]
		SNR _{myocardium,mean} (Mean [Min])	18.4 [16.6]	13.3 [11.2]	9.7 [8.6]
		g-factor _{whole-heart,mean} (Mean [Max])	1.1 [1.1]	1.3 [1.4]	1.5 [1.6]
32-Ch. Loop Antenna ⁹²	4CV	CNR (Mean \pm Std)	6.0 \pm n/a	6 \pm n/a	3.0 \pm n/a
		SNR _{whole-heart,mean} (Mean [Min])	20.0 [18.0]	15.0 [12.0]	12.0 [11.0]
		SNR _{myocardium,mean} (Mean [Min])	n/a	n/a	n/a
		g-factor _{whole-heart,mean} (Mean [Max])	1.3 [1.4]	1.3 [1.9]	1.6 [1.7]
	SAX	CNR (Mean \pm Std)	19.0 \pm n/a	12.0 \pm n/a	10.0 \pm n/a
		SNR _{whole-heart,mean} (Mean [Min])	23.0 [n/a]	20.0 [n/a]	17.0 [n/a]
		SNR _{myocardium,mean} (Mean [Min])	n/a	n/a	n/a
		g-factor _{whole-heart,mean} (Mean [Max])	1.3 [n/a]	1.4 [n/a]	1.4 [n/a]
8-Ch. TX/RX Fractionated dipole combined with 16-Ch. Loop Antenna ⁸⁸	4CV	CNR (Mean \pm Std)	10.3 \pm 1.2	n/a	n/a
		SNR _{whole-heart,mean} (Mean [Min])	11.9 [n/a]	n/a	n/a
		SNR _{myocardium,mean} (Mean [Min])	n/a	n/a	n/a
		g-factor _{whole-heart,mean} (Mean [Max])	1.0 [1.4]	1.0 [1.6]	1.1 [1.7]
	SAX	CNR (Mean \pm Std)	12.7 \pm 8.2	n/a	n/a
		SNR _{whole-heart,mean} (Mean [Min])	10.9 [n/a]	n/a	n/a
		SNR _{myocardium,mean} (Mean [Min])	n/a	n/a	n/a
		g-factor _{whole-heart,mean} (Mean [Max])	1.0 [1.1]	1.0 [1.3]	1.1 [1.4]
16-Ch. Bow-Tie ⁸⁷	4CV	CNR (Mean \pm Std)	11.0 \pm n/a	6.0 \pm n/a	5.0 \pm n/a
		SNR _{whole-heart,mean} (Mean [Min])	n/a	n/a	n/a
		SNR _{myocardium,mean} (Mean [Min])	29.0 [n/a]	24.0 [n/a]	21.0 [n/a]
		g-factor _{whole-heart,mean} (Mean [Max])	1.1 [n/a]	1.5 [n/a]	1.3 [n/a]
	SAX	CNR (Mean \pm Std)	9.0 \pm n/a	5.0 \pm n/a	4.0 \pm n/a
		SNR _{whole-heart,mean} (Mean [Min])	n/a	n/a	n/a
		SNR _{myocardium,mean} (Mean [Min])	29.0 [n/a]	25.0 [n/a]	20.0 [n/a]
		g-factor _{whole-heart,mean} (Mean [Max])	1.6 [n/a]	1.5 [n/a]	2.0 [n/a]

3.3 Broadband Antenna Application for Thermal MR

A broadband antenna concept requires a low reflection of the EM wave for a broad range of frequencies, where in the introduced design the MRI frequency of ^{19}F at 7.0 T represents the lower limit (≈ 280 MHz). The main lobe directivity showed a stable behaviour without splitting for the whole frequency band. The low-loss, low-permittivity material is beneficial in spreading the surface current of the tip area, which in the narrowband application are on the edges of the Bow-Tie part of the proposed antenna system (Figure 6). This finding concurs with previous reports on the SGBT antenna building block.⁵⁵ A step-by-step design approach, where first the antenna's copper structure is optimized and second the building block geometry is adapted was not feasible. The antenna design and the building block geometry reveal a strong EM influence among each other. A geometry optimization was therefore performed for the whole building block setup combined (Table 1, Section 2.2). Similar to the narrowband variant of the SGBT antenna, a dielectric pad is used to improve the EMF coupling of the antenna building block to the subject. The dielectric pad of the broadband antenna variant is an integral part of the introduced antenna, because it impacts the impedance, hence the reflection (S_{11}) and broadband properties. In comparison to the introduced narrowband antenna, the tuning and matching of the broadband SGBT is performed by adapting the antenna's geometry to achieve an impedance of close to $Z = 50 \pm j0 \Omega$ for the entire frequency range (Figure 2, Section 2.2). The broadband SGBT building block shows a high efficiency with material losses, ranging from 9% at 300 MHz to 16% at 500 MHz. These material losses can be reduced with dedicated low-loss materials (e.g. ceramics) close to the conductive copper elements of the antenna.

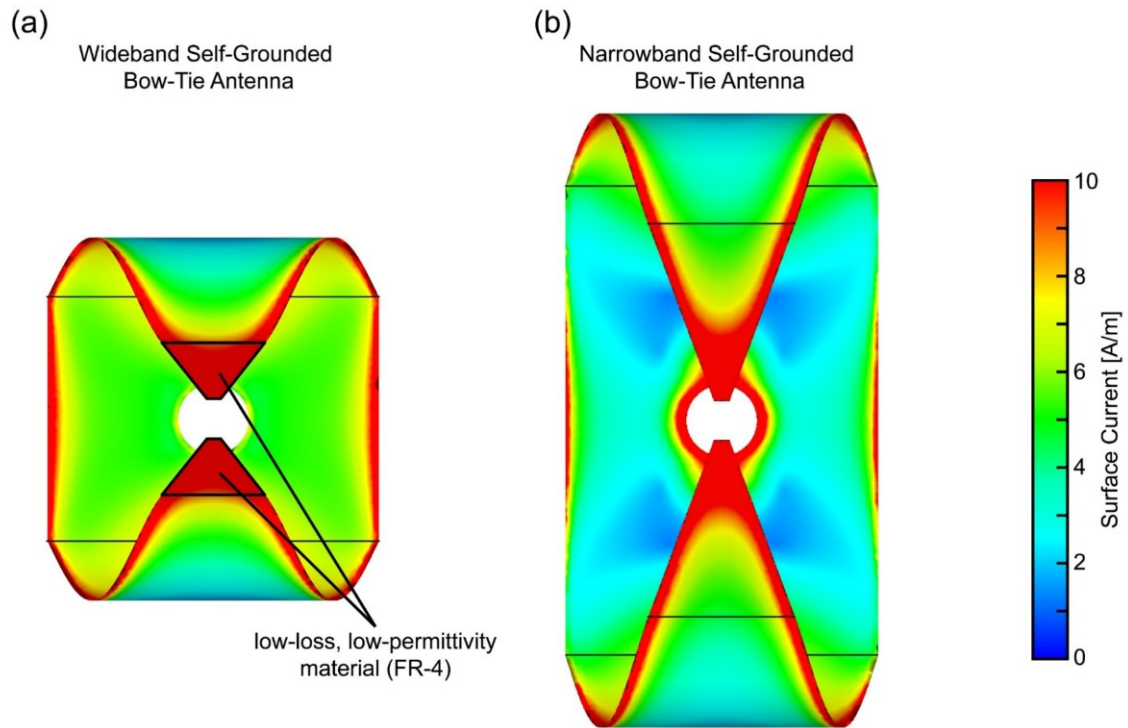


Figure 6: Electric surface current distribution on (a) the broadband Self-Grounded Bow-Tie antenna and (b) the narrowband Self-Grounded Bow-Tie antenna immersed in water as dielectric. The broadband antenna variant uses a low-loss, low-permittivity material to spread the current distribution and increase the broadband behaviour of the antenna. The presented antennas were tuned and matched to 297.2 MHz for a better comparison.

The introduced broadband SGBT building block design allows MRI of two nuclei (^{19}F and ^1H) at 7.0 T without adapting or switching the antenna system. The design furthermore facilitates RF thermal intervention at a broad frequency range integrated in a UHF-MRI environment. The validation process of the antenna was performed in the imaging regime (^{19}F and ^1H) and the thermal intervention regime. The imaging performance of the wideband SGBT building block was assessed using AFI for B_1^+ mapping and benchmarked against EMF simulations conducting a phantom study (Figure 5, Section 2.2). The deviation was found to be 17% or less, but without the loss correction (-1.22 dB) of the cables from the MRI system's RF amplifiers to the patient-table connectors. Elevated deviations were found in the vicinity of the phantom to the dielectric pad. The single antenna element measurement cannot offer an interference pattern for a more precise comparison, as it was provided for the narrowband SGBT antenna configuration (Figure 5, Section 2.2). The discrepancy between measurement and simulation was most likely based on manufacturing, antenna placement, and slice positioning deviations. Experimental assessment of ^{19}F imaging performance based on B_1^+ mapping was not

feasible, as no phantom could be manufactured economically with sufficient ^{19}F compound to allow a mapping procedure. High fluorine content nanoparticles prepared by emulsifying perfluoro-15-crown-5-ether (PFCE; Fluorochem, Hadfield, UK) with Pluronic F-68 (Sigma-Aldrich) were used in the phantom imaging study for a qualitative assessment (Figure 7, Section 2.2).¹⁴² In vivo experiments were conducted on the forearm and the thigh of a human subject including a fluorinated compound, which consists of flufenamic acid (101 mmol/L), a nonsteroidal anti-inflammatory drug (Figure 7, Section 2.2). The imaging results revealed a good FOV coverage with no ^1H of ^{19}F signal of the antenna itself; only the used dielectric pad introduced a ^1H signal. An arrangement of the antenna in an RF array with multiple channels will increase the FOV and will allow EMF control for B_1^+ shimming and targeted RF power deposition.

The thermal intervention performance of the broadband SGBT building blocks were investigated at 300 MHz, 400 MHz, and 500 MHz in the previously used phantom setup (Figure 6, Section 2.2). These thermal intervention frequencies are only examples, in a realistic application the frequency can be adjusted arbitrary in the whole provided bandwidth (approximately 280 MHz to 600 MHz). The thermal intervention simulation results revealed a rather uniform temperature rise for all frequencies, only for 300 MHz a slightly smaller area was heated. This behaviour is present in the simulations and measurements and is explained by increased losses in the antenna system and the phantom at higher frequencies. At the vicinity of the phantom, the temperature distribution varies between the simulations and measurements, implying a thermal modelling discrepancy of the dielectric pad (Figure 6, Section 2.2). The findings suggest, that the dielectric pad in the measurements results in a surface cooling, which was not correctly estimated in the EMF and temperature simulations. The most dominant difference was found in the outskirts perpendicular to the main lobe directivity, but without affecting the temperature rise along the Poynting vector of the E-field radiation. The agreement was further shown in 2D temperature plots, where a good qualitative and quantitative agreement was found between the simulation, the MR-thermometry measurements, and the fibre optical probe measurements.

3.4 RF Signal Chain Systems Design for Thermal MR

The thermal intervention signal chain in combination with the introduced broadband antenna (antenna array) is a crucial element of the Thermal MR system. It implements a control loop concept by providing the flexibility to adapt amplitude, phase, and frequency of the individual channels to improve the focal point quality. The scalability of the design allows the implementation of $n > 32$ individual RF channels. The introduced 32-channels version facilitates a high degree of freedom for a time- and frequency-multiplexed optimization approach. In contrary to the gold standard MR scanner signal chain, the proposed system allows an increased channel count (8- and 16- channels in MRI) and a full bandwidth (small transmitter bandwidth covering the Larmor frequency of the respective nuclei in MRI). Furthermore, the amplifier system used in MRI is designed for rather short RF pulses and not a continuous power delivery which constrains the available power for the thermal intervention.

The signal generator design was benchmarked in several steps: first the signal settling performance and temperature stability, second the interference point control in the electric field by E-field measurements, and third the implementation in an MRI environment with a 1- and a 2-channel application. The introduced signal generator is based on a PLL circuit, which provides a high phase and frequency tuning resolution. The frequency switching time reveal was a maximum of 2.6 ms, whereas amplitude and phase settling take place at less than 0.8 ms. This fast and stable switching in the thermal intervention session is of high importance for an improved focal point quality, especially with respect to a time-multiplexed, frequency mixed, or a time- and frequency-multiplexed approach.^{43–46}

For the validation of the envisioned Thermal MR setup the previously introduced wideband SGBT building block antenna was used in an 8-channel arrangement. The control and adaptation of the E-field interference pattern (Figure 3, Section 2.3) was provided within simulations and measurements. The result conceptually proves the feasibility of the envisioned setup with the use of a wideband antenna system. In this phantom experiment study, an intervention frequency of 400 MHz was used, but the wideband SGBT building block as well as the signal generator allow the use of an arbitrarily chosen intervention frequency within the range of the antenna's bandwidth.

An E-field interference results within a lossy material or within tissue in a local temperature increase. This temperature increase was shown to be present when using a single antenna setup in Section 2.2. With a rather short intervention time of only 2 minutes at $P_{in} = 100$ W at the SGBT antenna

port, temperature increases of $>10^{\circ}\text{C}$ at the vicinity of the phantom where achieved. The 1-channel thermal intervention with the developed signal generator in Section 2.3 revealed comparable results with a 10 minute intervention time and a $P_{\text{in}} = 17.78 \text{ W}$ (cumulative power 177.8 W versus 200 W for the previously reported wideband SGBT building block in Section 2.2). Experiments with the signal generator in Section 2.3 revealed reduced temperature increases during the treatment compared to the study in Section 2.2. This deviation is based on a variation in the intervention time, where at 10 minutes of intervention the focal point was enlarged due to thermal conduction. Furthermore, the phantom material used in the study is different to the phantom material used in Section 2.2. The losses within the phantom were measured to be $\sigma = 0.18 \text{ S/m}$ at 300 MHz for the signal generator measurements in Section 2.3 versus $\sigma = 0.72 \text{ S/m}$ at 300 MHz for the single element measurements in Section 2.2. A material with lower losses in Section 2.3 was used to reduce surface heating and enable a temperature rise within the phantom for a 2-channel experiment. Other than the experimental protocol and loss difference, the experimental setup used for the signal generator was modified with respect to the phantom geometry and the lack of a dielectric pad. The dielectric pad was not used in this experimental setup, because no in vivo experiments were conducted, and the rectangular shaped phantom did not require an antenna placement on an uneven subject surface. Both, the commercial signal generator (SMGL, Rohde & Schwarz, Memmingen, Germany) and the developed signal generator design, revealed excellent qualitative and quantitative agreement; both among each other as well as to fiberoptic probe measurements (Figure 4, Section 2.3). Simulation results on the other hand showed a deviation of $\leq 2.5^{\circ}\text{C}$ in the conducted measurements, suggesting modelling induced variations within the numerical simulation. The modelling errors include, boundary condition variations (air-flow in the MRI-bore and environment temperature), thermal property variations within the phantom, and manufacturing based discrepancies on the losses and properties of the broadband SGBT building block.

To provide an experimental proof of a constructive E-field interference pattern and control over the location of a temperature increase within an UHF-MRI system, a 2-channel setup at an intervention frequency of 400 MHz was used. The phase adjustments were performed by using the proposed signal generator design and a commercial arbitrary waveform generator (M8190A, Keysight, Santa Rosa, CA, USA) as a benchmark. Similar to the single channel thermal intervention measurements, minor differences were observed between the commercial and the proposed signal generator. Furthermore, a good qualitative agreement between the simulation and measurement was achieved. Quantitatively discrepancies between simulation and measurements were observed at the vicinity of the phantom. These deviations are based on imperfections of the used power amplifiers, where the output signals were phase-offset-dependent impacted by the crosstalk of the two

channels used. The simulations and measurements revealed a constructive interference at a phase difference of 0° with a temperature rise of approximately 2.5°C in the center of the phantom. The steerability of the focal point was proven by a phase difference of 90° between the two channels, where the focal point was shifted by approximately 18 mm (Figure 5, Section 2.3). These results are the conceptual proof of the envisioned Thermal MR setup, whereas the steerability and the focal point quality was limited due to the limited channel count. An increase of the channel count will provide an increased degree of freedom for improving the focal point quality, as was shown in the E-field measurements (Figure 3, Section 2.3).

4 Conclusions and Outlook

This thesis demonstrates the development, optimization, and application of a SGBT antenna within an UHF-MRI environment. The narrowband SGBT building block was introduced for CMR, but its field of application is versatile. The broadband SGBT building block is an integral element of the envisioned Thermal MR applicator design. Both antenna variants use a dielectric pad; whereas the narrowband variant uses a mechanically advanced hydrogel material, the wideband variant implements a H₂O filled flexible compartment. Utilising dielectric pads increase the efficiency of the SGBT building blocks for UHF-CMR and for Thermal MR, as it is observed and reported for hyperthermia applications.^{36,83,138}

To conclude the findings on the narrowband SGBT antenna, the cardiac TX/RX RF array is compatible with a multiple feeding RF power amplifier for PTX. The SGBT antenna array offers a high degree of freedom for the used CTX shim. Furthermore, it allows an improved excitation homogeneity through dynamic PTX with spoke- and kT-point excitation.^{32,143–146} The RF array contributes therefore to the technological basis for future clinical assessments of dynamic PTX techniques designed for UHF-CMR. Accessing the full potential of the SGBT antenna array with dynamic PTX requires appropriate multi-transmit systems that offer more than today's MRI system gold-standard of 8 to 16 TX channels. This high dipole antenna count and therefore high degree of freedom can be of high relevance for further B₀ increase, where a linear (curl-free) current pattern is dominant for achieving the UISNR and non-uniformities of B₁⁺ are enhanced.^{89,90} The introduced narrowband SGBT array demonstrates the application of the antennas in a highly modular manner, allowing a broad range of BMI for UHF-CMR, and paves the way for extended applications (e.g., abdominal imaging, pelvic imaging). Furthermore, smaller antenna designs opens the feasibility for studies on the optimal antenna placement to improve the B₁⁺ homogeneity and the efficiency of the antenna array.^{37,41,147,148}

The same findings and conclusions are applicable for the control of the E-field distribution and the focal point quality for the envisioned Thermal MR system. For an improved focal point quality, the degree of freedom is key. With the proposed wideband antenna concept, the frequency bandwidth adds to the amplitude and phase adjustment in an additional time multiplexed approach. The wideband antenna concept is a novel approach for UHF-MRI and permits the application of the antenna at various field strength without adaptation. The antenna building block in combination with the dielectric pad is widely independent of the loading condition, supports a wide range of anatomies, and provides a stable EMF pattern over a broad frequency range. The introduced antenna design is, to

the knowledge of the author, the first proposal of a broadband antenna design for Thermal MR, but further improvements in the broadband properties are conceivable. Several fundamental concepts to improve the broadband capacity and the antennas' efficiency such as multi-resonant structures, low-loss dielectric material for further size reduction, and metamaterials or metamaterial-like structures demand further investigation.^{149–152}

The developed signal-generator in combination with the wideband SGBT building block allows the application of a 32-channel Thermal MR setup with the antennas arranged in any shape (e.g. a ring) to improve the focal point quality (Figure 7). Besides the introduced elements in this work, essential parts for the Thermal MR system include a supervision module, power amplifiers for each thermal intervention channel, and an RF switch to switch between the thermal intervention signal chain and the MRI signal chain (Figure 3). The supervision module was recently proposed by Han H. et al. in a multi-channel RF supervision module.¹⁵³ This module allows detection and correction of frequency, phase, and amplitude discrepancies of the amplified signal in feedback loop; therefore, serving as a safety infrastructure (Figure 3).¹⁵³ As thermal intervention treatments are rather long with respect to the treatment time, movements of the subject are possible. Movements can cause the loss of the focal point and in the worst-case result in a thermal damage of tissue outside the TV. Hence, the direct detection of movement based on the loading condition of the antenna array through the supervision module improves the safety of the envisioned Thermal MR system.¹⁵³

With all components available for an integrated Thermal MR system experiments on the control of the focal point quality through a high degree of freedom is facilitated. Studies will reveal the application of a time-multiplexed, frequency-multiplexed, or a time- and frequency-multiplexed thermal intervention with the objective to approach the UISAR.^{41,43–45}



Figure 7: First Thermal MR applicator prototype based on the introduced wideband Self-Grounded Bow-Tie building block design. The prototype includes 20-channels in a circular, two-row arrangement for head applications for example.

References

1. OECD. Magnetic resonance imaging (MRI) units. Accessed on 12 April 2021. doi:10.1787/1a72e7d1-en
2. OECD. Magnetic resonance imaging (MRI) exams. Accessed on 12 April 2021. doi:10.1787/1d89353f-en
3. Edelstein WA, Glover GH, Hardy CJ, Redington RW. The intrinsic signal-to-noise ratio in NMR imaging. *Magn Reson Med*. 1986;3(4):604-618. doi:10.1002/mrm.1910030413
4. Hoult D., Richards R. The signal-to-noise ratio of the nuclear magnetic resonance experiment. *J Magn Reson*. 1976;24(1):71-85. doi:10.1016/0022-2364(76)90233-X
5. Vaughan JT, Garwood M, Collins CM, et al. 7T vs. 4T: RF power, homogeneity, and signal-to-noise comparison in head images. *Magn Reson Med*. 2001;46(1):24-30. doi:10.1002/mrm.1156
6. Pfrommer A, Henning A. The ultimate intrinsic signal-to-noise ratio of loop- and dipole-like current patterns in a realistic human head model. *Magn Reson Med*. 2018;80(5):2122-2138. doi:10.1002/mrm.27169
7. Lattanzi R, Wiggins GC, Zhang B, Duan Q, Brown R, Sodickson DK. Approaching ultimate intrinsic signal-to-noise ratio with loop and dipole antennas. *Magn Reson Med*. 2018;79(3):1789-1803. doi:10.1002/mrm.26803
8. Vaidya M V., Sodickson DK, Lattanzi R. Approaching ultimate intrinsic SNR in a uniform spherical sample with finite arrays of loop coils. *Concepts Magn Reson Part B Magn Reson Eng*. 2014;44(3):53-65. doi:10.1002/cmr.b.21268
9. Ocali O, Atalar E. Ultimate intrinsic signal-to-noise ratio in MRI. *Magn Reson Med*. 1998;39(3):462-473. doi:10.1002/mrm.1910390317
10. Pohmann R, Speck O, Scheffler K. Signal-to-noise ratio and MR tissue parameters in human brain imaging at 3, 7, and 9.4 tesla using current receive coil arrays. *Magn Reson Med*. 2016;75(2):801-809. doi:10.1002/mrm.25677
11. Ladd ME, Bachert P, Meyerspeer M, et al. Pros and cons of ultra-high-field MRI/MRS for human application. *Prog Nucl Magn Reson Spectrosc*. 2018;109:1-50. doi:10.1016/j.pnmrs.2018.06.001
12. Ibrahim E-SH, Arpinar VE, Muftuler LT, Stojanovska J, Nencka AS, Koch KM. Cardiac functional magnetic resonance imaging at 7T: Image quality optimization and ultra-high field capabilities. *World J Radiol*. 2020;12(10):231-246. doi:10.4329/wjr.v12.i10.231
13. Vaughan JT, Snyder CJ, Delabarre LJ, et al. Whole-body imaging at 7T: Preliminary results. *Magn Reson Med*. 2009;61(1):244-248. doi:10.1002/mrm.21751
14. Niendorf T, Paul K, Oezerdem C, et al. W(h)ither human cardiac and body magnetic resonance at ultrahigh fields? technical advances, practical considerations, applications, and clinical opportunities. *NMR Biomed*. 2016;29(9):1173-1197. doi:10.1002/nbm.3268

15. Erturk MA, Li X, Van de Moortele P-F, Ugurbil K, Metzger GJ. Evolution of UHF body imaging in the human torso at 7T: Technology, applications, and future directions. *Top Magn Reson Imaging*. 2019;28(3):101-124. doi:10.1097/RMR.000000000000202
16. Brown RW, Cheng YCN, Haacke EM, Thompson MR, Venkatesan R. *Magnetic Resonance Imaging: Physical Principles and Sequence Design*. Vol 2. John Wiley & Sons Ltd; 2014. doi:10.1002/9781118633953
17. Hoult DI. Sensitivity and power deposition in a high-field imaging experiment. *J Magn Reson Imaging*. 2000;12(1):46-67. doi:10.1002/1522-2586(200007)12:1<46::AID-JMRI6>3.0.CO;2-D
18. Niendorf T, Schulz-Menger J, Paul K, Huelnhagen T, Ferrari VA, Hodge R. High field cardiac magnetic resonance imaging. *Circ Cardiovasc Imaging*. 2017;10(6):1-13. doi:10.1161/CIRCIMAGING.116.005460
19. Snyder CJ, DelaBarre L, Metzger GJ, et al. Initial results of cardiac imaging at 7 tesla. *Magn Reson Med*. 2009;61(3):517-524. doi:10.1002/mrm.21895
20. Kramer CM, Barkhausen J, Bucciarelli-Ducci C, Flamm SD, Kim RJ, Nagel E. Standardized cardiovascular magnetic resonance imaging (CMR) protocols: 2020 update. *J Cardiovasc Magn Reson*. 2020;22(1):17. doi:10.1186/s12968-020-00607-1
21. Hernando D, Kellman P, Haldar JP, Liang Z-P. Robust water/fat separation in the presence of large field inhomogeneities using a graph cut algorithm. *Magn Reson Med*. 2010;63(1):79-90. doi:10.1002/mrm.22177
22. Thalhammer C, Renz W, Winter L, et al. Two-Dimensional sixteen channel transmit/receive coil array for cardiac MRI at 7.0 T: Design, evaluation, and application. *J Magn Reson Imaging*. 2012;36(4):847-857. doi:10.1002/jmri.23724
23. Hess AT, Bissell MM, Ntusi NAB, et al. Aortic 4D flow: Quantification of signal-to-noise ratio as a function of field strength and contrast enhancement for 1.5T, 3T, and 7T. *Magn Reson Med*. 2015;73(5):1864-1871. doi:10.1002/mrm.25317
24. Schmitter S, Schnell S, Ugurbil K, Markl M, Van de Moortele P-F. Towards high-resolution 4D flow MRI in the human aorta using kt-GRAPPA and B1+ shimming at 7T. *J Magn Reson Imaging*. 2016;44(2):486-499. doi:10.1002/jmri.25164
25. Wiesemann S, Schmitter S, Demir A, et al. Impact of sequence type and field strength (1.5, 3, and 7T) on 4D flow MRI hemodynamic aortic parameters in healthy volunteers. *Magn Reson Med*. 2021;85(2):721-733. doi:10.1002/mrm.28450
26. Suttie JJ, DelaBarre L, Pitcher A, et al. 7 Tesla (T) human cardiovascular magnetic resonance imaging using FLASH and SSFP to assess cardiac function: validation against 1.5 T and 3 T. *NMR Biomed*. 2012;25(1):27-34. doi:10.1002/nbm.1708
27. Rodgers CT, Piechnik SK, DelaBarre LJ, et al. Inversion recovery at 7 T in the human myocardium: Measurement of T₁, inversion efficiency and B₁ +. *Magn Reson Med*. 2013;70(4):1038-1046. doi:10.1002/mrm.24548
28. Huelnhagen T, Ku M-C, Reimann HM, et al. Myocardial effective transverse relaxation time T₂* is elevated in hypertrophic cardiomyopathy: A 7.0T magnetic resonance imaging study. *Sci Rep*. 2018;8(1):3974. doi:10.1038/s41598-018-22439-x

29. Huelnhagen T, Hezel F, Serradas Duarte T, et al. Myocardial effective transverse relaxation time T2* correlates with left ventricular wall thickness: A 7.0 T MRI study. *Magn Reson Med*. 2017;77(6):2381-2389. doi:10.1002/mrm.26312
30. Winter L, Kellman P, Renz W, et al. Comparison of three multichannel transmit/receive radiofrequency coil configurations for anatomic and functional cardiac MRI at 7.0T: implications for clinical imaging. *Eur Radiol*. 2012;22(10):2211-2220. doi:10.1007/s00330-012-2487-1
31. Meloni A, Hezel F, Positano V, et al. Detailing magnetic field strength dependence and segmental artifact distribution of myocardial effective transverse relaxation rate at 1.5, 3.0, and 7.0 T. *Magn Reson Med*. 2014;71(6):2224-2230. doi:10.1002/mrm.24856
32. Padormo F, Beqiri A, Hajnal J V., Malik SJ. Parallel transmission for ultrahigh-field imaging. *NMR Biomed*. 2016;29(9):1145-1161. doi:10.1002/nbm.3313
33. Dewhirst MW, Lee C-T, Ashcraft KA. The future of biology in driving the field of hyperthermia. *Int J Hyperth*. 2016;32(1):4-13. doi:10.3109/02656736.2015.1091093
34. Datta NR, Ordóñez SG, Gaip US, et al. Local hyperthermia combined with radiotherapy and/or chemotherapy: Recent advances and promises for the future. *Cancer Treat Rev*. 2015;41(9):742-753. doi:10.1016/j.ctrv.2015.05.009
35. Issels RD, Lindner LH, Verweij J, et al. Neo-adjuvant chemotherapy alone or with regional hyperthermia for localised high-risk soft-tissue sarcoma: a randomised phase 3 multicentre study. *Lancet Oncol*. 2010;11(6):561-570. doi:10.1016/S1470-2045(10)70071-1
36. Rijnen Z, Togni P, Roskam R, van de Geer SG, Goossens RHM, Paulides MM. Quality and comfort in head and neck hyperthermia: A redesign according to clinical experience and simulation studies. *Int J Hyperth*. 2015;31(8):823-830. doi:10.3109/02656736.2015.1076893
37. Oberacker E, Kuehne A, Oezerdem C, et al. Radiofrequency applicator concepts for thermal magnetic resonance of brain tumors at 297 MHz (7.0 Tesla). *Int J Hyperth*. 2020;37(1):549-563. doi:10.1080/02656736.2020.1761462
38. Oberacker E, Diesch C, Nadobny J, et al. Patient-specific planning for thermal magnetic resonance of glioblastoma multiforme. *Cancers (Basel)*. 2021;13(8):1867. doi:10.3390/cancers13081867
39. Stauffer PR. Evolving technology for thermal therapy of cancer. *Int J Hyperth*. 2005;21(8):731-744. doi:10.1080/02656730500331868
40. Winter L, Oezerdem C, Hoffmann W, et al. Thermal magnetic resonance: physics considerations and electromagnetic field simulations up to 23.5 Tesla (1GHz). *Radiat Oncol*. 2015;10(1):201. doi:10.1186/s13014-015-0510-9
41. Guérin B, Villena JF, Polimeridis AG, et al. Computation of ultimate SAR amplification factors for radiofrequency hyperthermia in non-uniform body models: impact of frequency and tumour location. *Int J Hyperth*. 2018;34(1):87-100. doi:10.1080/02656736.2017.1319077
42. Winter L, Niendorf T. Electrodynamics and radiofrequency antenna concepts for human magnetic resonance at 23.5 T (1 GHz) and beyond. *Magn Reson Mater Physics, Biol Med*. 2016;29(3):641-656. doi:10.1007/s10334-016-0559-y

43. Zastrow E, Hagness SC, Van Veen BD, Medow JE. Time-multiplexed beamforming for noninvasive microwave hyperthermia treatment. *IEEE Trans Biomed Eng.* 2011;58(6):1574-1584. doi:10.1109/TBME.2010.2103943
44. Kok H, van Stam G, Bel A, Crezee J. A mixed frequency approach to optimize locoregional RF hyperthermia. In: *2015 European Microwave Conference (EuMC)*. IEEE; 2015:773-776. doi:10.1109/EuMC.2015.7345878
45. Kuehne A, Oberacker E, Waiczies H, Niendorf T. Solving the time- and frequency-multiplexed problem of constrained radiofrequency induced hyperthermia. *Cancers (Basel)*. 2020;12(5):1072. doi:10.3390/cancers12051072
46. Stakhursky VL, Arabe O, Cheng K-S, et al. Real-time MRI-guided hyperthermia treatment using a fast adaptive algorithm. *Phys Med Biol.* 2009;54(7):2131-2145. doi:10.1088/0031-9155/54/7/019
47. Wust P, Seebass M, Nadobny J, Deuflhard P, Mönich G, Felix R. Simulation studies promote technological development of radiofrequency phased array hyperthermia. *Int J Hyperth.* 2009;25(7):517-528. doi:10.3109/02656730903287832
48. Rieke V, Butts Pauly K. MR thermometry. *J Magn Reson Imaging.* 2008;27(2):376-390. doi:10.1002/jmri.21265
49. Winter L, Oberacker E, Paul K, et al. Magnetic resonance thermometry: Methodology, pitfalls and practical solutions. *Int J Hyperth.* 2016;32(1):63-75. doi:10.3109/02656736.2015.1108462
50. Odéen H, Parker DL. Non-invasive thermometry with magnetic resonance imaging. In: *Theory and Applications of Heat Transfer in Humans*. John Wiley & Sons Ltd; 2018:267-299. doi:10.1002/9781119127420.ch15
51. Quesson B, de Zwart JA, Moonen CTW. Magnetic resonance temperature imaging for guidance of thermotherapy. *J Magn Reson Imaging.* 2000;12(4):525-533. doi:10.1002/1522-2586(200010)12:4<525::AID-JMRI3>3.0.CO;2-V
52. Eigentler TW, Kuehne A, Boehmert L, et al. 32-Channel self-grounded bow-tie transceiver array for cardiac MR at 7.0T. *Magn Reson Med.* 2021;86(5):2862-2879. doi:10.1002/mrm.28885
53. Yang J, Kishk A. A novel low-profile compact directional ultra-wideband antenna: The self-grounded bow-tie antenna. *IEEE Trans Antennas Propag.* 2012;60(3):1214-1220. doi:10.1109/TAP.2011.2180317
54. Eigentler TW, Winter L, Han H, et al. Wideband self-grounded bow-tie antenna for thermal MR. *NMR Biomed.* 2020;33(5):e4274. doi:10.1002/nbm.4274
55. Takook P, Persson M, Gellermann J, Trefná HD. Compact self-grounded Bow-Tie antenna design for an UWB phased-array hyperthermia applicator. *Int J Hyperth.* 2017;33(4):387-400. doi:10.1080/02656736.2016.1271911
56. Winter L, Özerdem C, Hoffmann W, et al. Design and evaluation of a hybrid radiofrequency applicator for magnetic resonance imaging and RF induced hyperthermia: Electromagnetic field simulations up to 14.0 Tesla and proof-of-concept at 7.0 Tesla. *PLoS One.* 2013;8(4):e61661. doi:10.1371/journal.pone.0061661

57. Han H, Eigentler TW, Wang S, et al. Design, Implementation, Evaluation and Application of a 32-Channel Radio Frequency Signal Generator for Thermal Magnetic Resonance Based Anti-Cancer Treatment. *Cancers (Basel)*. 2020;12(7):1720. doi:10.3390/cancers12071720
58. Bloch F. Nuclear induction. *Phys Rev*. 1946;70(7-8):460-474. doi:10.1103/PhysRev.70.460
59. Purcell EM, Torrey HC, Pound R V. Resonance absorption by nuclear magnetic moments in a solid. *Phys Rev*. 1946;69(1-2):37-38. doi:10.1103/PhysRev.69.37
60. Vaidya M V, Collins CM, Sodickson DK, Brown R, Wiggins GC, Lattanzi R. Dependence of B1- and B1+ field patterns of surface coils on the electrical properties of the sample and the MR operating frequency. *Concepts Magn Reson Part B Magn Reson Eng*. 2016;46(1):25-40. doi:10.1002/cmr.b.21319
61. Hoult DI. The principle of reciprocity in signal strength calculations? A mathematical guide. *Concepts Magn Reson*. 2000;12(4):173-187. doi:10.1002/1099-0534(2000)12:4<173::AID-CMR1>3.0.CO;2-Q
62. International Electrotechnical Commission. IEC 60601-2-33 Medical electrical equipment - Part 2-33: Particular requirements for the basic safety and essential performance of magnetic resonance equipment for medical diagnosis. *Int Electrotech Comm*. 2015;Ed. 3.2:1-121.
63. von Knobelsdorff-Brenkenhoff F, Frauenrath T, Prothmann M, et al. Cardiac chamber quantification using magnetic resonance imaging at 7 Tesla—a pilot study. *Eur Radiol*. 2010;20(12):2844-2852. doi:10.1007/s00330-010-1888-2
64. van Elderen SGC, Versluis MJ, Westenberg JJM, et al. Right coronary MR angiography at 7 T: A direct quantitative and qualitative comparison with 3 T in young healthy volunteers. *Radiology*. 2010;257(1):254-259. doi:10.1148/radiol.100615
65. Dabir D, Child N, Kalra A, et al. Reference values for healthy human myocardium using a T1 mapping methodology: results from the International T1 Multicenter cardiovascular magnetic resonance study. *J Cardiovasc Magn Reson*. 2014;16(1):69. doi:10.1186/s12968-014-0069-x
66. Singerman R., Denison T., Wen H, Balaban R. Simulation of B1 field distribution and intrinsic signal-to-noise in cardiac MRI as a function of static magnetic field. *J Magn Reson*. 1997;125(1):72-83. doi:10.1006/jmre.1996.1073
67. Morrison SF. Central control of body temperature. *F1000Research*. 2016;5(May):880. doi:10.12688/f1000research.7958.1
68. Evans SS, Repasky EA, Fisher DT. Fever and the thermal regulation of immunity: the immune system feels the heat. *Nat Rev Immunol*. 2015;15(6):335-349. doi:10.1038/nri3843
69. Repasky EA, Evans SS, Dewhirst MW. Temperature matters! And why it should matter to tumor immunologists. *Cancer Immunol Res*. 2013;1(4):210-216. doi:10.1158/2326-6066.CIR-13-0118
70. Hooper VD, Andrews JO. Accuracy of noninvasive core temperature measurement in acutely ill adults: The state of the science. *Biol Res Nurs*. 2006;8(1):24-34. doi:10.1177/1099800406289151
71. van Rhoon GC, Wust P. Introduction: Non-invasive thermometry for thermotherapy. *Int J Hyperth*. 2005;21(6):489-495. doi:10.1080/02656730500272963

References

72. Prinz C, Delgado PR, Eigentler TW, Starke L, Niendorf T, Waiczies S. Toward ¹⁹F magnetic resonance thermometry: spin–lattice and spin–spin-relaxation times and temperature dependence of fluorinated drugs at 9.4 T. *Magn Reson Mater Physics, Biol Med*. 2019;32(1):51-61. doi:10.1007/s10334-018-0722-8
73. Waiczies H, Guenther M, Skodowski J, et al. Monitoring dendritic cell migration using ¹⁹F/¹H magnetic resonance imaging. *J Vis Exp*. 2013;(73):e50251. doi:10.3791/50251
74. Ramos IT, Henningsson M, Nezafat M, et al. Simultaneous assessment of cardiac inflammation and extracellular matrix remodeling after myocardial infarction. *Circ Cardiovasc Imaging*. 2018;11(11):e007453. doi:10.1161/CIRCIMAGING.117.007453
75. Bonetto F, Srinivas M, Heerschap A, et al. A novel ¹⁹F agent for detection and quantification of human dendritic cells using magnetic resonance imaging. *Int J Cancer*. 2011;129(2):365-373. doi:10.1002/ijc.25672
76. Ji Y, Winter L, Navarro L, et al. Controlled release of therapeutics from thermoresponsive nanogels: A thermal magnetic resonance feasibility study. *Cancers (Basel)*. 2020;12(6):1380. doi:10.3390/cancers12061380
77. Langereis S, Keupp J, van Velthoven JIJ, et al. A temperature-sensitive liposomal ¹H CEST and ¹⁹F contrast agent for MR image-guided drug delivery. *J Am Chem Soc*. 2009;131(4):1380-1381. doi:10.1021/ja8087532
78. de Smet M, Langereis S, den Bosch S van, Grüll H. Temperature-sensitive liposomes for doxorubicin delivery under MRI guidance. *J Control Release*. 2010;143(1):120-127. doi:10.1016/j.jconrel.2009.12.002
79. Maloney E, Hwang JH. Emerging HIFU applications in cancer therapy. *Int J Hyperth*. 2015;31(3):302-309. doi:10.3109/02656736.2014.969789
80. Tillander M, Hokland S, Koskela J, et al. High intensity focused ultrasound induced in vivo large volume hyperthermia under 3D MRI temperature control. *Med Phys*. 2016;43(3):1539-1549. doi:10.1118/1.4942378
81. Lo YT, Lee SW. *Antenna Handbook*. (Lo YT, Lee SW, eds.). Boston, MA: Springer US; 1988. doi:10.1007/978-1-4615-6459-1
82. Brace C. Thermal tumor ablation in clinical use. *IEEE Pulse*. 2011;2(5):28-38. doi:10.1109/MPUL.2011.942603
83. Togni P, Rijnen Z, Numan WCM, et al. Electromagnetic redesign of the HYPERcollar applicator: toward improved deep local head-and-neck hyperthermia. *Phys Med Biol*. 2013;58(17):5997-6009. doi:10.1088/0031-9155/58/17/5997
84. Ji Y, Hoffmann W, Pham M, et al. High peak and high average radiofrequency power transmit/receive switch for thermal magnetic resonance. *Magn Reson Med*. 2018;80(5):2246-2255. doi:10.1002/mrm.27194
85. Raaijmakers AJE, Luijten PR, van den Berg CAT. Dipole antennas for ultrahigh-field body imaging: a comparison with loop coils. *NMR Biomed*. 2016;29(9):1122-1130. doi:10.1002/nbm.3356

References

86. Raaijmakers AJE, Ipek O, Klomp DWJ, et al. Design of a radiative surface coil array element at 7 T: The single-side adapted dipole antenna. *Magn Reson Med*. 2011;66(5):1488-1497. doi:10.1002/mrm.22886
87. Oezerdem C, Winter L, Graessl A, et al. 16-channel bow tie antenna transceiver array for cardiac MR at 7.0 tesla. *Magn Reson Med*. 2016;75(6):2553-2565. doi:10.1002/mrm.25840
88. Steensma BR, Voogt IJ, Leiner T, et al. An 8-channel Tx/Rx dipole array combined with 16 Rx loops for high-resolution functional cardiac imaging at 7 T. *Magn Reson Mater Physics, Biol Med*. 2018;31(1):7-18. doi:10.1007/s10334-017-0665-5
89. Lattanzi R, Sodickson DK, Grant AK, Zhu Y. Electrodynamics constraints on homogeneity and radiofrequency power deposition in multiple coil excitations. *Magn Reson Med*. 2009;61(2):315-334. doi:10.1002/mrm.21782
90. Lattanzi R, Sodickson DK. Ideal current patterns yielding optimal signal-to-noise ratio and specific absorption rate in magnetic resonance imaging: Computational methods and physical insights. *Magn Reson Med*. 2012;68(1):286-304. doi:10.1002/mrm.23198
91. Solomakha G, Svejda JT, van Leeuwen C, et al. A self-matched leaky-wave antenna for ultrahigh-field magnetic resonance imaging with low specific absorption rate. *Nat Commun*. 2021;12(1):1-11. doi:10.1038/s41467-020-20708-w
92. Graessl A, Renz W, Hezel F, et al. Modular 32-channel transceiver coil array for cardiac MRI at 7.0T. *Magn Reson Med*. 2014;72(1):276-290. doi:10.1002/mrm.24903
93. Dieringer MA, Renz W, Lindel T, et al. Design and application of a four-channel transmit/receive surface coil for functional cardiac imaging at 7T. *J Magn Reson Imaging*. 2011;33(3):736-741. doi:10.1002/jmri.22451
94. Gräßl A, Winter L, Thalhammer C, et al. Design, evaluation and application of an eight channel transmit/receive coil array for cardiac MRI at 7.0T. *Eur J Radiol*. 2013;82(5):752-759. doi:10.1016/j.ejrad.2011.08.002
95. Raaijmakers AJE, Italiaander M, Voogt IJ, et al. The fractionated dipole antenna: A new antenna for body imaging at 7 Tesla. *Magn Reson Med*. 2016;75(3):1366-1374. doi:10.1002/mrm.25596
96. Steensma B, Moortele P, Ertürk A, et al. Introduction of the snake antenna array: Geometry optimization of a sinusoidal dipole antenna for 10.5T body imaging with lower peak SAR. *Magn Reson Med*. 2020;84(5):2885-2896. doi:10.1002/mrm.28297
97. Alon L, Lattanzi R, Lakshmanan K, et al. Transverse slot antennas for high field MRI. *Magn Reson Med*. 2018;80(3):1233-1242. doi:10.1002/mrm.27095
98. Ertürk MA, Raaijmakers AJE, Adriany G, Uğurbil K, Metzger GJ. A 16-channel combined loop-dipole transceiver array for 7 Tesla body MRI. *Magn Reson Med*. 2017;77(2):884-894. doi:10.1002/mrm.26153
99. Cicchetti R, Miozzi E, Testa O. Wideband and UWB antennas for wireless applications: A comprehensive review. *Int J Antennas Propag*. 2017;2017:1-45. doi:10.1155/2017/2390808

100. Christ A, Kainz W, Hahn EG, et al. The virtual family - development of surface-based anatomical models of two adults and two children for dosimetric simulations. *Phys Med Biol*. 2010;55(2):N23-N38. doi:10.1088/0031-9155/55/2/N01
101. Athey TW, Stuchly MA, Stuchly SS. Measurement of radio frequency permittivity of biological tissues with an open-ended coaxial line: Part I. *IEEE Trans Microw Theory Tech*. 1982;30(1):82-86. doi:10.1109/TMTT.1982.1131021
102. IT'IS Foundation. Tissue Properties Database V4.0. IT'IS Foundation. doi:10.13099/VIP21000-04-0
103. Lemdiasov RA, Obi AA, Ludwig R. A numerical postprocessing procedure for analyzing radio frequency MRI coils. *Concepts Magn Reson Part A*. 2011;38A(4):133-147. doi:10.1002/cmr.a.20217
104. Kuehne A, Waiczies H, Niendorf T. Massively accelerated VOP compression for population-scale RF safety models. *ISMRM 25 Annu Meet*. 2017:#0478.
105. Eichfelder G, Gebhardt M. Local specific absorption rate control for parallel transmission by virtual observation points. *Magn Reson Med*. 2011;66(5):1468-1476. doi:10.1002/mrm.22927
106. Kuehne A, Goluch S, Waxmann P, et al. Power balance and loss mechanism analysis in RF transmit coil arrays. *Magn Reson Med*. 2015;74(4):1165-1176. doi:10.1002/mrm.25493
107. Roemer PB, Edelstein WA, Hayes CE, Souza SP, Mueller OM. The NMR phased array. *Magn Reson Med*. 1990;16(2):192-225. doi:10.1002/mrm.1910160203
108. Yarnykh VL. Actual flip-angle imaging in the pulsed steady state: A method for rapid three-dimensional mapping of the transmitted radiofrequency field. *Magn Reson Med*. 2007;57(1):192-200. doi:10.1002/mrm.21120
109. Yarnykh VL. Optimal radiofrequency and gradient spoiling for improved accuracy of T1 and B1 measurements using fast steady-state techniques. *Magn Reson Med*. 2010;63(6):1610-1626. doi:10.1002/mrm.22394
110. Morrell GR. A phase-sensitive method of flip angle mapping. *Magn Reson Med*. 2008;60(4):889-894. doi:10.1002/mrm.21729
111. Carinci F, Santoro D, von Samson-Himmelstjerna F, Lindel TD, Dieringer MA, Niendorf T. Characterization of phase-based methods used for transmission field uniformity mapping: A magnetic resonance study at 3.0T and 7.0T. Yacoub E, ed. *PLoS One*. 2013;8(3):e57982. doi:10.1371/journal.pone.0057982
112. Nehrke K, Börnert P. DREAM - a novel approach for robust, ultrafast, multislice B1 mapping. *Magn Reson Med*. 2012;68(5):1517-1526. doi:10.1002/mrm.24158
113. Sled JG, Pike GB. Correction for B1 and B0 variations in quantitative T2 measurements using MRI. *Magn Reson Med*. 2000;43(4):589-593. doi:10.1002/(SICI)1522-2594(200004)43:4<589::AID-MRM14>3.0.CO;2-2
114. Chung S, Kim D, Breton E, Axel L. Rapid B1+ mapping using a preconditioning RF pulse with TurboFLASH readout. *Magn Reson Med*. 2010;64(2):439-446. doi:10.1002/mrm.22423

References

115. Sacolick LI, Wiesinger F, Hancu I, Vogel MW. B1 mapping by Bloch-Siegert shift. *Magn Reson Med*. 2010;63(5):1315-1322. doi:10.1002/mrm.22357
116. Park DJ, Bangerter NK, Javed A, Kaggie J, Khalighi MM, Morrell GR. A statistical analysis of the Bloch - Siegert B1 mapping technique. *Phys Med Biol*. 2013;58(16):5673-5691. doi:10.1088/0031-9155/58/16/5673
117. Pohmann R, Scheffler K. A theoretical and experimental comparison of different techniques for B1 mapping at very high fields. *NMR Biomed*. 2013;26(3):265-275. doi:10.1002/nbm.2844
118. Morrell GR, Schabel MC. An analysis of the accuracy of magnetic resonance flip angle measurement methods. *Phys Med Biol*. 2010;55(20):6157-6174. doi:10.1088/0031-9155/55/20/008
119. Lutti A, Hutton C, Finsterbusch J, Helms G, Weiskopf N. Optimization and validation of methods for mapping of the radiofrequency transmit field at 3T. *Magn Reson Med*. 2010;64(1):229-238. doi:10.1002/mrm.22421
120. Dietrich S, Aigner CS, Kolbitsch C, et al. 3D Free-breathing multichannel absolute Mapping in the human body at 7T. *Magn Reson Med*. 2021;85(5):2552-2567. doi:10.1002/mrm.28602
121. Rincón-Domínguez T, Menini A, Solana AB, et al. Accelerated multi-snapshot free-breathing B1+ mapping based on the dual refocusing echo acquisition mode technique (DREAM): An alternative to measure RF nonuniformity for cardiac MRI. *J Magn Reson Imaging*. 2019;49(2):499-507. doi:10.1002/jmri.26234
122. Wang J, Mao W, Qiu M, Smith MB, Constable RT. Factors influencing flip angle mapping in MRI: RF pulse shape, slice-select gradients, off-resonance excitation, and B0 inhomogeneities. *Magn Reson Med*. 2006;56(2):463-468. doi:10.1002/mrm.20947
123. Hamilton J, Franson D, Seiberlich N. Recent advances in parallel imaging for MRI. *Prog Nucl Magn Reson Spectrosc*. 2017;101:71-95. doi:10.1016/j.pnmrs.2017.04.002
124. Blaimer M, Breuer F, Mueller M, Heidemann RM, Griswold MA, Jakob PM. SMASH, SENSE, PILS, GRAPPA: how to choose the optimal method. *Top Magn Reson Imaging*. 2004;15(4):223-236. doi:10.1097/01.rmr.0000136558.09801.dd
125. Sodickson DK, Manning WJ. Simultaneous acquisition of spatial harmonics (SMASH): Fast imaging with radiofrequency coil arrays. *Magn Reson Med*. 1997;38(4):591-603. doi:10.1002/mrm.1910380414
126. Pruessmann KP, Weiger M, Scheidegger MB, Boesiger P. SENSE: Sensitivity encoding for fast MRI. *Magn Reson Med*. 1999;42(5):952-962. doi:10.1002/(SICI)1522-2594(199911)42:5<952::AID-MRM16>3.0.CO;2-S
127. Rabanillo I, Aja-Fernandez S, Alberola-Lopez C, Hernando D. Exact calculation of noise maps and g-Factor in GRAPPA using a k-space analysis. *IEEE Trans Med Imaging*. 2018;37(2):480-490. doi:10.1109/TMI.2017.2760921
128. Hansen MS, Beatty P. ISMRM 2014 sunrise course on parallel imaging. ISMRM 22. Annual Meeting. https://github.com/hansenms/ismrm_sunrise_matlab. Published 2014.

129. Robson PM, Grant AK, Madhuranthakam AJ, Lattanzi R, Sodickson DK, McKenzie CA. Comprehensive quantification of signal-to-noise ratio and g-factor for image-based and k-space-based parallel imaging reconstructions. *Magn Reson Med*. 2008;60(4):895-907. doi:10.1002/mrm.21728
130. Hindman JC. Proton resonance shift of water in the gas and liquid states. *J Chem Phys*. 1966;44(12):4582-4592. doi:10.1063/1.1726676
131. Poorter J De, Wagter C De, Deene Y De, Thomsen C, Ståhlberg F, Achten E. Noninvasive MRI thermometry with the proton resonance frequency (PRF) method: In vivo results in human muscle. *Magn Reson Med*. 1995;33(1):74-81. doi:10.1002/mrm.1910330111
132. Peters RTD, Hinks RS, Henkelman RM. Ex vivo tissue-type independence in proton-resonance frequency shift MR thermometry. *Magn Reson Med*. 1998;40(3):454-459. doi:10.1002/mrm.1910400316
133. McDannold N. Quantitative MRI-based temperature mapping based on the proton resonant frequency shift: Review of validation studies. *Int J Hyperth*. 2005;21(6):533-546. doi:10.1080/02656730500096073
134. Malmberg CG. Dielectric constant of deuterium oxide. *J Res Natl Bur Stand (1934)*. 1958;60(6):609-612. doi:10.6028/jres.060.060
135. Teeuwisse WM, Brink WM, Haines KN, Webb AG. Simulations of high permittivity materials for 7T neuroimaging and evaluation of a new barium titanate-based dielectric. *Magn Reson Med*. 2012;67(4):912-918. doi:10.1002/mrm.24176
136. van Gemert JHF, Brink WM, Webb AG, Remis RF. High-permittivity pad design for dielectric shimming in magnetic resonance imaging using projection-based model reduction and a nonlinear optimization scheme. *IEEE Trans Med Imaging*. 2018;37(4):1035-1044. doi:10.1109/TMI.2018.2791179
137. O'Reilly TPA, Webb AG, Brink WM. Practical improvements in the design of high permittivity pads for dielectric shimming in neuroimaging at 7T. *J Magn Reson*. 2016;270:108-114. doi:10.1016/j.jmr.2016.07.003
138. Arunachalam K, Maccarini PF, Schlorff JL, Birkelund Y, Jacobsen S, Stauffer PR. Design of a water coupling bolus with improved flow distribution for multi-element superficial hyperthermia applicators. *Int J Hyperth*. 2009;25(7):554-565. doi:10.3109/02656730903124506
139. Trefná HD, Ström A. Hydrogels as a water bolus during hyperthermia treatment. *Phys Med Biol*. 2019;64(11):115025. doi:10.1088/1361-6560/ab0c29
140. Meliadó EF, van den Berg CAT, Luijten PR, Raaijmakers AJE. Intersubject specific absorption rate variability analysis through construction of 23 realistic body models for prostate imaging at 7T. *Magn Reson Med*. 2019;81(3):2106-2119. doi:10.1002/mrm.27518
141. Larkman DJ. The g-factor and coil design. In: *Parallel Imaging in Clinical MR Applications*. Vol 3. Berlin, Heidelberg: Springer Berlin Heidelberg; 2007:37-48. doi:10.1007/978-3-540-68879-2_3
142. Waiczies S, Lepore S, Sydow K, et al. Anchoring dipalmitoyl phosphoethanolamine to nanoparticles boosts cellular uptake and fluorine-19 magnetic resonance signal. *Sci Rep*. 2015;5(1):8427. doi:10.1038/srep08427

143. Aigner CS, Dietrich S, Schmitter S. Three-dimensional static and dynamic parallel transmission of the human heart at 7T. *NMR Biomed.* 2021;34(3):e4450. doi:10.1002/nbm.4450
144. Schmitter S, DelaBarre L, Wu X, et al. Cardiac imaging at 7 tesla: Single- and two-spoke radiofrequency pulse design with 16-channel parallel excitation. *Magn Reson Med.* 2013;70(5):1210-1219. doi:10.1002/mrm.24935
145. Schmitter S, Moeller S, Wu X, et al. Simultaneous multislice imaging in dynamic cardiac MRI at 7T using parallel transmission. *Magn Reson Med.* 2017;77(3):1010-1020. doi:10.1002/mrm.26180
146. Aigner CS, Rund A, Abo Seada S, et al. Time optimal control-based RF pulse design under gradient imperfections. *Magn Reson Med.* 2020;83(2):561-574. doi:10.1002/mrm.27955
147. Takook P, Trefna HD, Zeng X, Fhager A, Persson M. A computational study using time reversal focusing for hyperthermia treatment planning. *Prog Electromagn Res B.* 2017;73(1):117-130. doi:10.2528/PIERB16111605
148. Kok HP, de Greef M, Borsboom PP, Bel A, Crezee J. Improved power steering with double and triple ring waveguide systems: The impact of the operating frequency. *Int J Hyperth.* 2011;27(3):224-239. doi:10.3109/02656736.2011.561270
149. Gianvittorio JP, Rahmat-Samii Y. Fractal antennas: a novel antenna miniaturization technique, and applications. *IEEE Antennas Propag Mag.* 2002;44(1):20-36. doi:10.1109/74.997888
150. Islam MM, Islam MT, Samsuzzaman M, Faruque MRI. Compact metamaterial antenna for UWB applications. *Electron Lett.* 2015;51(16):1222-1224. doi:10.1049/el.2015.2131
151. Werner DH, Ganguly S. An overview of fractal antenna engineering research. *IEEE Antennas Propag Mag.* 2003;45(1):38-57. doi:10.1109/MAP.2003.1189650
152. Webb AG. Dielectric materials in magnetic resonance. *Concepts Magn Reson Part A.* 2011;38A(4):148-184. doi:10.1002/cmr.a.20219
153. Han H, Oberacker E, Kuehne A, et al. Multi-channel RF supervision module for thermal magnetic resonance based cancer therapy. *Cancers (Basel).* 2021;13(5):1001. doi:10.3390/cancers13051001

List of Author's Publications

Publications

Dez. 2018: Prinz C, Delgado PR, Eigentler TW, Starke L, Niendorf T, Waiczies. Toward 19F magnetic resonance thermometry: spin–lattice and spin–spin-relaxation times and temperature dependence of fluorinated drugs at 9.4 T. *Magn Reson Mater Phy.* 2019; 32(1):51-61. doi: <https://doi.org/10.1007/s10334-018-0722-8>.

Jun. 2019: Boehmert L, Kuehne A, Waiczies H, Wenz D, Eigentler TW, Funk S, von Knobelsdorff-Brenkenhoff F, Schulz-Menger J, Nagel AM, Seeliger E, Niendorf T. Cardiorenal sodium MRI at 7.0 Tesla using a 4/4 channel 1 H/ 23 Na radiofrequency antenna array. *Magn Reson Med.* 2019; 82(6):2343–2356. doi: <https://doi.org/10.1002/mrm.27880>.

Feb. 2020: Eigentler TW, Winter L, Han H, Oberacker E, Kuehne A, Waiczies H, Schmitter S, Boehmert L, Prinz C, Trefna H, Niendorf T. Wideband Self-Grounded Bow-Tie Antenna for Thermal MR at 7.0 Tesla. *NMR Biomed.* 2020; 33(5):e4274. doi: <https://doi.org/10.1002/nbm.4274>.

(used in Section 2.2)

Jun. 2020: Oberacker E, Kuehne A, Ozerdem C, Nadobny J, Weihrauch M, Beck M, Zschaek S, Diesch C, Eigentler TW, Waiczies H, Ghadjar P, Wust P, Winter L, Niendorf T. Radiofrequency applicator concepts for thermal magnetic resonance of brain tumors at 297 MHz (7.0 Tesla). *International Journal of Hyperthermia.* 2020; 37(1):549-563. doi: <https://doi.org/10.1080/02656736.2020.1761462>.

Jul. 2020: Han H, Eigentler TW, Wang S, Kretov E, Winter L, Hoffmann W, Grass E, Niendorf T. Design, Implementation, Evaluation and Application of a 32-Channel Radio Frequency Signal Generator for Thermal Magnetic Resonance Based Anti-Cancer Treatment. *Cancers.* 2020; 12(7):1720. doi: <https://doi.org/10.3390/cancers12071720>.

(used in Section 2.3)

Feb. 2021: Han H, Oberacker E, Kuehne A, Wang S, Eigentler TW, Grass E, Niendorf T. Multi-Channel RF Supervision Module for Thermal Magnetic Resonance Based Cancer Therapy. *Cancers*. 2021; 13(5):1001. doi: <https://doi.org/10.3390/cancers13051001>.

Mar. 2021: Herrmann CJJ, Els A, Boehmert L, Periquito, Eigentler TW, Millward JM, Waiczies S, Kuchling J, Paul F, Niendorf T. Simultaneous T₂ and T₂* mapping of multiple sclerosis lesions with radial RARE-EPI. *Magn Reson Med*. 2021; 86(3):1383-1402. doi: <https://doi.org/10.1002/mrm.28811>.

May. 2021: Eigentler TW, Kuehne A, Boehmert L, Dietrich S, Els A, Waiczies H, Niendorf T. 32-Channel Self-Grounded Bow-Tie Transceiver Array for Cardiac MR at 7.0 Tesla. *Magn Reson Med*. 2021; 86(5):2862-2879. doi: <https://doi.org/10.1002/mrm.28885>.

(used in Section 2.1)

Conference Proceedings

May. 2019: Eigentler TW, Winter L, Han H, Oberacker E, Kuehne A, Boehmert L, Trefna H, Niendorf T. Ultra-Wideband Self-Grounded Bow-Tie Antenna Building Block for Thermal Intervention, Diagnostic MRI and MR-thermometry at 7.0 Tesla. *ISMRM 27. Annual Meeting, 2019; #3827.*

May. 2019: Eigentler TW, Boehmert L, Kuehne A, Wenz D, Oberacker E, Han H, Winter L, Niendorf T. Compact Self Grounded Bow Tie Antenna Resonator for Cardiac MRI at 7.0 Tesla. *ISMRM 27. Annual Meeting, 2019; #0436.*

May. 2019: Oberacker E, Kuehne A, Oezerdem C, Millward JM, Diesch C, Eigentler TW, Nadobny J, Zschaeck S, Ghadjar P, Wust P, Winter L, Niendorf T. Power Considerations for Radiofrequency Applicator Concepts for Thermal Magnetic Resonance Interventions in the Brain at 297 MHz. *ISMRM 27. Annual Meeting, 2019; #3828.*

May. 2019: Han H, Wang S, Eigentler TW, Winter L, Grass E, Niendorf T. Design, evaluation and application of a 16-channel Frequency Synthesizer Module for Thermal Magnetic Resonance. *ISMRM 27. Annual Meeting, 2019; #3826.*

May. 2019: Boehmert L, Kuehne A, Waiczies H, Wenz D, Eigentler TW, Nagel AM, Niendorf T. Cardiorenal Sodium MRI at 7.0 Tesla Using an 8-Channel ¹H/²³Na RF Coil Array. *ISMRM 27. Annual Meeting, 2019; #0560.*

Aug. 2020: Eigentler TW, Kuehne A, Boehmert L, Oberacker E, Lippert S, Niendorf T. 32-Channel Lightweight Dipole RF array for Cardiac MRI at 7.0 Tesla. *ISMRM 28. Annual Meeting, 2020; #4037*

Aug. 2020: Han H, Eigentler TW, Grass E, Niendorf T. Multi-Channel RF Power and Phase Supervision Systems Technology for Thermal Magnetic Resonance: Development, Evaluation and Application. *ISMRM 28. Annual Meeting, 2020; #1281*

Aug. 2020: Oberacker E, Diesch C, Nadobny J, Kuehne A, Eigentler TW, Ghadjar P, Wust P, Niendorf T. Patient Specific Planning of Thermal Magnetic Resonance: An EMF Simulation Study in Realistic Glioblastoma Multiforme. *ISMRM 28. Annual Meeting, 2020; #0280*

Aug. 2020: Oberacker E, Kuehne A, Eigentler TW, Diesch C, Nadobny J, Ghadjar P, Wust P, Niendorf T. Multi-Radiofrequency Thermal Magnetic Resonance Targeting Glioblastoma Multiforme. *ISMRM 28. Annual Meeting, 2020; #4138*

Aug. 2020: Oberacker E, Kuehne A, Diesch C, Eigentler TW, Nadobny J, Ghadjar P, Wust P, Niendorf T. RF Power Deposition Optimization Algorithms for Thermal MR Targeting Human Brain Tumors. *ISMRM 28. Annual Meeting, 2020; #0121*

Oct. 2020: Eigentler TW, Kuehne A, Boehmert L, Oberacker E, Lippert S, Niendorf T. 32-Channel Lightweight Dipole RF array for Cardiac MRI at 7.0 Tesla. *ESMRMB 37. Annual Scientific Meeting, 2020; S05.04*

Sep. 2021: Eigentler TW, Nurzed B, Kuehne A, Niendorf T. RF Coil Concepts for Cardiac MRI at 10.5 T and 14.0 T: Does an Increase in Channel Count Help?. *12th Annual Scientific Symposium on Ultrahigh Field Magnetic Resonance, 2021; P6*

Sep. 2021: Herrmann CJJ, Els A, Boehmert L, dos Santos Periquito J, Eigentler TW, Millward JM, Waiczies S, Kuchling J, Friedemann P, Niendorf T. Simultaneous T2 and T2* Mapping of Multiple Sclerosis Lesions with Radial RARE-EPI. *12th Annual Scientific Symposium on Ultrahigh Field Magnetic Resonance, 2021; P6*

Acknowledgements

The last years were challenging, yet also exciting and rewarding for me. My thesis as well as the underlying projects wouldn't have been possible without the extensive support of many people along the way.

First, I want to thank my supervisor Prof. Dr. rer. nat. Niendorf for his support and guidance during all my projects. It was a great mixture of “showing me the direction” and “long leash”. This helped me to find my own path, without getting lost in the sometimes-overwhelming amount of opinions and options. Next, I am grateful to Prof. Dr.-Ing. Marc Kraft for giving me the opportunity to be part of the TU Berlin and supporting my projects.

Further, I want to thank my colleagues-turned-friends at the Berlin Ultrahigh Field Facility, the Physikalisch-Technische Bundesanstalt in Berlin, and MRI.Tools GmbH. A special thanks is dedicated to André Kühne, who provided me with the best professional support I could imagine. No matter which RF-development related question I raised, you were able to help me every single time. Laura Böhmert: Thank you so much for your endorsement during long days of soldering and testing, and for making even the most tedious days in the laboratory a lot of fun. Looking back, I'm really grateful for all the support and knowledge sharing from Christoph Aigner, Sebastian Dietrich, and Sebastian Schmitter – your deep know-how, your openness, and sparring was a true booster for all of my projects. Furthermore, I would also like to thank Lukas Winter, Hana Dobsicek Trefna, Carl Herrmann, Haopeng Han, Ludger Starke, Min-Chi Ku, Daniel Wenz, Jason Millward, Sonia Waiczies, Antje Els, Joao Perquito, and Eva Oberacker as well as the rest of the Berlin Ultrahigh Field Facility for your kind advice and hands-on support whenever needed as well as the great cooperation throughout my PhD journey.

Well beyond my PhD program, I am deeply thankful for every friend in my life and of course my family for always having my back. First of all, Heidi und Gerhard, I could not have wished for better parents. You always have an open ear and an open heart and supported me and every one of my decisions with a “no matter what” attitude. Knowing that you are always there if anything does not work out, even difficult decisions become easy ones. Furthermore, I would also like to thank my brother Matthias with his family Niki, Celina, and Felina, Renate, Karl, Margarete, Andreas, Hedwig, and Wilhelm as well as all other members of my family for guiding me in my decisions and making me who I am today.

Celebrations are always best when shared with friends, and here I don't even know where to begin to honour each and every one namely. I thank my oldest friends from my hometown - Christoph, Peter, Maximilian, Matthias, Daniel, Christof, David, and Manu. I cannot imagine my life without the experiences I made with you and the many memories we share. My curiosity in medical engineering and science was fuelled by my civil service time at St. John's Ambulance in Innsbruck, Austria. Not only did I discover new areas of interest, but throughout the civil service and many years of volunteering, I found friends for life that need to be mentioned within this thesis. I would like to thank Volker, Philip, Daniel, Martin and Clemens as well as all the others for their great support along the way and the countless funny but also stressful moments – I learned a lot. The interest in medical engineering and some lucky coincidences resulted in my first professional position at Medel. It was a great and interesting time, but more importantly I met many great people, that I can still call my friends: Niko, Lisa, Simon, Yasmin, Bernhard, Robert, and Andreas – thank you for all the inspiration, support and fun times. Writing this thesis not only gave me a lot of professional opportunities, but also brought me to Berlin. A big thank you to all my friends in Berlin, who made the new city the sweetest place on earth for me. Jan, Juliane, Rob, Colin, Josie, Anna, and Chris: Thank you for making this such a special place and for ensuring a well-balanced life besides work with a lot of good discussions, and one or two after work drinks, dinner evenings, and parties.

Finally, I want to thank my biggest supporter and best friend. Debbie, without you I would not have been able to move to Berlin, conduct my research, write the thesis, and prepare my PhD defense. You were and are always there to help me with your excellent presentation skills, your brilliant mind, and your bright soul. Your uncompromising support especially during stressful and packed working days made my PhD student time joyful, inspiring, and rewarding. I'm very happy for the memories we were able to share and look forward to the memories we will continue building together.

The best comes at the end, so this last paragraph is reserved for my daughter Svea. You came into my life right at the end of my PhD program and managed to completely turn our lives upside down – in the best possible way. I hope to always be able to see you smile, laugh, and learn. You're only a few months old, yet you teach me about the really important things in life and help me to always focus my perspective.

“Never confuse education with intelligence, you can have a PhD and still be an idiot.”

Richard P. Feynman